DEVELOPMENT AND TESTING OF BRIDGE WEIGH-IN-MOTION METHODS FOR TRUCK CHARACTERISTICS AND BRIDGE LOAD RATING

A Dissertation

by

SHENGYI SHI

Submitted to the Graduate and Professional School of
Texas A&M University
in partial fulfillment of the requirements for the degree of

DOCTOR OF PHILOSOPHY

Chair of Committee,	Matthew Yarnold
Committee Members,	Stefan Hurlebaus
	John Mander
	David Jeong
Head of Department,	Zachary Grasley

May 2023

Major Subject: Civil Engineering

ABSTRACT

This research study developed and quantitatively evaluated the concept of Bridge Weigh-In-Motion (B-WIM) and advanced knowledge within the field. The primary objective of B-WIM systems is to instrument a bridge to obtain the axle information (i.e., weights, number, speed, and spacings) and weight information (i.e., axles and gross) of trucks that cross the structure. A secondary objective of B-WIM is to evaluate the bridge itself. The challenge of B-WIM is to accurately obtain this information through robust sensing technology and post-processing algorithms. B-WIM (compared to pavement WIM) is potentially less disruptive to traffic, more durable, more economical, safer to install, and able to produce accurate truck-traffic data and bridge assessment information. This research study realized these advantages through the development of a B-WIM system that included extensive experimental testing followed by field validation on in-service bridges. A testbed bridge was utilized for preliminary B-WIM system development and testing before the deployment on in-service bridges. A load cell based B-WIM system was developed and quantitatively evaluated. Three in-service bridges were selected, and B-WIM systems for each bridge were developed and deployed. Data were collected and utilized for live load analysis and validation through an independent portable pavement WIM system. The systems on in-service bridges were able to accurately identify truck axle and weight information and the validation results were deemed satisfactory. Side-by-side challenge was investigated for both the load cell and strain gauge systems utilizing the distribution factors. In addition, an approach was developed to identify bridge parameters, such as distribution factors and composite action from B-WIM data. The final bridge evaluations included refined site-specific load ratings. Finally, guidelines for future B-WIM implementation were developed.

DEDICATION

To my parents and wife.

ACKNOWLEDGEMENTS

I would like to express my deepest gratitude to my committee chair, Dr. Matthew Yarnold, and my committee members, Dr. Stefan Hurlebaus, Dr. John Mander, and Dr. David Jeong, for their invaluable insight, guidance and support throughout the course of this research.

I would like to thank many students assisted with instrumentation installation, testing and removal of the B-WIM systems, including Eric Stoddard, Yang Shen, Claire Gasser, Ryan Booth, and Hilaire Garza. I would also like to thank Claire Barden for her help on the bridge load rating work.

Thanks also go to my friends and colleagues and the department faculty and staff for making my time at Texas A&M University a great experience.

Finally, thanks to my mother and father for their encouragement and to my wife for her patience and love.

CONTRIBUTORS AND FUNDING SOURCES

Contributors

This work was supervised by a dissertation committee consisting of Dr. Matthew Yarnold, Dr. Stefan Hurlebaus and Dr. John Mander of the Department of Civil and Environmental Engineering and Dr. David Jeong of the Department of Multidisciplinary Engineering.

The bridge selection information for Section 4 was provided by Dr. Matthew Yarnold. The bridge load ratings in Section 7 were conducted in part by Claire Barden of the Department of Civil and Environmental Engineering.

All other work conducted for the thesis dissertation was completed by the student independently.

Funding Sources

This work was also made possible in part by the Texas Department of Transportation (TxDOT) and the Federal Highway Administration (FHWA) under Grant Number TxDOT 0-7038. Its contents are solely the responsibility of the authors and do not necessarily represent the official views of the TxDOT and FHWA.

NOMENCLATURE

AASHTO	American Association of State Highway and Traffic Officials
B-WIM	Bridge Weigh-In-Motion
CDF	Cumulative Distribution Function
CIP	Cast-In-Place
DAQ	Data Acquisition System
DF	Distribution Factor
GVW	Gross Vehicle Weight
IM	Dynamic Load Allowance
LFR	Load Factor Rating
LTPP	Long-Term Pavement Performance
LVDT	Linear Variable Differential Transformer
ME	Mechanistic Empirical
mph	Miles Per Hour
N/A	Not Applicable
NBI	National Bridge Inventory
PCP	Prestressed Concrete Panel
p-WIM	Portable Weigh-In-Motion
TTI	Texas A&M Transportation Institute
TxDOT	Texas Department of Transportation
WIM	Weigh-In-Motion

TABLE OF CONTENTS

Page

LIST OF FIGURES

Page

LIST OF TABLES

Page

1. INTRODUCTION

1.1. Background

Monitoring the traffic crossing a bridge provides essential information for transportation planning and the assessment of existing pavement and bridge infrastructure. The most widely used method for monitoring the weight of vehicles on the highway is static weigh stations (Lansdell et al. 2017). Although static weigh stations provide accurate weight measurement, they have the disadvantage of requiring all traffic to leave the highway and take a relatively long time to weigh each vehicle. Moreover, the costs of system installation and maintenance are expensive (Deesomsuk and Pinkaew 2010). Pavement Weigh-in-Motion (WIM) systems were developed as a solution to weigh moving trucks. WIM is the process by which vehicles are characterized while traversing a given corridor. This characterization includes the gross vehicle weight (GVW), axle information (i.e., weights, number, and spacings), vehicle classification, and vehicle speed. A pavement WIM system usually has weighing sensors embedded in the pavement. Installation and maintenance of the system have to interrupt the traffic and cut the pavement surface, which causes inconvenience in practices (Wang and Wu 2004).

To overcome some of the challenges of the above systems, Bridge Weigh-In-Motion (B-WIM) was developed. The concept of B-WIM was first proposed in the 1970s by Fred Moses (Moses 1979). The core idea is to instrument a bridge so it may be used as a scale to weigh and characterize the vehicles (namely trucks) passing over the structure. Compared to pavement WIM, B-WIM has many advantages. For example, the

B-WIM systems are installed underneath the bridge structure, and the installation and maintenance can be done without lane closures or causing damage to the pavement. Since the sensors are installed under the bridge, they are almost free from direct vehicle wheel impact and harsh environment, which is beneficial for the durability of the system. The B-WIM system can be portable when using reusable sensors for rapid surveys for heavy trucks on different sites. Furthermore, the B-WIM systems have similar components as bridge health monitoring systems. In the meantime, a B-WIM can be used for bridge assessment and health monitoring with proper design (Christenson et al. 2011). Overall, the B-WIM system is less disruptive to traffic, more durable, more economical, safer to install, and able to produce accurate traffic and bridge assessment data.

1.2. Research Goal and Objectives

The overarching goal of this research study was to develop and quantitatively evaluate a B-WIM system that builds off prior B-WIM research and advance knowledge within the field.

The primary objective was to develop a B-WIM system that reliably identifies the following information for each passing truck:

- Gross vehicle weight.
- Axle weights.
- Number of axles.
- Axle spacings.
- Average speed.

- Vehicle classification (i.e., trucks Class 4 and higher).

Development of the B-WIM system included quantitative evaluation of the accuracy of the results from a reliable and independent source.

The secondary objective of the study was to develop a methodology to evaluate and monitor the bridge's performance utilizing the B-WIM data. This included strategies for identifying bridge parameters such as:

- Live load distribution factors.
- Percent composite action.
- Site-specific load ratings.

1.3. Research Approach

1.3.1. Introduction

The approach used to achieve the research goal and objectives was to divide the research study into seven tasks. Figure 1.1 graphically illustrates these tasks and their interrelationships, along with the corresponding sections within this dissertation. In general, the research included extensive experimental testing, along with substantial code development for the B-WIM algorithms. A summary of each task is provided in the subsections below. The results of each task are presented at length in the following sections.

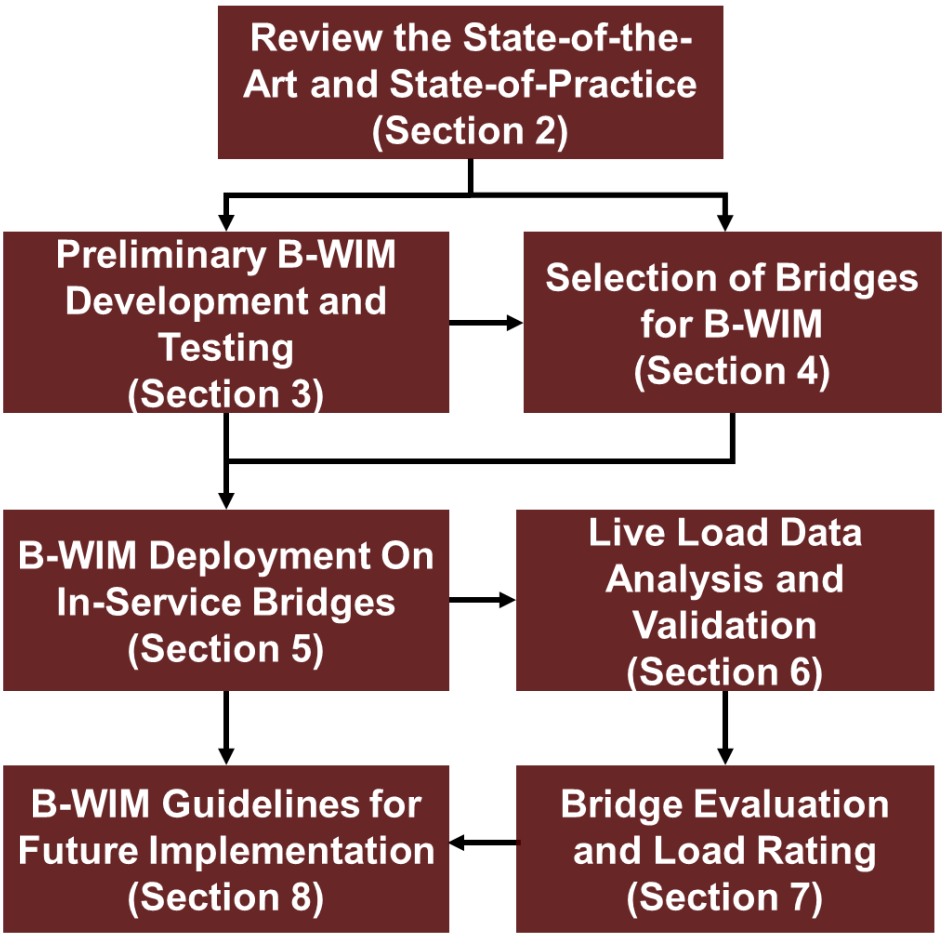

Figure 1.1 Approach Followed to Achieve the Research Objectives.

1.3.2. Review the State-of-the-Art and the State-of-Practice

A comprehensive literature review was compiled related to the development of B-WIM methodologies, experimental testing, and applications. The comprehensive review includes papers published in journals and conferences, along with agency reports. The main focus was on B-WIM data processing algorithms and applications. Key findings of the literature review were documented. These findings were used in this study to guide the development of the preliminary B-WIM system and the in-service bridge selections.

1.3.3. Preliminary B-WIM Development and Testing

A preliminary B-WIM system and data processing algorithms were developed. The Texas A&M University RELLIS Bridge was used as a testbed. Four different types of sensors (i.e., strain gauges, load cells, displacement gauges, and accelerometers) were installed underneath the bridge according to the instrumentation plan designed by the researchers. One tractor-trailer truck and two single-unit trucks were used to conduct full-scale testing. Each truck passed the bridge with various speeds on three different paths. The testing included single truck crossing scenarios and multiple vehicles crossing scenarios. Data were processed mainly for the single truck scenarios. The researchers focused on strain gauge and load cell data when evaluating the B-WIM system performance. Truck information results obtained from different algorithms were compared with the known measured values (i.e., radar gun, measuring tape, and static scales) for their overall accuracy. In addition, preliminary B-WIM setup guidelines were established.

1.3.4. Selection of In-Service Bridges for B-WIM

Three in-service Texas Department of Transportation (TxDOT) bridges for B-WIM were selected. The Texas Highway Freight Network along with energy sector areas were focused. The highway corridors with existing permanent pavement WIM stations were considered for potential validation resources. National Bridge Inventory (NBI) data were utilized to target the vulnerable bridges (for overload) that may benefit from further evaluation. In addition, the selection of the bridges followed the preliminary criteria developed in the previous research task. Due to the COVID-19 travel concerns, it was

preferred to reduce travel to the greatest extent possible. Therefore, bridges in close proximity to the researchers were reviewed first using Assetwise (TxDOT's asset management system). Two prestressed concrete bridges and one steel bridge were selected. After the selection, advantages and challenges of each bridge were summarized.

1.3.5. B-WIM Deployment on In-Service Bridges

B-WIM systems for each of the three selected in-service bridges were developed and the bridges were instrumented consecutively (not concurrently). Sensors and equipment were reused to reduce the costs. The purpose of this decision was so that improvements could be made from each deployment. The specific details of each B-WIM setup (e.g., sensor arrangement, etc.) and installation process were documented. As a critical step to ensure the functionality of the system, calibration tests were conducted after the instrumentation installation. Trucks with known weight were utilized for calibration tests. The calibration trucks crossed the bridge several times with different speeds in different lanes. Most of the calibration tests were conducted with normal flow of traffic.

After the calibration test, the B-WIM system kept recording normal traffic data for one to three months. This length of measurement provided sufficient data to obtain a good spectrum of vehicle classification (i.e., truck Class 4–13). In addition, the data was adequate for evaluation of the structure. A trigger was set for each bridge to record only the truck events rather than small cars (detected by magnitude), which significantly reduced the data storage requirements.

1.3.6. Live Load Data Analysis and Validation

The live load truck data recorded from three B-WIM systems was processed to determine the passing trucks' gross weight, axle weight, axle number, axle spacing, vehicle speed, and vehicle (truck) classification. The algorithms utilized for the data processing were primarily developed in the previous research tasks. The accuracy of the axle detection and weight calculation algorithms for multiple types of sensors were evaluated based on the calibration test results. In addition, several two-hour windows of data after the calibration were processed, and the information for each truck crossing the bridges was determined. These two-hour B-WIM results were compared with independent WIM data as a validation study. The research team (led by Lubinda Walubita) installed portable WIM (p-WIM) units near Bridge #1 (both lanes) and Bridge #2 (outside lane only) specifically for the B-WIM validation study. Overall, the field validation studies showed relatively similar results, which were quantified for each truck criteria.

1.3.7. Bridge Evaluation and Load Rating

A methodology for bridge evaluation and load rating within a B-WIM system was developed. This methodology was evaluated through the three selected in-service bridges that were instrumented for B-WIM purposes. Since these B-WIM setups included strain gauges across the bridge cross section near the midspan, the live load distribution factors (DFs) could be reliably obtained. The DFs calculated for one-lane loaded and two-lane loaded cases were compared with the results from the American Association of State Highway and Traffic Officials (AASHTO) Load Factor Rating

(LFR) method. The B-WIM system of the steel bridge (Bridge #3) had supplemental strain gauges installed along with the web of two beams. The neutral axis of the beams was calculated utilizing the live load data for composite action assessment.

1.3.8. B-WIM Guidelines for Future Implementation

Findings from the previous research tasks of this research study were utilized to develop technical guidelines for B-WIM systems. The guidelines included the following aspects:

- B-WIM system components.
- Bridge selection criteria for B-WIM.
- B-WIM system deployment.
- B-WIM data processing, analysis, and interpretation.

1.4. Contributions

The contributions of the present research study are as follows:

Accuracy quantifications. A lot of prior research focused on experimental testing or numerical simulations for different B-WIM algorithms without independent evaluation of accuracies. In this research study, one non-service testbed bridge and three in-service highway bridges were selected and B-WIM systems were deployed on the bridges. Two of the in-service bridges had portable WIM system installed independently near the bridges. Several time windows were selected and data from both systems were processed and compared to quantify the accuracies of the B-WIM systems.

Load cell application for B-WIM. Conventional B-WIM systems are strain-based. One challenge of B-WIM is getting accurate axle weights. In the preliminary

development and testing task of this research study, a load-cell based B-WIM system was developed and quantitatively evaluated with full-scale field tests. Different weight calculation algorithms were compared and the axle weights can be identified from load cell data with a reasonable accuracy. Details are presented in Section 3.

Sensor layout investigation. Different types of sensors for axle detection and weigh calculation were explored in the B-WIM deployment of the three in-service bridges. LVDTs installed on the bearings of the two in-service concrete bridges showed potential for axle detection purpose (bearing needs to be newer). Strain rosette installed on the girders were explored as alternative axle detection (using the vertical gauge of the rosette) and weight calculation method. The location of the vertical gauge was varied to evaluate the accuracies of different locations. The investigation results from all of the different types of sensors that were compared and summarized in Section 6.

Multiple vehicle presence problem. The muti-vehicle present scenarios especially side-by-side cases remained as a challenge. Utilizing the distribution factors within the area method algorithm gave reasonable results on estimating the GVWs of the side-by-side trucks. This was explored for both load cell systems and strain gauge systems using field test data.

Bridge assessment with B-WIM results. A methodology for bridge evaluation and load rating within a B-WIM system was developed and evaluated through the three in-service bridges. Distribution factors obtained from the live load data improved the load ratings. As a benefit of bridge evaluation using the B-WIM system, actual trucks were load rated to provide an assessment of the in-service performance. In addition, a finite

element model of the selected in-service steel bridge was developed and calibrated based on B-WIM results. The influence of the concrete deck slab modulus and the bearings longitudinal stiffness, on the neutral axis was investigated. See Section 7 for details.

Guidelines for future implementation. Utilizing the findings from the literature, the testbed bridge, and the three in-service bridges, technical guidelines for B-WIM systems were developed in this study. The guidelines cover the bridge selection criteria, B-WIM deployment and data processing and interpretation aspects. Details can be found in Section 8.

Automation. Efforts were made in this research study to minimize the manual procedures for data processing. Algorithms were programed to automatically read the field collected data and divide the data into individual truck passing event. The midspan strain gauges were used to determine the passing lane of the truck or detect side-by-side cases. For single truck passing events, the program automatically selected the corresponding axle detection sensors to obtain truck axle information and classify the trucks. The GVW and axle weights of the truck were then calculated based on the prior information. Corresponding truck information as well as bridge distribution factors were provided as results for further use.

1.5. Organization of the Dissertation

Following this introductory section, the subsequent sections each provide a comprehensive summary of the research tasks followed by a concluding section. Section 2 provides a comprehensive literature review related to the types of WIM, B-WIM algorithms, B-WIM methods, and bridge evaluation. Relevant journal papers and reports

are summarized within the section. Section 3 describes the preliminary development and testing of a B-WIM system in a testbed bridge, including design, installation, and full-scale testing. Also, the results are analyzed and compared. Section 4 summarizes the selection of three in-service bridges for B-WIM with their advantages and challenges. Section 5 and Section 6 document the deployment of the B-WIM system on each in-service bridge and the live load data analysis and validation, respectively. The calibration test and result analysis are also provided in these sections. Section 7 outlines the bridge evaluation of each selected in-service bridge based on B-WIM results and the calculation of the refined load rating factors. Section 8 presents the B-WIM guidelines. Section 9 provides a summary, conclusions, and recommendations for future research.

2. LITERATURE REVIEW

2.1. Overview

This section presents an overview of the state-of-the-art and the state-of-practice in the field of WIM systems. According to the ASTM 1318-09 standard (ASTM 2009), WIM is the process of measuring the dynamic tire forces of a moving vehicle and estimating the corresponding tire loads of the static vehicle. WIM systems are used to determine vehicle characteristics, including vehicle weight information and axle information. Section 2.2 and Section 2.3 summarize the permanent and portable WIM systems, respectively. Section 2.4 thoroughly reviews B-WIM systems.

2.2. Permanent Weigh-In-Motion Systems

2.2.1. Introduction

The Federal Highway Administration and state departments of transportation have commonly used permanent WIM stations. Permanent WIM stations are considered the most accurate and desired method of generating traffic data. However, the associated costs (e.g., installation, operation, and maintenance) are some of the key challenges limiting the statewide installation of permanent WIM stations on a large percentage of the road network.

Efforts to develop and use WIM systems to collect truck weight data in the United States can be traced back to the early 1950s. One of the earliest examples is a WIM system developed in 1951 by Norman and Hopkins at the U.S. Bureau of Public

Roads (Hopkins 1952). The WIM system used a floating reinforced concrete platform that was embedded in the roadway and supported at its corners by strain gauge load cells. The measurements were acquired by taking photographs of the traces from an oscilloscope, as shown in Figure 2.1.

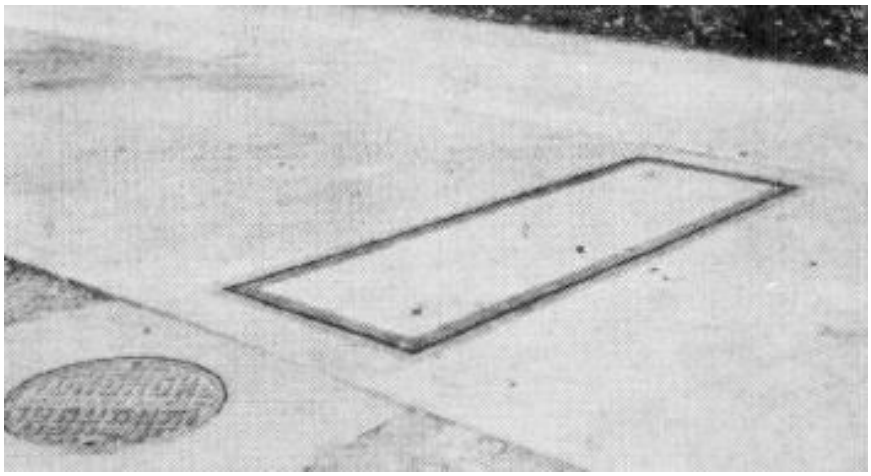

Figure 2.1 WIM System Developed in 1951 (reprinted from Hopkins 1952).

According to the ASTM 1318-09 standard, WIM systems shall be specified to meet the needs of the user for intended applications in accordance with four different types, as shown in Table 2.1. Type IV WIM systems have not yet been approved for use in the United States. They are allowed for conceptual development purposes and for use at weight enforcement stations to detect weight-limit or load-limit violations.

Table 2.1 Functional Performance Requirements for WIM Systems (reprinted from ASTM 2009).

Function	Tolerance for 95% Compliance				
	Type I	Type II	Type III	Type IV	
				Value ≥ lb	±lb
Wheel load	±25%		±20%	5,000	300
Axle load	±20%	±30%	±15%	12,000	500
Axle-group load	±15%	±20%	±10%	25,000	1,200
Gross vehicle weight	±10%	±15%	±6%	60,000	2,500
Speed	±1 mph				
Axle spacing and wheelbase	±0.5 ft				

2.2.2. Components of a WIM System

The major components of permanent WIM systems include (FHWA 2018):

- WIM sensors embedded in the roadway surface or placed on the surface to detect vehicle weight and classification. The combination of WIM sensors and loop detectors within a weighing lane is called the sensor array.
- Electronics to control system functions, measure and process sensor outputs, and provide vehicle records for display and storage.
- Infrastructure that includes conduit, directional bore, cabinet, poles, and junction boxes.

- Support devices, such as power (i.e., alternating current, wind, or solar) devices to operate the WIM electronics, lightning protection, grounding rods, and communication devices to transmit the collected data to a remote server.
- Software and/or firmware installed in the WIM electronics to process sensor measurements and to analyze, format, and temporarily store collected data.

Figure 2.2 shows one example of a typical WIM system design. Two full-lane-width WIM sensors are installed in each lane, providing a double-threshold configuration in this example.

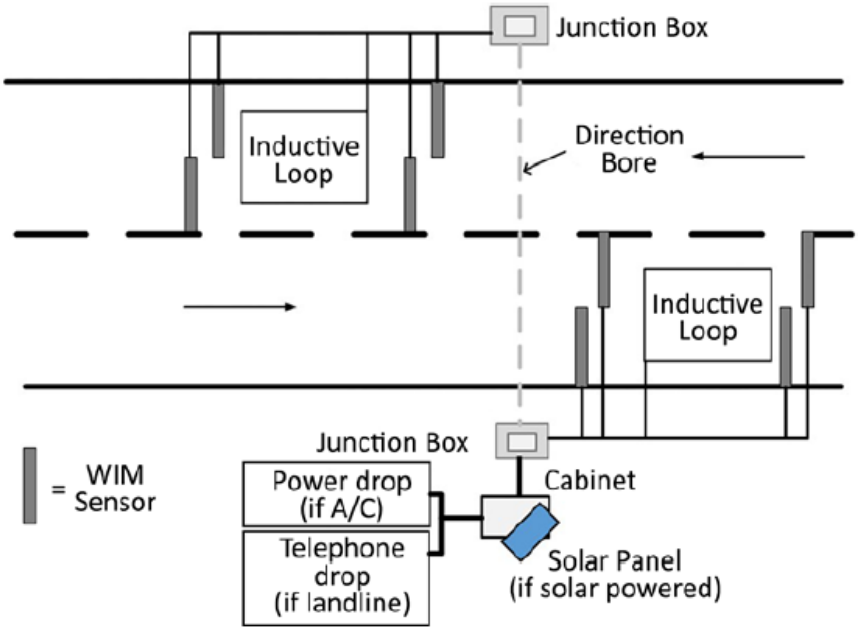

Figure 2.2 Typical Two-Lane Bidirectional WIM System Design (reprinted from FHWA 2018).

2.2.3. Weight Sensors

The weight sensor is the most fundamental and important component in the WIM system because it directly measures the force applied by the vehicles passing over the sensor.

The principal weight sensor types used extensively for permanent WIM system installations include:

- Piezoelectric.
- Bending plate.
- Load cell.

These weight sensor types primarily differ according to their principle of operation. Each sensor type also has its own advantages and disadvantages with respect to its use for WIM systems.

2.2.3.1. Piezoelectric Sensors

Piezoelectric sensors are the most common WIM sensors for data collection purposes (Bushman and Pratt 1998). The basic construction of the typical sensor consists of a copper strand, surrounded by a piezoelectric material, which is covered by a copper sheath. When pressure is applied to the piezoelectric material, a voltage is generated in proportion to the force. The sensor is actually embedded in the pavement, and the load is transferred through the pavement. The characteristics of the pavement therefore affect the output signal. By measuring and analyzing the charge produced, the sensor can be used to measure the weight of a passing tire or axle group. There are a number of variations on the shape, size, and packaging of the sensors produced to obtain better results, easier installation, and longer life.

WIM system designs using piezoelectric weight sensors commonly employ two separate lines of sensors, spaced a distance apart, and are installed perpendicular to the lane direction (a double-threshold system). This increases the accuracy of the weight

measurements and vehicle classification data. Three basic types of piezoelectric sensors are available for WIM applications:

- Piezoceramic sensors.
- Piezopolymer sensors.
- Piezoquartz sensors.

Figure 2.3 shows a double-threshold WIM installation with these sensors.

Figure 2.3 Double-Threshold WIM System Setup with Piezoquartz Sensors (reprinted from Hallenbeck and Weinblatt 2004).

Piezoelectric sensors are low maintenance. In addition, they have low sensitivity to changes in temperature and are easy to install. However, since the sensor relies on structural support from the pavement, if the pavement strength is significantly affected by environmental conditions, the sensor output may also be affected.

2.2.3.2. Bending Plate Sensors

Bending plate sensors use a different approach to determine vehicle weight than piezoelectric sensors. Bending plate weight sensors use strain gauges mounted to the

underside of high-strength, rectangular steel plates called weigh pads. The bending plate scale is typically installed in a lane with two inductive loops and an axle sensor to provide vehicle length and axle spacing information. As a vehicle passes over the bending plate, the system records the strain measured by the strain gauge and calculates the dynamic load. The static load is estimated using the measured dynamic load and calibration parameters (McCall and Vodrazka Jr 1997). Figure 2.4 shows examples of bending plate scales for WIM.

(a) Staggered Bending Plate Installation and Inductive Loops (reprinted from Hallenbeck and Weinblatt 2004)

(b) Bending Plate WIM Scale Used for Vehicle Weighing (reprinted from VPG 2011)

Figure 2.4. Bending Plate Scale.

The bending plate has proven to be one of the most accurate WIM technologies available in the United States, capable of producing consistent data over time when regularly maintained (FHWA 2018).

2.2.3.3. Load Cell Sensors

Load cell–based WIM systems use load cells for the weight sensor. A load cell is a transducer that converts an externally applied force into a proportional electrical signal. The single load cell scale consists of two weighing platforms with a single hydraulic load cell installed at the center of each platform to measure the force applied to the scale. Besides hydraulic devices, most currently available WIM systems with load cells use strain gauge–type sensors. When a force is applied to the sensing element, the strain gauges measure the principal strains on the beam web, which are used to determine the applied load. The sensing element is capable of measuring high forces, is insensitive to the point of loading, and offers good resistance to side loads (VPG 2011). Figure 2.5 shows an example of a load cell scale.

Figure 2.5. Load Cell–Based Weight Sensors (reprinted from IRD 2019).

This sensor is the most accurate among the commercially available WIM sensors. The scale frame and vault have an expected service life of 25 years. On the other hand, the load cell scale is the most expensive and time consuming WIM sensor to install. The installation of a load cell scale requires the use of a crane and the installation of a concrete vault.

2.2.3.4. Fiber-Optic Sensors

Fiber-optic sensors have also been explored for use as weight sensors for WIM systems. They can function at high speeds, have low temperature dependency, do not require an electric supply, and can process data in real time. Several fiber-optic sensor technologies, such as fiber Bragg grating (FBG) and Fabry-Perot interferometry, have already been used for the experimental investigation of pavement behavior and

pavement monitoring with positive results. Fiber-optic strain gauges, telecom fiber-optic cables, and fiber-optic strain plates have been developed (Kara De Maeijer et al. 2019).

2.2.4. Vehicle Classification Sensors

Vehicle classification data are needed for pavement design and rehabilitation as well as for traffic analysis. Most WIM systems also collect data used for vehicle classification. Vehicle classification can be accomplished from the measurements recorded by the weight sensors. However, in some cases, a combination of weight sensors and sensors from a dedicated axle detector installed in the pavement are used.

2.2.4.1. Inductive Loop Detectors

Inductive loops are frequently installed in the roadway as part of the WIM array. They consist of four parts:

- A wire loop of one or more turns of wire embedded in the roadway pavement.
- A lead-in wire running from the wire loop to a pull box.
- A lead-in cable connecting the lead-in wire at the pull box to the controller.
- An electronics unit housed in the controller cabinet. The electronics unit contains an oscillator and amplifiers that excite the embedded wire loop (Klein et al. 2006).

The primary role of loop detectors in WIM systems is to trigger the system to start and stop the weight measurement and classification sequence for each passing vehicle. Dual-loop detectors can be used to provide various information, including

vehicle speed, axle spacing, and vehicle length as the vehicle passes over the WIM station.

2.2.4.2. Cameras

Some WIM systems incorporate automatic number plate recognition or license plate recognition cameras to read vehicle registration plates to catalog passing vehicles. Such systems commonly use infrared lighting to compensate for headlights and poor weather conditions that might affect recognition any time of day.

Another type of camera that may be used for WIM systems is the internet protocol camera, which is a type of digital video camera used to capture a photograph of an entire vehicle from its side to send and receive data via the internet. Such systems provide high-resolution color images or video that may require a central network video recorder to handle the recording and storage. Photo imaging systems such as these are sometimes integrated with WIM systems used for screening purposes in weight enforcement applications, such as virtual WIM. Video cameras are not commonly used with WIM systems designed for traffic data collection purposes but can be used to evaluate and validate vehicle classification algorithms employed by the WIM system in these instances.

2.2.4.3. Laser Scanning

Laser scanning technology is used not only for vehicle presence detection, but also for three-dimensional (3D) vehicle shape recognition and classification. Such systems, often mounted over the traffic lane, typically emit two eye-safe laser beams to scan the

roadway and passing vehicles to create a 3D image of the object. Unlike a traditional camera that collects color information about surfaces within its field of view, a 3D scanner collects distance information about surfaces within its field of view. These distances are then used to reconstruct the 3D position of each point on the subject vehicle. When a vehicle enters the beam, the measured distance decreases, and the corresponding vehicle height is calculated based on simple geometry. As the vehicle moves along, the second beam is broken in the same manner. The vehicle speed and length are estimated by measuring the time difference between the breaking of the two beams. Data collected by the sensor are processed and transmitted in real time. This technology can be incorporated into a WIM system design for truck screening in enforcement applications but may be considered too expensive to employ with WIM systems used for traffic data collection.

2.3. Portable Weigh-in-Motion Systems

Portable WIM systems are relatively new technology compared to permanent WIM systems. As a result, only limited studies have objectively evaluated their applicability, their ease of handling, and the reliability of the obtained data. Several commercial, low-speed portable WIM systems are currently available, such as DAW 300 PC (IRD 2019). This particular system uses portable bending plates that weigh vehicles up to 44,000 lb per axle at speeds up to 4 mph. The manufacturer claims ±3 percent accuracy.

A more precise, low-speed portable WIM system for vehicle speeds of 3 mph is also commercially available. CAPTELS CET 10-4 SLIM weighs vehicles up to 60,000 lb per axle with a declared accuracy of ±2 percent for vehicles traveling at the

recommended speed. This portable WIM system employs metal weigh pads fashioned from strengthened aluminum and covered with a special coating (Kineo 2019).

A highly accurate, slow-speed portable WIM developed by Oak Ridge National Laboratory was originally designed for military use to control Air Force cargo loads. Advanced software features enable tracking and military vehicle location services, as well as calculating vehicle center of balance (Abercrombie et al. 2005).

Kwon (2012) developed a weigh-pad-based portable WIM system and compared it to permanent WIM stations on Minnesota highways. Figure 2.6 shows this particular WIM uses a RoadTrax Brass Linguini piezoelectric sensor. The sensor was placed between two convey belts for rapid road installations. The corresponding results indicated good correlations between the portable and permanent systems in terms of the GVW, speed, and axle specification data.

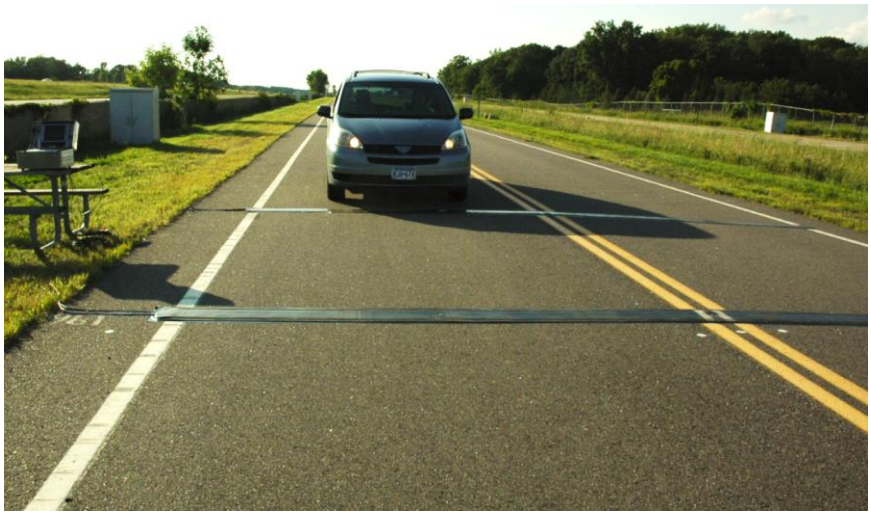

Figure 2.6. Installed Weigh Pads with Air Cavity and the Test Vehicle (reprinted from Kwon 2012).

In 2015, SRF Consulting Group, Inc., evaluated this weigh pad–based portable WIM system (Petersen et al. 2015). During this project, the portable WIM system was deployed 20 times. In general, the system matched automatic traffic recorder volumes within 6 percent and road tube volumes within about 15 percent. On average, speed accuracy was within 5 percent; speed accuracy at many sites was within 2 percent. Classification accuracy generally matched baseline data, although some classes, such as two-axle classes, matched better when an axle spacing–based classification was used instead of a weight-based system. However, there were some noticeable issues. Figure 2.7 shows the damage to the pad caused by weather and vehicles.

Figure 2.7. Weather-Pulled Pads (reprinted from Petersen et al. 2015).

Refai et al. (2014) implemented a portable WIM system to collect traffic data on Oklahoma highways and found it—at merely 10 percent of the cost—to be a viable alternative to permanent systems. Figure 2.8 shows the installation of the system.

Figure 2.8. Two-Lane Portable WIM System Deployment (reprinted from Refai et al. 2014).

Researchers have successfully used the portable WIM system on several Texas highways (Figure 2.9) to collect site-specific mechanistic empirical (ME)-compatible traffic data, with a data accuracy of 87 to 90 percent (Faruk et al. 2016). Key contributing factors to this accuracy improvement have been a rigorous on-site calibration regime and improved sensor installation techniques through the use of metal plates. However, on highway locations or sites (mostly high-volume roads) where the more accurate permanent WIM stations are available, use of portable WIM is not necessary unless as a supplement or where site-specific traffic data are needed. Basically, portable WIMs are very practical and ideal for collecting and generating site- or project-specific traffic data in areas where permanent WIM stations are unavailable, such as most of the farm-to-market roads in Texas.

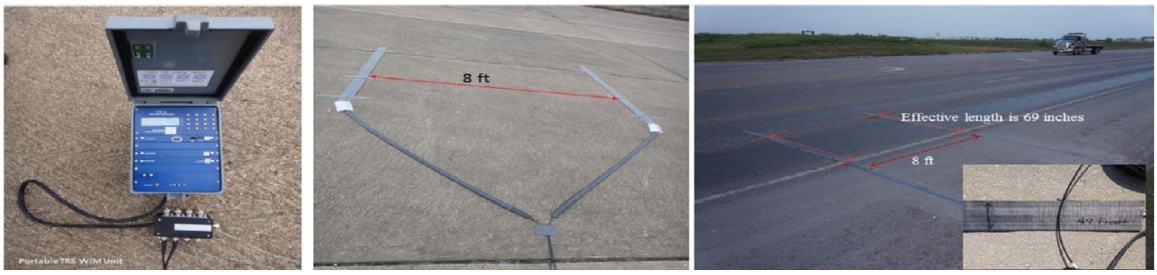

Figure 2.9. Portable WIM Unit and Piezo Sensor Setup on the Pavement Surface (reprinted from Faruk et al. 2016).

Walubita et al. (2021) conducted a study to comparatively evaluate two different sensor installation methods for routine traffic data measurements:

- The pocket tape method.
- The metal plate method.

The two methods, shown in Figure 2.10, were comparatively evaluated in terms of their practicality, simplicity of installation, cost-effectiveness, resource/manpower needs, environmental sensitivity and endurance, consistency, data accuracy, and statistical reliability of the traffic data measurements. The metal plate sensor installation method proved superior to the pocket tape method, attaining an accuracy of about 92.5 percent.

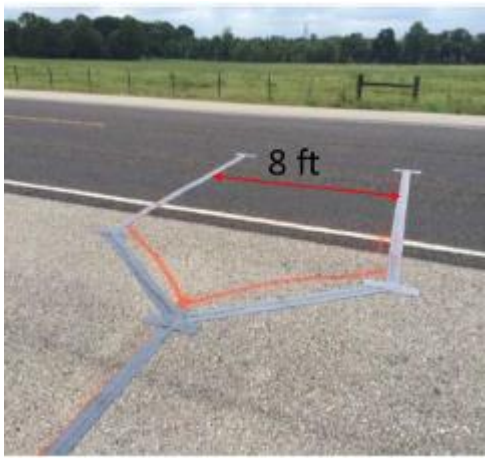

(a) Piezo Sensor Installation Using Pocket Tapes

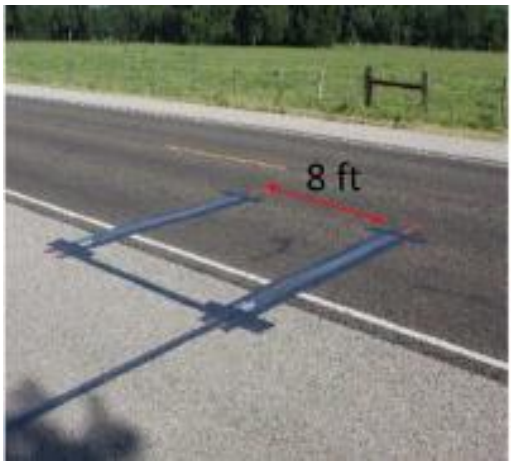

(b) Piezo Sensor Installation Using Custom-Devised Metal Plates

Figure 2.10. Installations of the Two WIM Systems (reprinted from Walubita et al. 2021).

2.4. Bridge Weigh-in-Motion Systems

2.4.1. Introduction

B-WIM is the process of instrumenting a bridge so it may be used as a scale to weigh the vehicles (i.e., trucks) passing over the structure. The overall purpose of B-WIM systems is to classify the truck loading along a given corridor, just the same as permanent or portable pavement WIM. This should include the GVW, axles weights, number of axles, axle spacing, speed, and vehicle classification. B-WIM (compared to pavement WIM) is potentially less disruptive to traffic, more durable, more economical, safer to install, and able to produce accurate traffic data. However, unlike other WIM systems that measure all the vehicle types (i.e., Class 1-13), the B-WIMs are predominantly focused on trucks, namely Class 4 and higher.

Many different research studies and applications of B-WIM have been performed over the last 40 years. However, two main aspects define each system:

- The algorithm used for processing the bridge response data to obtain the truck information described previously.
- The instrumentation (i.e., layout, type of sensors, and data acquisition equipment) measuring the bridge response.

In some cases, there is a third aspect, which includes the type of refined information recorded about the bridge itself (e.g., live load distribution factors). Background on each of these three B-WIM defining aspects is provided below.

2.4.2. B-WIM Algorithms

2.4.2.1. Moses Algorithm

The concept of B-WIM was first proposed by Moses in the 1970s (Moses 1979; Snyder and Moses 1985). The algorithm was based on the fact that a moving load along a bridge induces stresses in proportion to the product of the value of the influence line and the axle load magnitude. For a beam-slab bridge, the measured bending moment at time step *k* can be obtained by summing the individual bending moment of each girder, as shown in Eq. (2.1):

$$M_k^M = ES\sum \varepsilon_i \tag{2.1}$$

where E is the modulus of elasticity, S is the section modulus of the i^{th} girder, and ε_i is the measured strain in the i^{th} girder.

The theoretical bending moment caused by the number of axles on the bridge, at instant *k*, is given by Eq. (2.2):

$$M_k^T = \sum_{i=1}^{N} A_i I_{(k-C_i)} \tag{2.2}$$

$$C_i = \left(L_i \times f\right) / v \tag{2.3}$$

where N is the number of axles, A_i is the weight of axle i, $I_{(k\text{-}Ci)}$ is the influence line ordinate for axle i at scan k, C_i is the number of scans corresponding to axle distance L_i (defined in Eq. (2.3)), L_i is the distance between axle i and the first axle, f is the scanning frequency in hertz, and v is the speed.

The Moses algorithm uses the fact that substantial measurements are available during the truck crossing to smooth out the dynamic components. The dynamic bridge response is "filtered" out by defining an error function, *ER*, which minimizes the sum of the squares of the differences between the measured M_K^M and theoretical M_K^T, with strain records as shown in Eq. (2.4):

$$ER = \sum_{k=1}^{K} \left[M_k^M - M_k^T \right]^2 \tag{2.4}$$

where k is the scan number, K is the total number of scans, and M_K^M is the measured bending moment at scan k.

Differentiating the error function, *ER*, with respect to the axle weights, *A*, allows the unknown axle weights to be solved by using a least-squares fit between the measured and theoretical strains.

B-WIM systems using the Moses algorithm generally tend to be more accurate in estimating GVWs than individual axle weights. This happens because it is difficult to distinguish the contribution of each axle from a long, continuous strain record for the whole truck weight. The final system of equations used to solve axle weight becomes ill-

conditioned, resulting in poor axle weight estimation (O'Brien et al. 2009). Also, the dynamic effect of the bridge and moving vehicles, the transverse position of vehicles, and the presence of multiple vehicles can affect the accuracy of the Moses algorithm.

2.4.2.2. Moving Force Identification

The moving force identification (MFI) method finds the forces that minimize the difference between bridge measurements and what is calculated from the dynamic equations. This method seeks to obtain the complete time history of the vehicle axle forces when a vehicle passes the bridge. This method has the potential to be very accurate in the identification of static axle weights since the complete history of the time-varying forces allow the dynamic effects of the vehicle to be identified and removed when calculating the static axle weights. Several classic MFI methods were developed, including the interpretive method, the time domain method, and the frequency–time domain method.

González et al. (2008) used first-order Tikhonov regularization on a two-dimensional (2D) orthotropic plate bridge model to solve the MFI problem. Four main steps were followed to solve the MFI problem:

- Convert the equilibrium equation of motion to a vector matrix differential equation suitable for dynamic programming.
- Formulate the inverse problem as a least-squares minimization with Tikhonov regularization.
- Use dynamic programming that provides an efficient solution to the problem.
- Solve for the optimal regularization parameter using Hansen's L-curve method.

Tikhonov regularization was used to provide a bound to the error and smoother solutions to the MFI problem. The L-curve was chosen to obtain the optimal regularization parameter. A finite element (FE) method was used to construct an equivalent dynamic model of the bridge. The wheels of a two-axle vehicle were treated as individual moving forces.

Rowley et al. (2009) conducted experimental testing of an MFI B-WIM algorithm. The MFI algorithm requires an FE mathematical model that accurately represents the static and dynamic behavior of the bridge structure. The method of dynamic programming requires that the equilibrium equation of motion be converted to a discrete time integration scheme. In this case the equilibrium equation of motion is reduced to an equation in modal coordinates defined by Eq. (2.5):

$$\left[I\right]_{n_z x n_z}\left\{z\right\}_{n_z x_1}+2\zeta\left[\Omega\right]_{n_z x n_z}\left\{z\right\}_{n_z x_1}+\left[\Omega\right]_{n_z x n_z}\left\{z\right\}_{n_z x_1}=\Phi^T\left[L\left(t\right)\right]_{n_{dof} x n_g}\left\{g\left(t\right)\right\}_{n_g x_1} \quad (2.5)$$

where Φ is the modal matrix of normalized eigenvectors, n_z is the number of modes to be used in the inverse analysis, [Ω] is a diagonal matrix containing the natural frequencies, ζ is the percentage damping, and [*L(t)*] is a time-varying location matrix relating the n_g applied vehicle forces of the vector *g(t)* to the degrees of freedom (n_{dof}) of the original FE model.

Fitzgerald et al. (2017) investigated the use of an MFI algorithm with Tikhonov regularization to calculate vehicle axle loads. This method has the advantage of allowing the choice of regularization parameter to be based on a realistic calculated axle-weight ratio. The axle forces are then calculated by minimizing the objective function (*Y*), shown in Eq. (2.6):

$$Y\left(X_j, g_j\right) = \sum_{j=1}^{N}\left(QX_j - d_j\right), I\left(QX_j - d_j\right) + \left(g_j, Bg_j\right) \quad (2.6)$$

where N is the number of time steps, d is a vector of bridge measurements at each time step, Q extracts the relevant model displacements corresponding to the bridge measurements used, I is the identity matrix, and B is the Tikhonov regularization parameter.

Lai et al. (2019) introduced an MFI-based B-WIM approach with mode superposition to reduce the number of degrees of freedom of the system. Bellman's optimality principle and Tikhonov regularization were used to find the load force in the inverse dynamic programming. A prestressed concrete bridge model and a three-axle truck model were developed to conduct simulations and investigate the accuracy of the presented algorithm. The results showed that this approach had better estimation of the GVW than the individual axle weight. Also, the research found:

- The number of measurements, sampling rate, signal noise level, and vehicle speed affect the accuracy of the method.
- Too low or too high of a sampling rate decreases the accuracy dramatically.
- Increasing the number of measurements increases the accuracy but negatively affects the B-WIM application.
- The MFI B-WIM approach is a robust event with a high noise level.

Wu and Law (2010) presented a stochastic identification algorithm that can deal with complex random excitation forces with large uncertainties and system parameters with small uncertainties. The algorithm is formed based on the established statistical relationship between the random excitation forces and the structural responses, which

are assumed to be Gaussian and are represented by the Karhunen-Loéve expansion. A simply supported Euler-Bernoulli beam was modeled and simulated with multiple moving loads. Case studies including the effect of the number of samples used and the level of randomness were conducted to check on the robustness of the proposed algorithm.

Although the MFI methods have the potential to be very accurate, they usually require detailed FE models and expensive computational resources. Furthermore, most of the current MFI theories are based on simple bridge models.

2.4.2.3. Influence Line Algorithms

In recent years, extensive research has been carried out to improve the original Moses algorithm in terms of vehicle weight estimation (axle and gross). For the Moses algorithm, the accuracy of the influence line is critical for the B-WIM system to achieve an accurate identification. Znidaric and Baumgartner (1998) conducted a study to monitor the effect of correct choice of the influence line on B-WIM accuracy. Two bridge lengths were chosen for this study, a short 2 m (6.6 ft) span and a longer 32 m (105 ft) span. For the simulated signals, influence lines within the two limit cases (i.e., the ideal simply supported and completely fixed support conditions, as Figure 2.11 shows) were selected. The signals were later reprocessed using other influence lines. The prediction of axle weights was very inaccurate if a wrong influence line was chosen, especially for the longer 32-m span bridge. Correct calculation of the influence line is therefore of critical importance to obtain accurate B-WIM results. Znidaric and Baumgartner (1998) proposed revising the theoretical influence line by adjusting the

support conditions and smoothing the peaks interactively to take account of the smeared footprint to achieve better consistency with the real situation.

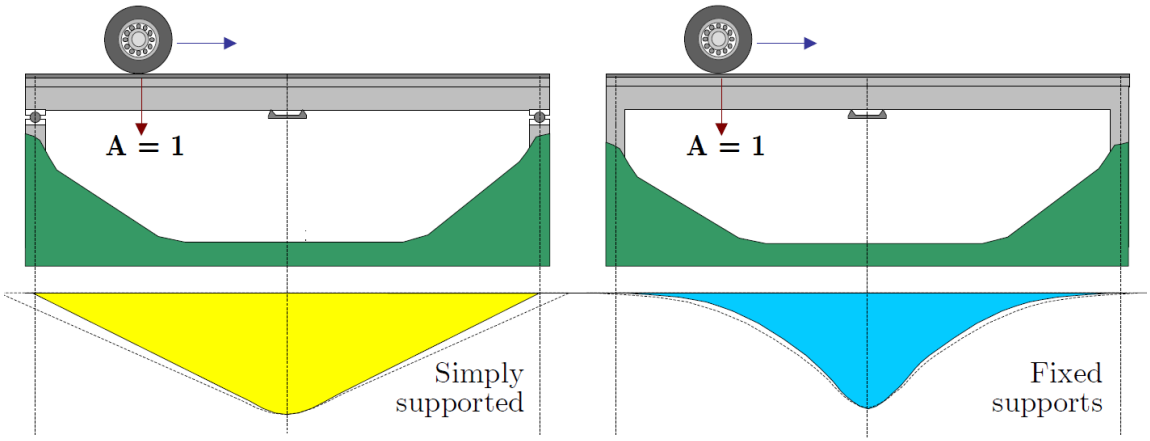

Figure 2.11. Midspan Bending Moment Influence Lines for Simply and Fixed Supported Bridges (reprinted from Quilligan 2003).

McNulty (1999) developed a point-by-point graphical method of manually deriving the influence line from the bridge response to the calibration truck. A crude estimate of the influence line is adjusted on the basis of a graphical comparison of theoretical and measured strain in a spreadsheet program, usually Excel®. The method can be used in all circumstances, but its accuracy relies on the skill of the operator since it requires the manual adjustment of each point.

O'Brien et al. (2006) presented a method to generate the influence line from direct measurements. A matrix equation was constructed for the calculation of influence ordinates for a bridge from measured load effects. A three-axle pre-weighed truck was used for field tests. By using the least-squares method, the error function defined in Eq. (2.4) is minimized with respect to the influence ordinate, while the axle weights of the

calibration vehicle are already known. Thus the measured response of a load effect is converted into the influence line of that effect. Zhao et al. (2015) verified this method using field tests.

To generate a continuous influence line, some researchers adopted a polynomial function to describe the influence line. Yamaguchi et al. (2009) applied B-WIM to a two-span continuous curved bridge with skew. The influence lines were constructed in the form of a ninth-degree polynomial function for local strains, and the optimal coefficients of the polynomial function were determined by minimizing the error function.

Ieng (2014) pointed out that O'Brien's method did not take into account the variability of the effects of the calibration vehicle on the bridge and is not robust enough for B-WIM applications. Ieng improved the influence line estimation by using the maximum likelihood estimation principle, which is less sensitive to one specific signal that is usually corrupted by noise.

2.4.2.4. Influence Area Method

Ojio and Yamada (2002) proposed a method to calculate vehicle weights based on the principle that the area under the response curve can be expressed as the product of the GVW and the area under the influence line, that is, the influence area. This can be shown by Eq. (2.7):

$$A = \sum_{n=1}^{N} P_n \int_{-\infty}^{+\infty} IL(x)\,dx = GVW \sum_{n=1}^{N} \int_{-\infty}^{+\infty} IL(x)\,dx \tag{2.7}$$

where A is the influence area, N is the number of axles of the vehicle, P_n is the axle weight of the nth axle, $IL(x)$ is the function of the influence line, and x is the position of the first axle.

The area under the response curve can be obtained by numerically integrating the response of the bridge. Thus, with a calibration vehicle of a known weight, the weight of another vehicle with unknown weight can be obtained by Eq. (2.8):

$$GVW = A \times \frac{GVW_c}{A_c} \tag{2.8}$$

where GVW is the GVW of the unknown vehicle, A is the area under the response curve for the vehicle with the unknown weight, A_c is the area under the response curve for the calibration truck, and GVW_c is the GVW of the calibration truck.

Using this method, the speed of the vehicle was calculated from peak strains at different longitudinal locations on the structure. A direct vehicle speed was calculated by dividing the distance between the two locations by the time interval between the corresponding peaks. While the implementation of this algorithm is easy and does not require axle detections, one obvious disadvantage is that identifying the weight of individual axles becomes very difficult.

2.4.2.5. Reaction Force Method

Ojio and Yamada (2005) also proposed a method where the measured reaction force at the support is used to calculate the axle weights. This method uses the influence line of the reaction force of a simply supported bridge. An important feature of such an influence line is that a sharp edge appears at the beginning of the influence line. The axle

weights can be calculated from the height of the edge. This method is simple and easy to use. However, the disadvantages are:

- The dynamic effect of the axle forces is not accounted for, which causes errors in the identified axle weights.
- The reaction forces are difficult to measure in practice.
- The method is only applicable to bridges without a skew angle.

2.4.2.6. Methods for Multiple Vehicles

One of the challenges for B-WIM techniques is identifying multiple vehicles simultaneously on the structure. Accordingly, researchers have conducted studies to address this issue. Quilligan (2003) proposed a 2D B-WIM algorithm as an extension of the Moses algorithm. In the 2D algorithm, the influence surface concept is used instead of the influence line. Influence surfaces are analogous to influence lines of beam structures. The influence surface represents the influence of a unit concentrated load, $P(x,y) = 1$ at position (x,y), on displacement or strain resultants at a measurement point $Q(u,v)$, as shown in Figure 2.12. For the purposes of B-WIM, the influence surface can be defined as the bending moment or strain at the point of measurement due to a moving wheel load moving across the bridge. The axle weights can be found by following the same minimization routine as used in the Moses algorithm. However, the disadvantage of this algorithm is that it requires a detailed FE model of the bridge, which comes at the cost of complex calculations and time-consuming calibrations.

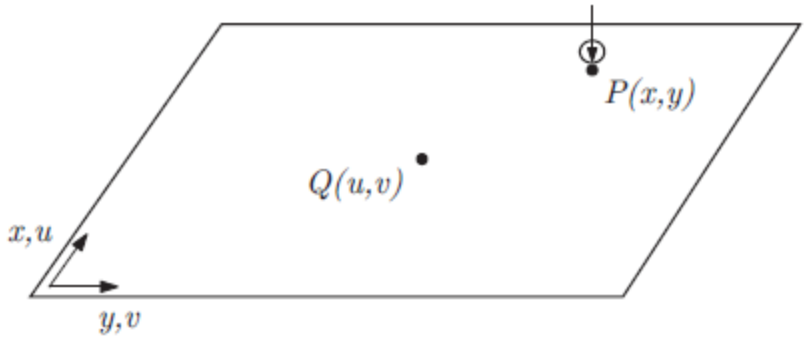

Figure 2.12. Influence Surface Method (reprinted from Quilligan 2003).

Žnidarič et al. (2012) proposed a sensor strip method as an enhancement of the original Moses algorithm. The idea is to separate sensors into groups for each lane. Instead of summing the strains into one value at each time step, the strains are summed within each group to provide extra information on the load distribution of traffic, which increases the solvability of the system equations using linear methods. The strips method was tested on bridges in Slovenia and Brazil and showed that the method significantly increases the accuracy of a B-WIM system.

Chen et al. (2019) developed a method considering the presence of multiple vehicles. For vehicles driving in different lanes, a distribution factor is introduced to decouple the tangled strain response due to the spatial effect of a bridge. The distribution factor can be calibrated by driving a test vehicle in each lane. The original signal can be filtered using empirical mode decomposition to obtain a quasi-static response of the bridge, as shown in Figure 2.13. A series of indoor experiments considering two vehicle models with different scenarios was conducted. The experimental results illustrated that

this method is feasible under the designed scenarios without much variation in the identification accuracy.

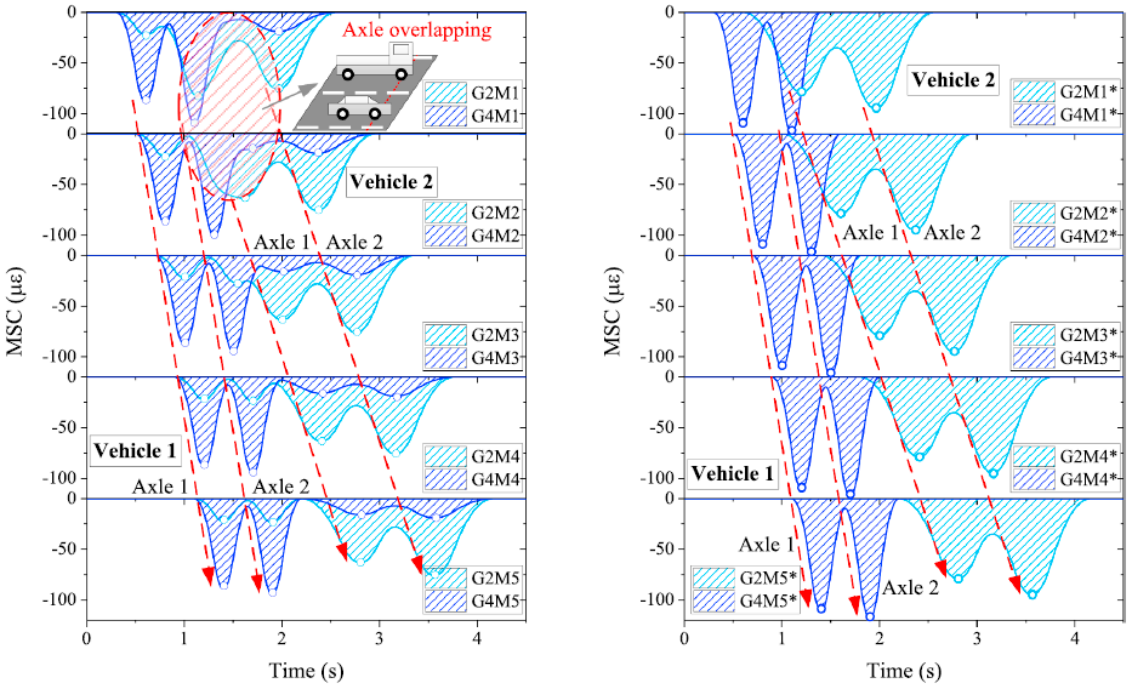

Figure 2.13. Method Considering Load Spatial Distribution on a Bridge (reprinted from Chen et al. 2019).

2.4.2.7. Wavelet Transform

Wavelet analysis is a technique that provides a powerful tool to solve many difficult engineering problems. This exciting new method has been applied to many fields such as signal processing, data compression, computer graphics, etc. The wavelet transform is a solution to overcome the shortcomings of the Fourier transform. Wavelet analysis can be used to provide an enhanced time-frequency resolution desirable for B-WIM applications.

Chatterjee et al. (2006) used a reverse biorthogonal wavelet basis function *rbio2.4* to analyze nothing-on-the-road (NOR) signals. Experiments were conducted on a concrete box culvert using strain gauges with a 512 Hz sampling frequency and a test vehicle with five axles. As Figure 2.14 shows, all five axles can be visualized (five pronounced peaks) after performing continuous wavelet transform. Researchers concluded that the wavelet approach (using *rbio2.4*) is highly effective at identifying vehicle axles.

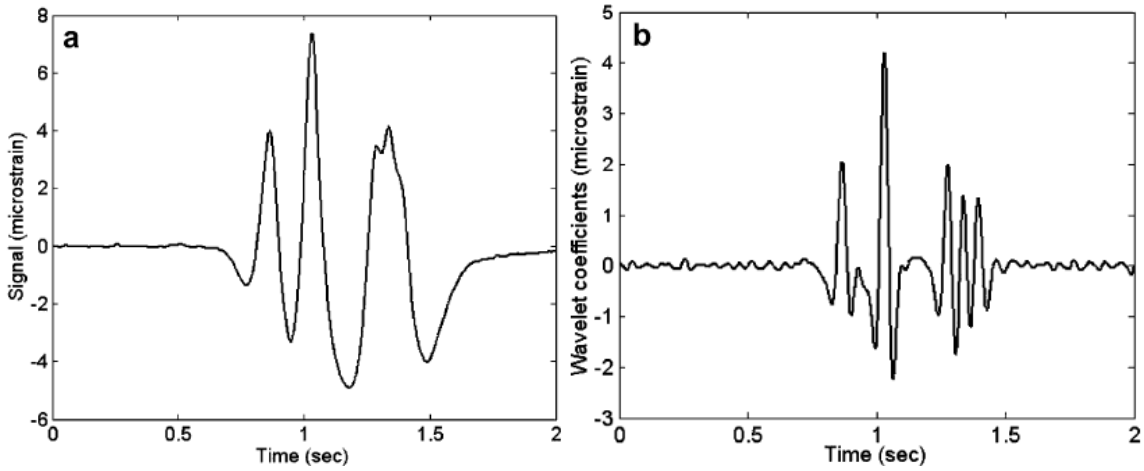

(a) Original Strain Signal (b) Strain Signal after Wavelet Transformation

Figure 2.14. Strain Signal and Wavelet Transform of a Test Vehicle (reprinted from Chatterjee et al. 2006).

Lechner et al. (2010) developed a B-WIM system with one single displacement sensor and the wavelet-based signal processing approach to determine vehicle speed, the distance between axles, and the axle load. Two bridges were instrumented in this study. Linear variable differential transformer (LVDT) displacement sensors with a detection limit of 30 mm were mounted under the bridges next to the cracks, as shown in Figure

2.15. The number of axles, the distance between axles, and the speed of the vehicle were obtained from the crack displacement signal by means of wavelet decomposition. In a subsequent step, the axle loads were found by optimizing the measured crack displacement signal, which can be approximated by a superposition of influence lines. However, the oscillating behavior of bridges caused by heavy vehicles and uneven road surfaces on the bridge had a negative effect on the result quality.

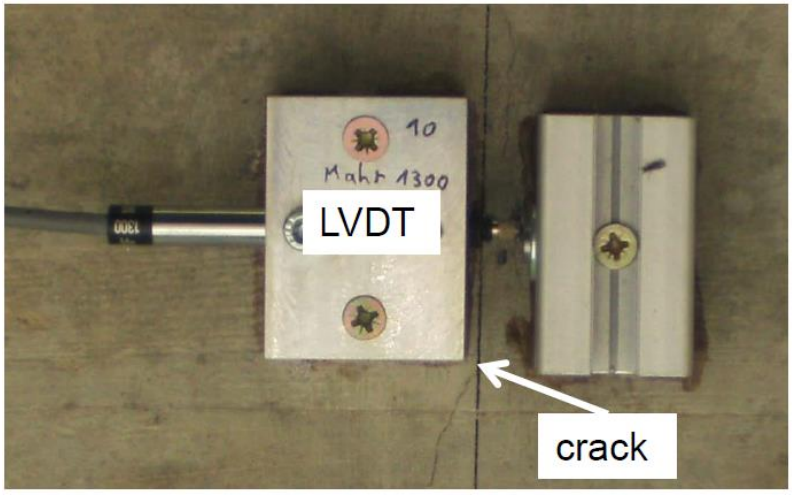

Figure 2.15. LVDT Sensor Installed under the Bridge and Existing Crack in the Bridge Structure (reprinted from Lechner et al. 2010).

Yu et al. (2017) employed the wavelet technique to identify vehicle axles from the signals of the bridge global responses (i.e., weighing sensors). Numerical simulations were conducted, and the effect of sampling frequency, road surface condition, and measurement noise on the identification accuracy were investigated. The sampling frequency of the data acquisition system had significant influence on the identification accuracy. A higher sampling frequency leads to sharper peaks in the transformed signal, but the results are influenced by noises. Reduced sampling frequency increases the scale

of the peaks induced by the vehicle axles, which decreases the effect of noise, but it is difficult to identify peaks, especially in cases where vehicles travel at relatively higher speeds.

2.4.2.8. Other Methods

He et al. (2019) developed a novel B-WIM algorithm called the virtual axle (VA) method. In this method, a vehicle is assumed to have a large number of VAs that are evenly distributed in the longitudinal direction and can cover the whole range of the wheelbase. All axles other than the true ones are assumed to have zero weight. Pre-calibrated bridge influence lines, measured bridge responses, and pre-acquired vehicle speeds are used to identify the true axles and their weights. Figure 2.16 shows an example of a three-axle truck. Scaled vehicle-bridge interaction model tests were carried out, and the VA method showed good accuracy (i.e., less than 7.6 percent error for axle weight). The advantage of the VA method is that once vehicle speed is known, axle detection and weight prediction can be completed by only one weighing sensor.

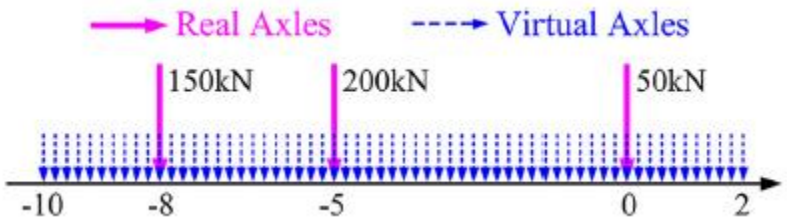

Figure 2.16. Real and Virtual Axles of a Three-Axle Truck (reprinted from He et al. 2019).

Kim et al. (2011) developed a new algorithm for extraction of the influence line and the load position and magnitude from the time signal of strains measured in the deck

plate of a bridge. The overall layout of the method proposed is very similar to Moses' original algorithm. However, an optimal linear filter was used to minimize the error function. The influence line can be calculated as an optimal linear filter that, applied to the autocorrelation of the wheel load signal, gives the cross correlation between the measured time signal and the wheel load signal. A field test was conducted with strain gauges attached to the steel deck plate. The highly local deck plate response gave very good axle weight and gross weight estimation results.

Kim et al. (2009) developed a B-WIM algorithm based on artificial neural networks (ANNs). The algorithm is formed by two neural networks, one for the GVW calculation using the signal from the weighing sensors and one for the axle weight calculation using the signal from the free-of-axle detector (FAD) sensors. The training data were acquired from an adjacent pavement-based WIM station. Field tests found that the developed B-WIM algorithm based on the ANN shows similar accuracy with the traditional B-WIM algorithm using the influence line concept. Since the proposed ANN algorithm does not require any knowledge of the bridge behavior, it could serve as a potential tool to address the issues faced by the traditional B-WIM algorithms, such as application on long-span bridges and bridges with a rough road surface and the identification of multiple vehicles.

Zhao et al. (2012) investigated a new method of filtering the strain signal. A filtered B-WIM algorithm was developed and verified based on field WIM data. By applying filters to the measured moment strain response by removing the effect resulting from bridge dynamic, multi-span interaction, time delays, and boundary conditions,

researchers obtained the true static response as required for WIM weight calibration. This new filtered algorithm provides improved predictions in both single-axle weights and GVWs. This algorithm can be illustrated with Eq. (2.9):

$$M^{WIM} = M^{Load} + M^{Vibration} + M^{Stiffness} + M^{Boundary} + M^{Time} \quad (2.9)$$

where M^{WIM} is the moment from WIM testing, M^{Load} is the moment effect from loads, $M^{Vibration}$ is the moment effect from vibration, $M^{Stiffness}$ is the moment effect from elastic stiffness, $M^{Boundary}$ is the moment effect from boundary conditions, and M^{Time} is the moment effect from time delay.

Jian et al. (2019) introduced a traffic-sensing methodology in combination with influence line theory and computer vision technique. A local regression algorithm named locally weighted scatterplot smoothing (LOWESS) is used to achieve the filtering process in the time domain so that the static strain induced by the vehicle can be obtained. The LOWESS uses a polynomial regression model. The advanced convolution neural network–based computer vision algorithm, named YOLO V3, was applied to fulfill the vehicle recognition tasks. With the installation of strain gauges and the computer vision technology, GVW and real-time vehicle classification can be achieved. Figure 2.17 shows the vehicle recognition from the monitoring camera, and Figure 2.18 shows the installation of the B-WIM system for the tested bridge.

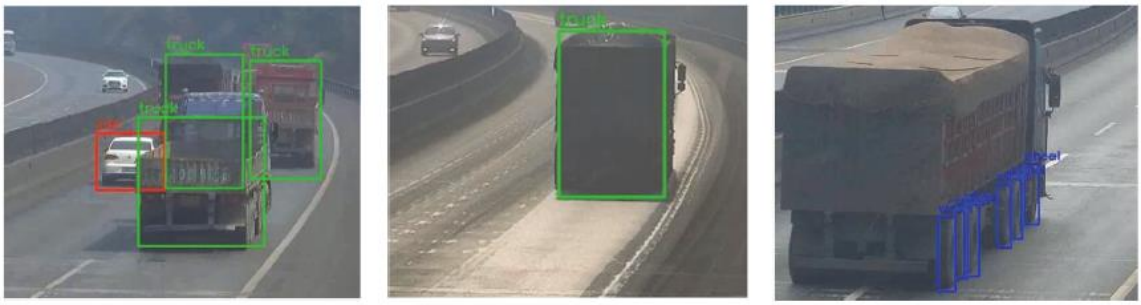

Figure 2.17. Vehicle Recognition Results for Different Scenarios (reprinted from Jian et al. 2019).

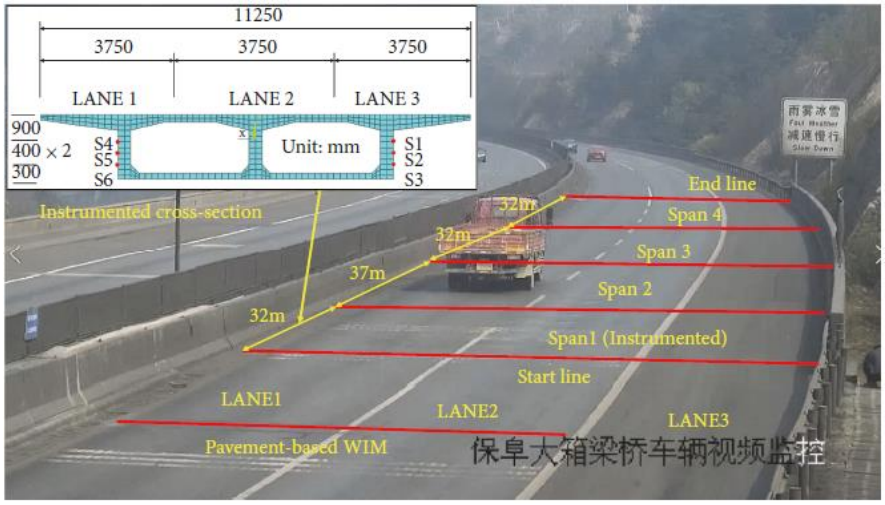

Figure 2.18. Instrumented Section of the Tested Bridge (reprinted from Jian et al. 2019).

2.4.3. B-WIM Instrumentation Methods

2.4.3.1. Introduction

An on-site B-WIM system usually consists of a data acquisition system, a communication system, a power supply system, and sensors, as shown in Figure 2.19.

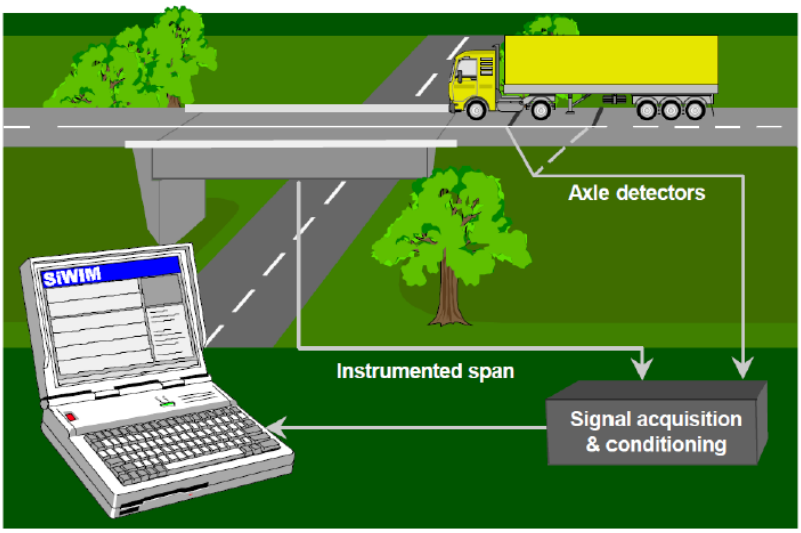

Figure 2.19. Typical B-WIM System (reprinted from O'Brien and Kealy 1998).

The sensors can be divided into two main categories, axle-detecting sensors and weighing sensors. The following sections introduce the typical instrumentation approaches for B-WIM systems and the types of sensors used.

2.4.3.2. Axle Detectors

Axle-detecting sensors are used to identify the presence of vehicle axles from which the speed and axle spacing can be calculated in a B-WIM system. Axle detection is an indispensable part of the B-WIM system. The traditional instruments for axle detection include tape switches and pneumatic tubes. However, the installation of axle detectors on the pavement usually requires lane closure. In addition, the poor durability of sensors can diminish the advantage of the B-WIM systems over the pavement-based WIM systems.

There has been a significant emphasis in recent years to develop B-WIM systems that do not require axle detectors on the road surface. This allows installation,

maintenance, and replacement to be carried out without interfering with traffic. This is an important advantage on busy routes where worker safety and congestion are key issues. In Europe, FAD or NOR data acquisition was proposed in the Weighing-In-Motion of Axles and Vehicles for Europe project (Jacob and O'Brien 2005) and is becoming the prevailing type of B-WIM. The basic idea of the FAD approach is to use FAD sensors to replace traditional axle detectors on the road surface. The FAD sensors measure the local strain responses and pick up a sharp peak upon each axle passage above the sensor location. However, the FAD algorithm is not applicable to all types of bridges. Kalin et al. (2006) summarizes the appropriateness of different types of bridges for FAD. In general, the bridges suitable for the FAD algorithm should have the following:

- A short span length. Relatively long spans can be used with transverse supports. Secondary members, such as transverse cross beams or stiffeners, are required to divide the bridge into sub-spans. This is because longer spans have joint contributions of several axles, which make it difficult to distinguish individual axles.
- A thin superstructure for slab bridges (i.e., less than 15 inches). A thick slab ‘‘smears’’ the peaks induced by the vehicle axles.
- A smooth road surface and approach span. A rough surface condition causes significant dynamic effects, which impose additional peaks in the signal.
- The types of bridges that have already been tested using the FAD approach include orthotropic deck bridges, short-integral bridges with a slab

superstructure, and beam-slab bridges with secondary members. Figure 2.20 shows these structures.

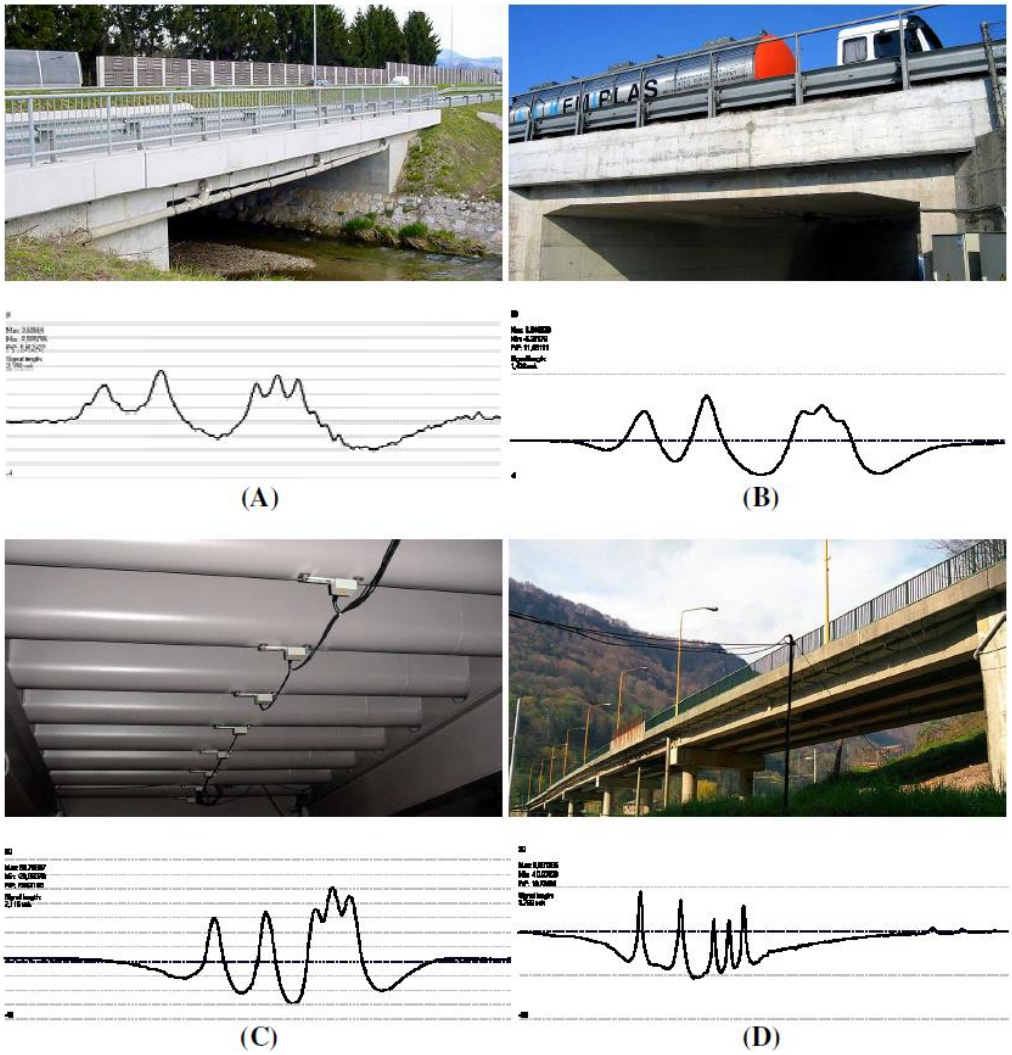

Figure 2.20. Four Bridges Tested with NOR Axle Detection along with the Measured Response (Peaks Indicate Axles) (reprinted from Kalin et al. 2006).

In the case of beam and slab bridges (girder bridges), the strains in the slab are sensitive to the transverse location of the vehicle on the structure. To address this issue, O'Brien et al. (2012) proposed a novel axle detection system using shear strain sensors

based on the assumption that each axle passage induces a sudden change in the shear strain. Numerical simulations were carried out to test the concept of using a shear strain sensor to detect axles. The preliminary recommendation for the location of the axle detector is at the interface of the web and the flange. However, further work is needed to assess the feasibility of this method.

2.4.3.3. Strain Measurement–Based B-WIM

The selection of an appropriate type of sensor for strain measurement becomes crucial to ensure the accuracy of the measurement and reliable operation of the system. Strain responses are used in modern commercial B-WIM systems. These sensors are commonly used within B-WIM systems for overall vehicle weight detection. However, there are methods for using strain gauges for axle detection. Foil strain gauges have been commonly used for strain measurements. When the measured material is strained, the foil deforms and causes the electrical resistance to change. This change is calibrated to reflect the equivalent change in strain. Foil strain gauges can be attached to the surface of the structural components. They are cheap and have acceptable accuracy, which makes them suitable for experimental tests and short-term measurements. However, they are less suitable for long-term field measurements due to their poor durability and susceptibility to electromagnetic interferences and environmental changes.

Kolev et al. (2016) used foil strain gauges for a B-WIM study for the Connecticut Department of Transportation. The Meriden Bridge (steel girder) located at I-91 N in Connecticut was used for field evaluation. González and OBrien (1998) carried out a

feasibility study of B-WIM in orthotropic steel decks. The stiffeners were instrumented with foil strain gauges and proved sufficient.

Vibrating wire strain gauges operate on a very different concept than electrical resistance gauges. They work based on the principle that the change in strain causes a change in the tension in the wire (inside the gauge), which leads to a variation in the resonant frequency of the wire. Vibrating wire strain gauges have good durability, and their installation requires little surface preparation. The historic drawback of vibrating wire strain gauges is that they have a low scanning rate. However, recent advancements now allow these sensors to sample relatively high (200 Hz). This is still not to the same level as electrical resistance gauges.

Fiber-optic sensors, especially FBG sensors, have become increasingly popular in the field of bridge instrumentation. FBG sensors use the relationship between the change of the wavelength in the reflected light spectrum and the strain induced by forces or temperature changes to measure the strain. FBG sensors have the following advantages when compared to conventional strain gauges:

- FBG sensors are immune to electromagnetic interferences, which eliminate noise from external sources to a certain degree.
- FBG sensors have good durability, which makes them suitable for long-term measurements.
- FBG sensors are small and can be multiplexed, which allows for easy installation of multiple sensors on large structures.

These advantages make FBG sensors a candidate for B-WIM applications. However, the cost of FBG sensors and the data acquisition system required is a disadvantage over the other types of strain gauges.

Chen et al. (2018) introduced an alternative B-WIM system with long-gauge FBG sensors. Compared to conventional point sensors, long-gauge FBG sensors are more robust. An in-situ test on an expressway bridge was performed to initially verify its feasibility. The bridge used in this test was a simply supported reinforced concrete bridge, as Figure 2.21 shows. Positive results were obtained regarding the use of FBG sensors for B-WIM systems. The total relative error of speed and wheelbase monitoring was around 5 percent, and the error for gross weight was around 7 percent.

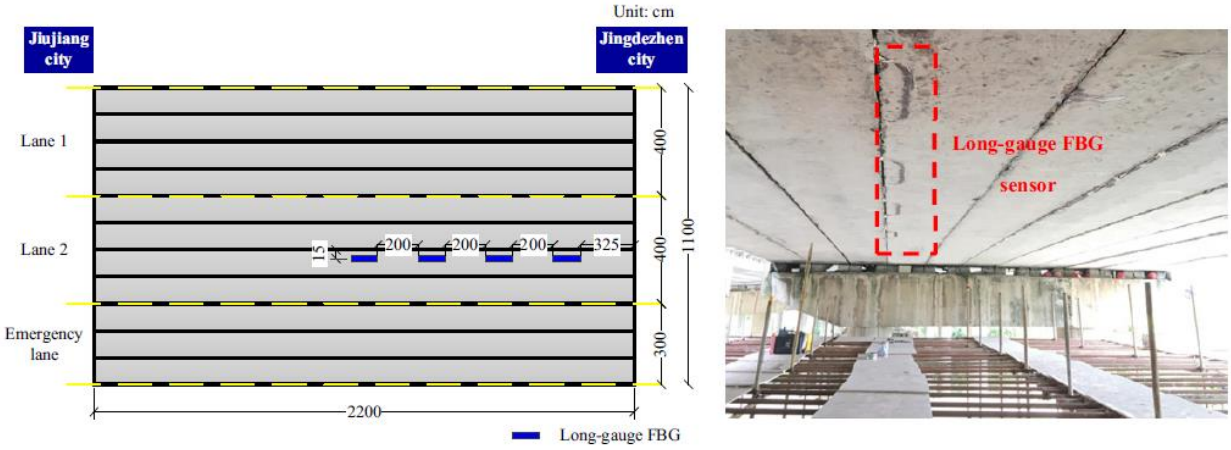

Figure 2.21. Installation Locations of Long-Gauge FBG Sensors (reprinted from Chen et al. 2018).

Iowa State University developed a B-WIM system to assess the weight and configuration of farm-to-market vehicles and other implements of husbandry (Dahlberg et al. 2018). The instrumented bridge is a 48-ft-long single-span bridge, with four steel

girders and a concrete deck. Twenty-four strain gauges were placed on the bridge deck bottom and on the top and bottom flanges of the girders, as Figure 2.22 shows. This system provided useful vehicle classification determination.

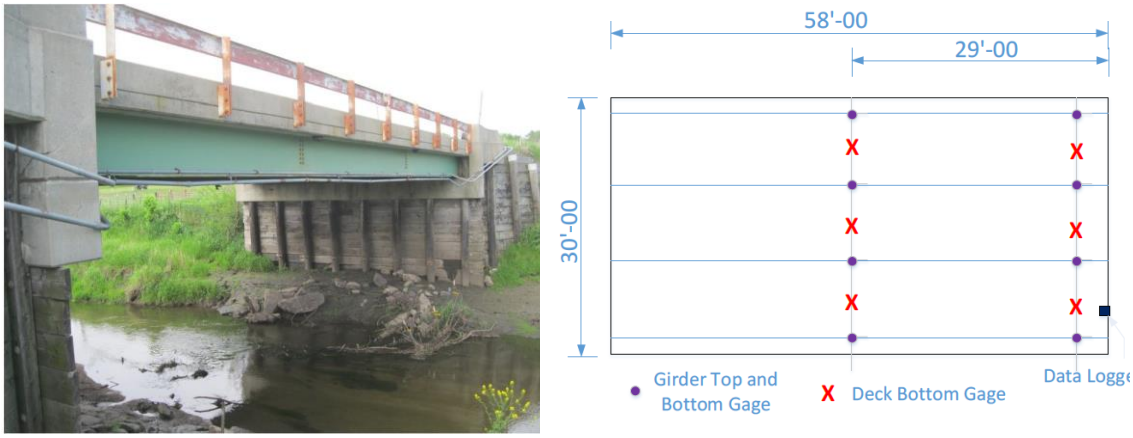

(a) Instrumented Bridge (b) Sensor Placement

Figure 2.22. Instrumentation of the Bridge Located on Story County Road E-18 (reprinted from Dahlberg et al. 2018).

A cable-stayed bridge over the Great Western Highway in New South Wales, Australia, was instrumented to investigate the axle-detection schemes with strain gauges and shear rosettes (Kalhori et al. 2018). The instrumented span has a length of 7.9 m (26.0 ft) and a deck width of 6.3 m (20.6 ft). The signals were collected at 600 Hz. Field testing was performed, and only axle groups could be identified for the shear strains measured at the midspan of the bridge. The bending strain response of the deck in the transverse direction failed to identify the closely spaced axles. The effect of the lateral location of the vehicle was also investigated with three different lateral locations, as Figure 2.23 shows. Researchers concluded that the longitudinal strain under the deck has the potential to identify the presence of individual axles if the location of the wheel is

very close to the lateral location of the sensor on the bridge. The shear rosettes at the beginning of the bridge provided reliable identification of all individual axles.

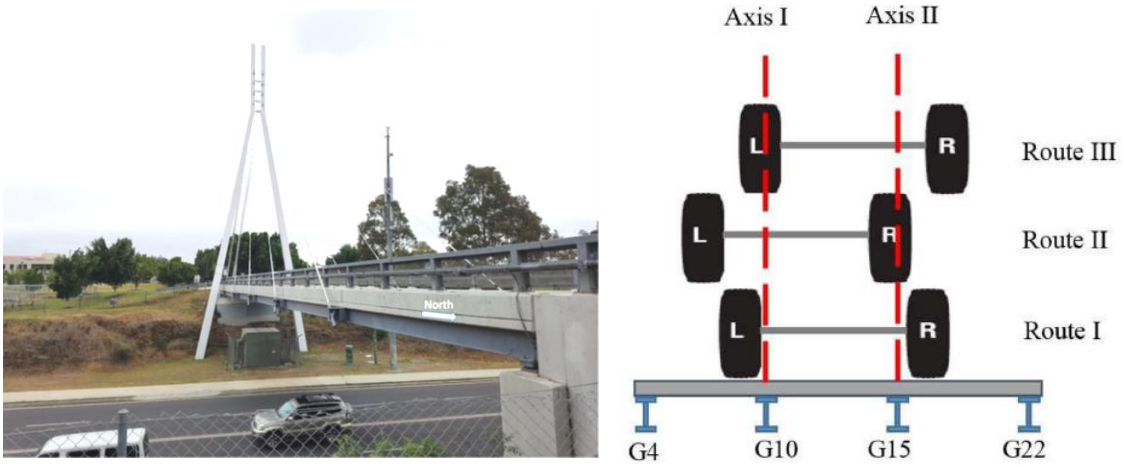

(a) Instrumented Bridge (b) Lateral Location of the Vehicle on Different Routes

Figure 2.23. Instrumented Cable-Stayed Bridge and Lateral Location of the Vehicle on Different Routes (reprinted from Kalhori et al. 2018).

2.4.3.4. Other Measurement Methods

B-WIM systems in which sensing technologies other than strain gauges are used for strain measurement and axle detection have also been investigated during recent years. Kumar et al. (2018) proposed a portable B-WIM system for GVW estimation and vehicle axle detection that consists of only accelerometers. Unlike strain gauges, accelerometers can be easily attached to and detached from a painted steel surface using magnets. The acceleration recorded by the accelerometer was integrated twice to determine the displacement of a bridge. However, determination of displacement from acceleration is difficult because the accuracy of the integrated displacement data is lost because of measurement errors such as sensor self-noise and errors resulting from the

limitations of analog-to-digital conversion. Moreover, the initial speed and displacement—bridge conditions that are essential for the double integration—were unknown because of the continuous vibration of the bridge caused by moving traffic. Also, the construction of the system was time consuming since 11 accelerometers were used for the B-WIM system.

Sekiya et al. (2017) subsequently developed a simplified portable B-WIM system through field measurements. The test bridge was a single-span composite steel girder bridge with three main girders. In this method, only one accelerometer was used to determine bridge displacement responses for all lanes, as Figure 2.24 shows. Instead of the least-squares method, Fourier transformation was used to calculate the influence line in this study. Field measurements showed that the micro electronic mechanical systems (MEMS) accelerometers can accurately determine the vehicle axles, axle spacings, and speeds. The accuracy of the displacement response determined from acceleration data is an important factor which greatly influences the accuracy of the weight estimation.

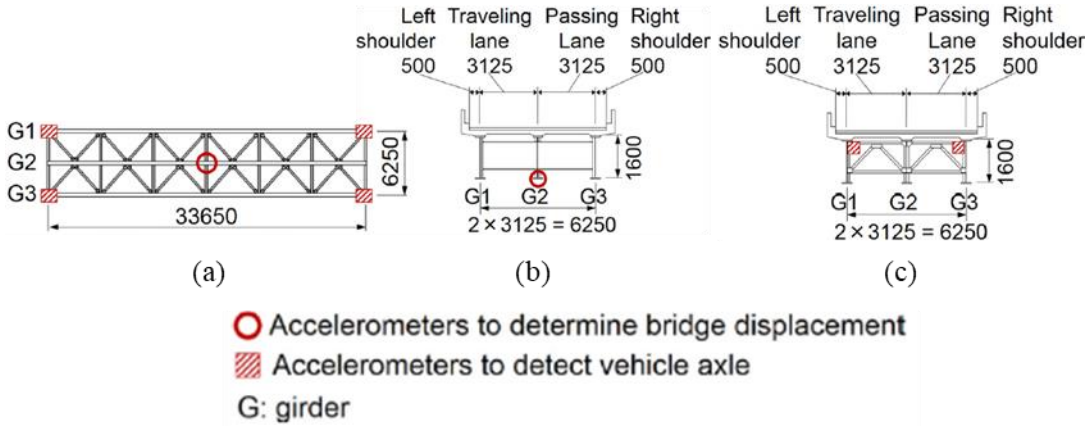

Figure 2.24. Test Bridge and Installation Positions of Accelerometers in the Study (reprinted from Sekiya et al. 2017).

NOR axle detecting systems do not always provide clear identification of axle configurations due to the type of structure or the transverse position of the load. Ojio et al. (2016) proposed a new technique of axle detection using vision-based methods. The vision method is also referred to as contactless B-WIM. It uses two cameras that are time synchronized. The first camera measures sub-millimeter deflections of the underside of the bridge and is positioned in the underpass of the bridge. A telescope is attached to the camera to detect the deflection of the bridge. A second camera is set up on the bridge surface, monitors the passing traffic, and is used to determine the axle spacing. A motion-tracking software package (PV-Studio 2D, in this case) captured the deflection of the target point, which was a sensor bolt in the midspan of the girder. The axle spacing distances were calculated from the number of frames between the axles passing a notional vertical line in the video image frames of vehicles traversing the bridge. The accuracy of GVW measurement by this system was relatively low. Moreover, some environmental conditions, such as when the camera is affected by wind-induced vibration or ground vibration and when it is too dark to capture images, make the determination of deflection with a camera difficult. Overall, this method has the potential to provide axle configurations without disrupting the flow of traffic. The disadvantage of this setup is the low accuracy, high cost, and durability issues of the equipment. Figure 2.25 shows the setup of the camera system in the underpass of Loughbrickland Bridge in Northern Ireland.

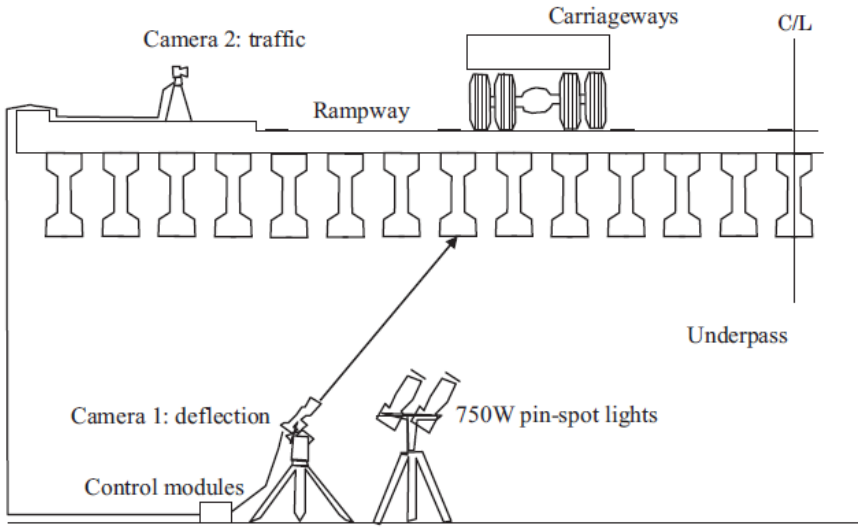

Figure 2.25. Contactless B-WIM System (reprinted from Ojio et al. 2016).

Helmi et al. (2015) developed a method based on the measurement of shear strains by way of optical-fiber strain rosettes at the bridge abutments. In this method, GVW is the ratio of the slopes of the shear force and shear influence lines. Vehicle speed is acquired from the time stamp difference between the two strain rosettes. A bridge was instrumented, as Figure 2.26 shows. Field tests were conducted, and the results pertaining to the crawl speed tests yielded good results with low measurement errors. There are some limitations of this approach. For instance, the approach approximates linear response for the influence lines when the girder is continuous. In addition, dynamic effects increased the difficulty of filtering the data. More work needs to be done in the future.

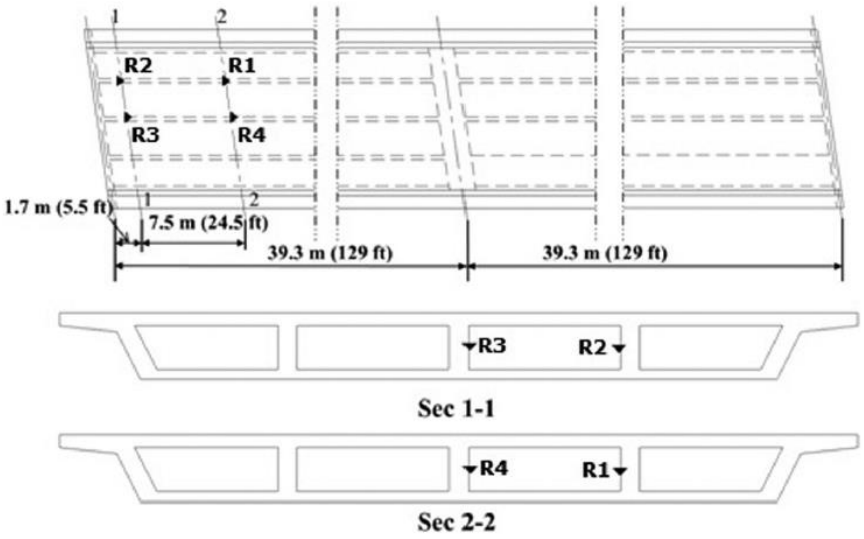

Figure 2.26. Different Views and Instrumentation Layout of the Southbound Section of the I-5 Bridge (reprinted from Helmi et al. 2015).

Oskoui et al. (2019) proposed a B-WIM system using the end rotation influence lines due to the truck axle loads, measured by a special rotation sensor installed at a bridge abutment. The proposed approach is based on the relationship between the load and the load-induced rotations in structures. As Figure 2.27 shows, the rotation and wheel sensors were installed at a bridge site in Lagrange, Georgia. The field tests showed errors less than 15 percent for this B-WIM system.

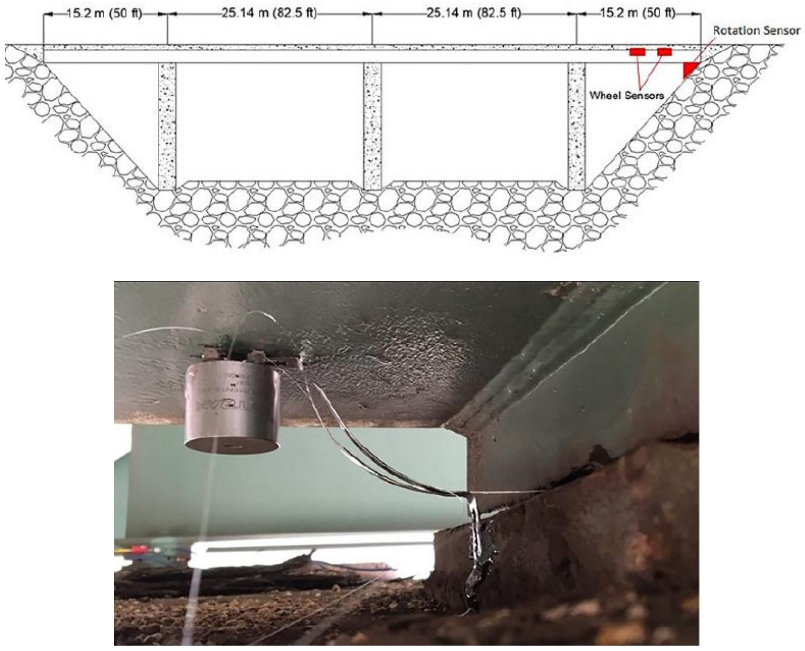

Figure 2.27. Installation Plan and Rotation Sensor Installed under the Girder (reprinted from Oskoui et al. 2019).

2.4.4. Bridge Assessment Using B-WIM Systems

Bridge structural health monitoring (SHM) aims to detect, locate, and quantify structural changes (potentially as a result of damage) by the acquisition of data measured in situ on the bridge. The SHM systems can also be used for other purposes, such as load estimation, monitoring of construction and repair work, and validation of design assumptions regarding the static and dynamic behavior of the structure. B-WIM can provide useful traffic characterization information. Information about the real loads affecting a given structure helps explain the damage mechanisms and improve maintenance. In bridges, traffic information can help reduce costs both in assessment and design. Traffic load models can be relatively conservative compared to the actual

load carried by the structure. Additionally, B-WIM can be used to identify the dynamic characteristics of the traffic at a given site (González 2011).

González (2011) presented case studies on two different types of bridges with SHM and B-WIM. The first bridge was a steel railway bridge located in Stockholm, Sweden. Theoretical studies concluded that the fatigue life of the bridge had been exhausted, and several fatigue cracks had been discovered. Strain gauges and accelerometers were used for both SHM and B-WIM purposes. The information obtained from the B-WIM system provided useful information that can be used by bridge engineers (e.g., for bridge rating and remaining fatigue life estimation), traffic engineers (e.g., for traffic simulations), and railway managers (e.g., for train wheel defect detection). The second bridge was a highway suspension bridge located in Sweden. This bridge is supported at the abutments on sliding bearings. Large wearing was discovered at the bearings. The B-WIM system developed for this bridge helped the researchers understand the loads acting on the bearings, the traffic events, the type of traffic passing over the bridge, and the dynamic displacements of the bridge girders.

Christenson et al. (2011) established a dual-purpose SHM and B-WIM system for a steel girder bridge. The B-WIM algorithm used strain measurements from the steel girders. The algorithm was built based on a theory from research by Ojio and Yamada (2002) and by Wall et al. (2009) The GVW was obtained from the influence area method. The second time derivative of the measured strain was used to identify vehicle axle information (e.g., vehicle speed, axle number, and axle spacing), and the axle weights were calculated by the relative magnitudes of the peaks in the second time

derivative of the strain. Field tests were conducted to determine the accuracy of the proposed B-WIM method, and SHM was carried out using the dynamic response to truck traffic (e.g., peak strain on girders, distribution of the strain in girders, and location of the neutral axis at each girder). A probabilistic SHM approach was adopted to detect global damage in the highway bridge. A prototype SHM/B-WIM system was then developed, including an automatic data acquisition system to monitor dynamic beam strains and vertical acceleration due to traffic loading and the corresponding surface temperature of the bridge girders, as shown in Figure 2.28.

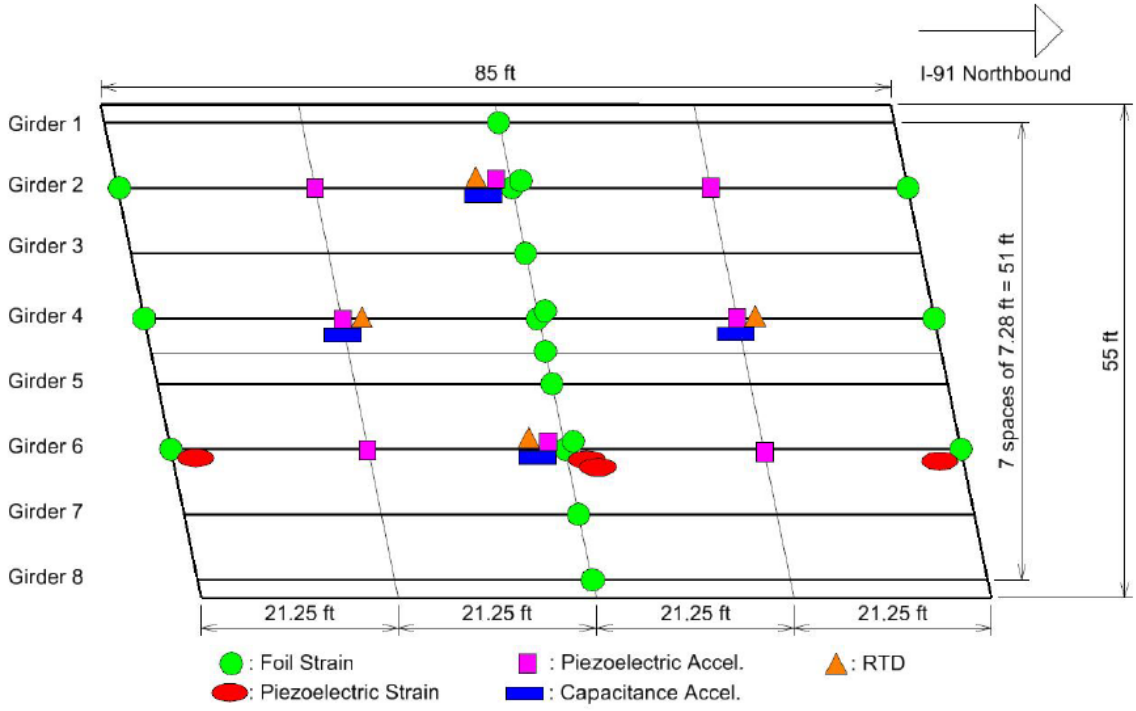

Figure 2.28. Schematic of Sensor Layout and Sensor Type for the Bridge (reprinted from Christenson et al. 2011).

Zhang et al. (2019) presented a virtual monitoring approach for fatigue life assessment of orthotropic steel deck bridges. The concept of this method is to use B-

WIM to weigh the axles of vehicles passing over the bridge and then to calculate the strains at other points on the bridge using vehicle information and the influence surfaces for these points. The ISs for the points without sensors are obtained using an updated FE model based on modal testing. Thus, the fatigue damage calculation can be carried out for any location on the bridge. An orthotropic steel deck bridge located in China was tested to investigate the method. Figure 2.29 shows the details of the bridge and sensor installation. Four different influence line/surface calculation algorithms were compared, and researchers concluded that using the influence surface gave the most accurate results. The traffic information measured from the B-WIM system was combined with the influence surface at the monitoring point to calculate the corresponding strains and stress ranges in the fatigue evaluation.

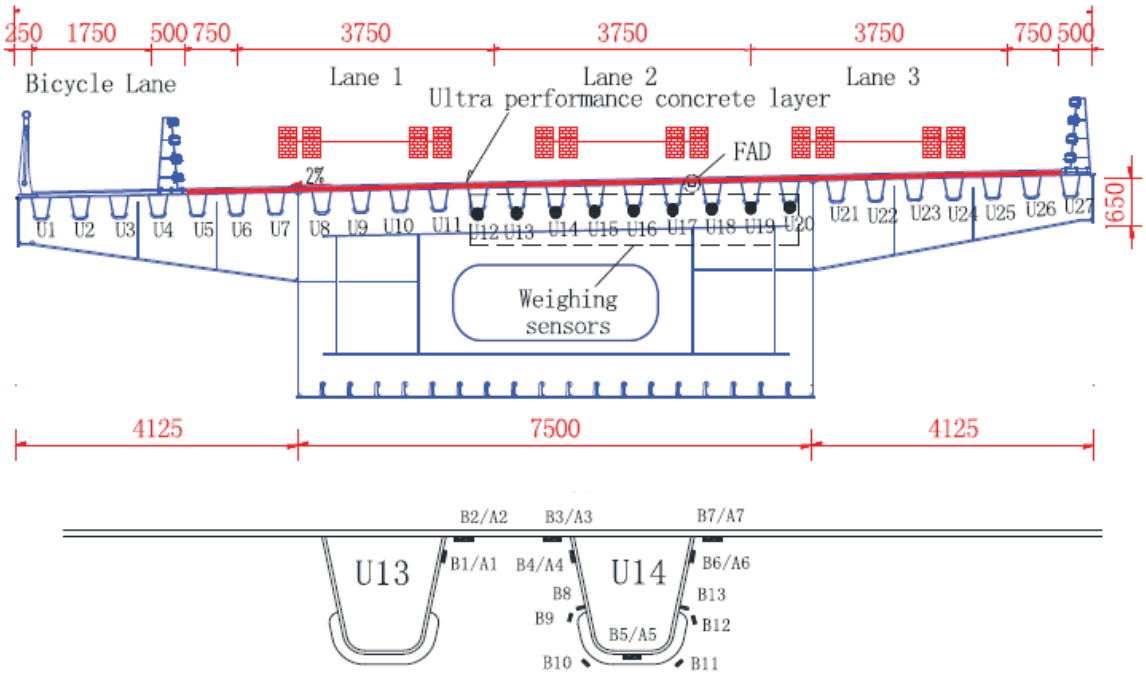

Figure 2.29. Details of the Tested Bridge and Layout of Strain Sensors at Fatigue-Sensitive Detail (reprinted from Zhang et al. 2019).

Two projects—Sustainable and Advanced Materials for Road Infrastructure (from the European Commission's 5th Framework Program in 2006) and Assessment and Rehabilitation of Central European Highway Structures (from the 6th Framework Program in 2009)—proposed two new approaches:

- Soft load testing.
- Optimized evaluation of the dynamic amplification factor.

Both are based on B-WIM measurements and enhance the results of bridge assessment, with the ultimate goal to rationalize spending of resources for road infrastructure maintenance (Žnidaric and Kulauzovic 2018).

Jacob et al. (2012) applied B-WIM to bridge fatigue assessment. A cable-stayed steel box orthotropic deck bridge (Millau Viaduct Bridge) was instrumented with a B-WIM system. Figure 2.30 shows the installation of extensometers at one span of the bridge. The SiWIM algorithm was used to obtained traffic information (e.g., the number of trucks, distribution of GVWs, and dimensions of trucks) and assess the real influence lines of the bridge. Then, the rain-flow histograms with the S-N curves and Miner's law were used to assess the fatigue damage and estimated lifetime of the bridge. Similarly Guo et al. (2012) performed a fatigue reliability assessment for steel bridge details integrating WIM data and probabilistic finite element analyses. Traffic information obtained from B-WIM system, such as the number of axles, axle weights, axle spacing, and transversal position of vehicles, were considered as uncertainties for probabilistic finite element analysis.

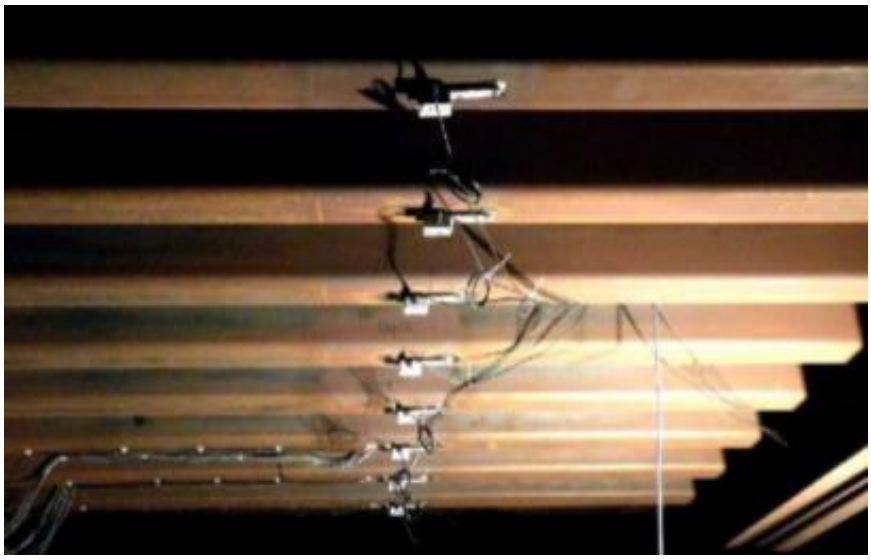

Figure 2.30. Sensors Glued to the Bottom of the Longitudinal Stiffeners at the Midspan of the First Span (reprinted from Jacob et al. 2012).

2.5. Literature Summary

B-WIM systems typically use the flexural deformations of a bridge caused by vehicles (trucks) crossing over the structure. These deformations are commonly measured using strain sensors attached to the structural members and are analyzed to estimate the GVWs and axle loads of passing traffic. Two main approaches to B-WIM have been used. The first approach uses strain sensors mounted on the bridge to determine GVW and a separate axle detection sensor installed on the road. The second approach uses only strain sensors installed on the bridge for both weight measurements and axle detection. The second approach is the more desirable since it simplifies the overall design, installation, operation, and maintenance of the B-WIM system as compared to the first approach.

The advantage of B-WIM systems is that they have the capability to identify truck-traffic information with comparable accuracy to pavement WIM systems. In addition, the sensors can be removed and reinstalled on a different structure. The portability of the sensors provides some flexibility regarding where the system is installed to collect traffic data that is not available with pavement WIM systems. Another advantage of B-WIM systems is the potential for using the measured bridge responses for truck-traffic data collection and for evaluating the performance of the structure itself. In many cases, the same sensors on a structure can provide data that can be used for both objectives. In other cases, additional sensors of the same type and with the same signal conditioning requirements can be added to the structure to supplement the sensors needed for traffic characterization. Some examples of such applications could include prescreening, bridge rating, remaining fatigue life evaluations, and bridge condition monitoring.

Several challenges have been identified for the development of a B-WIM system. These challenges are listed below and the general approach of this research to address them.

- Limited independent quantification of accuracy. Most studies used the calibration trucks to obtain the accuracies of the proposed B-WIM systems. Some studies focused on lab testing or numerical simulations to evaluate the accuracies. There is a lack of accuracy quantification. In this research study, three in-service bridges were instrumented for B-WIM testing. Two of the in-service bridges had portable WIM system installed independently near the bridges. Several time

windows were selected and traffic data from both systems were processed and compared to quantify the accuracies of the B-WIM systems.

- The development of B-WIM for long-span bridges has had less success. This is partly due to the potential for multiple vehicles in one lane on one span simultaneously, which makes it more difficult to identify the individual vehicle information. In addition, there may be increased dynamic effects along with the potential for vehicle speed changes during the crossing of long bridges. Therefore, shorter span bridges were focused for B-WIM testing in this research study.
- The Moses algorithm has several drawbacks such as limited accuracy and efficiency. The improved algorithms aim to address these shortcomings. For example, the influence area method can be used to estimate the GVW. However, it is difficult to identify the individual axle weights. The MFI methods can be accurate but require detailed bridge finite element models, which can be computationally expensive. As a result, there is no consensus toward the optimum B-WIM algorithm. In this study, full-scale field tests were conducted on instrumented bridges. Area method was applied to the collected data from different types of sensors to evaluate the accuracy and feasibility of this method for GVW calculation. Reaction force method was evaluated on the testbed bridge with installed load cells for axle weight calculation. Data from the strain gauges installed under the bridge deck was utilized to evaluate the axle weight calculation accuracy.

- There are a variety of measurement methods for a B-WIM system, such as longitudinal strain, acceleration, shear strain, and bridge end rotation measurement. Among all the methods, longitudinal strain-based measurement is the most commonly used B-WIM system. Relatively high sampling frequency is required for axle detection, which requires significant data storage and power requirements. For this reason, FBG sensors or electrical resistance strain gauges are typically used. In this research study, strain gauges were used as the main sensor for axle detection and weigh calculation purposes. In the testbed bridge tests, load cells were utilized for B-WIM application and the results were compared with the strain gauges. During the in-service bridge tests, different measurement methods such as strain rosette and LVDT were studied and the results were compared.

The literature makes several suggestions:

- The ideal bridges for B-WIM are relatively short, simple-span structures. This minimizes the issues with multiple vehicles in one lane on the structure at a time. In addition, the vehicle speed is essentially constant.
- To improve the accuracy of B-WIM results, the surface condition should be relatively smooth to reduce dynamic amplification.
- The multiple-presence issue (i.e., side-by-side vehicles) may be addressed by running calibration vehicles at different transverse locations to obtain the distribution factors due to the spatial effect of the bridge. This was explored in the testbed bridge testing and one of the in-service bridge testing.

- Wavelet transformation can be a powerful tool to retrieve individual axle information from the measured data. The second time derivative of the strain value can provide information on the axle number, average speed, axle spacing, and axle weight. In this study, the second derivative of the strain response was used to process response from axle detection strain gauges. Wavelet transformation was not included in this study.
- The influence area method is an easy and effective approach to estimate the GVW. However, this method does not account for the dynamic amplification of the bridge response. The accuracy of area method was evaluated in this study.
- B-WIM systems can also be used to evaluate the bridge itself with minimal (if any) modifications to the instrumentation setup. In this research study, responses from midspan strain gauges of the three in-service bridge B-WIM systems were utilized to obtain the distribution factors and refined bridge load ratings were conducted based on these factors. One of the in-service bridges had strain gauges installed on the web of the girders, which were used for composite action analysis based on field measured data.

3. B-WIM DEVELOPMENT AND PRELIMINARY TESTING

3.1. Overview

This section presents the development and preliminary testing of a B-WIM system. The approach was to conduct full-scale testing on a testbed bridge at the Texas A&M-RELLIS campus. A comprehensive array of sensors was installed along the bridge structure. This was to allow for research of different B-WIM methods. The sensors were recorded during the passing of three different test trucks traveling at different speeds, lane position, direction, and configurations. The test data were processed with several algorithms, many of which were obtained from the work presented in Section 2. A preliminary B-WIM performance study was conducted through comparison of the algorithm results with independent measurements of the test trucks. In addition, preliminary setup guidelines were developed.

3.2. Testbed Bridge

Conducting full-scale testing on a testbed bridge was the approach used to study the preliminary B-WIM instrumentation and data processing algorithms. The RELLIS Bridge (formerly known as Riverside Bridge) was the structure chosen and is located at the RELLIS campus. This bridge is not in service and is positioned at the edge of an old airport runway. The advantages of the RELLIS Bridge are the unlimited access and control of the live load application. The underside access is also ideal for installation of sensors. Figure 3.1 shows the geographic location of the bridge.

Figure 3.1. Location of the RELLIS Bridge (Google Maps 2020).

The RELLIS Bridge was constructed under a previous TxDOT project (Terzioglu 2015). The structure is a prestressed concrete slab beam bridge. The bridge has a 46.6 ft span length (from center to center of the bearing pads) and an overall width of 34.0 ft (see Figure 3.2). The bridge superstructure is comprised of four beams (TxDOT 5SB15) with prestressed concrete panel (PCP) stay-in-place forms. The 4.0-inch-thick PCPs are 8.0 ft long and have an overall width of 5.3 ft. To accommodate the camber of the prestressed slab beams, the cast-in-place (CIP) deck thickness varies slightly along the length. The minimum deck thickness (cast-in-place plus PCP) at the center of the bridge is 8.0 inches.

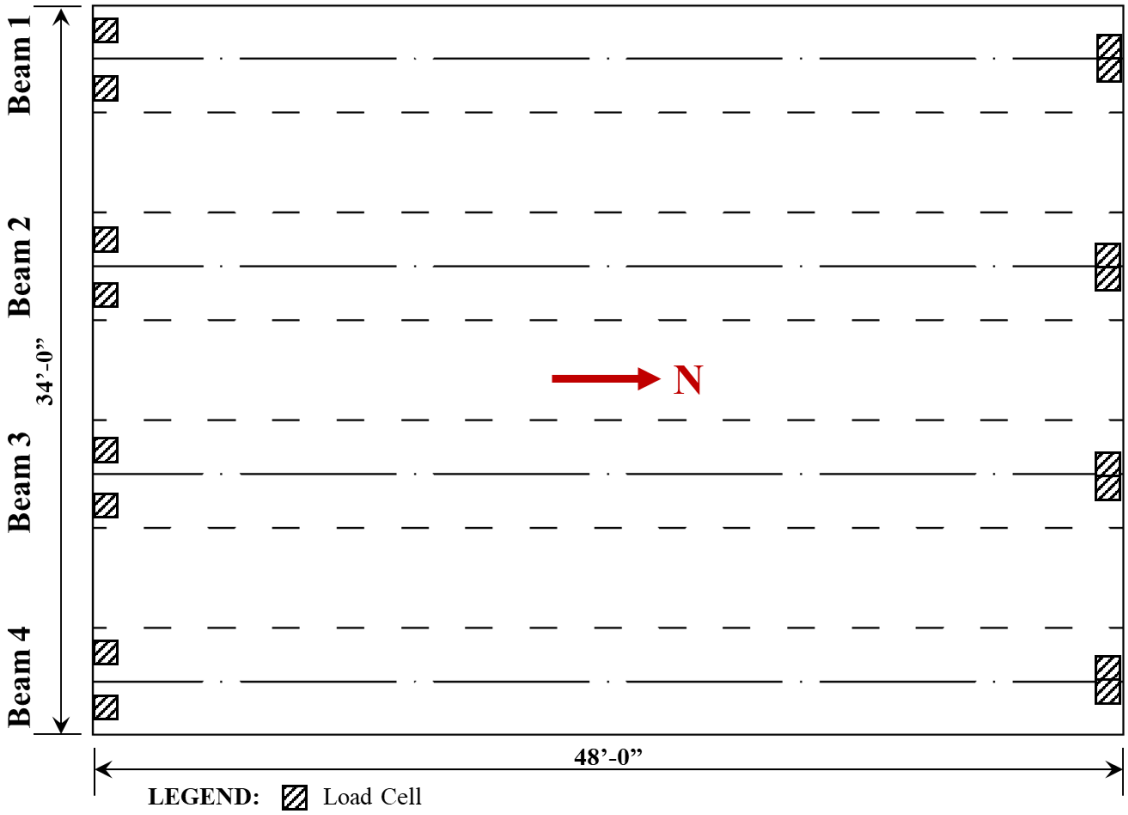

Figure 3.2. Plane View of the RELLIS Bridge.

One of the requirements under the previous TxDOT project was to identify the lateral distribution for the individual girders. To achieve this, a total of 16 load cells (two per bearing) were placed at both the north and south ends beneath each beam (see Figure 3.3a). The slab beams rest on top of bearing pads. The load cell assemblies are between the bearing pads and the bridge abutment seat. Figure 3.3 illustrates the construction of the bridge.

(a) Load Cells at South and North Ends

(b) Slab Beam Placement

(c) Completed Bridge

Figure 3.3. Load Cells and RELLIS Bridge Construction.

3.3. Preliminary B-WIM System Design

3.3.1. Instrumentation Plan

The instrumentation plan for the RELLIS Bridge was designed based on the objectives of this task and site-specific conditions. The primary constraints for a B-WIM system are:

- Rugged setup to withstand field conditions.
- Reusable setup.
- Installation within one day.
- Minimal (preferably no) traffic disruption during installation.
- Sensor configurations to allow for sufficient data processing.

To meet these constraints, the main preliminary B-WIM system was designed to be strain-based and installed underneath the bridge. However, the bridge was over instrumented with various types of sensors to explore the possibility and accuracy of other instrumentation methodologies and algorithms.

Four types of sensors were used, including 16 strain gauges, 16 load cells, 4 string potentiometers, and 8 accelerometers. As mentioned above, the strain gauges were the primary instrumentation for this preliminary study. These gauges were divided into two groups, which were based on their purpose. The first strain gauge grouping was installed underneath the bridge deck close to the north and south ends. These sensors are referred to as “axle detection” gauges. They provide localized effects valuable for vehicle axle information and speed data. The other grouping is referred to as “weight” gauges and are installed on the bottom surface of the girders at the bridge midspan to

capture the global behavior. These sensors provide valuable information for the overall vehicle weight along with bridge information such as lateral distribution, dynamic amplification, etc.

As mentioned earlier, the load cells were located at each bearing. These sensors were also critical for the preliminary study. Logistically, it is not practical to have load cells for most future B-WIM applications. However, other reaction force measurements are possible (e.g., strain gauges mounted to neoprene bearings or strain gauge rosettes attached to the beam webs). The researchers explored the value of this type of information, compared to the deck and beam strain data, to evaluate the benefits of reaction force measurements in B-WIM systems. The other sensors (i.e., load cells, string potentiometers, and accelerometers) were located to provide complimentary information (further details below).

Figure 3.4 and Figure 3.5 show the plan and cross section views of the designed and implemented instrumentation plan for the RELLIS Bridge in this task, respectively. It should be noted that two strain gauges were installed on the webs of Beams 2 and 3 to explore the composite behavior between the beams and deck.

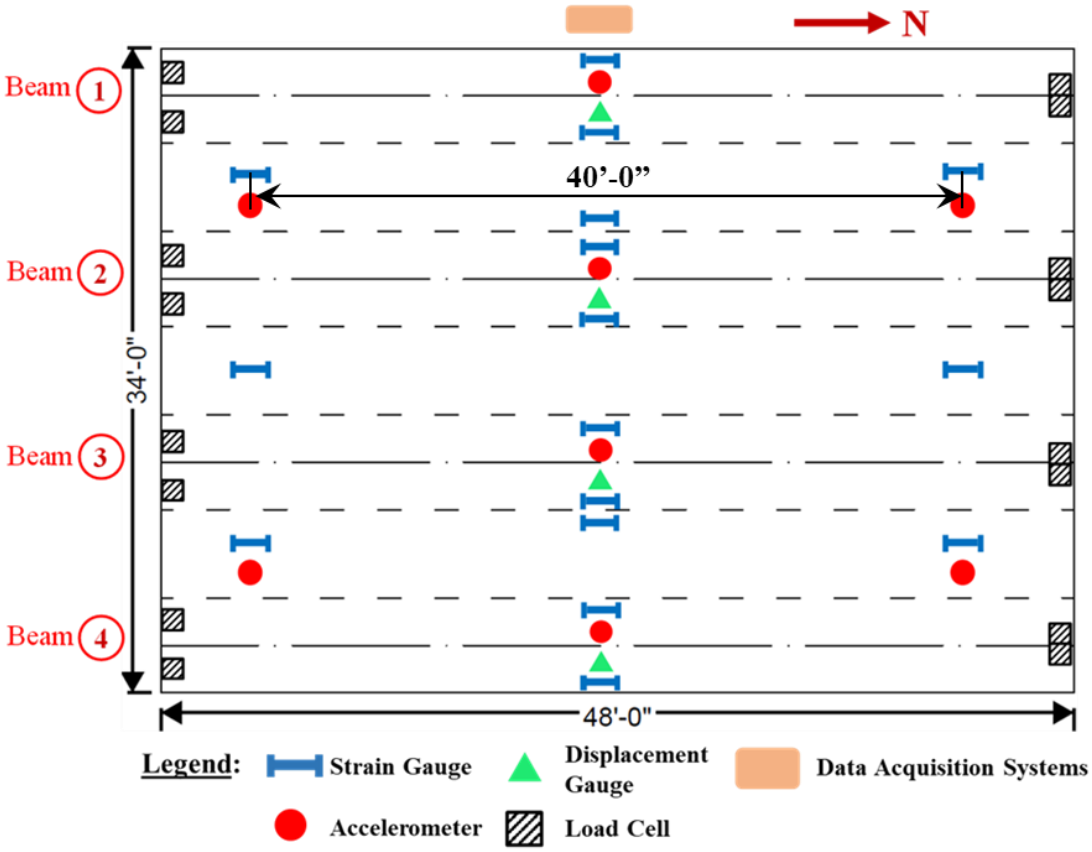

Figure 3.4. Sensor Layouts and Types for the RELLIS Bridge (Plan View).

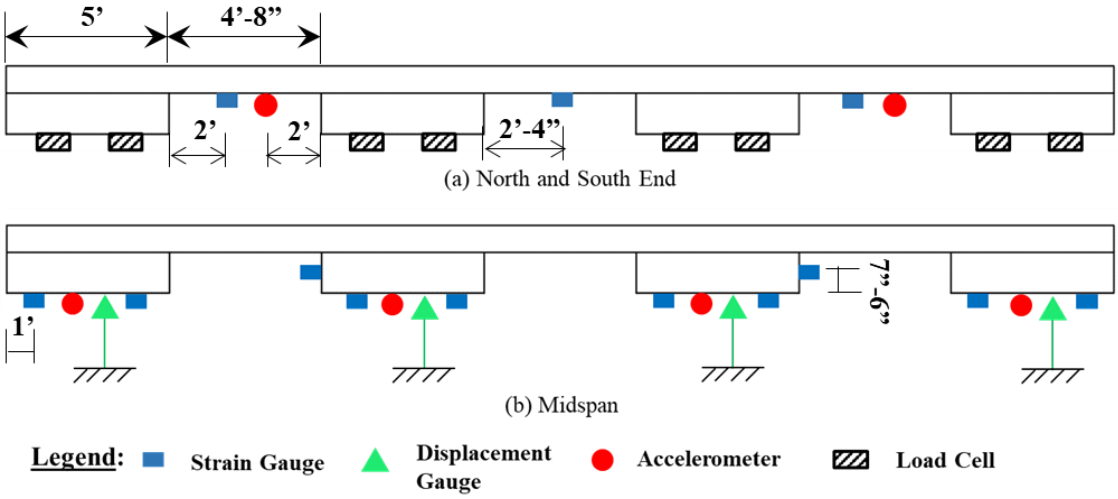

Figure 3.5. Sensor Layouts and Types for the RELLIS Bridge (Cross Sections).

3.3.2. Sensors and Data Acquisition Systems

3.3.2.1. Strain Gauges

The strain gauges used in the instrumentation were the ST350 produced by Bridge Diagnostics, Inc. (BDI). The ST350 reusable strain gauges have multiple uses and are highly durable due to their rugged, waterproof construction. The ST350 internal circuitry consists of a full Wheatstone bridge with four fully active 350Ω foil gauges optimized to provide a high electrical output for a given strain magnitude. The BDI strain gauges have a resolution of one microstrain. Compared to foil-type gauges, the installation is faster and easier.

The strain gauges were sampled at two different rates. The first consisted of 400 Hz sampling frequency for the axle detection gauges. The weight gauges were sampled with a 200 Hz frequency. These sampling frequencies were set based on information from the literature and the capabilities of the data acquisition system. Figure 3.6a shows the strain gauges used in this task.

3.3.2.2. Load Cells

To obtain reactions at the ends of the beams, the existing load cells were utilized. There were two different load cell assemblies due to the two-bearing-pad and one-bearing-pad configurations. At the south end of the bridge, there were two bearing pads (9.0 inches × 9.0 inches) at the corners of the slab beams. At the north end of the bridge, the bearing pads (9.0 inches × 18.0 inches) were at the center of the beam. The load cells were placed between a 1.0-inch-thick bottom steel plate and a 1.5-inch-thick top steel plate.

The load cells installed under the slab beams in the previous project were Cooper LGP 312 100K compression only pancake load cells with a 0 to 100,000 lb measurement range and a linearity of ±0.1 percent. The sampling rate of the load cells were set to be 500 Hz for this task. Figure 3.6b shows the LGP 312 100K load cell.

3.3.2.3. String Potentiometers

A total of four Celesco string potentiometers were installed underneath the four slab beams at midspan to measure the bridge vertical deflections. Figure 3.6c shows the string potentiometers used during the field test. The sampling rate was set at 500 Hz.

3.3.2.4. Piezoelectric Accelerometers

A total of eight piezoelectric accelerometers (Model 4507 manufactured by Brüel & Kjaer Sound & Vibration Measurement) were used for this task. Four of them were installed underneath the deck at both ends of the bridge between beams 1 and 2 and beams 3 and 4. The other four sensors were attached at the midspan of each slab beam. All the accelerometers had a sampling rate of 500 Hz and were oriented vertically. Figure 3.6d shows the piezoelectric accelerometers used in this task.

3.3.2.5. Data Acquisition Systems

Two different data acquisition (DAQ) systems were utilized for the preliminary study. The first system controlled the strain gauge setup. This system was comprised of Campbell Scientific equipment. The GRANITE 9 all-digital measurement and control DAQ was designed as the core of the data-acquisition network. Several GRANITE

measurement modules were integrated with the GRANITE 9, including three VOLT 116s and one VOLT 108. Figure 3.6f shows the GRANITE 9 and extension modules. A Measurement and Computing Strain Book/616 DAQ unit was used as the second system and was connected to a laptop personal computer. The Strain Book/616 DAQ unit has an eight-channel data acquisition capacity and can transfer up to one million samples per second. Three WBK16/SSH extension modules with eight DSUB9 input channels per module were utilized for the load cells and string potentiometers. Also, another WBK18 extension module with eight Bayonet Neill-Concelman input channels was used for the piezoelectric accelerometers. Figure 3.6e shows the main box and extension modules of the DAQ system.

(a) BDI ST350 Strain Transducer

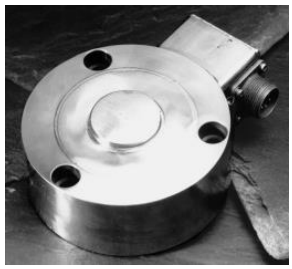

(b) Cooper LGP 312 100K Load Cell

(c) Celesco String Potentiometers

(d) Brüel & Kjaer Accelerometer

StrainBook/616

WBK16/SSH

WBK18

(e) Strain Book/616 and Extension Modules

GRANITE 9

VOLT 116

VOLT 108

(f) GRANITE 9 and Extension Modules

Figure 3.6. Data Acquisition System and Instrumentation.

3.4. Test Preparation

The preparation for the preliminary B-WIM system full-scale test included instrumentation installation, DAQ code development, truck selection and path marking, camera setup, and test vehicle preparation.

3.4.1. Instrumentation Installation

The strain gauges, string potentiometers, and accelerometers were installed underneath the bridge by the research team. The load cells were integrated with the bridge during the construction. Therefore, only validation of their functionality was required. The overall instrumentation plan, shown in Figure 3.4 and Figure 3.5, was followed.

High strength epoxy was utilized for attaching the strain gauges to the bridge beams and deck. Loctite 410 adhesive (with accelerator) was used for initial attachment. Loctite 5-minute general purpose epoxy was applied to ensure sufficient strength. Figure 3.7a and Figure 3.7c show an installed strain gauge along the bottom of a beam.

The string potentiometers were screwed to a wooden block, which was attached to a steel plate. These plates were put on the concrete floor below the beams at midspan. Along the bottom surface of the beams a wooden block was attached with epoxy. The block included a steel hook. Therefore, a high-strength string could be connected between the potentiometer and the hook. Figure 3.7d shows the string potentiometer setup.

To install the accelerometers, steel plates were attached to the surface underneath the bridge with epoxy. The accelerometers were mounted to the steel plates by a

magnetic connection. Figure 3.7a also shows an installed accelerometer along the bottom of a beam.

Table 3.1 summarizes the setup information of the sensors installed on the bridge for this task. The strain gauges were connected to the GRANITE DAQ at the west side underneath the bridge (Figure 3.7e). A CRBasic program was written to control the sensor sampling rates. The rest of the sensors were connected to the StrainBook DAQ in a shed near the bridge through existing cables (Figure 3.7f). To control this DAQ, a program was written using DASYLab Software.

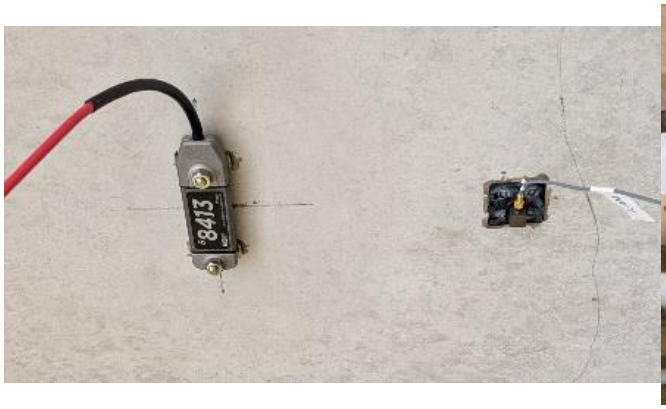

(a) Strain Gauge and Accelerometer at Bridge Ends

(b) Load Cell

(c) Strain Gauges Installed at Midspan

(d) String Pots at Midspan

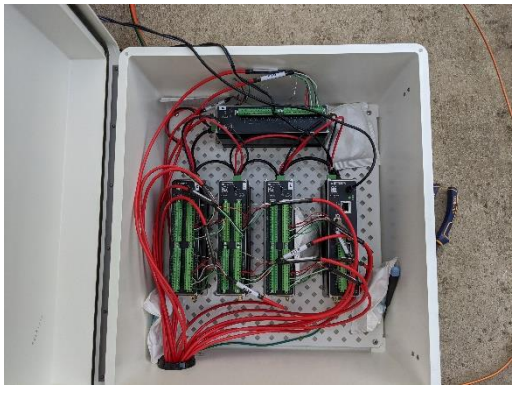

(e) GRANITE 9 and Modules

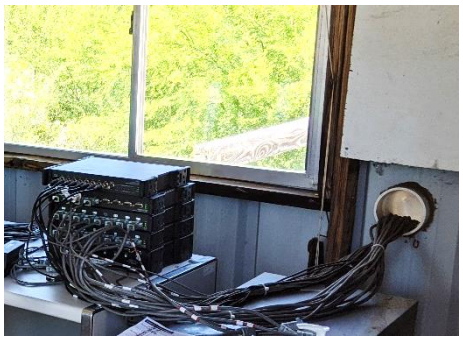

(f) StrainBook and Modules

Figure 3.7. Instrumentation Installation.

Table 3.1. Summary of Sensor Information of the Preliminary System.

Sensor Type	Purpose	Sampling Rate	Quantity	Location
Strain Gauge	Weight Measurement/Bridge Assessment	200 Hz	8	Midspan
Strain Gauge	Bridge Assessment	200 Hz	2	Web of Beam
Strain Gauge	Axle Detection	400 Hz	6	North/South End
String Pots	Weight Measurement	500 Hz	4	Midspan
Accelerometer	Weight Measurement	500 Hz	4	Midspan
Accelerometer	Axle Detection	500 Hz	4	Midspan
Load Cell	Weight Measurement/Axle Detection	500 Hz	16	North/South End

3.4.2. Test Trucks

Three trucks with different weights were selected for the preliminary B-WIM system testing. For convenience, they were named as Truck A, B, and C. Truck A is a tractor-trailer with five axles. The total weight of Truck A is 79,510 lb. Truck B and C are single unit trucks (i.e., two axles) with static weights of 33,020 lb and 22,300 lb, respectively. The axle weights and axle spacings are summarized in Table 3.2. Figure 3.8 to Figure 3.10 show the photos of each truck along with the axle weights and spacings.

Table 3.2. Axle Information of the Test Vehicles.

Truck Name	Axle Weight (lb)					Axle Spacing			
	Axle 1	Axle 2	Axle 3	Axle 4	Axle 5	Axle 1 to 2	Axle 2 to 3	Axle 3 to 4	Axle 4 to 5
A	9950	19440	19700	15210	15210	11'-7"	4'-3"	40'-6"	4'-0"
B	12100	20920	N/A	N/A	N/A	20'-5"	N/A	N/A	N/A
C	8190	14110	N/A	N/A	N/A	17'-3.5"	N/A	N/A	N/A

Figure 3.8. Truck A Information.

Figure 3.9. Truck B Information.

Figure 3.10. Truck C Information.

3.4.3. Truck Paths

The RELLIS Bridge was built as a two-lane bridge. However, to explore more vehicle lateral positions the bridge was divided into three 8.0-ft-wide lanes. This also allowed for multiple vehicle scenarios, such as two vehicles traveling side-by-side or opposite directions (within Lanes 1 and 3), while keeping a safe distance between two vehicles. The vehicle paths were spray painted, as shown in Figure 3.11. Due to the safety reasons, the first lane started 5 ft away from the west edge of the bridge since the barrier impact capacity was minimal.

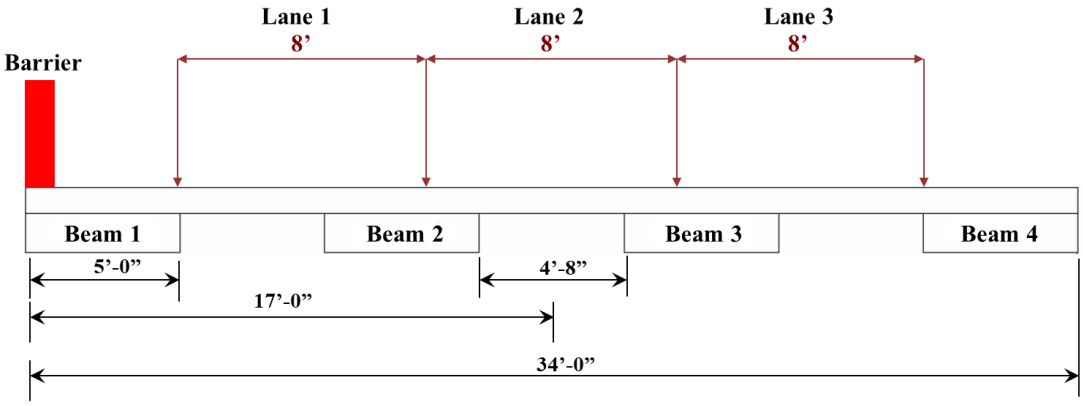

(a) Illustration of the Vehicle Paths

(b) Spray Paint to Mark the Lanes

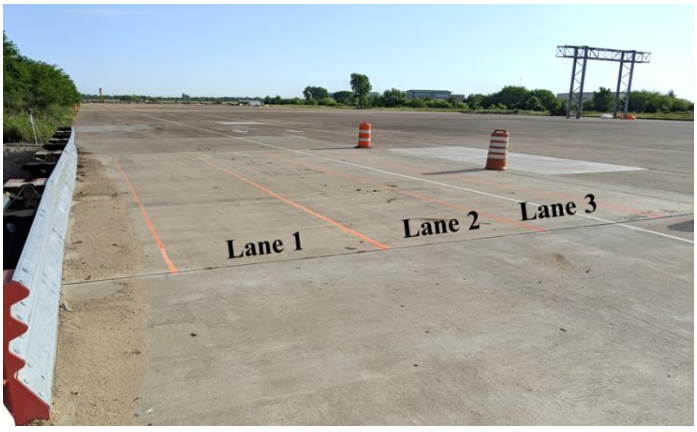

(c) Three Lanes

Figure 3.11. Schematic of the Test Lanes.

3.5. Field Testing at the RELLIS Bridge

The full-scale field testing took place on May 7, 2020. Three GoPro cameras were setup to record the testing from different angles. The first camera was placed to have a field of view perpendicular to traffic and aligned with the middle of the bridge. The second camera was placed behind the barrier at the north end of the bridge. The last camera was attached on the roof of the shed at the south end to get an overhead view. Figure 3.12 shows the camera locations.

Two laptops were used to control the DAQs during the field test. The data was continuously reviewed to ensure sufficient data quality. This included the general magnitude of response checks, review of data trends, etc. Figure 3.13 shows the operation of DAQs during the testing. Also note that a radar gun was operated by a research team member to measure the average speed of the trucks.

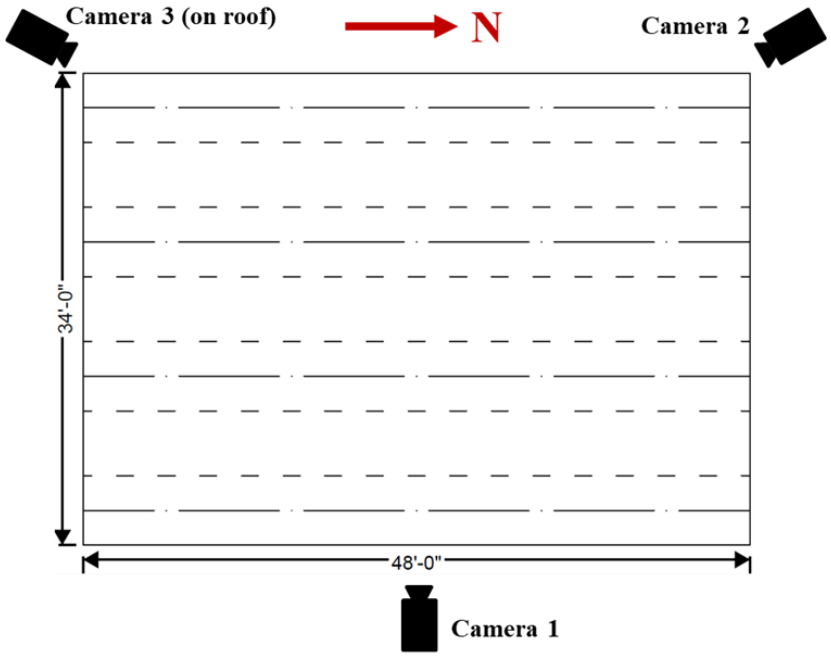

Figure 3.12. Illustration of Camera Placement.

Figure 3.13. Operation of the DAQs.

An array of traffic scenarios was tested to evaluate the performance of the B-WIM system. The majority of the tests were implemented with a single truck traveling in one of the three lanes from north to south or south to north. A total of 72 single vehicle tests were conducted with speeds of approximately 10, 20, 30, 40 and 50 mph. Due to the safety concern, no trucks passed Lane 1 at 50 mph. A total of six back-to-back scenario tests were implemented. In this condition, Truck B followed Truck A at a close distance when passing the bridge on different paths. Five side-by-side scenario tests were conducted; the purpose of these tests was to explore the sensor responses when two vehicles were traveling on the bridge simultaneously. To ensure the safety of the drivers, Truck A and Truck B only used Lane 1 and Lane 3 during the side-by-side tests. The last

test scenario was Truck A and Truck B crossing the bridge in opposite directions. Again, for driver's safety, only Lane 1 and Lane 3 were used, and the speed of the two trucks were set at 20 mph.

Table 3.3 shows a summary of the tests implemented. Figure 3.14 to Figure 3.19 illustrate examples of typical tests of each scenario.

Table 3.3 Summary of Field Testing at RELLIS Bridge.

Test Scenario	Designed Speed (mph)	Number of Tests
Single Vehicle	10	12
	20	17
	30	19
	40	20
	50	4
Back-to-Back	20	3
	40	3
Side-by-Side	20	2
	30	2
	40	1
Opposite Direction	20	4

(a) Vehicle Entered the RELLIS Bridge from the South

(b) Vehicle Reached Midspan of the RELLIS Bridge

(c) Vehicle Left the RELLIS Bridge

(d) Vehicle Reached Midspan on Lane 1

(e) Vehicle Entered on Lane 1

Figure 3.14. Test #1—Truck A Passed Lane 1 from South at 20 mph.

(a) Vehicle Entered the RELLIS Bridge from the North

(b) Vehicle Reached Midspan of the RELLIS Bridge

(c) Vehicle Left the RELLIS Bridge

(d) Vehicle Reached Midspan on Lane 2

(e) Vehicle Entered on Lane 2

Figure 3.15. Test #64—Truck B Passed Lane 2 from North at 30 mph.

(a) Vehicle Entered the RELLIS Bridge from the South

(b) Vehicle Reached Midspan of the RELLIS Bridge

(c) Vehicle Left the RELLIS Bridge

(d) Vehicle Reached Midspan on Lane 3

(e) Vehicle Entered on Lane 3

Figure 3.16. Test #85—Single Vehicle—Truck C Passed Lane 3 from South at 40 mph.

(a) First Vehicle Entered the RELLIS Bridge from the South

(b) Second Vehicle Entered the RELLIS Bridge

(c) Second Vehicle Reached the Midspan While the First Vehicle Left the Bridge Already

(d) Two Vehicles on Lane 2

(e) Back-to-Back Scenario

Figure 3.17. Test #37—Back-to-Back—Truck A and B Passed Lane 2 from South at 20 mph.

(a) Two Vehicles Entered the RELLIS Bridge from the South

(b) Two Vehicle Reached Midspan of the RELLIS Bridge

(c) Vehicles Left the RELLIS Bridge

(d) Two Vehicles on Lane 1 and 3

(e) Side-by-Side Scenario

Figure 3.18. Test #44—Side-by-Side—Truck A and B Traveled at 30 mph Simultaneously.

(a) Two Vehicles Entered the RELLIS Bridge from Opposite Directions

(b) Two Vehicles Reached Midspan of the RELLIS Bridge from Opposite Directions

(c) Vehicles Left the RELLIS Bridge from Opposite Directions

(d) Two Vehicles on Lane 1 and 3

(e) Opposite Direction Scenario

Figure 3.19. Test #50—Opposite Direction—Truck A and B Traveled at 20 mph.

3.6. Data Processing

The data processing mainly focused on the strain gauge and load cell data. There were several assumptions as part of the data processing. The B-WIM methods employed assumed that the RELLIS Bridge behaved as a simply supported span. It was also assumed that the truck loads could be modeled as a group of concentrated forces moving across the bridge structure at a constant speed. The bridge and truck dynamics were not explicitly modeled and were primarily removed through data filtering techniques to obtain the static content.

3.6.1. Axle Information

The axle information herein includes the axle number, axle spacing, and average speed. The field test data were processed in MATLAB. An important initial step in the data processing is to identify the peaks (or spikes) in the axle detection data. These peaks depict the instance that an axle is right above the gauge, which is critical information for the B-WIM algorithms. For the preliminary study, the peaks were manually selected to obtain accurate axle numbers and their ordinates in each data set. The rest of the axle information was calculated automatically with different algorithms. Overall, the final goal in this study is to develop a fully automated program to obtain all axle information with high accuracy.

3.6.1.1. Strain Gauge

Data from the axle detection strain gauges installed on south and north ends of the bridge were retrieved from the DAQ and initially processed with a low-pass filter. A low-pass

filter allows signals below a cutoff frequency (passband) and attenuates signals above the cutoff frequency (stopband). By removing some frequencies, the filter creates a smoothing effect. In other words, the filter produces slow changes in output values to make it easier to see trends and boost the overall signal-to-noise ratio with minimal signal degradation. The cutoff frequency was set as 1 Hz. Figure 3.20 shows an example of an original dataset with the filtered data.

There were two methodologies used to process the strain data. The first method was to use the filtered data directly. The second method was to use the second derivative of the measured data. In general, the second derivative of strain is proportional to the second derivative of the bending moment. For a concentrated load, the second derivative of moment is a function that shows an abrupt change in loading. In reality, each negative peak on the plot of strain second derivatives depicts the instance an axle is right above the strain gauge. Figure 3.21 shows the second derivative of a strain dataset when Truck A passed the bridge in Lane 1.

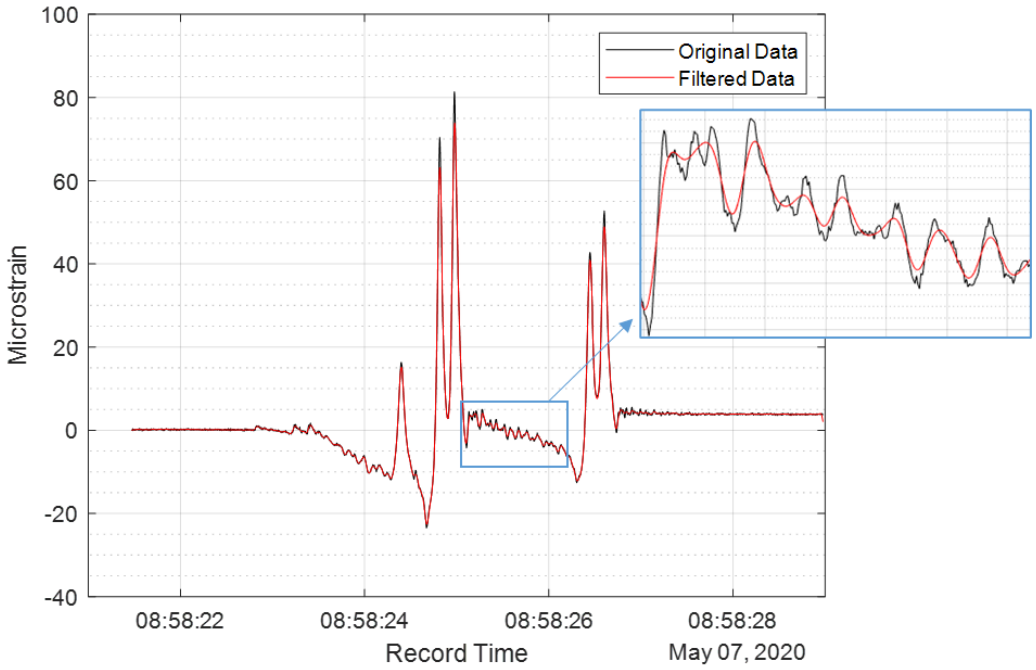

Figure 3.20. Original Data and Filtered Data from a Strain Gauge in a Truck A Test.

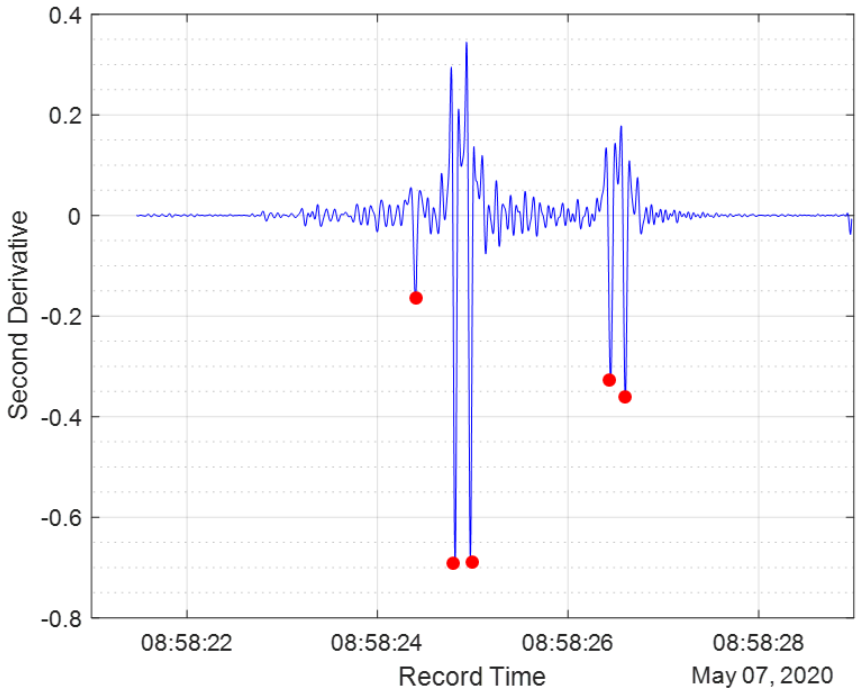

Figure 3.21. Second Derivative of Measured Strain in a Truck A Test.

Since the measured strain data had a high quality and low noise level, the first method was used to save computation time. Each spike or peak in the measured data indicates a truck axle passing the strain gauge, where the axle numbers are obtained directly by counting the number of peaks. The average speed of the vehicle, *v*, is determined from Eq. (3.1):

$$v = \frac{l}{\Delta t_1} \tag{3.1}$$

where *l* is the distance between the south and north strain gauges (40.0 ft for the RELLIS Bridge) and Δt_1 is the time duration (seconds) of the first axle passing the two sensors.

The time difference of each axle passing over the south or north end of the strain gauges are provided in the measured strain time history data. The product of time difference and the calculated average speed provides the truck's axle spacing, d_n, as given by Eq. (3.2):

$$d_n = v \times \left(t_{n+1} - t_n\right), \;\; n = 1, 2, 3, \cdots, n-1 \tag{3.2}$$

where t_n is the time that the n^{th} axle reaches the south or north end strain gauge.

Figure 3.22 to Figure 3.24 illustrate measured strain data examples of each type of truck during the testing. It was found that only the axle detection strain gauges underneath the deck of the truck lane could show clear peaks when the axles passed over the sensor. The remaining axle detection gauges underneath other lanes had much lower response values and more noises. This indicates the importance of clearly identifying the truck lane position within the algorithm. The sign (positive or negative) of the peaks depends on the location of the gauge. For example, when the trucks were traveling on

Lane 1 or Lane 3, the south end strain gauge data had peaks with negative magnitude, while the north end data had positive peaks. When the trucks passed the bridge on Lane 2, both ends showed positive peaks. It was also found that the north end strain gauges had larger peak magnitude than the south end strain gauges.

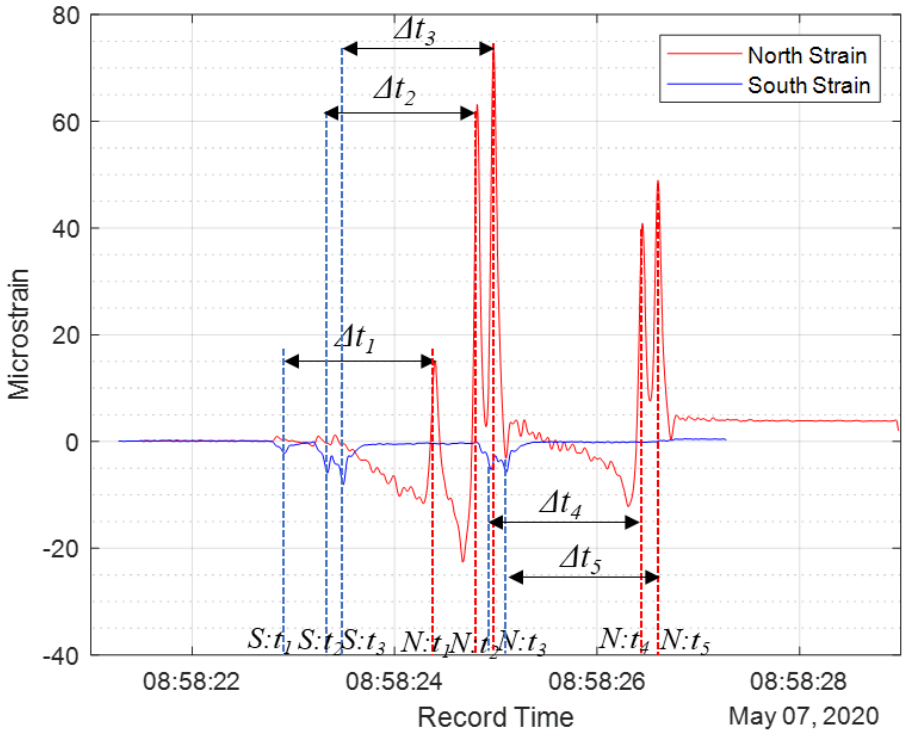

Figure 3.22. Strain Gauge Axle Information—Truck A in Lane 1 from the South at 20 mph.

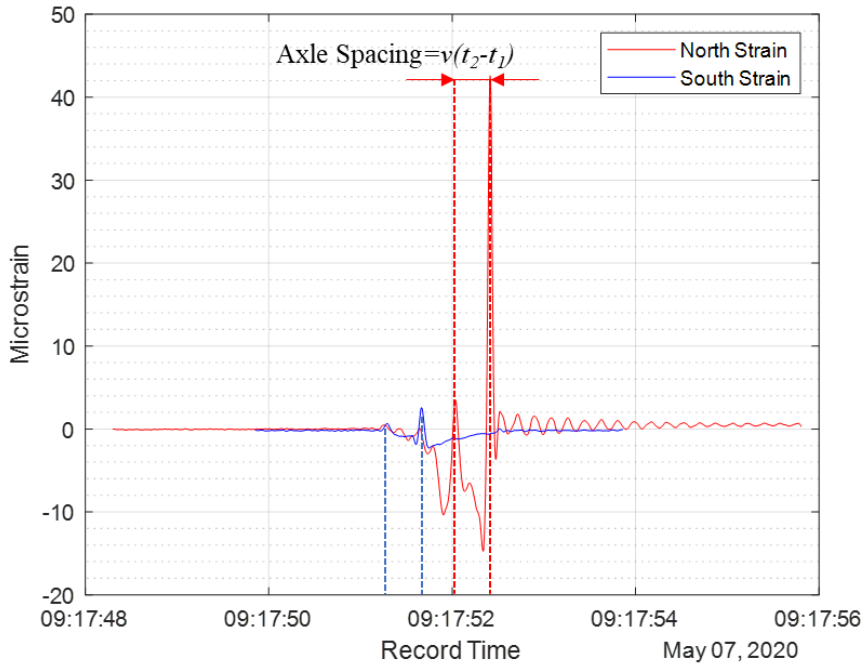

Figure 3.23. Strain Gauge Axle Information—Truck B in Lane 2 from the South at 40 mph.

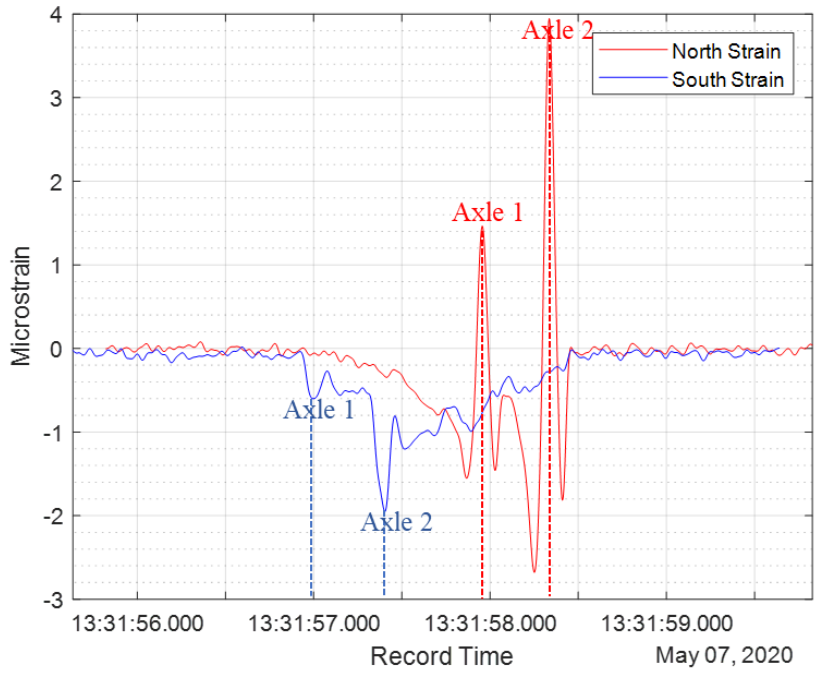

Figure 3.24. Strain Gauge Axle Information—Truck C in Lane 3 from the South at 30 mph.

The accuracy of the results was evaluated using the percent error method. In this section percent error was simply calculated using Eq. (3.3):

$$Error = \frac{C - M}{M} \times 100\% \tag{3.3}$$

where *C* represents the calculated result and *M* represents the measured (i.e., known) value from the radar gun, measuring tape, or static scales. Later in Section 3.7 the results are summarized as percent accuracy since this is a standard WIM approach.

Average velocities of each truck, in single vehicle tests, were calculated. The histogram of errors for the calculated average speeds is shown in Figure 3.25. The mean value of the errors is −1.3 percent with a standard deviation of 3.7 percent. Figure 3.26 shows the cumulative density function (CDF) of the errors.

The errors of axle spacing were also calculated. These errors have a mean of −1.2 percent and standard deviation of 5.2 percent. Figure 3.27 and Figure 3.28 show the histogram and CDF of errors, respectively.

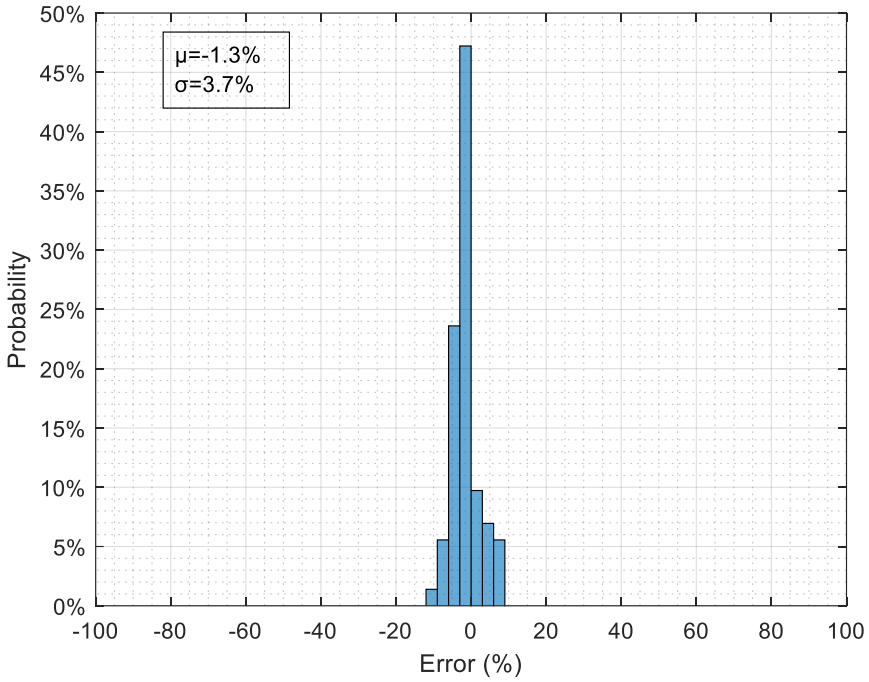

Figure 3.25. Histogram of Average Speed Errors (Strain Gauge).

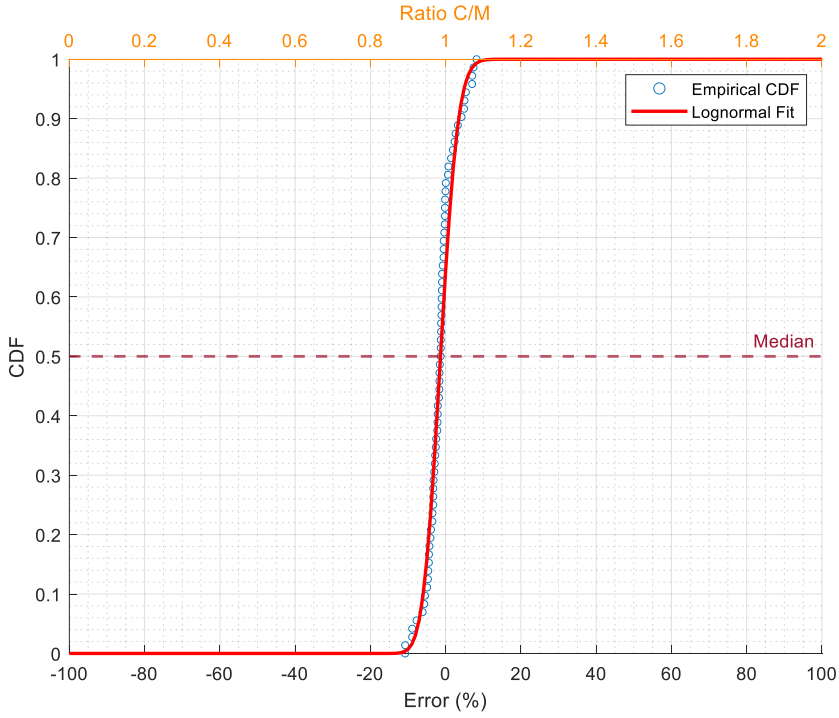

Figure 3.26. CDF of Average Speed Errors (Strain Gauge).

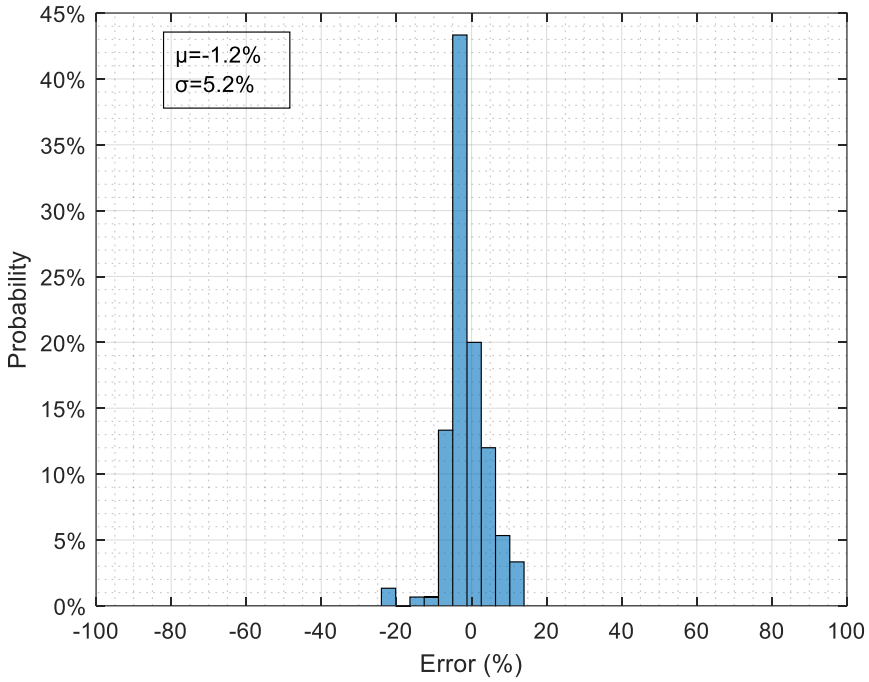

Figure 3.27. Histogram of Axle Spacing Errors (Strain Gauge).

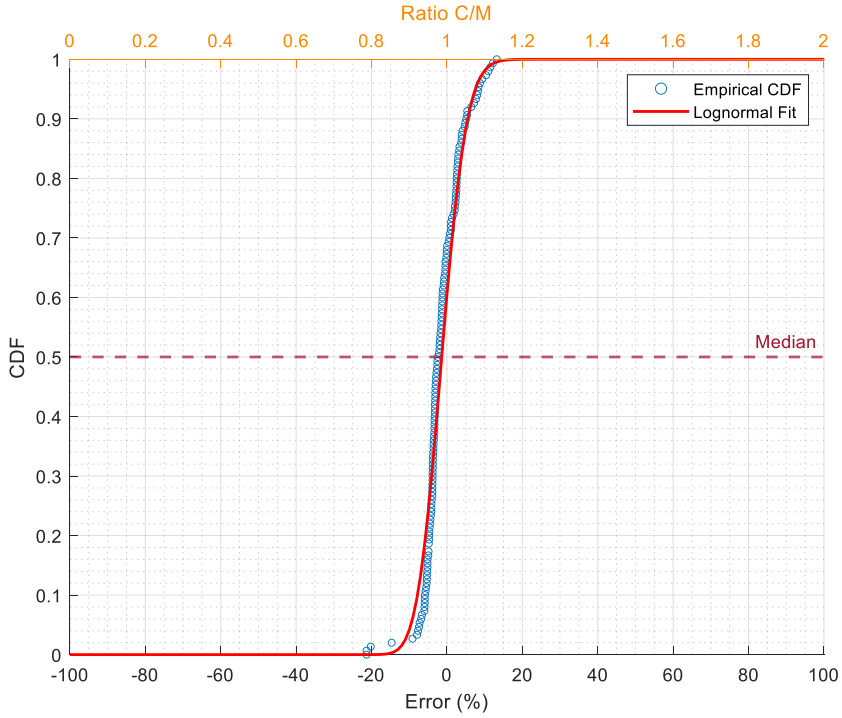

Figure 3.28. CDF of Axle Spacing Errors (Strain Gauge).

3.6.1.2. Load Cell

The load cell data were initially processed by a minimum-order low-pass filter with a cut-off frequency of 1 Hz. The filter was used to smooth the data for better peak detection results. To find the corresponding peaks (or spikes) of the passing axles, the second derivative of the reaction force data was used. This provided clear peaks when the vehicle reached the load cell.

Figure 3.29 shows the measured data and the second derivative from the load cells underneath the south side of Beam 2, with Truck A passing the bridge from the south at 10 mph. In this test, the second derivative of the south side load cell data exhibits peaks when the truck enters the bridge. The negative peaks in the second derivative from the north side load cell data indicate the truck axles leaving the bridge. The average speed and axle spacing can be determined by implementing Eq. (3.1) to Eq. (3.2). The distance l between the south and north end load cells is 46.6 ft. Figure 3.30 to Figure 3.32 demonstrate examples of the second derivative of the measured data in different truck tests and the resulting information obtained.

Average speed error of each truck test was analyzed, and the histogram is shown in Figure 3.33. The results have a mean value of 0.5 percent and a standard deviation of 4.5 percent. Figure 3.34 shows the CDF of the errors. The errors of axle spacing were calculated and shown in Figure 3.35 and Figure 3.36. The mean of the errors is −0.9 percent, and the standard deviation is 5.1 percent.

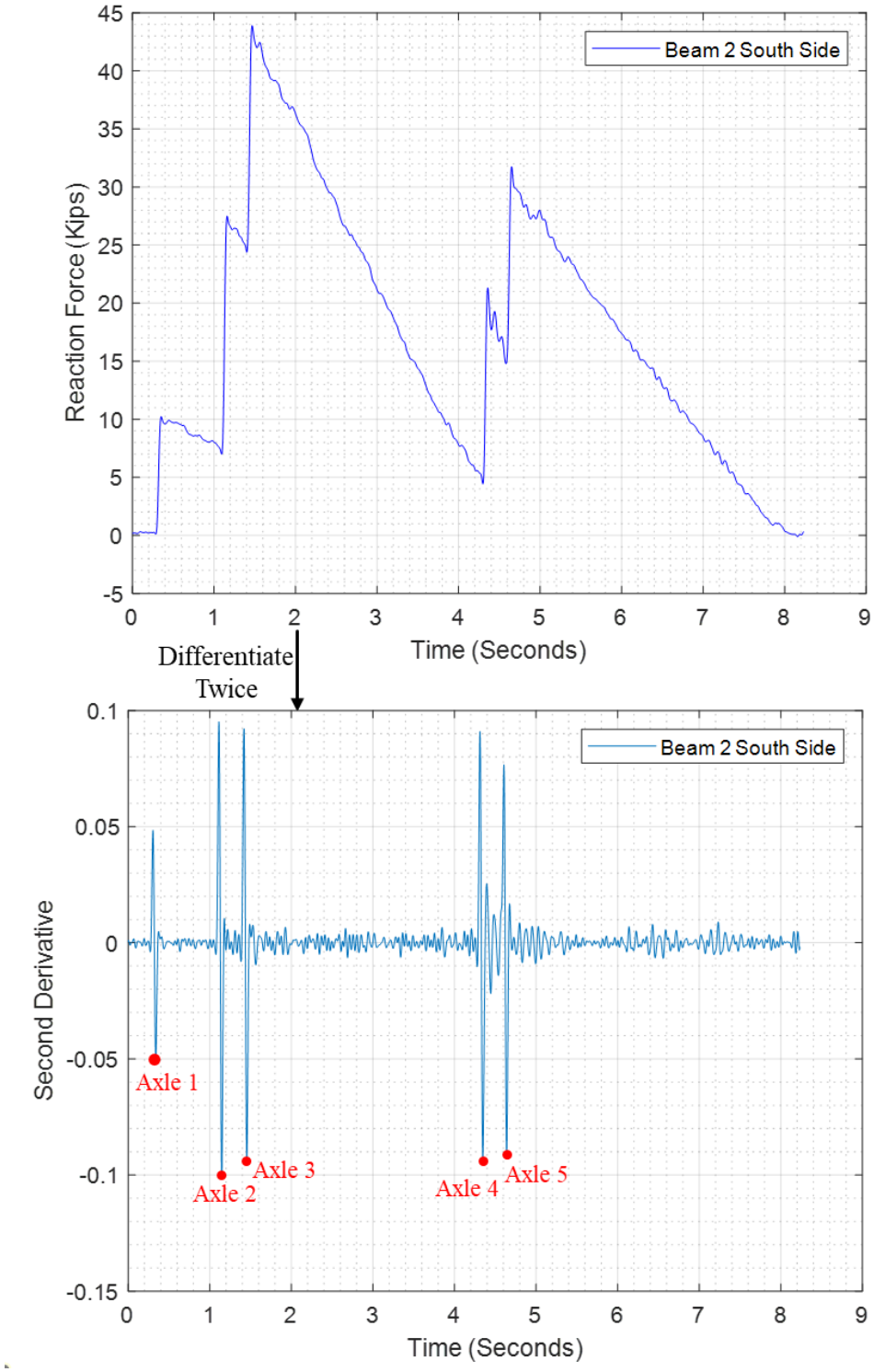

Figure 3.29. Measured Load Cell Data and Second Derivative of the Data.

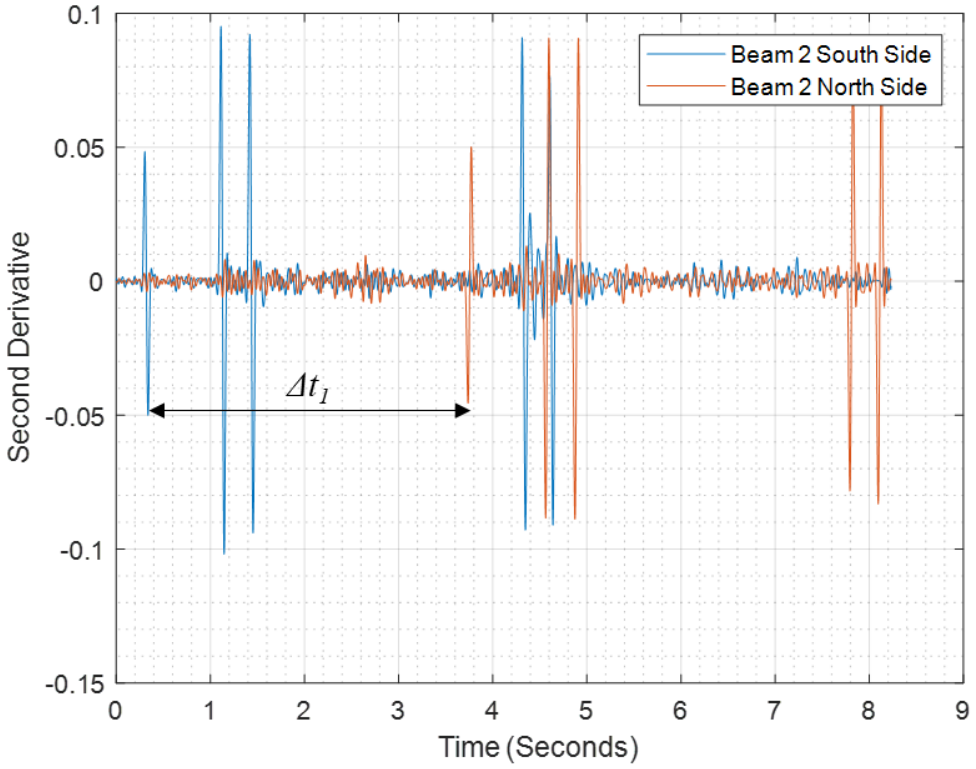

Figure 3.30. Load Cell Axle Information—Truck A in Lane 2 from the South at 10 mph.

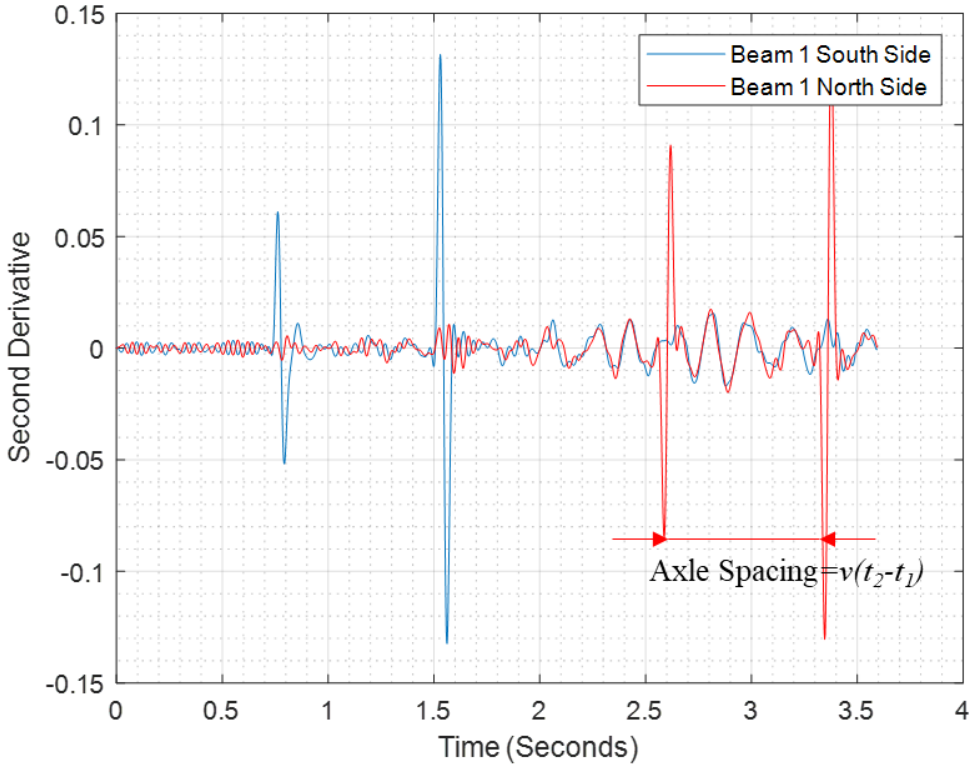

Figure 3.31. Load Cell Axle Information—Truck B in Lane 1 from the South at 20 mph.

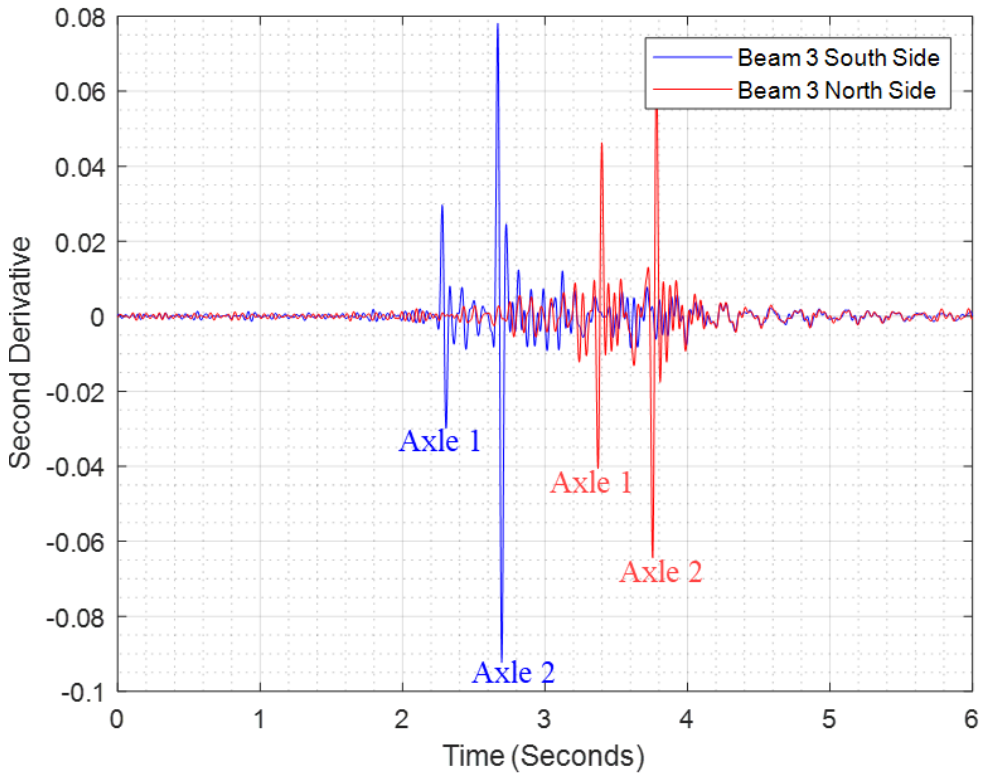

Figure 3.32. Load Cell Axle Information—Truck C in Lane 3 from the South at 30 mph.

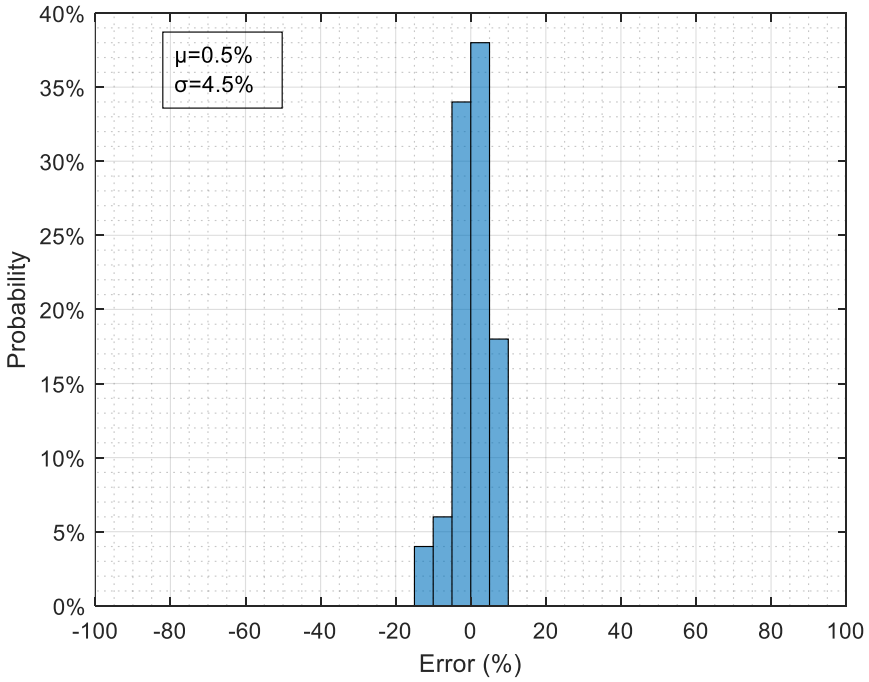

Figure 3.33. Errors of Average Speed (Load Cell).

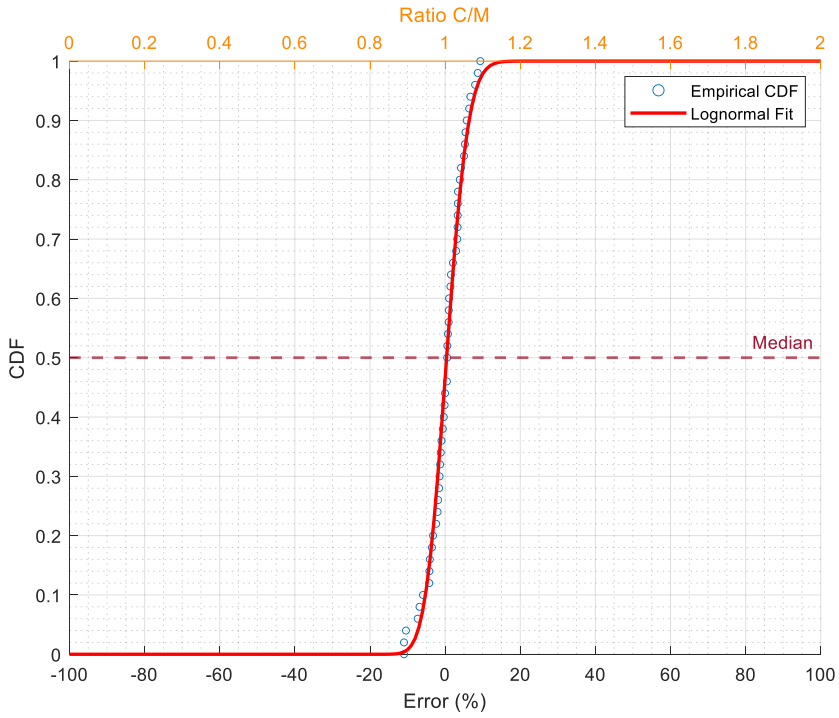

Figure 3.34. CDF of Average Speed Errors (Load Cell).

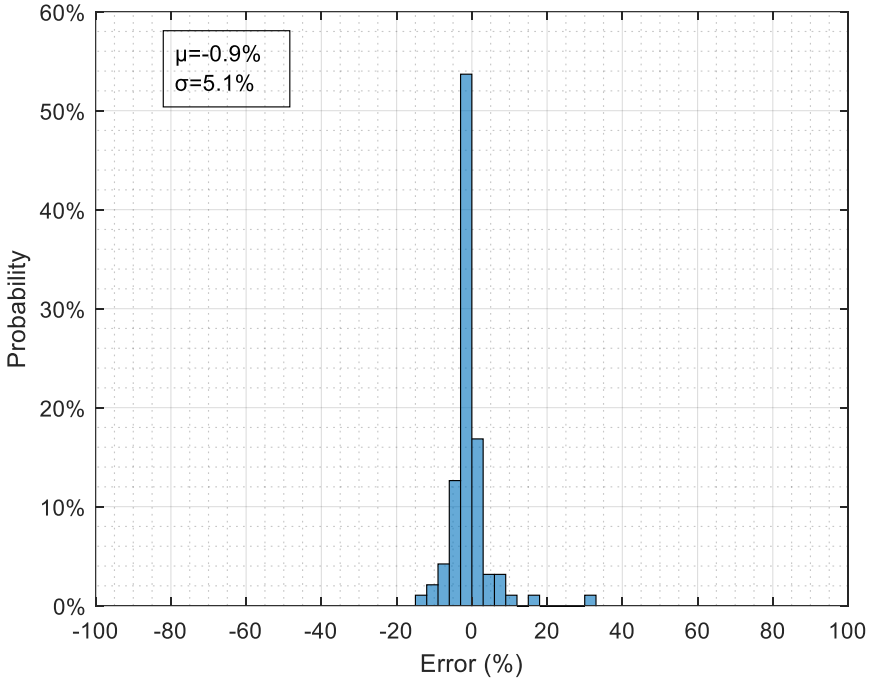

Figure 3.35. Histogram of Axle Spacing Errors (Load Cell).

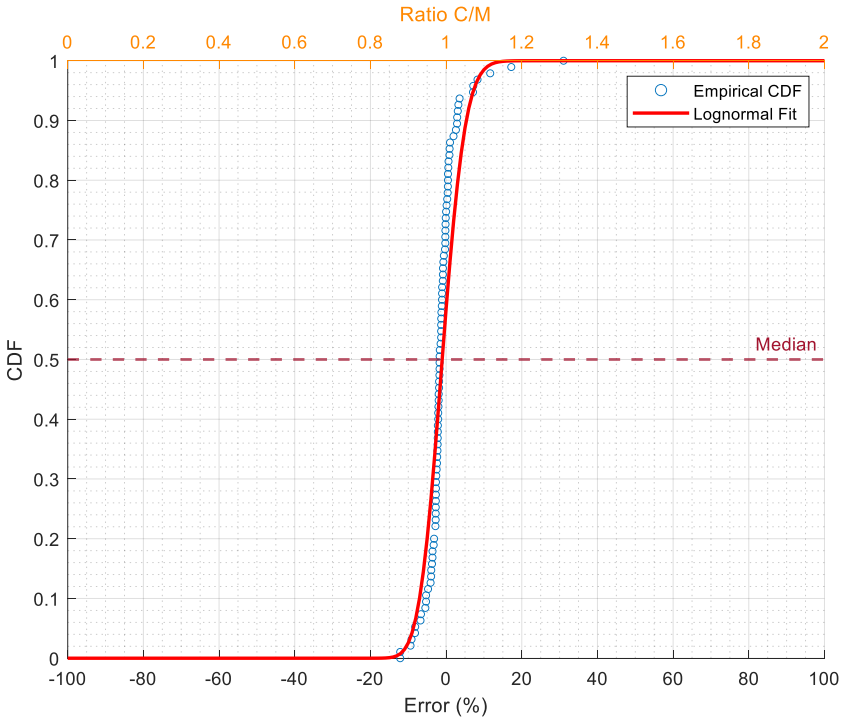

Figure 3.36. CDF of Axle Spacing Errors (Load Cell).

3.6.2. Weight Information

The weight information herein includes the GVW and the individual axle weights of a truck. Several algorithms were applied to identify the weight information. The data processed were from the weighing sensors (i.e., midspan strain gauges and load cells). The axle information required in some weight calculation algorithms were obtained from the algorithms in the previous section.

3.6.2.1. Area Method—Strain Gauge

The area method was proposed by (Ojio and Yamada 2002) to determine the GVW. This method is based on the principle that the area under the response curve can be expressed as the product of the GVW and the area under the influence line, that is, the influence area. This is shown in Eq. (3.4):

$$A = \sum_{n=1}^{N} P_n \int_{-\infty}^{+\infty} IL(x)\,dx = GVW \sum_{n=1}^{N} \int_{-\infty}^{+\infty} IL(x)\,dx \tag{3.4}$$

where A is the influence area, N is the number of axles of the vehicle, P_n is the axle weight of the n^{th} axle, $IL(x)$ is the function of the influence line, and x is the position of the first axle.

The area under the response curve can be obtained by numerically integrating the response of the bridge. Thus, with a calibration vehicle of a known weight, the weight of another vehicle with unknown weight can be obtained by Eq. (3.5):

$$GVW_u = A \times \frac{GVW_c}{A_c} \tag{3.5}$$

where GVW_u is the GVW of the unknown vehicle, A is the area under the response curve for the vehicle with the unknown weight, A_c is the area under the response curve for the calibration truck, and GVW_c is the GVW of the calibration truck.

It was found that the accuracy of this method was influenced by the lateral position of the truck when it passed the bridge. A separate algorithm was developed to identify the truck lane. Taking the spatial effect of the bridge into consideration, the induced strain area of all the eight weighing sensors underneath the beams at midspan were summed for a total area of each test. Figure 3.37 shows the induced strain area of the weighing sensors.

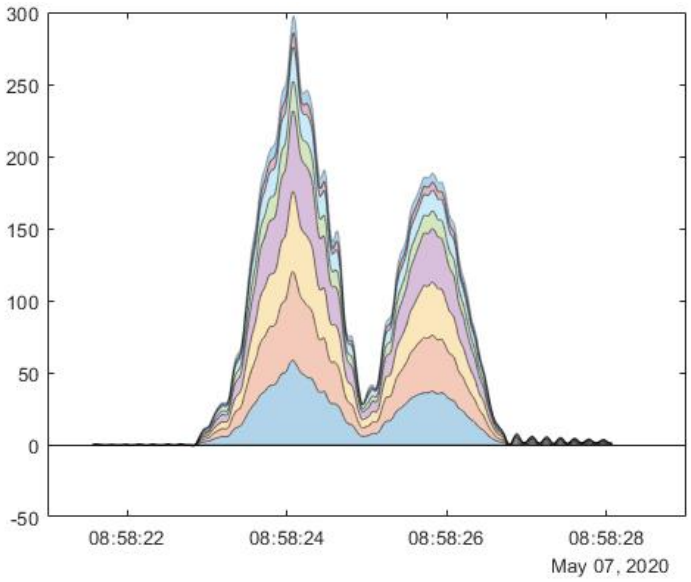

Figure 3.37. Example Area of Strain Induced in a Test.

Each truck test dataset of the single vehicle tests (72 in total) was used as a calibration truck to calculate the weight of the remaining trucks. The speed of the trucks must be accounted for since the total area is a function of the speed. Figure 3.38 provides

the total strain area versus truck speed for Truck A. (Truck B and C produce similar results.) A relatively linear relationship was observed.

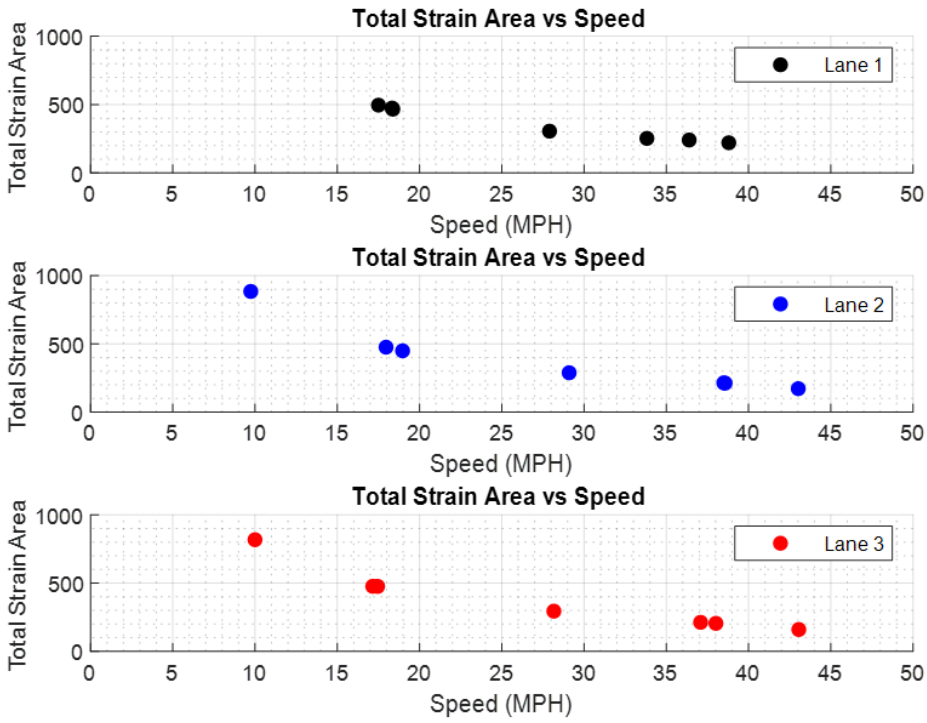

Figure 3.38. Truck A Total Strain Area versus Speed.

Combining the sum of strain area from each weighing sensor as well as the speed effect, the researchers developed a method named total area method with an adjustment coefficient α. In this method, the ratio between the weight of the calibration truck and the test truck is given by Eq. (3.6). The adjustment coefficient α is defined by Eq. (3.7), and then the unknown GVW of a test vehicle can be determined by Eq. (3.8).

$$\frac{GVW_u}{GVW_c} = \frac{\left(\sum_{i=1}^{8} A_{u_i}\right) \times v_u}{\left(\sum_{i=1}^{8} A_{c_i}\right) \times v_c} \tag{3.6}$$

$$\alpha = \frac{GVW_c}{\sum_{i=1}^{8} A_{c_i} \times v_c} \tag{3.7}$$

$$GVW_u = \left(\sum_{i=1}^{8} A_{u_i}\right) \times v_u \times \alpha \tag{3.8}$$

where GVW_u is the unknown weight of a test truck, GVW_c is the weight of the calibration truck, A_{ui} is the measured strain area of i^{th} strain gauge in a test, A_{ci} is the strain are of i^{th} strain gauge in the calibration test, v_u is the average speed of the test truck, and v_c is the average speed of the calibration truck.

The histogram of errors of the calculated GVW is shown in Figure 3.39. The mean value of the errors is −0.7 percent with a standard deviation of 11.6 percent. Figure 3.40 shows the CDF of the errors. Each single vehicle test was used as a calibration test to calculate the truck GVWs of the remaining tests. The errors of GVW are affected by the error of calculated average speed and the quality of the induced strain area data.

Theoretically, the axle weights are relative to the magnitudes of the negative peaks of the second derivative of the strain as each axle passes over the bridge midspan. However, the strain from the midspan gauges did not provide clear peaks. As a result, the data from the axle detection sensors were used to obtain the axle weights, which caused some errors. However, the final accuracy of axle weights using strain gauge data is summarized in Section 3.7.

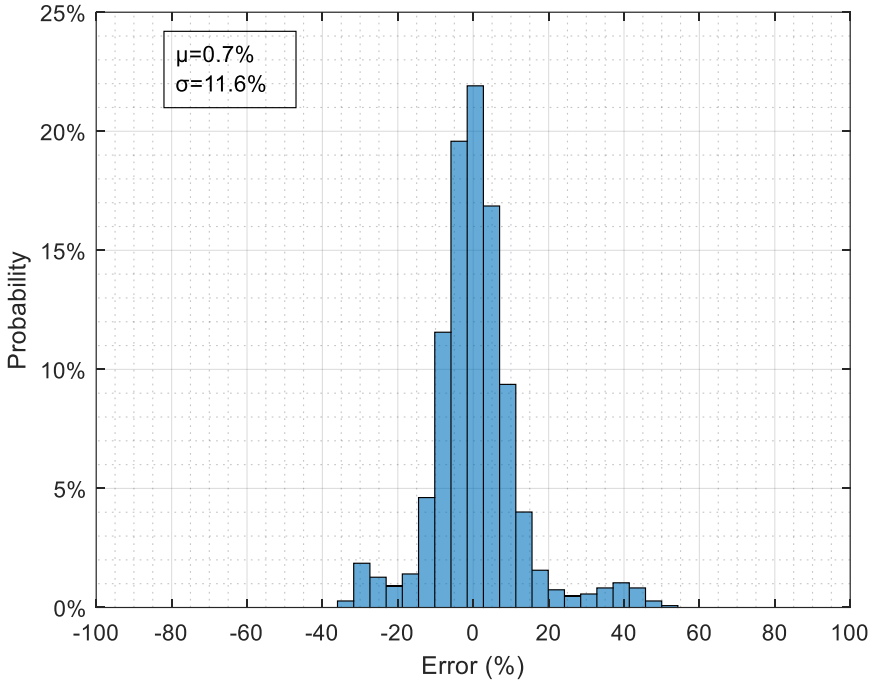

Figure 3.39. Histogram of GVW Errors by Total Area Method (Strain Gauge).

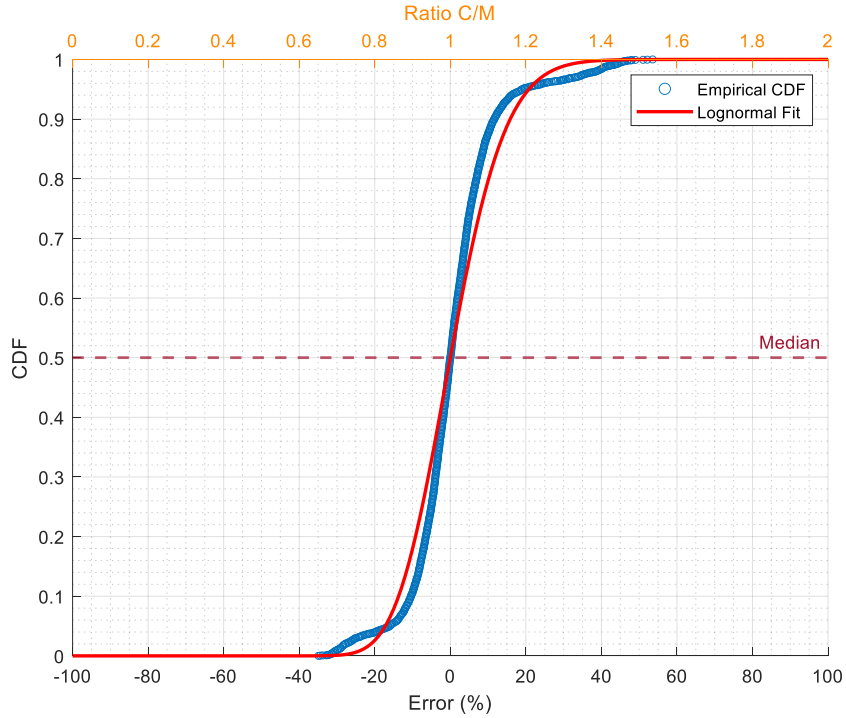

Figure 3.40. CDF of GVW Errors by Total Area Method (Strain Gauge).

3.6.2.2. Area Method—Load Cell

Similar to the strain data, the total area method was applied to the load cell data. Eq. (3.6) to Eq. (3.8) were used to determine the GVW of an unknown vehicle. It should be noted that the total area was changed to the sum of the area of reaction forces from the 16 load cells. Figure 3.41 shows an example of the area from one load cell during a test.

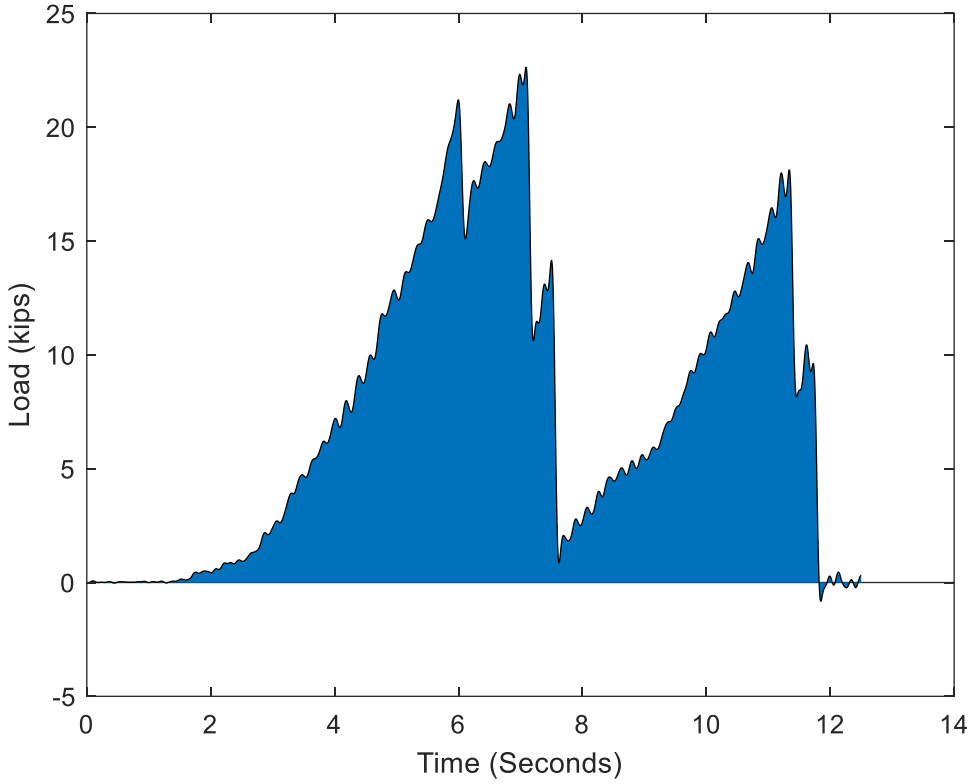

Figure 3.41. Area of the Reaction from a Test.

The GVW of each truck in single vehicle tests were calculated based on each calibration truck test. The histogram of the calculated GVW errors is shown in Figure 3.42. The mean value of the errors is 1.2 percent with a standard deviation of 16.2 percent. Figure 3.43 shows the CDF of the errors.

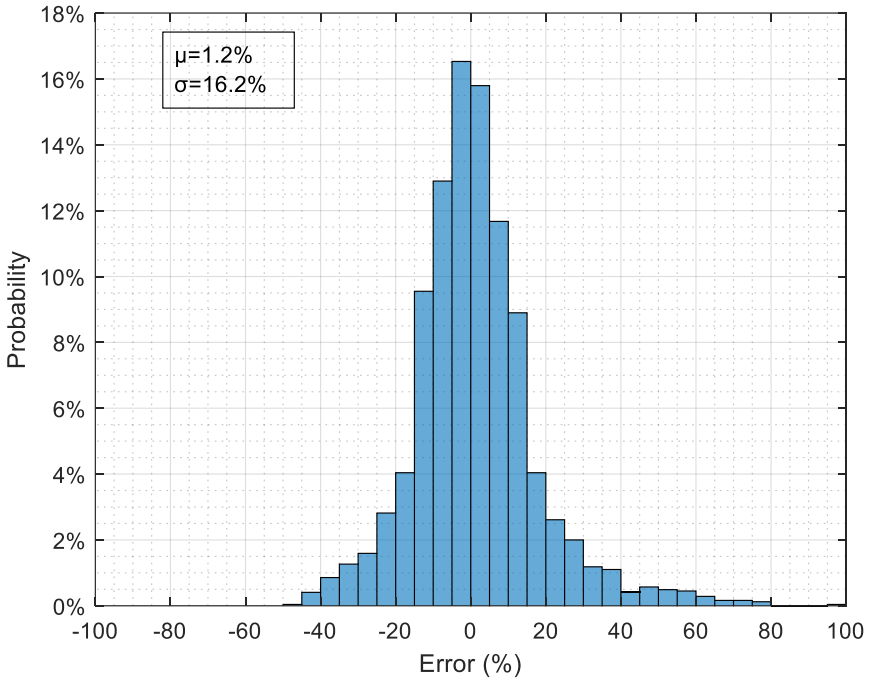

Figure 3.42. Histogram of GVW Errors by Total Area Method (Load Cell).

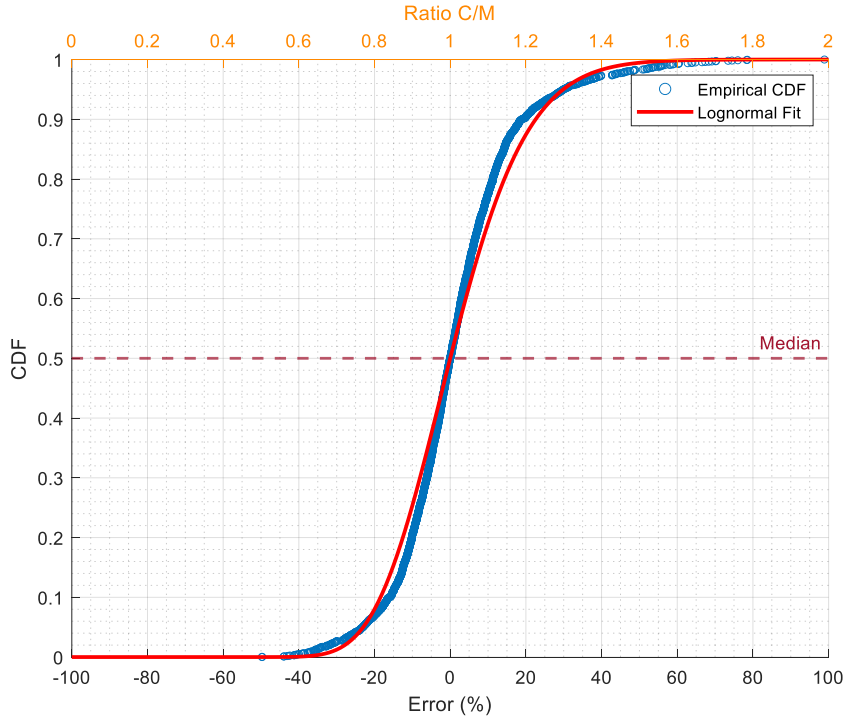

Figure 3.43. CDF of GVW Errors by Total Area Method (Load Cell).

3.6.2.3. Reaction Force Method—Load Cell

The reaction force method (Ojio and Yamada 2005) uses the measured reaction at the support to calculate the axle weights. This method uses the influence line of the reaction for a simply supported bridge. The axle weights can be calculated using the influence line. The GVW can then be calculated by summing the axle weights. With the load cells installed on both ends of the RELLIS Bridge, this method is feasible to apply. Figure 3.44 shows the influence line of the support reaction for the RELLIS Bridge when a 1-kip unit load passes the bridge in either direction.

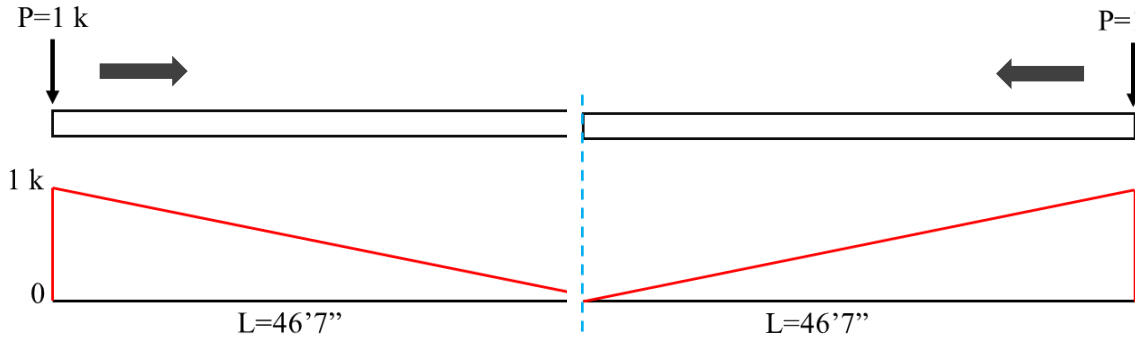

(a) South End Load Cell Reaction (a) North End Load Cell Reaction

Figure 3.44. Reaction Force Influence Line of the RELLIS Bridge.

Each selected peak in the load cell time history plot is the time step when an axle of a vehicle passes the load cell. The reaction can be calculated by multiplying the axle weight with the influence ordinate (*I*) accordingly. It is obvious that the first axle weight equals the sum of first peak found in the time history of all beams. The influence

ordinates of the rest of the axles can be calculated using similar triangles with the axle spacing obtained previously.

Among the three test trucks, applying the reaction force method to Truck B and Truck C is very straightforward since their axle spacings are within the length of the bridge. However, the total length of Truck A is longer than the bridge, which means some of the axles would be outbound while other axles were entering the bridge. Therefore, the related influence ordinates were set to be 0 when the axles were not on the bridge.

The following uses a Truck A test as an example. Figure 3.45 shows the time history data of Beam 1 when Truck A passed the bridge in Lane 1 from the south.

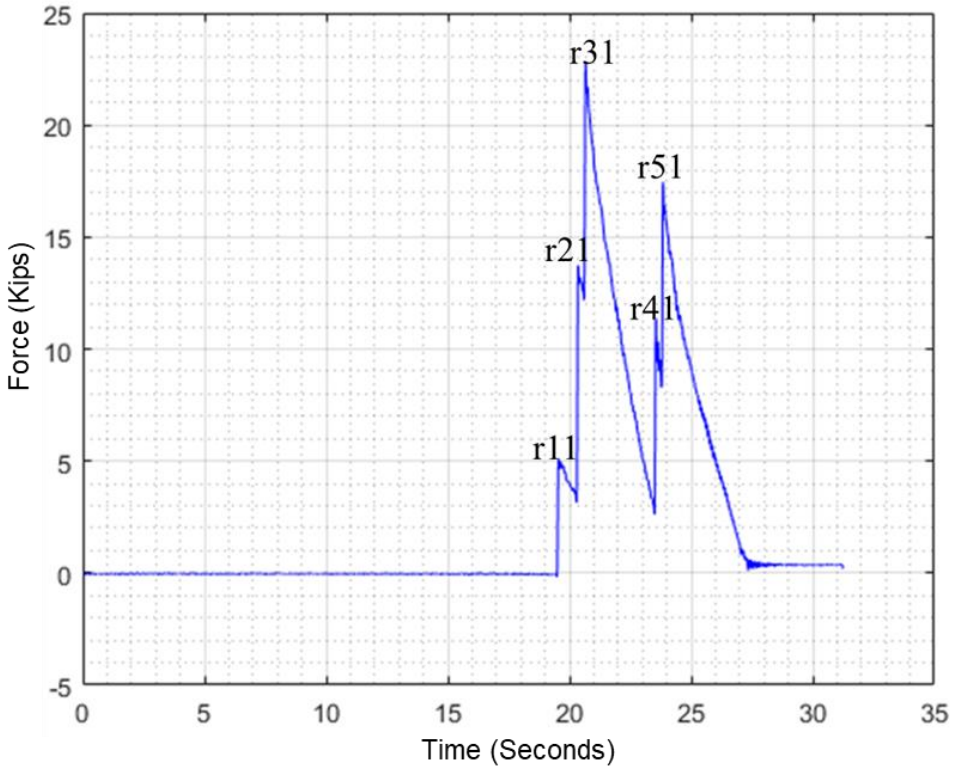

Figure 3.45 Load Cell Data of Beam 1.

The reaction force R_n can be calculated by summing the peak values of all the beams at the south end of the n^{th} peak, as Eq. (3.9) shows.

$$R_n = \sum_{i=1}^{N} r_{ni} \tag{3.9}$$

where n is the number of the peak, N is the number of the beams (for the RELLIS Bridge, N is 4), and r_{ni} is the n^{th} reaction force of the i^{th} beam at the south end.

The scenario of Truck A passing the bridge with a span length L can be divided into five stages as a demonstration (shown graphically in Figure 3.46). At stage 1, the first axle (Axle 1) reaches the centerline of the load cell at the south end while the rest of the axles have not entered the bridge. The influence ordinate of Axle 1 is equal to the height of the influence line, which is 1.0, and the rest of the axles have influence ordinates of 0. At stage 2, the second axle reaches the centerline of the load cell, and the first axle moves forward the distance between Axle 1 and Axle 2 (d_1). The influence ordinate of Axle 2 is 1.0, where the influence ordinate of Axle 1 can be calculated. This was done using the similar triangles with the obtained d_1, which equals to $(L-d_1)/L$. At stage 3, the truck moves forward another distance between Axle 2 and Axle 3 (d_2). Axle 3 has an influence ordinate of 1.0, and the influence ordinates of Axle 2 and Axle 1 are calculated as $(L-d_2)/L$ and $(L-d_2-d_1)/L$, respectively. At stage 4, Axle 4 enters the south end of the bridge while Axle 1 exits the bridge. Therefore, the influence ordinate of Axle 4 is 1.0, and the influence ordinate of Axle 3 and Axle 2 are $(L-d_3)/L$ and $(L-d_3-d_2)/L$, respectively. The Axle 1 influence ordinate is changed to 0. At stage 5, Axle 1 and Axle 2 exit the bridge and therefore have influence ordinates of 0. Axle 4 and Axle 3

have influence ordinates of $(L-d_4)/L$ and $(L-d_4-d_3)/L$, respectively. The influence ordinate of Axle 5 is 1.0.

Figure 3.46 graphically summarizes the stages for this illustration. Since the reaction force is equal to the production of axle weights and influence ordinates, five equations with five unknown axle weights can constructed as:

Stage 1: $P_1 \times 1 + P_2 \times 0 + P_3 \times 0 + P_4 \times 0 + P_5 \times 0 = R_1$

Stage 2: $P_1 \times \frac{L - d_1}{L} + P_2 \times 1 + P_3 \times 0 + P_4 \times 0 + P_5 \times 0 = R_2$

Stage 3: $P_1 \times \frac{L - d_2 - d_1}{L} + P_2 \times \frac{L - d_2}{L} + P_3 \times 1 + P_4 \times 0 + P_5 \times 0 = R_3$

Stage 4: $P_1 \times 0 + P_2 \times \frac{L - d_3 - d_2}{L} + P_3 \times \frac{L - d_3}{L} + P_4 \times 1 + P_5 \times 0 = R_4$

Stage 5: $P_1 \times 0 + P_2 \times 0 + P_3 \times \frac{L - d_4 - d_3}{L} + P_4 \times \frac{L - d_4}{L} + P_5 \times 1 = R_5$

The axle weights can then be obtained by solving the five equations above. The GVW can be obtained by simply summing all of the calculated axle weights. For the trucks entering the bridge from the north side, the steps are identical by using the influence line shown in the right side of Figure 3.44.

Stage Number	Truck Position	Influence Ordinates Illustration
#1		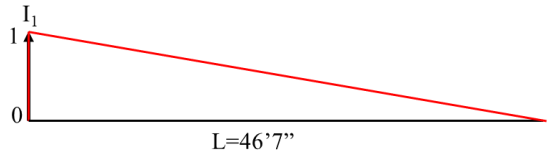
#2	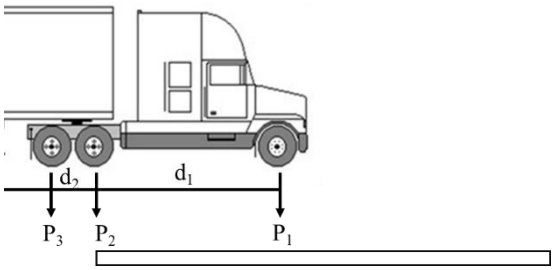	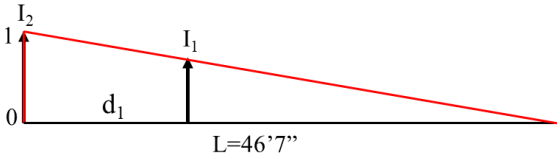
#3	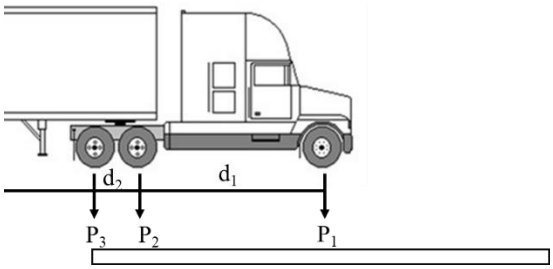	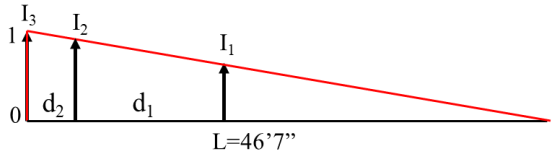
#4	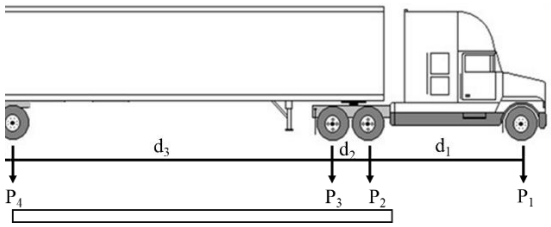	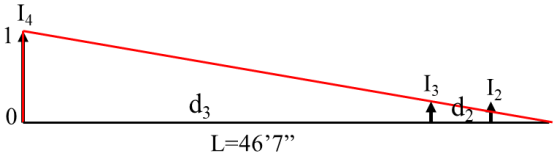
#5	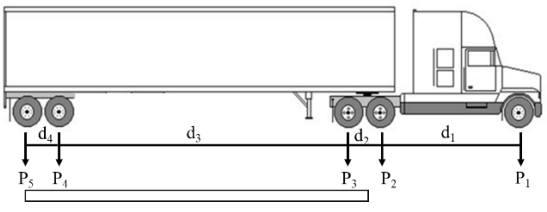	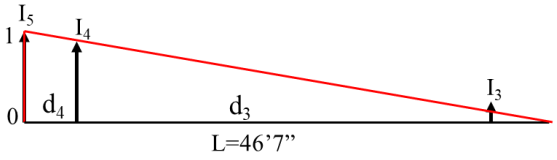

Figure 3.46. Truck Position and Influence Ordinates.

In general, for trucks with various axle numbers, the influence ordinates can be constructed as an n-by-n matrix, shown in Eq. (3.10), where I_n^j is the influence ordinate of the n^{th} axle at the j^{th} stage. The axle weights are structured as an n-by-1 matrix, as shown in Eq. (3.11). Eq. (3.12) shows the n-by-1 matrix of the reaction forces, where R_n is calculated by Eq. (3.9).

$$\mathbf{I} = \begin{bmatrix} 1 & 0 & \cdots & \cdots & 0 & 0 \\ I_1^2 & 1 & \cdots & \cdots & 0 & 0 \\ I_1^3 & I_2^3 & \ddots & & \vdots & \vdots \\ I_1^4 & I_2^4 & I_3^4 & \ddots & \vdots & \vdots \\ \vdots & \vdots & \vdots & & 1 & 0 \\ I_1^n & I_2^n & I_3^n & \cdots & \cdots & 1 \end{bmatrix} \tag{3.10}$$

$$\mathbf{P} = \begin{bmatrix} P_1 \\ P_2 \\ P_3 \\ \vdots \\ P_n \end{bmatrix} \tag{3.11}$$

$$\mathbf{R} = \begin{bmatrix} R_1 \\ R_2 \\ R_3 \\ \vdots \\ R_n \end{bmatrix} \tag{3.12}$$

The final equation in matrix format is given by Eq. (3.13), and the solutions of the axle weights are obtained by Eq. (3.14). In addition, GVW is calculated by Eq. (3.15).

$$\mathbf{I} \times \mathbf{P} = \mathbf{R} \tag{3.13}$$

$$\mathbf{P} = \mathbf{R} \times \mathbf{I}^{-1} \tag{3.14}$$

$$GVW = \sum_{1}^{n} P_{n} \tag{3.15}$$

The truck weight results were obtained from the reaction force method and compared with the measured weights (using static scales). The percentage of errors for GVW are shown in Figure 3.47 and Figure 3.48. The calculated GVW errors have a mean of −9.0 percent and standard deviation of 7.0 percent. The calculated axle weights of each truck have errors with a mean of −8.2 percent and standard deviation of 13.7 percent, as shown in Figure 3.49 and Figure 3.50. The hypothesized reason for the under prediction of the weights is the method for identifying the truck axle position. The second derivative method was used to automate the time each axle was over the load cells (manual peak picking not used). There appears to be a slight delay in this prediction, which reduced the influence line ordinate used along with the load cell value. The exact time of the second derivative calculation does not precisely coincide with the point in time the axles are over the center of the load cells. This can be corrected through offset of the data.

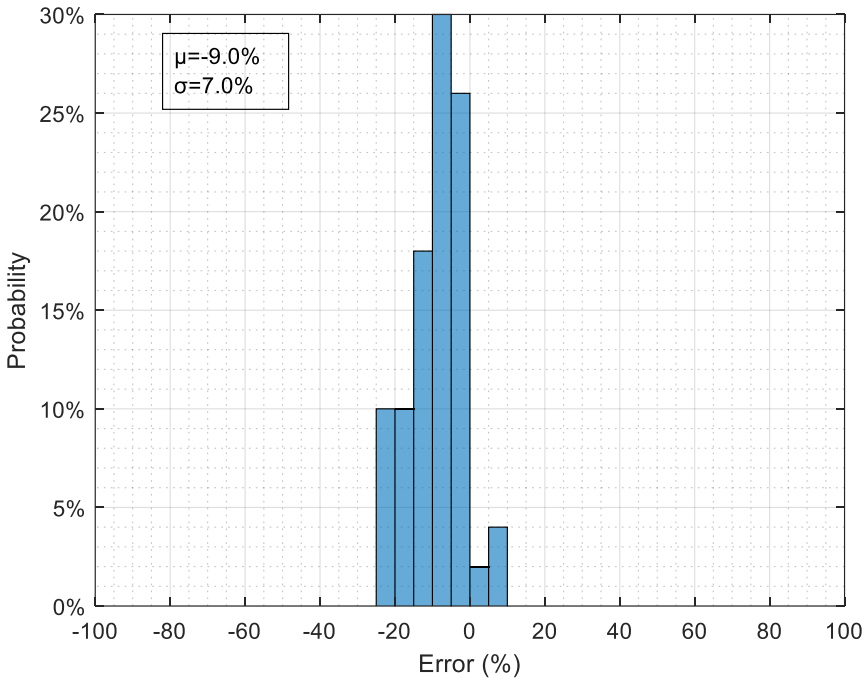

Figure 3.47. Histogram of GVW Errors by Reaction Force Method.

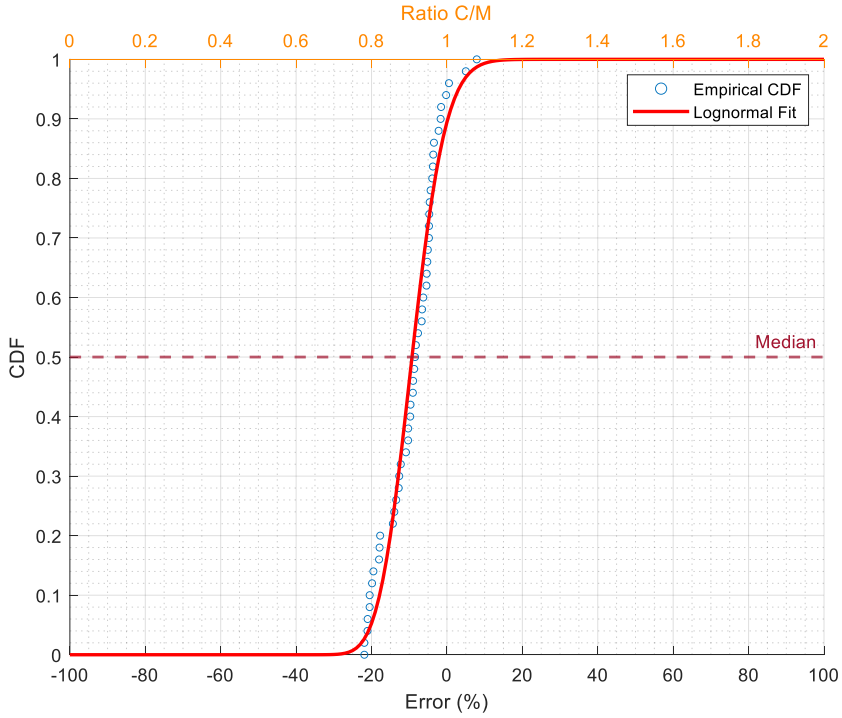

Figure 3.48. Histogram and CDF of GVW Errors by Reaction Force Method.

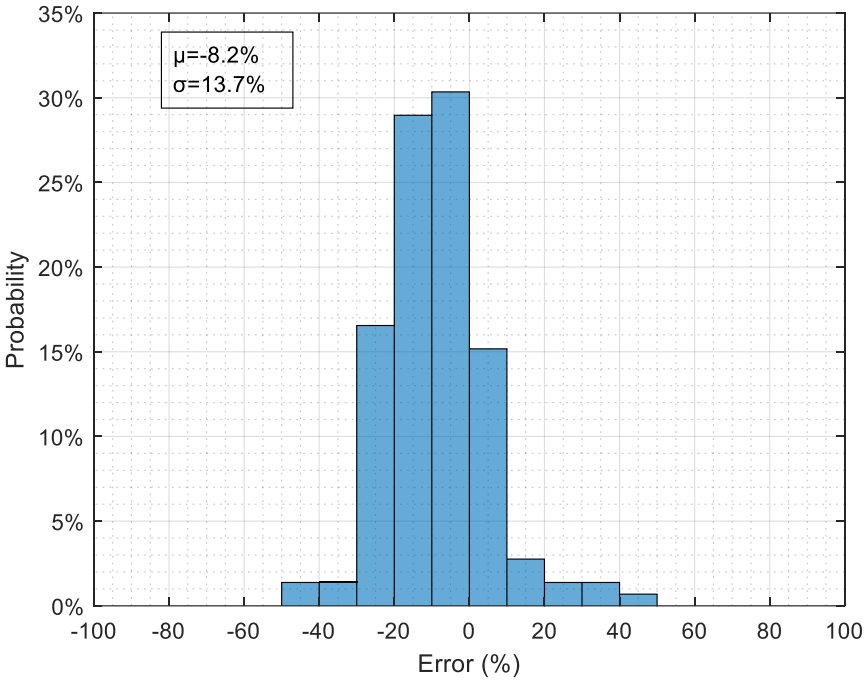

Figure 3.49. Histogram of Axle Weight Errors by Reaction Force Method.

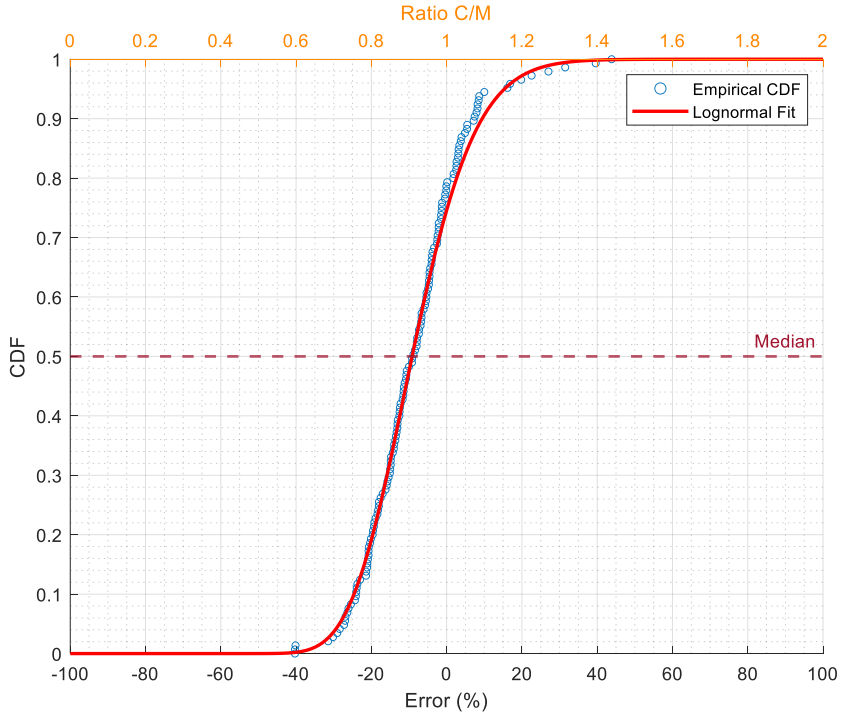

Figure 3.50. CDF of Axle Weight Errors by Reaction Force Method.

3.6.3. Side-by-side Cases Discussion

The individual GVW of the side-by-side trucks can be relatively challenging for BWIM systems. In this study these side-by-side GVWs were obtained by utilizing the area method and load cell distribution factors. For example, consider Truck A travels on Lane 1 (left lane), while Truck B travels on Lane 3 (right lane). The combined GVW (GVW_{total}) of the two trucks can be obtained by the area method introduced previously (assume two trucks pass the bridge with the same speed). The load cell distribution factor for this truck passing event (DF_i) can be determined by Eq. (3.16):

$$DF_i = \frac{r_i}{\sum_1^N r_i} \tag{3.16}$$

where N is the number of beams; and r_i is the reaction force of the i^{th} beam. By calculating the DF of each test, the average distribution factors when one truck passes the left lane (DFL_i) and the right lane (DFR_i) can be obtained. Using the i^{th} beam, two equations can be constructed as shown in Eq. (3.17). and Eq. (3.18):

$$GVW_A + GVW_B = GVW_{total} \tag{3.17}$$

$$DFL_i \cdot GVW_A + DFR_i \cdot GVW_B = DF_i \cdot GVW_{total} \tag{3.18}$$

The gross weight of each truck (GVW_A and GVW_B) can be determined by solving the above equations.

The distribution factors of each single-truck test were calculated and the results were averaged to get the DFL and DFR values. The DFL, DFR and the DFs of the 4 side-by-side tests (named as S1 to S4) are summarized in Table 3.4. It should be noted that in Test S1 to Test S3, Truck A (79,510 lb static weight) traveled on Lane 1 and

Truck B (33,020 lb static weight) traveled on Lane 3. In Test S4, Truck A traveled on Lane 3 and Truck B traveled on Lane 1.

The weight of each truck of the side-by-side tests was calculated using the results for each beam. As summarized in Table 3.5, it was found that when using the distribution factor for calculating the weight of side-by-side trucks, the average accuracy ranged from 76% to 87%. Since the individual weight of each truck is distributed from the sum weight of the trucks using this method, the accuracy is significantly influenced by the accuracy of GVW_{total} calculation by area method.

Table 3.4. Load Cell Distribution Factor Summary.

Configuration		Distribution Factor			
		Beam 1	**Beam 2**	**Beam 3**	**Beam 4**
DFL		0.35	0.56	0.08	0.01
DFR		0.01	0.05	0.57	0.37
DF	Test S1	0.29	0.36	0.23	0.12
	Test S2	0.28	0.37	0.22	0.13
	Test S3	0.27	0.35	0.21	0.16
	Test S4	0.15	0.22	0.36	0.27

Table 3.5. GVW Calculation of Each Truck and Average Accuracy Summary.

Test	Truck	GVW (kg)			
		Beam 1	**Beam 2**	**Beam 3**	**Beam 4**
S1	A	88,186	63,942	74,638	72,421
	B	17,879	42,124	31,428	33,644
S2	A	88,065	69,299	78,762	74,209
	B	22,469	41,235	31,772	36,326
S3	A	86,017	64,902	81,103	62,666
	B	23,789	44,904	28,703	47,140
S4	A	64,585	74,020	62,093	81,569
	B	46,135	36,700	48,626	29,151
Average Accuracy		76%	80%	87%	87%

3.6.4. Bridge Information

Historically, evaluation of the bridge itself has not been a requirement for B-WIM systems. However, the researchers have included this as an objective for the final B-WIM system developed as part of this study. While evaluation of the RELLIS Bridge was not an objective of this task, preliminary bridge evaluation metrics were explored to prepare for future tasks. This included a preliminary evaluation of field-measured live load distribution factors, composite action, and dynamic amplification using a B-WIM setup.

3.6.4.1. Live Load Distribution Factors

Bridge beams are commonly evaluated using line-girder analysis, which simplifies a 3D structural system to allow for 1D analysis. One of the important parameters in this analysis is live load distribution factors. Distribution factors provide a percentage of the live loading that is carried by a single beam. The most common approach for field identification of distribution factors (for a beam bridge) is to instrument every beam within a single bridge cross-section (common with B-WIM systems). The sensors are placed on the same location of each beam (e.g., bottom of the bottom flange). This captures the transverse distribution of live load response as the live load passes over the structure. The strains for each girder at a given time can then be used to find the live load distribution factors, as shown in Eq. (3.19):

$$g = \frac{\varepsilon_i}{\sum_1^n \varepsilon_i} \tag{3.19}$$

where ε_i is the measured strain in the i^{th} girder, g is the live load distribution factor for each girder, and n is the total number of girders in a cross-section.

For the RELLIS Bridge preliminary study, distribution factors were calculated for the interior beams. The response from all three trucks traveling in all lanes were analyzed. Figure 3.51 provides example midspan strain gauge data sets for Truck A in Lane 1 and 2. In addition to the one-lane loaded distribution factors, two-lane loaded distribution factors were obtained using superposition. In all cases Eq. (3.19) was used. The results of the analysis produced an interior beam moment distribution factor equal to 0.51. As a means of comparison, the prior TxDOT study found the interior beam distribution factor to be 0.65 for dump truck loading. The lower distribution factor from this study is appropriate since the truck positioning and truck type was not created for the worst case lateral distribution loading. The comparison indicates the identified distribution factor to be reasonable.

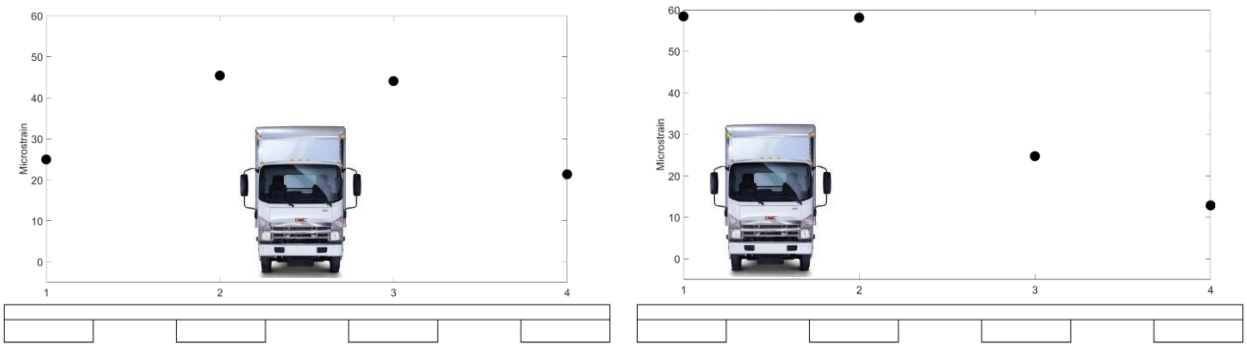

Figure 3.51. Examples of Midspan Strain Lateral Distribution.

3.6.4.2. Composite Action

The level of composite action refers to the continuity of the beams with the deck slab. Fully composite behavior indicates 100 percent continuity; thus the beams deform with the slab. Non-composite behavior is the opposite. The composite behavior may be uncertain due to the loss of as-built plans, long-term degradation of an originally designed fully composite bridge, or even a bridge that was designed as non-composite but has other mechanisms to behave as partial or even fully composite. As a result of this uncertainty, field measurements can accurately determine the composite behavior of the bridge.

For the RELLIS Bridge, the uncertainty of composite action was relatively low. The plans and construction photos clearly indicate composite reinforcement. However, field verification was performed in preparation for future tasks. The conventional approach to field determine the level of composite action is to measure the longitudinal strain response at multiple positions along the height of a beam cross section. These measurements are then utilized to identify the neutral axis (i.e., location of zero strain), assuming a linear strain profile. Beams 2 and 3 were instrumented with supplemental strain gauges at the mid-height. Figure 3.52 illustrates an example data set and the resulting neutral axis location near the top of the beam. This is consistent with manual calculation of the neutral axis position for a fully composite system.

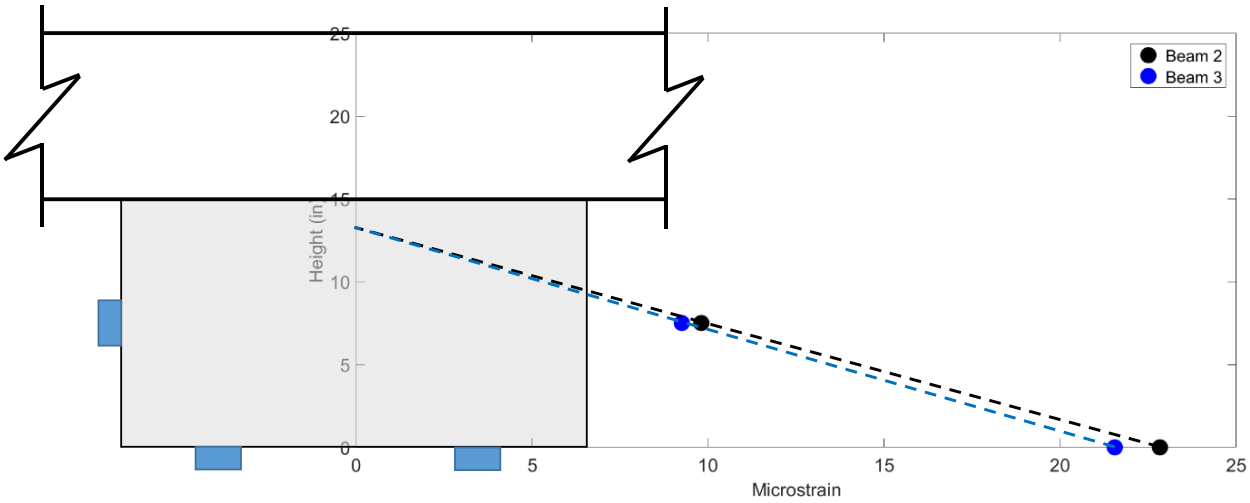

Figure 3.52. Approximate Field Identified Neutral Axis Location (Beam Lateral Dimension Is Not to Scale).

3.6.4.3. Dynamic Amplification

The static live load demands on bridges are amplified by the dynamic effect of moving vehicles. The magnitude of this dynamic effect is a function of the bridge dynamic properties, the properties of the truck itself, the vehicle speed, and the roadway surface. In design and evaluation, this effect is typically captured with a factor (typically 33 percent) that is termed dynamic load allowance or impact factor (*IM*). The general definition of *IM* is the percentage increase of the maximum dynamic response. Eq. (3.20) expresses this definition:

$$IM = \frac{R_{dyn} - R_{sta}}{R_{sta}} \tag{3.20}$$

where R_{dyn} and R_{sta} represent the maximum dynamic and static responses at a given location on the bridge, respectively.

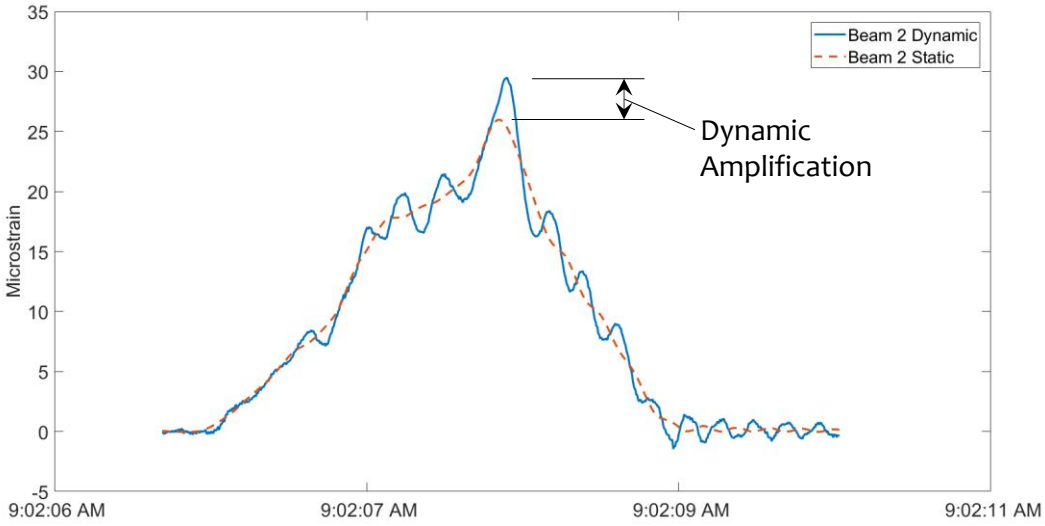

Figure 3.53. Illustration of Dynamic Amplification.

For the RELLIS Bridge, the dynamic impact factor was calculated for a subset of the data. Again, this was conducted as preliminary research for future tasks. The data evaluated were the midspan Beam 2 strain measurements from single vehicle passes in Lane 2 (all three trucks) traveling from 10 to 50 mph. The results are summarized in Table 3.6. The magnitudes were relatively consistent with the prior TxDOT study. The observed maximum dynamic amplification at the midspan was 56 percent. This value was obtained for Beam 2 when Truck C was driven along Lane 2 from the south at a speed of 29 mph. The average impact factor was 26 percent with a standard deviation of 15.5 percent.

Table 3.6. Impact Factor of Beam 2 in Different Tests.

Test Number	Truck	Heading Direction	Speed (mph)	IM
5	A	North	18	9%
6	B	North	17	37%
11	A	North	30	14%
12	B	North	27	45%
19	A	North	39	15%
20	B	North	37	24%
23	A	North	10	9%
26	A	North	18	12%
27	B	North	18	36%
32	A	North	39	16%
33	B	North	39	19%
51	A	North	43	6%
52	B	North	47	23%
55	A	North	10	6%
56	B	North	10	25%
59	A	South	10	7%
60	B	South	10	29%
63	A	South	30	14%
64	B	South	28	35%
69	C	North	17	41%
72	C	North	29	54%
75	C	North	37	39%
78	C	North	30	48%
81	C	North	29	56%
84	C	North	38	43%
87	C	North	10	16%

3.7. Preliminary B-WIM Performance Study

To compare the performance of each preliminary B-WIM algorithm and sensor combination to standard WIM systems, the errors were converted to accuracies. Eq. (3.21) shows the calculation of accuracy:

$$Accuracy = \frac{\sum_1^m \left(1 - |Error|\right)}{m} \times 100\% \tag{3.21}$$

where m is the number of data points. The accuracy herein represents the average accuracy of the calculated truck axle information or weight results.

It should be noted that most of the calculated results are based on manual peak selection, which gives higher accuracy with respect to the axle numbers and peak time. The accuracy of the results will reduce when using an automatic data processing program. An algorithm for automatic peak detection is developed in Section 6. For the preliminary research, the larger focus was on the prediction of average speed, axle spacing, gross weight, and axle weight.

Table 3.7 and Table 3.8 summarize the accuracy of axle and weight information from the preliminary algorithms and sensors, respectively. The reference datum used for these accuracy computations were the truck speedometer readings, manual speed gun measurements, and manual static scale weight measurements.

Table 3.7. Accuracy of Axle Information.

Parameters	Strain Gauge (Time History)	Load Cell (Second Derivative)
Axle Number	100%*	100%*
Average Speed	97%	97%
Axle Spacing	96%	97%

** The axle peaks were identified by manual review of the data for this preliminary study.*

Table 3.8. Accuracy of Weight Information.

Parameters	Strain Gauge (Area Method)	Load Cell (Area Method)	Load Cell (Reaction Force Method)
GVW	92%	89%	91%
Axle Weight	69%	N/A	87%

3.8. Preliminary B-WIM Setup Guidelines

The preliminary guidelines were grouped into three categories. The first is instrumentation, which includes information on the sensor types and sensor arrangements/locations. The second category is data processing algorithms, which relates to the instrumentation setup selected. The last category focuses on bridge selection criteria for successful B-WIM systems. General information on each category is provided below.

3.8.1. Instrumentation

For ***axle detection***, two different sensor setups are recommended. One setup is strain gauges mounted to the bottom surface of the deck at each end of the bridge (every bay). The other setup is some form of reaction measurement at each bearing (both ends). This can be a direct measurement such as load cells. However, this is typically not realistic. Therefore, indirect measurements such as strain gauges attached to neoprene bearings, or high resolution displacement gauges, to correlate the reactions with bearing deformation. Another option is strain gauge rosettes along the beam web at the bearings to measure the shear strain. Indirect reaction measurements are explored in B-WIM deployment on in-service bridges (Section 5) and live load data analysis (Section 6). For whichever axle

detection setup, the peaks (or spikes) in the data allow for the identification of axles crossing the sensor, which can be used for the axle number, axle spacing, and vehicle classification (namely trucks Class 4–13).

Two different ***weight detection*** sensor setups are recommended. The first is to utilize a reaction measurement (same options as stated above) to identify the axle forces, which can be summed to get the GVW. The other setup is to instrument all the girders with strain gauges at the bridge midspan. This approach provides accurate GVW prediction but provides relatively low accuracy for individual axle weights. At each girder, it is recommended to instrument the bottom of the beam for the highest response. The controlling limit state should dictate the sensor arrangement utilized for ***bridge evaluation***. For example, if flexural strength at midspan controls, then each girder should be instrumented with strain gauges at midspan. Conversely, if shear at the ends control, then strain gauges rosettes should be attached to the girder webs of each beam. All beams should be instrumented to allow for calculation of distribution factors and other parameters. This information can be utilized to calculate site-specific load ratings. Supplemental sensors can be installed to evaluate other bridge parameters. A common example is the level of composite action. If composite action is uncertain, then at least one additional gauge should be installed on the web of the girder at multiple girder locations. This location on the web should be far enough away from the neutral axis to produce a measurable response. If fatigue is a concern, specific members or connections can be instrumented with strain gauges to measure the stress magnitude and number of cycles for a refined fatigue life estimate.

3.8.2. Data Processing

The data processing algorithms utilized to characterize the vehicles as described in Section 3.6 is dictated by the instrumentation setup. In most cases the sampling rate should be relatively high (200Hz to 500Hz). The sampling rate must be balanced with the data storage and power capabilities of the B-WIM system. A low-pass filter is also recommended in most cases to remove some of the high frequency content.

For ***axle detection***, an algorithm utilizing the second derivative method is recommended. This allows for relatively clearly defined peaks that facilitate better detection of the axle position and time. This can be used for either axle detection sensor setup discussed above. If the measured response has clearly defined peaks, then this signal can be utilized to reduce processing time.

Two algorithms are recommended for ***weight detection***. The first is the reaction force algorithm utilizing reaction measurements. This approach allows for axle and GVW identification. The second recommended algorithm is the total area method, which can be used with reaction measurements or midspan strain measurements. However, the area method is preferred for GVW identification. Specific axle weights have shown less than sufficient accuracy.

3.8.3. Preliminary Bridge Selection Criteria

The preliminary bridge selection criteria were developed to improve the accuracy of the B-WIM results, which were based on the literature review and preliminary testing. These criteria were developed to guide the selection of in-service bridges in the next task,

presented in Section 4. The final bridge selection guidelines were established in Section 8. The preliminary selection criteria include:

- ***Type: Spread Multi-Girder***. The reason is to provide sufficient data across the width of the bridge to identify the lane of the vehicle. In addition, accessibility to the bottom of the deck is important for some instrumentation setups.
- ***Span: Simple***. This criterion essentially eliminates the influence of the adjacent spans, which simplifies the B-WIM algorithms. Expansion joints at each end of the span are preferred. However, simple span beams with a continuous deck slab (or link slab) is acceptable.
- ***Length: 30–80 ft***. Short span lengths reduce the likelihood of vehicles back-to-back on the bridge at the same time. This also minimizes varying vehicle speeds on the bridge. However, if the bridge is too short, the time gap between axle detection at each end (for speed measurement) becomes more challenging.
- ***Traffic Direction: Single***. The data processing is simplified, and the accuracy is increased for bridges that carry a single direction of traffic.
- ***Approach Pavement: Smooth***. This is particularly important for spans at an abutment. The pavement-to-bridge transition should be relatively smooth to minimize the dynamic amplification. Higher data amplification requires additional filtering to extract the static content, which can reduce the accuracy of the results.
- ***Underside Access: Favorable***. It is preferred to have underside access that allows for installation within one day that does not disrupt traffic. Therefore, dry

ground with a vertical clearance less than 20 ft is desirable. Utilizing a snooper truck is not preferred since it requires lane closures.

3.9. Preliminary Testing Summary

This section provided an overview of the efforts to develop a preliminary B-WIM system and data processing algorithms. The RELLIS Bridge was used as a testbed. Four different types of sensors (i.e., strain gauges, load cells, displacement gauges, and accelerometers) were installed underneath the bridge according to the instrumentation plan designed by the research team. One tractor-trailer truck and two single-unit trucks were used to conduct full-scale testing. Each truck passed the bridge with various speeds on three different paths. The testing included single-truck crossing scenarios and multiple-vehicle crossing scenarios. Data were processed mainly for the single-truck scenarios. The research study focused on strain gauge and load cell data when evaluating the B-WIM system performance. Truck information results obtained from different algorithms were compared with the known measured values (i.e., radar gun, measuring tape, and static scales) for their overall accuracy. In addition, preliminary B-WIM setup guidelines were provided.

The axle detection strain gauges installed underneath the bridge deck at both ends provided clear data peaks when each vehicle axle passed on the bridge. The axle numbers were counted directly from the strain data. This was used for automated identification of the axle speed, average speed, and axle spacing. The results yielded relatively high accuracy, which are quantified below.

The weight detection strain gauges underneath the beams at midspan provided sufficient information to calculate the GVW using a modified area method algorithm. The researchers took the spatial behavior of the bridge and truck velocities into consideration and developed the total area method. The calculated GVW results had an average accuracy of 92 percent when compared to static scale weight measurements. However, the axle weight was not able to be calculated from the weighing sensors since peaks were not distinct from the data. Axle detection sensor data were used to calculate the axle weights, which produced an accuracy of 69 percent.

The load cells installed at each bearing were used as axle and weight detection sensors. Axle information was obtained by taking the second derivative of the data, which showed high accuracy. The GVW was calculated using the area method similar to the strain gauges. Another algorithm, named the reaction force method, was also successfully implemented. This method calculated the axle weights first based on the reaction force influence line, then calculated the GVW by summing the individual axle weights. When compared to static scale weight measurements, the area and reaction force methods provided accuracies of 89 percent and 91 percent, respectively, for the GVW. As for the axle weight results, the reaction force method provided an accuracy of 87 percent. The total weight of the two trucks in a side-by-side event can be determined using the Area Method. The approach to calculate individual truck weight was to utilize the beam distribution factors identified in the calibration tests, which produced reasonable GVW results (average accuracies ranging from 76% to 87%).

4. SELECTION OF IN-SERVICE BRIDGES FOR B-WIM TESTING

4.1. Overview

Three in-service TxDOT bridges were selected for B-WIM testing and field validation. The three bridges selected met the preliminary criteria established in Section 3. In addition, it was desired to locate at least one bridge near an active permanent WIM station (preferably two). This would allow for a comparison of the results. Further information on the approach taken for bridge selection is provided below followed by a description of each bridge.

4.2. Approach

The approach for bridge selection was to first locate the active permanent WIM stations across the state of Texas. Figure 4.1 shows the active WIM stations as of July 13, 2020. (Inactive and pending stations are not included in the figure.)

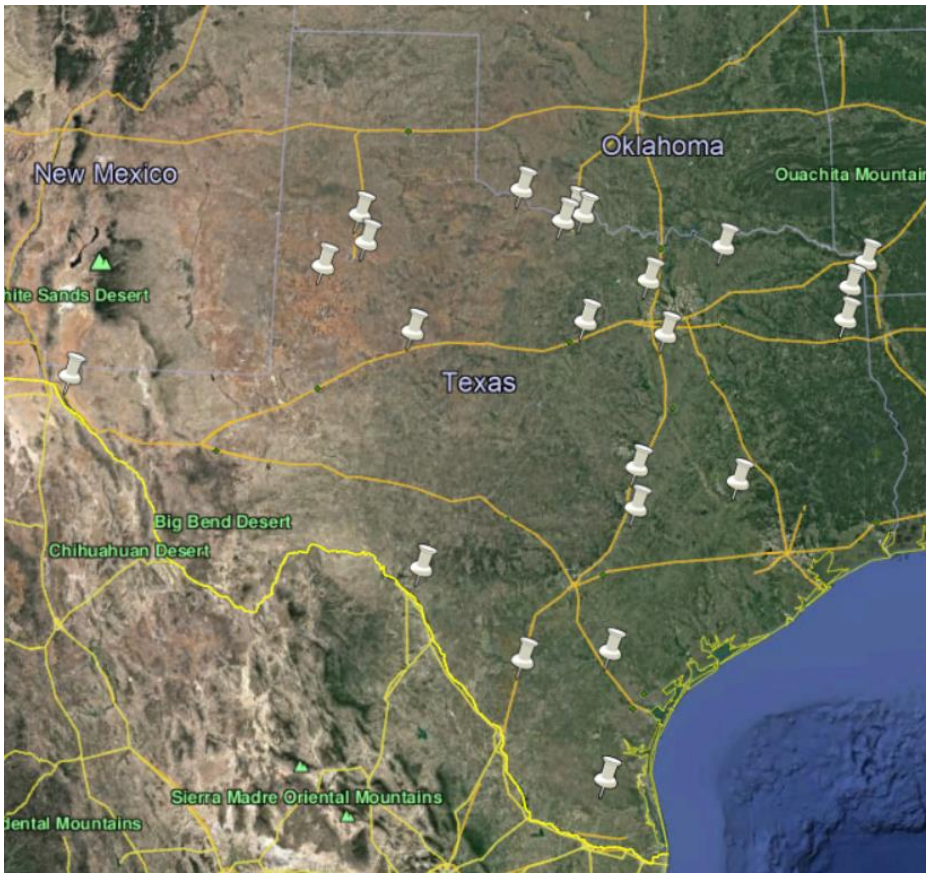

Figure 4.1. Texas Active Permanent Pavement WIM Stations (July 13, 2020).

One of the active stations is located in the Bryan District on State Highway (SH) 6, which is in close proximity to the research team. Due to the COVID-19 travel concerns, it was preferred to reduce travel to the greatest extent possible. Therefore, bridges along this corridor were reviewed first using Assetwise (TxDOT's asset management system). The reviews utilized the preliminary bridge selection criteria developed in Section 3. These criteria were established to improve the accuracy of the B-WIM results. The criteria were revised as necessary throughout the research study and are presented in the technical guidelines in Section 8.

For each bridge reviewed, the preliminary bridge selection criteria were consulted. Two prestressed concrete bridges were selected on this corridor since they met the selection criteria and were relatively different. It was desired to test a steel bridge as well to diversify the research study. The approach for selecting the steel bridge was to filter the NBI data to reduce the potential candidates. Thereafter, Assetwise was used to review these bridges and make a selection. The NBI data filtering criteria only selected steel bridges that were/had:

- On-system.
- Steel structure type.
- Simple span.
- Average daily traffic (ADT) greater than 10,000.
- No skew.
- Not over a railroad.
- Max span less than 100 feet.
- One or two lanes of traffic.

4.3. In-Service Bridges Selected

4.3.1. Bridge #1—SH 6 NB over Navasota River (1st Span)

Bridge #1 (ID 170210005002053) was a prestressed concrete I-beam bridge that was built in 1971. It is located on the southern side of the Bryan District on SH 6 at GPS coordinates 30°25’08.1”N 96°06’22.8”W. The structure is in relatively close proximity to the permanent pavement WIM station #LW554, though it had many other positive attributes for a B-WIM system. Figure 4.2 shows the bridge location along with the

permanent WIM station LW554, named as Bryan WIM in this report. Figure 4.3 and Figure 4.4 provide an elevation and underside view of the structure, respectively.

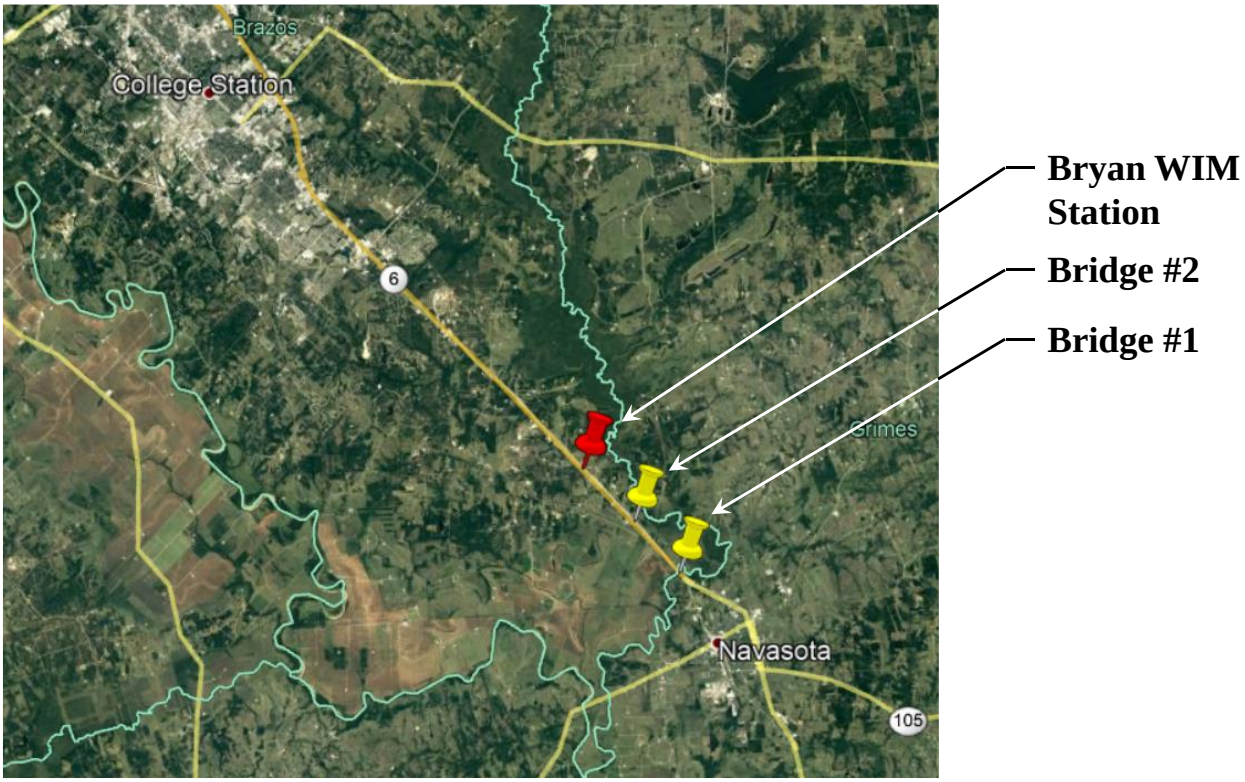

Figure 4.2. Bridges #1 and #2 Locations and the Bryan WIM Station (Station# LW554).

Figure 4.3. Bridge #1 Elevation View.

Figure 4.4. Bridge #1 Underside View.

4.3.1.1. Advantages of Bridge #1

This structure was selected as the first in-service bridge since it met all the selection criteria (see Table 4.1) and is near the Bryan WIM station LW554. The location was also a positive since it is within the research team's geographical area and easy reach (travel time is roughly 30 minutes). Another advantage is the significant truck traffic along SH 6 in the Bryan District. Correspondence with the Bryan District had indicated that this corridor received a relatively high percentage of truck permit requests. Therefore, more than sufficient heavy truck data were deemed feasible. In addition, the bridge was nearly

50 years old and was designed for HS20 loading. Therefore, an assessment of the bridge itself was considered beneficial.

Table 4.1: Bridge #1 Selection Criteria Results.

Bridge Selection Criteria	Results
Type: Spread multi-girder	Yes
Span: Simple	Yes (expansion joints at both ends)
Length: 30–80 ft	Yes (70'-0")
Traffic Direction: One-way	Yes (two lanes)
Approach Pavement: Smooth	Likely (1st span selected)
Underside Access: Favorable	Yes (entire span over grass)

4.3.1.2. Challenges of Bridge #1

While this bridge had many advantages, there were a few challenges (or disadvantages). The first was the age of the structure (built in 1971). With nearly 50 years of service, the behavior may not be as linear as a new structure. Secondly, the expansion joints at each end of the span may increase the dynamic amplification of the response data. Finally, a challenge for comparison of the B-WIM with the WIM data would be the presence of one on-ramp and one off-ramp between the sites. Despite these challenges, it was believed the advantages were much greater, making it a good candidate for B-WIM research.

4.3.2. Bridge #2—SH 6 NB over 2154 (South End Span)

Bridge #2 (ID 170210005002165) was a prestressed concrete I-beam bridge that was built in 2010. It is located on the southern side of the Bryan District on SH 6 at GPS

coordinates 30°26’27.5”N 96°07’38.9”W. The structure was even closer to the Bryan permanent WIM station LW554 than Bridge #1 (Figure 4.2). Despite being close to Bridge #1, there were differences in the structures that helped compliment the research findings. This included the age of the structure (nearly 40 years younger) and the concrete deck details (i.e., precast panels along with the continuous deck slab detail). Figure 4.5 and Figure 4.6 provide an elevation and underside view of the structure, respectively.

Figure 4.5. Bridge #2 Elevation View.

Figure 4.6. Bridge #2 Underside View.

4.3.2.1. Advantages of Bridge #2

This structure was selected as the second in-service bridge since it met all the selection criteria (see Table 4.2). It is within close proximity to the Bryan WIM station LW554 (i.e., about 20 to 30 minutes travel time) and is relatively different from Bridge #1. Again, the location was also a positive since it was within the research team's reach and along SH 6, which has significant truck traffic. In addition, the bridge was roughly 10 years old, so the condition of the bridge was considered good, and the information gathered was fairly applicable to modern TxDOT bridges.

Table 4.2: Bridge #2 Selection Criteria Results.

Bridge Selection Criteria	Results
Type: Spread Multi-Girder	Yes
Span: Simple	Yes (deck is continuous)
Length: 30–80 ft	Yes (75'-0")
Traffic Direction: One-way	Yes (two lanes)
Approach Pavement: Smooth	Likely (1st span selected)
Underside Access: Favorable	Yes (over the concrete slope protection away from traffic)

4.3.2.2. Challenges of Bridge #2

While this bridge had many advantages, there are a few challenges associated with it. The first challenge was the continuous deck slab on the bridge. This would provide some rotational restraint at the south side of the span. A similar challenge to Bridge #1 (but relatively less) would be the comparison of the B-WIM with the WIM data. One on-ramp was present between the sites. Another logistical challenge was the angle of the concrete slope protection under the bridge. Access to the abutment end would be relatively easy. However, reaching mid-span would require some planning. Despite these challenges, it was believed the advantages presented warranted it to be selected as a candidate for the B-WIM research.

4.3.3. Bridge #3—IH 35 SB over Spring Creek Relief (North End Span)

Bridge #3 (ID 30490019501029) was a steel rolled I-beam bridge that was built in 1948 and rehabilitated in 1985. It is located north of Fort Worth on IH 35 at GPS coordinates

33°28’07.99”N 97°09’49.04”W. Figure 4.7 shows the bridge location. Figure 4.8 and Figure 4.9 provide an elevation and underside view of the structure, respectively.

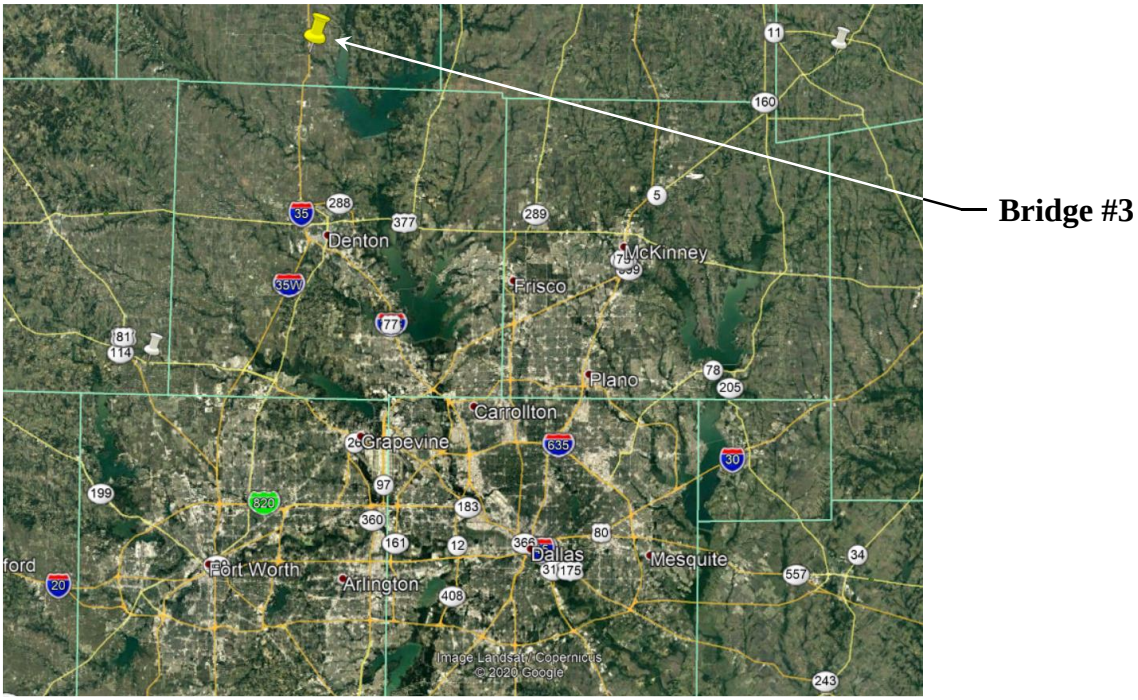

Figure 4.7. Bridge #3 Location.

Figure 4.8. Bridge #3 Elevation View.

Figure 4.9. Bridge #3 Underside View.

4.3.3.1. Advantages of Bridge #3

This structure was selected as the third in-service bridge since it met all the selection criteria in Table 4.3 and is a steel structure. Another advantage of the bridge is the relatively significant traffic it carries (i.e., ADT equal to 25,812), which included substantial heavy truck-traffic data. In addition, the bridge was relatively old (even considering the rehabilitation) and had a 25-ton inventory load rating. An assessment of the bridge itself was also considered beneficial.

Table 4.3: Bridge #3 Selection Criteria Results.

Bridge Selection Criteria	Results
Type: Spread Multi-Girder	Yes
Span: Simple	Yes (expansion joints at both ends)
Length: 30–80 ft	Yes (50'-0")
Traffic Direction: One-way	Yes (two lanes)
Approach Pavement: Smooth	Likely (1st span selected)
Underside Access: Favorable	Yes (over the concrete slope protection away from traffic)

4.3.3.2. Challenges of Bridge #3

While this bridge had many advantages, some challenges existed. The first was the age of the structure (built in 1948/1985). With many years of service, the behavior may not be as linear as a new structure due to accumulated effects (e.g., corrosion, over-height truck impacts, etc.). Secondly, the expansion joints at each end of the span could increase the dynamic amplification of the response data. Finally, the travel distance (i. e.,

3.5 hours) to the bridge was a disadvantage. However, despite these challenges it was believed the advantages merited it to be a good candidate for B-WIM research.

4.4. Bridge Selection Process Summary

Overall, three bridges were selected for B-WIM research and field testing. All three bridges met the preliminary selection criteria developed in the previous task (Section 3). In addition, these three structures represent a large portion of the TxDOT bridge inventory. A general comparison of the three structures is shown in Table 4.4.

Table 4.4: Overall Bridge Comparison.

	Bridge #1	**Bridge #2**	**Bridge #3**
Highway	SH 6	SH 6	IH 35
District	Bryan	Bryan	Fort Worth
GPS location	30°25’08.1”N 96°06’22.8”W	30°26’27.5”N 96°07’38.9”W	33°28’07.99”N 97°09’49.04”W
Type	Prestressed I-Beam	Prestressed I-Beam	Steel I-Beam
Year Built	1971	2010	1948/1985
Span Length	70'-0"	75'-0"	50'-0"
Deck Type	7.5" Cast-in-Place	8" Precast Panels/Cast-in-Place	9.75" Cast-in-Place
Deck Continuity	None	One End	None
Number of Beams	6	5	6
Traffic Lanes	2	2	2
ADT	16,659	18,803	25,812
Proximity to Permanent WIM Station	4 miles (LW 554)	2 miles (LW 554)	N/A

5. B-WIM DEPLOYMENT ON IN-SERVICE BRIDGES

5.1. Overview

This section presents the deployment of the B-WIM systems on the three in-service bridges, including system design, installation, calibration testing, and data recording. On Bridge #1, two different types of sensors, strain gauges, and linear variable displacement transducers (LVDTs) were installed along the structure. This was to allow for the research of different B-WIM methods. A tractor-trailer was used as the calibration truck. This truck had an axle that could be lifted or released to create two different axle configurations and axle weight arrangements. The design, installation, and calibration tests of the B-WIM system for Bridge #2 and Bridge #3 are also summarized in this section.

Bridge #2 used strain gauges and LVDTs. A 5-axle end dump truck was utilized for the calibration. In addition to strain gauges, Bridge #3 had two accelerometers installed. Two different vehicles, a 3-axle truck and a 6-axle truck, were utilized in the calibration tests of Bridge #3. Portable WIM systems were installed near Bridge #1 and Bridge #2 due to maintenance being performed on the permanent WIM station LW554 at the time. Figure 5.1 shows the locations of the Bryan permanent WIM station LW554, portable WIM setup, and first two bridges.

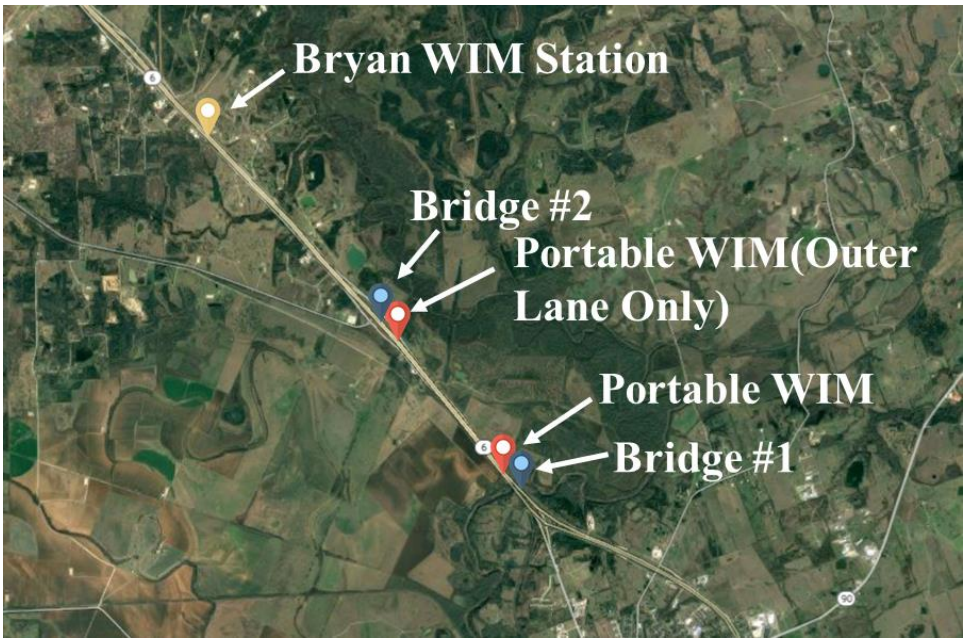

Figure 5.1. Location of Bridge #1 and #2 and Pavement WIM Stations (Google Maps 2021).

5.2. Bridge #1 B-WIM System

5.2.1. Instrumentation Plan

The instrumentation plan for Bridge #1 was designed based on the constraints for a B-WIM system and site-specific conditions. The main B-WIM system was designed to be strain-based and installed underneath the bridge. However, the bridge was further instrumented with several LVDTs to explore the possibility and accuracy of other instrumentation methodologies and algorithms.

The instrumentation setup included 17 strain gauges and 6 LVDTs. The strain gauges were divided into three groups based on their purpose. The first strain gauge grouping was installed underneath the bridge deck close to the north and south ends. These sensors are referred to as “axle detection” gauges. They provide localized effects

valuable for vehicle axle information and speed. The other grouping is referred to as "weight" gauges installed on the bottom surface of the girders near midspan to capture global behavior. These sensors provide valuable information for the overall vehicle weight along with bridge information such as lateral distribution, dynamic amplification, etc. The third grouping includes three strain gauges which construct a strain rosette at the south end of Beam #4. The strain rosette captures the shear response from the beam. It was added as an exploration of load cell alternatives to study both "axle detection" and "weight" identification. The LVDTs installed at the south end bearings were also used as an exploration of load cell alternatives.

The "weight" gauges were not installed precisely at midspan due to the field logistics of setting a ladder on the slope protection. The location of the midspan "weight" gauges was moved 5.8 ft towards the north. The quarter span "axle detection" gauges on both sides were moved towards the diaphragms due to field logistics while working on the ladder.

Figure 5.2 and Figure 5.3 show the plan and cross-sectional views of the implemented instrumentation on Bridge #1, respectively.

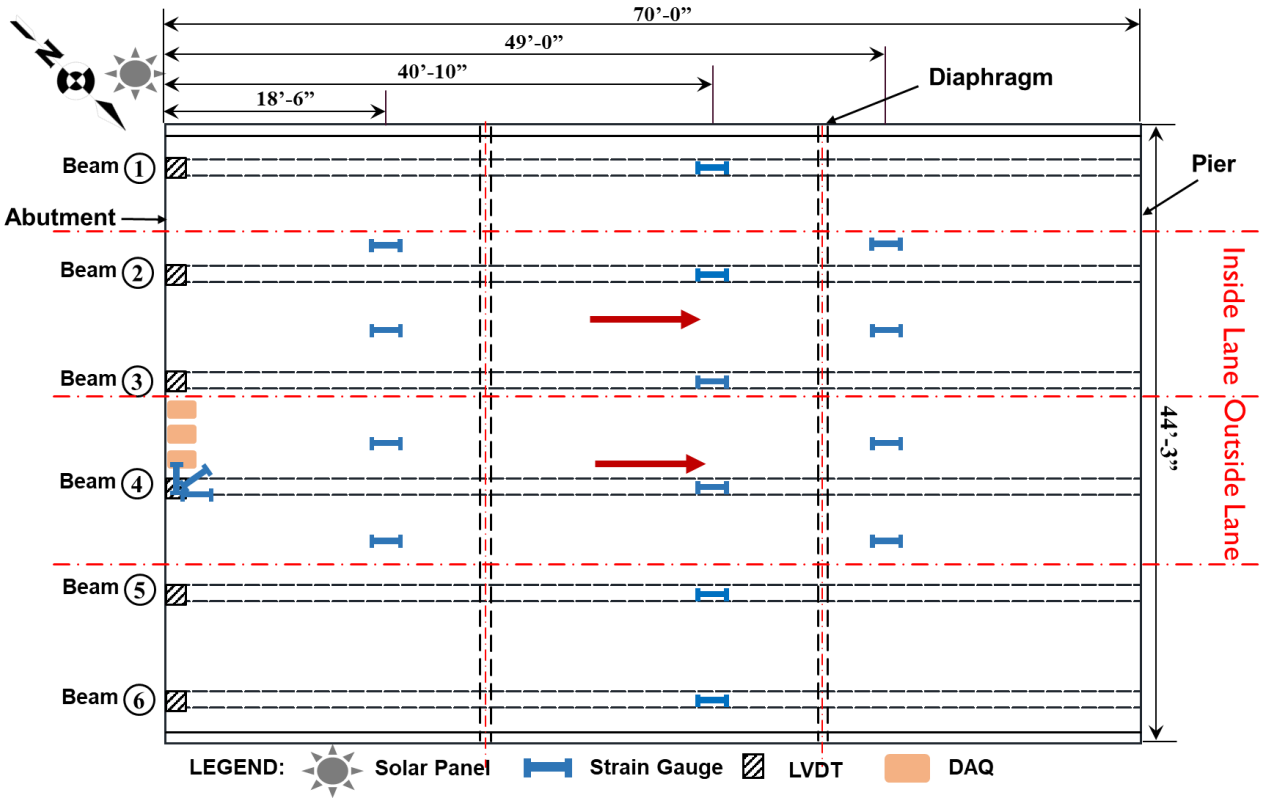

Figure 5.2. Sensor Layout for Bridge #1 (Plan View).

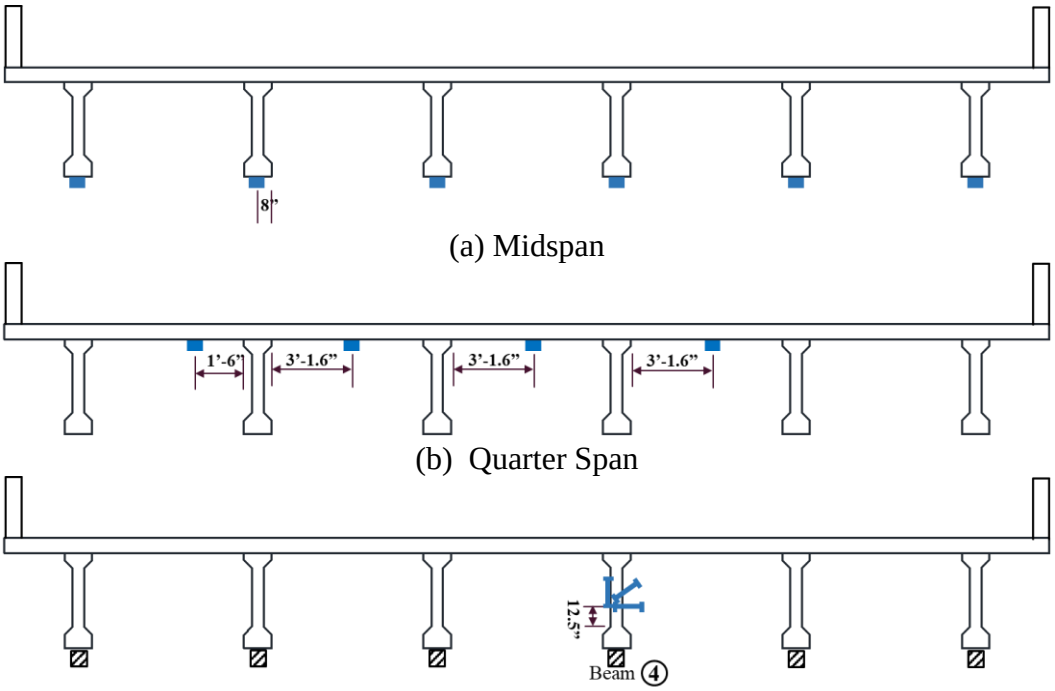

(a) Midspan

(b) Quarter Span

(c) South End

Figure 5.3. Sensor Layouts for Bridge #1 (Cross Sections).

5.2.2. Sensors and Data Acquisition Systems

5.2.2.1. Strain Gauges

The strain gauges used in the instrumentation were the ST350 produced by BDI. The ST350 reusable strain gauges have multiple uses and are highly durable due to their rugged, waterproof construction. The ST350 internal circuitry consists of a full Wheatstone bridge with four fully active 350Ω foil gauges optimized to provide high electrical output for a given strain magnitude. The BDI strain gauges have a resolution of one microstrain. Compared to foil-type gauges, the installation is faster and easier.

The strain gauges were sampled at two different rates. The first consisted of a 500 Hz sampling frequency for the axle detection gauges and the strain rosette. The

weight gauges were sampled with a 100 Hz frequency. These sampling frequencies were set based on information from the literature and the capabilities of the data acquisition system. The weight gauges were also utilized to trigger data recording of the truck events (Class 4 or higher). When any of the weight gauges reached a specified threshold value, the system was triggered and recorded the data one second before and after the triggered time. Figure 5.4a shows the strain gauges used in this task.

5.2.2.2. LVDTs

To obtain deformation at the bearing pads, six LVDTs were utilized. The DCTH100AG DC to DC LVDT displacement transducer has a measurement range of −0.1 inch to 0.1 inch. The strength of the LVDT sensors is that there is no electrical contact across the transducer position sensing element, which for the user of the sensor means clean data, infinite resolution, and relatively long life. These LVDTs have a linearity of around 0.1 percent, which will capture the small displacement at the bearing pads. They were sampled at a 500 Hz frequency. Figure 5.4b shows the LVDT.

5.2.2.3. Data Acquisition Systems

The DAQ systems controlled the strain gauge and LVDT setup. This system was comprised of Campbell Scientific equipment. The GRANITE 9 all-digital measurement and control DAQ was designed as the core of the data-acquisition network. Several GRANITE measurement modules were integrated with the GRANITE 9, including six VOLT 116s and one VOLT 108. Figure 5.4c shows the GRANITE 9 and extension

modules. The system status was checked remotely with a cellular module and a multiband omnidirectional antenna, as shown in Figure 5.5a and Figure 5.5b.

(a) BDI ST350 Strain Transducer

(b) RDP LVDT

GRANITE 9

VOLT 116

VOLT 108

(c) GRANITE 9 and Extension Modules

Figure 5.4. Data Acquisition System and Instrumentation (Bridge #1).

(a) Cell Modem

(b) Multiband Omnidirectional Antenna

Figure 5.5. Cell Modem and Antenna.

5.2.3. Instrumentation Installation

The strain gauges and LVDTs were installed underneath the bridge by the research team. The overall instrumentation plan, shown in Figure 5.2 and Figure 5.3, was followed.

High-strength epoxy was utilized for attaching the strain gauges to the bridge beams and deck. Loctite 410 adhesive (with accelerator) was used for the initial attachment. Then Loctite 5-minute general-purpose epoxy was applied to ensure sufficient strength. Figure 5.6a shows a strain gauge installed underneath the bridge deck at quarter span. Figure 5.6c shows an installed strain gauge along the bottom of a beam at midspan.

The strain rosette was attached to the beam following the same installation steps as the other strain gauges. The vertical strain gauge was parallel to the edge of the beam web, and the horizontal strain gauge was perpendicular to the vertical gauge. The diagonal strain gauge had a 45-degree angle with both vertical and horizontal gauges. Figure 5.6b shows the strain rosette.

The LVDTs required mounting blocks attached to the abutment. For each mounting block, two holes were drilled in the concrete; the LVDTs were then tightened into the mounting blocks, and concrete anchors were utilized to fix the mounting blocks on the concrete surface. Figure 5.6d also shows an installed LVDT with a mounting block at the south end of a beam.

Table 5.1 summarizes the setup information of the sensors installed on the bridge for this task. The strain gauges and LVDTs were connected to the GRANITE DAQ at the south side underneath the bridge (Figure 5.6e). A CRBasic program was written to control the sensor sampling rates. As shown in Figure 5.6f, one 12V 100 Ah battery was used to support the power of the six LVDTs. The other battery was the power source for the DAQ system and was charged by a 150W solar panel. This solar panel was installed

at the south side of the bridge for optimum performance. Figure 5.7 shows the installation of the solar panel.

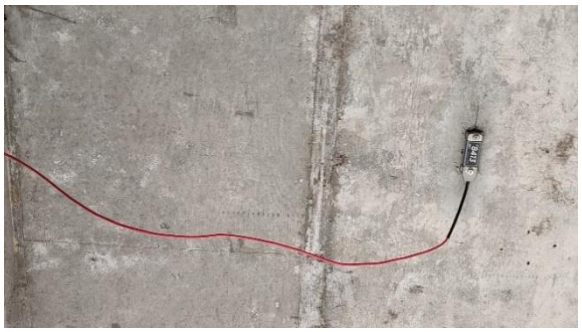

(a) Strain Gauge at Quarter Span

(b) Strain Rosette at South End

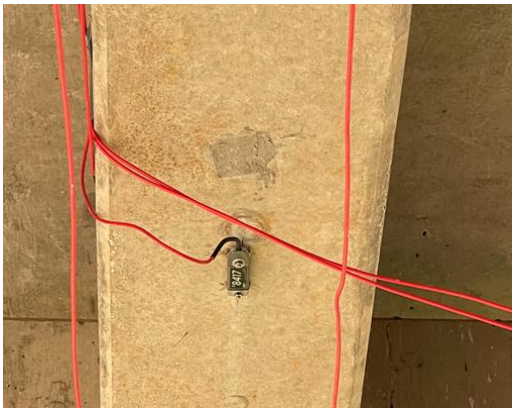

(c) Strain Gauges Installed at Midspan

(d) LVDT at South End

(e) GRANITE 9 and Modules

(f) Batteries

Figure 5.6. Instrumentation Installation (Bridge #1).

Table 5.1. Summary of Sensor Information (Bridge #1).

Sensor Type	Purpose	Sampling Rate	Quantity	Location
Strain Gauge	Weight Measurement/Bridge Assessment	100 Hz	6	Midspan
Strain Gauge	Axle Detection	500 Hz	8	North/South Quarter Span
Strain Gauge (As Strain Rosette)	Weight Measurement/Axle Detection	500 Hz	3	South End
LVDT	Weight Measurement/Axle Detection	500 Hz	6	South End

Figure 5.7. Installation of the Solar Panel.

5.2.4. Bridge #1 Calibration Test

5.2.4.1. Test Truck and Travel Paths

A TTI tractor-trailer was used as the vehicle for the calibration test. As previously mentioned, this truck had an axle that could be lifted or released to create two different axle configurations. For convenience, they were named Truck A and B. Truck A was a tractor-trailer with five axles, and Truck B had six axles. A roller was loaded to add extra weight to the trailer. This resulted in a total weight of roughly 80,000 lb. The specific axle weights and axle spacings are summarized in Table 5.2. The loaded tractor-trailer is shown in Figure 5.8. Figure 5.9 and Figure 5.10 show the axle weights and spacings of the two configurations, respectively.

Table 5.2. Axle Information of the Test Vehicles (Bridge #1).

Truck Name	Axle Weight (lb)						Axle Spacing				
	Axle 1	Axle 2	Axle 3	Axle 4	Axle 5	Axle 6	Axle 1 to 2	Axle 2 to 3	Axle 3 to 4	Axle 4 to 5	Axle 5 to 6
A	14,600	16,900	16,750	15,800	16,200	N/A	20'-11.5"	4'-0"	33'-11.5"	4'-2"	N/A
B	11,800	9250	13,700	13,400	15,800	15,750	16'-4.5"	4'-7"	4'-0"	33'-11.5"	4'-2"

Figure 5.8. TTI Tractor-Trailer Loaded with a Roller Compactor.

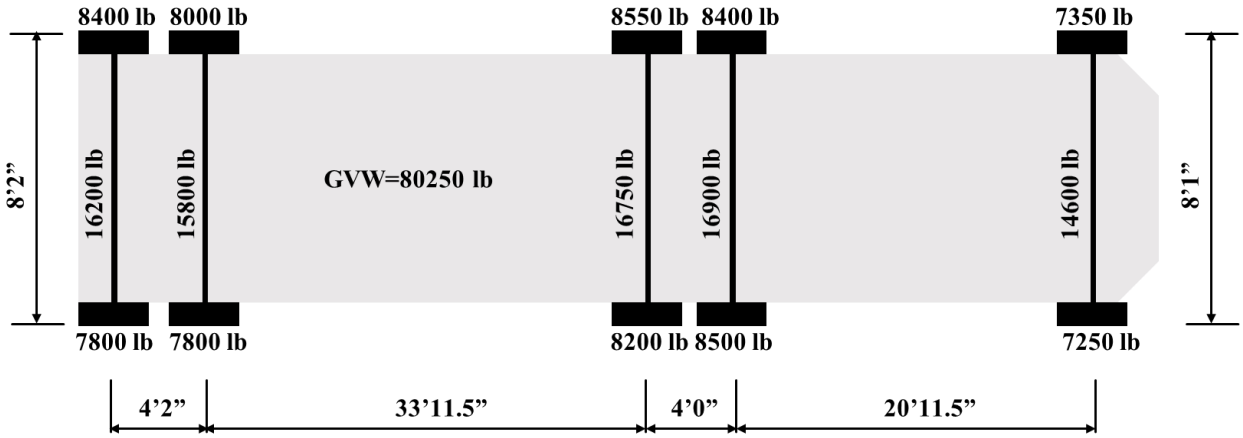

Figure 5.9. Truck A Information (Bridge #1).

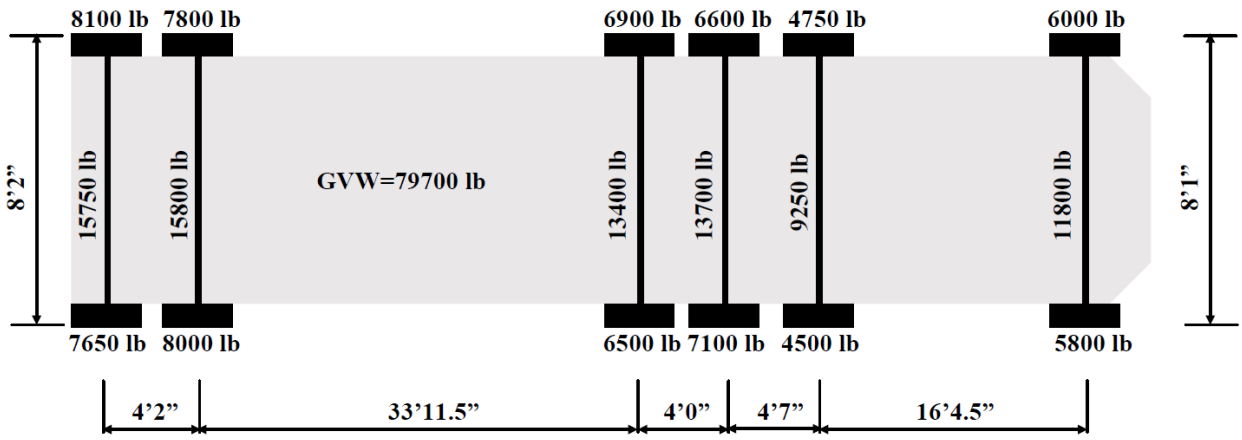

Figure 5.10. Truck B Information (Bridge #1).

The bridge has two lanes of traffic. It was planned for the truck to drive along the center of the two paths shown in Figure 5.11. Path 2 was the inside (or left) lane, and Path 1 was the outside (or right) lane.

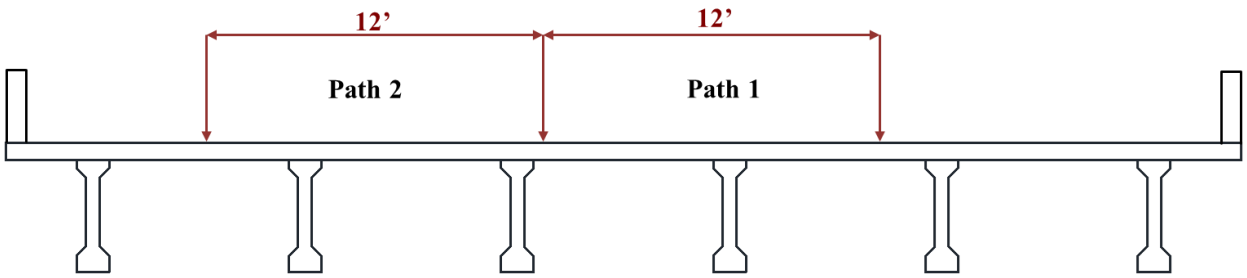

Figure 5.11. Schematic of the Vehicle Paths (Looking North).

5.2.4.2. Field Testing

The field calibration took place on March 11, 2021. One GoPro camera was set up to record the calibration testing. A laptop was used to control the DAQs during the field test. The data were continuously reviewed to ensure sufficient data quality. This included the general magnitude of response checks, review of data trends, etc. Figure

5.12 shows the monitoring of DAQs during the testing. A radar gun was operated by a research team member to measure the average speed of the calibration truck (Figure 5.13). These speeds were corroborated by the truck driver.

Figure 5.12. Monitoring the DAQs in Real-Time.

Figure 5.13. Speed Measurement with a Radar Gun.

A total of 20 test runs were conducted with different speeds of approximately 4, 15, 50, 60, and 70 mph. Traffic control was coordinated to shut the outside lane (Lane 1) for the three crawl speed (4 mph) tests and three low speed (15 mph) tests with Truck A. 50 mph, 60 mph, and 70 mph tests were conducted with normal traffic on the inside lane. The axle was then released, and Truck B passed the inside lane (Lane 1) at 50, 60, and 70 mph. The traffic control was then completed, and both lanes were opened. The rest of the tests were conducted with Truck A or Truck B with normal traffic.

Table 5.3 shows a summary of the calibration tests implemented. Figure 5.14 and Figure 5.15 illustrate examples of test scenarios.

Table 5.3. Summary of Calibration Testing (Bridge #1).

Test Number	Truck Type	Truck Path	Speed (mph)
1	A	1	4
2	A	1	4
3	A	1	4
4	A	1	15
5	A	1	15
6	A	1	15
7	A	2	50
8	A	2	50
9	A	2	60
10	A	2	70
11	B	2	70
12	B	2	60
13	B	2	50
14	A	1	50
15	A	1	70
16	A	1	60
17	B	1	70
18	B	1	70
19	B	1	50
20	B	1	60

Figure 5.14. Truck A Passing the Outside Lane (Bridge #1).

Figure 5.15. Truck B on the Inside Lane (Bridge #1).

5.3. Bridge #2 B-WIM System

5.3.1. Instrumentation Plan

The instrumentation plan for Bridge #2 was designed with the same type of sensors as Bridge #1, which included 17 strain gauges and 3 LVDTs. The strain gauges were divided into two groups based on their purpose. The first strain gauge grouping was installed as strain rosettes at the north and south ends of Beam #2 and Beam #4. They worked for both “axle detection” and “weight” purposes. The other grouping, referred to as “weight” gauges, were installed on the bottom surface of the girders at midspan to capture global behavior. The LVDTs installed at the south end bearings of Beam #2, Beam #3, and Beam #4 were also used as an exploration of load cell alternatives. Again, due to the field logistics of setting a ladder on the slope, the midspan strain gauges were not installed at the exact center. The location of the midspan gauges was moved 3 ft, 6 inches toward the south.

It was found that the strain rosettes on the north end of the bridge could not accurately provide corresponding peaks of the passing trucks (see calibration results analysis in Section 6 for details). Two more strain gauges were installed underneath the bridge deck between Beam #2 and Beam #3 for axle detection of inside lane traffic and between Beam #3 and Beam #4 for outside lane traffic. Figure 5.16 shows the instrumentation plan after the modification. Figure 5.17 shows the cross-section views of the instrumentation plan.

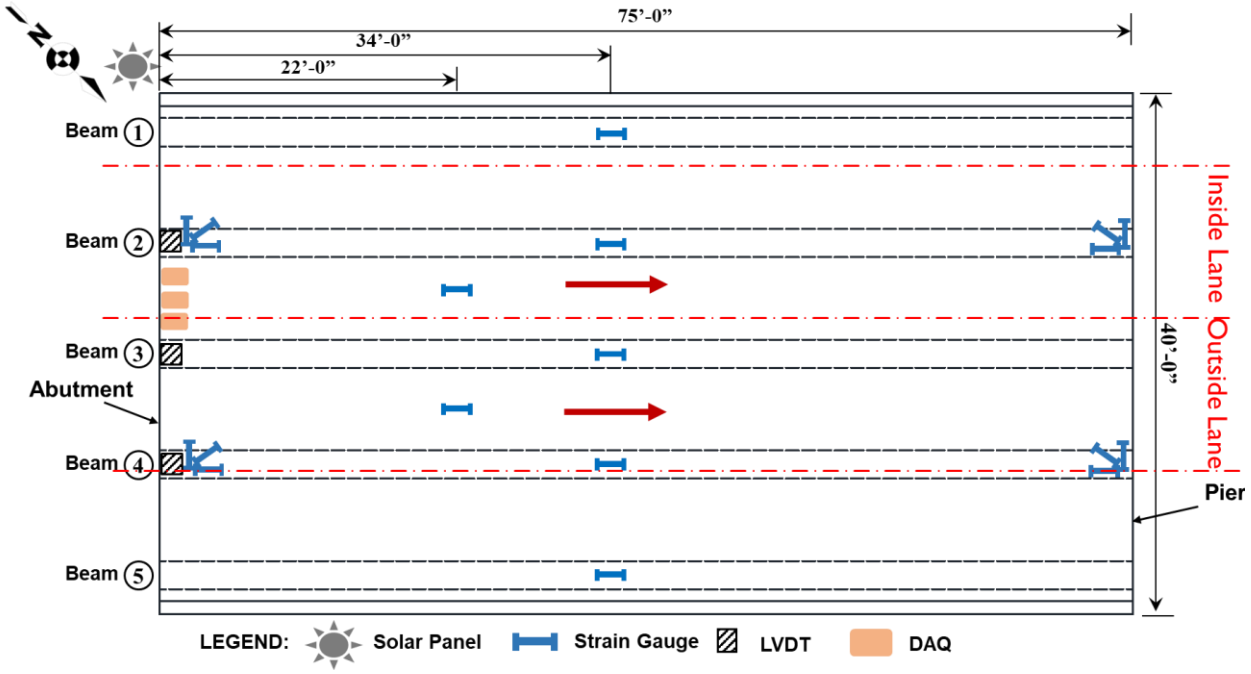

Figure 5.16. Modified Bridge #2 Instrumentation Plan.

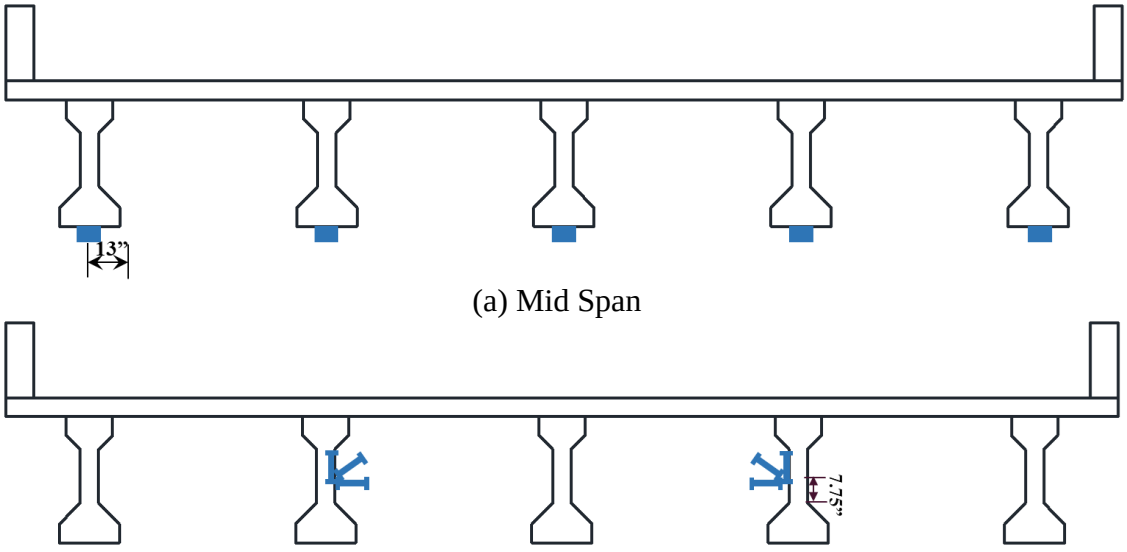

(a) Mid Span

(b) North/South End

Figure 5.17. Sensor Layout for Bridge #2 (Cross Sections Looking North).

5.3.2. Instrumentation Installation

The sensors, DAQs, and solar panel installed on Bridge #1 were taken down and reused on Bridge #2. The strain gauges and LVDTs were installed with the same methodologies mentioned above. Figure 5.18 to Figure 5.22 show the installation of Bridge #2.

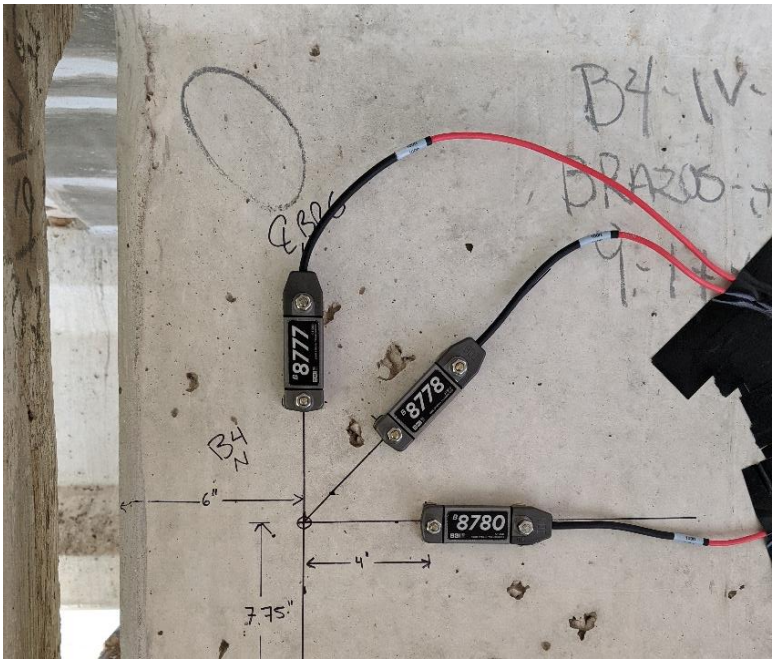

Figure 5.18. Strain Rosette at North End (Bridge #2).

Figure 5.19. LVDT at South End (Bridge #2).

Figure 5.20. Midspan Strain Gauges (Bridge #2).

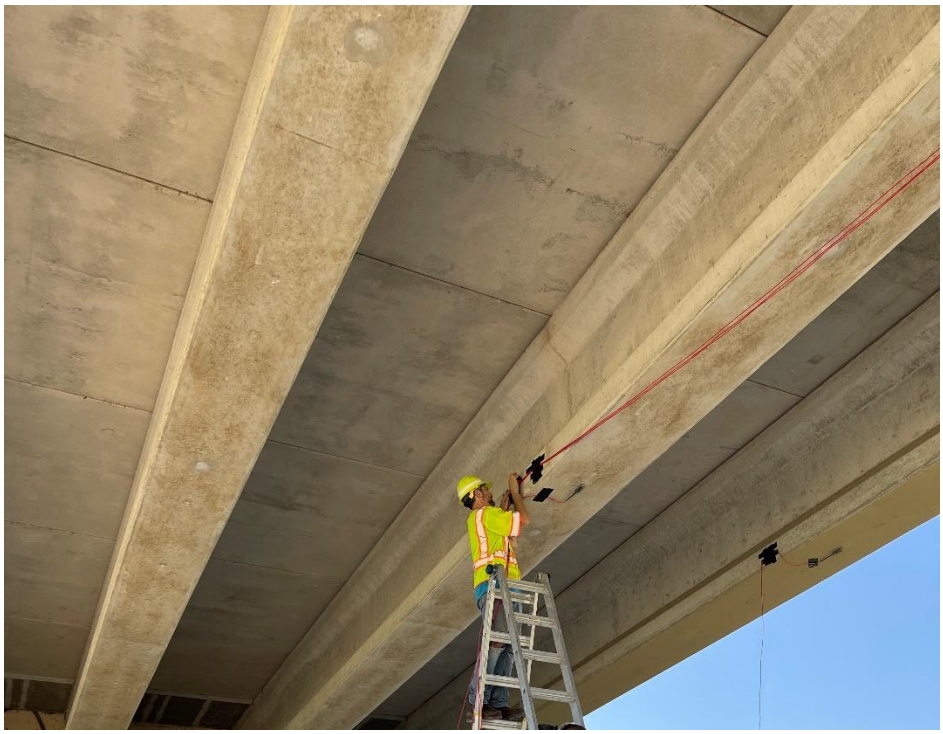

Figure 5.21. Installing Strain Gauges (Bridge #2).

Figure 5.22. Installed Solar Panel (Bridge #2).

5.3.3. Bridge #2 Calibration Test

5.3.3.1. Test Truck and Travel Paths

A five-axle end dump truck was used for the calibration test on Bridge #2. The truck was loaded with a total weight of roughly 64,850 lb. The specific axle weights and axle spacings are summarized in Table 5.4. The loaded truck is shown in Figure 5.23. Figure 5.24 shows the axle weights and spacings configurations.

This bridge also had two lanes of traffic. It was planned for the truck to drive along the center of the two lanes at different speeds.

Table 5.4. Axle Information of the Test Vehicle (Bridge #2).

Axle Weight (lb)					Axle Spacing			
Axle 1	**Axle 2**	**Axle 3**	**Axle 4**	**Axle 5**	**Axle 1 to 2**	**Axle 2 to 3**	**Axle 3 to 4**	**Axle 4 to 5**
9950	14,200	13,350	13,950	13,400	14'-2.5"	4'-5"	23'-10"	4'-3"

Figure 5.23. Calibration Truck for Bridge #2.

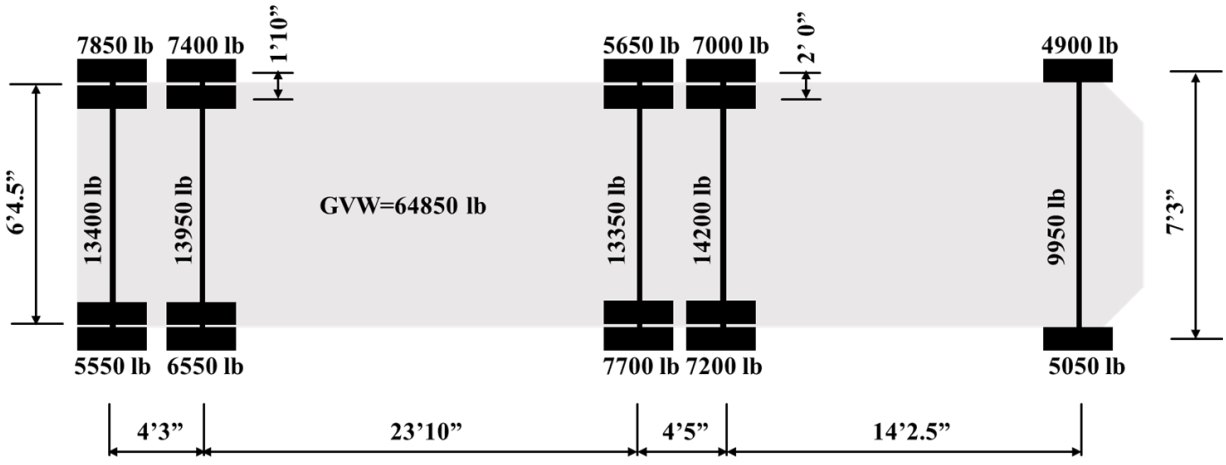

Figure 5.24. Bridge #2 Calibration Truck Information.

5.3.3.2. Field Testing

The field calibration took place on July 16, 2021. Two GoPro cameras were set up to record the vehicles passing the bridge and vehicles coming from the portable WIM station outside lane. A laptop was used to control the DAQs during the field test. The data were continuously reviewed to ensure sufficient data quality. A total of eight test runs were conducted with different speeds of approximately 50, 60, 70, and 80 mph. All the tests were conducted with normal traffic on both lanes, so no traffic control was required. Figure 5.25 and Figure 5.26 illustrate examples of the test scenarios. Table 5.5 shows a summary of the tests implemented.

Figure 5.25. Truck Passing the Outside Lane (Bridge #2).

Figure 5.26. Truck Passing the Inside Lane (Bridge #2).

Table 5.5. Summary of Calibration Tests (Bridge #2).

Test Number	Truck Path	Speed (mph)
1	Outside Lane	50
2	Outside Lane	60
3	Outside Lane	60
4	Outside Lane	71
5	Outside Lane	76
6	Inside Lane	60
7	Inside Lane	70
8	Inside Lane	74

5.4. Bridge #3 B-WIM System

5.4.1. Instrumentation Plan

The instrumentation plan for Bridge #3 was designed with two different types of sensors, including 20 strain gauges and 2 accelerometers. LVDTs were not utilized since steel bearings were present. The strain gauges were divided into different groups based on their purposes. The first strain gauge grouping was installed as strain rosettes around 3.0 ft from the center of the bearing at the north end of Beam #3 and Beam #4. They worked for both “axle detection” and “weight” purposes. The second grouping was vertical gauges installed around 3.0 ft from the center of the bearing at the north end of Beam #2 and Beam #5. Two additional vertical strain gauges were installed at the center of the bearing at the north end of the next bridge span (same beams). They were utilized for “axle detection” purposes. Another grouping was two strain gauges installed underneath the bridge deck for “axle detection” purpose. The fourth grouping was referred to as “weight” gauges installed on the bottom surface of the girders at midspan to capture global behavior. The last grouping included two strain gauges installed on beam webs at midspan of Beam #3 and Beam #4; they were used for bridge assessment. The accelerometers installed near the north end bearings of Beam #3 and Beam #4 were also used as an exploration of alternative axle detection methods.

Due to the field logistics, the midspan strain gauges were not installed at the exact center. The location of the midspan gauges was 19.6 ft from the north end of the beam. Figure 5.27 and Figure 5.28 show the plan and cross-section views of the implemented instrumentation plan for Bridge #3, respectively.

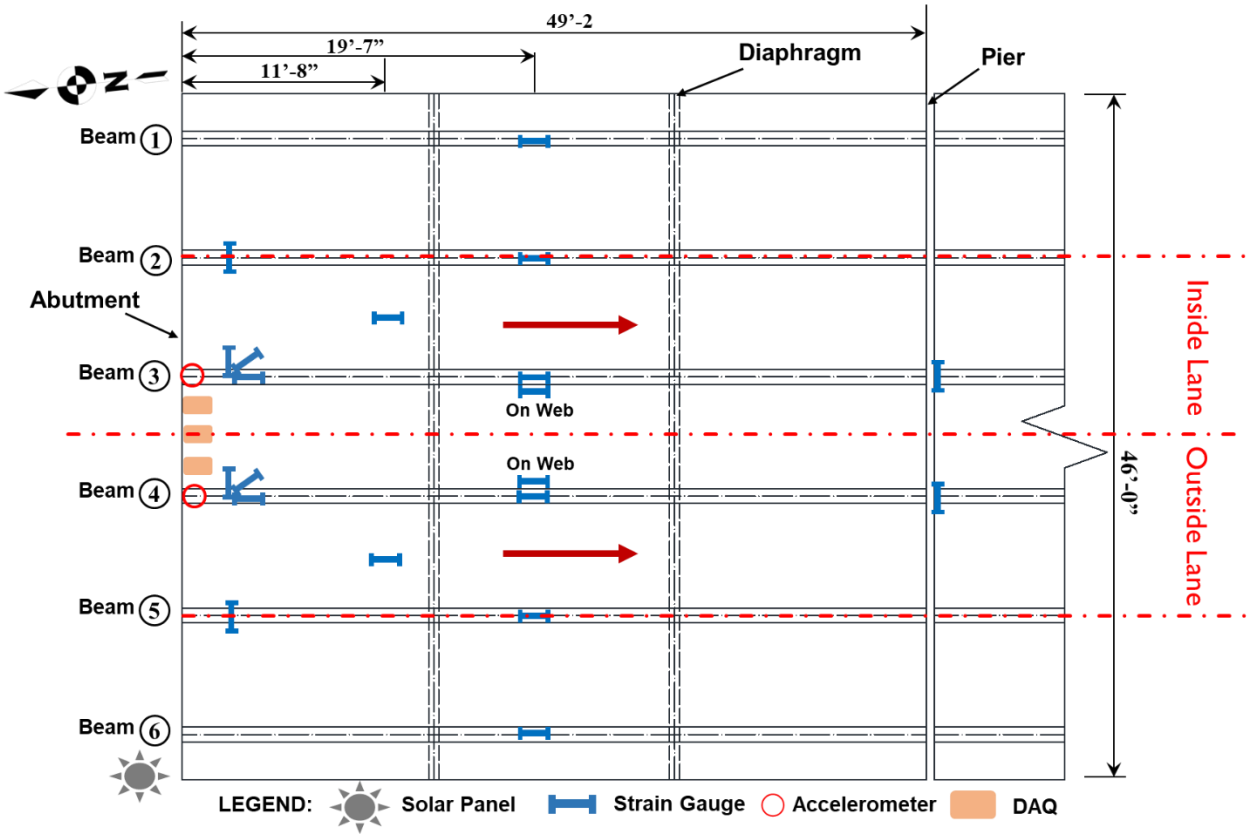

Figure 5.27. Sensor Layout for Bridge #3 (Plan View).

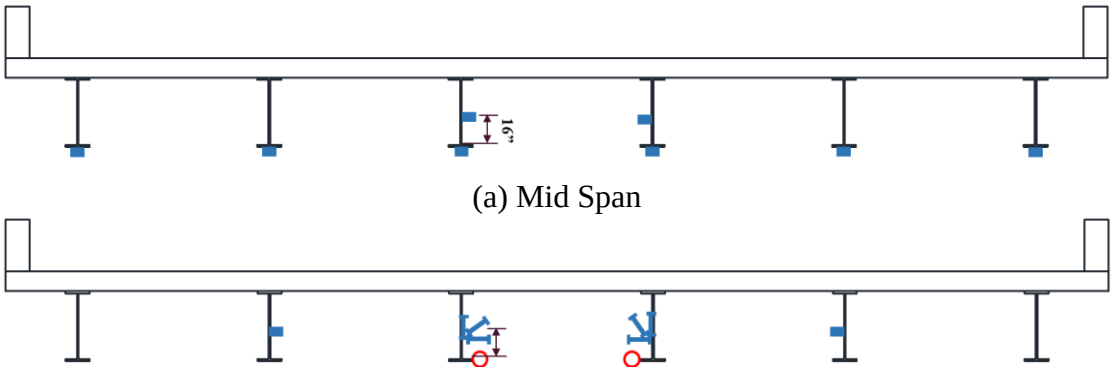

(a) Mid Span

(b) North End

Figure 5.28. Sensor Layout for Bridge #3 (Cross Sections Looking South).

5.4.2. Instrumentation Installation

The sensors, DAQs, and solar panel installed on Bridge #2 were taken down and reused on Bridge #3. The strain gauges were installed with the same methodologies previously discussed for Bridges #1 and #2. The accelerometers were installed with magnets. Figure 5.29 to Figure 5.35 show the installation of Bridge #3.

Figure 5.29. Strain Rosette at North End (Bridge #3).

Figure 5.30. Vertical Strain Gauge at Second Span (Bridge #3).

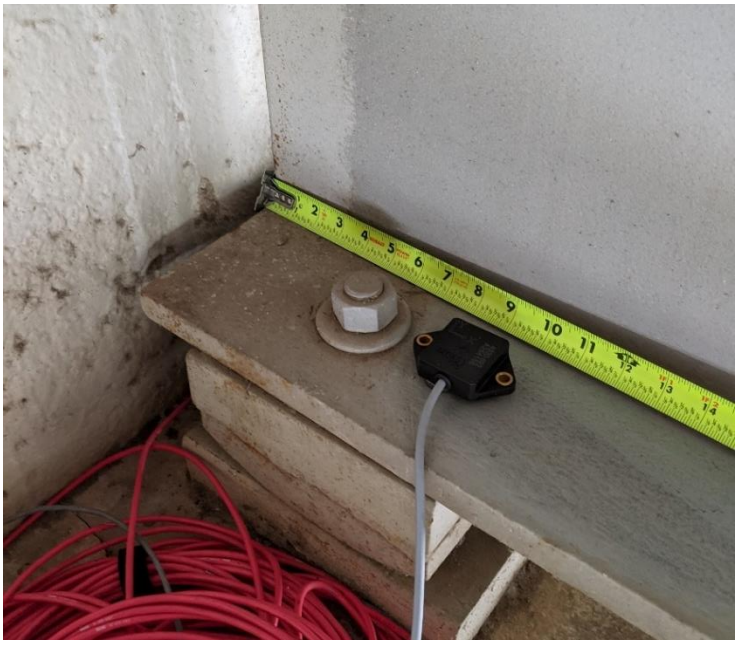

Figure 5.31. Accelerometer at North End (Bridge #3).

Figure 5.32. Vertical Strain Gauge at North End (Bridge #3).

Figure 5.33. Midspan Strain Gauges (Bridge #3).

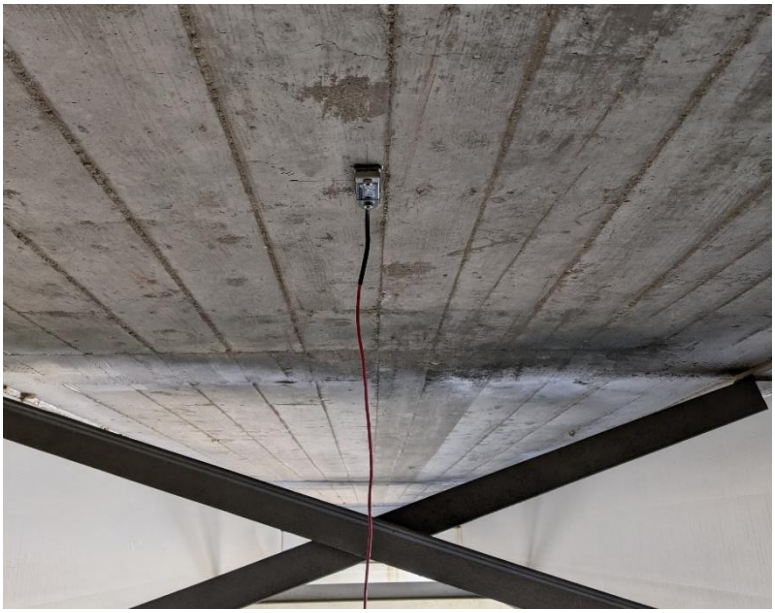

Figure 5.34. Strain Gauge Underneath the Bridge Deck (Bridge #3).

Figure 5.35. Installed Solar Panel (Bridge #3).

5.4.3. Bridge #3 Calibration Test

5.4.3.1. Test Truck and Travel Paths

A three-axle and a six-axle truck were used for the calibration test on Bridge #3. For convenience, they were named Truck A and B. Truck A was a dump truck with three axles, and Truck B was a dump truck with a trailer that had six axles. They had GVWs of 48,600 lb and 84,100 lb, respectively. The specific axle weights and axle spacings are summarized in Table 5.6. The loaded trucks are shown in Figure 5.36 and Figure 5.37. Figure 5.38 and Figure 5.39 show the axle weights and spacings of the two calibration trucks, respectively.

Table 5.6. Axle Information of the Test Vehicles (Bridge #3).

Truck Name	Axle Weight (lb)						Axle Spacing				
	Axle 1	Axle 2	Axle 3	Axle 4	Axle 5	Axle 6	Axle 1 to 2	Axle 2 to 3	Axle 3 to 4	Axle 4 to 5	Axle 5 to 6
A	11,500	18,850	18,250	N/A	N/A	N/A	14'-0"	4'-5"	N/A	N/A	N/A
B	10,850	19,300	18,900	13,200	11,000	10,850	14'-0"	4'-5"	24'-4"	4'-1"	4'-1"

Figure 5.36. Calibration Truck A for Bridge #3.

Figure 5.37. Calibration Truck B for Bridge #3.

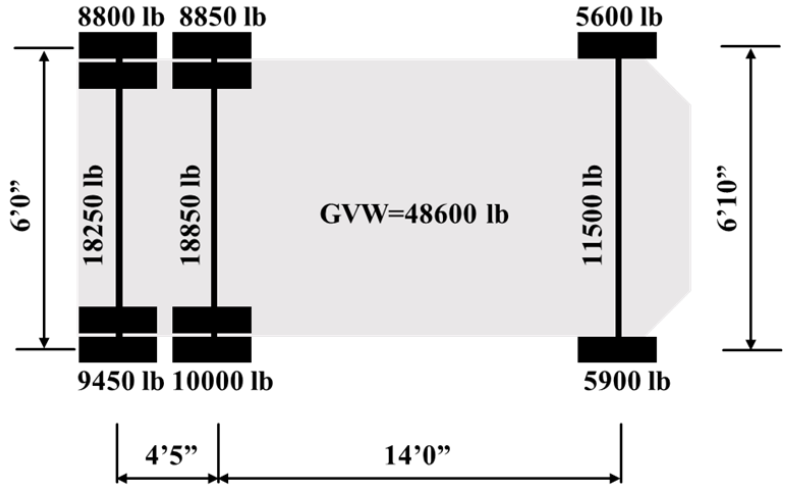

Figure 5.38. Bridge #3 Calibration Truck A Information.

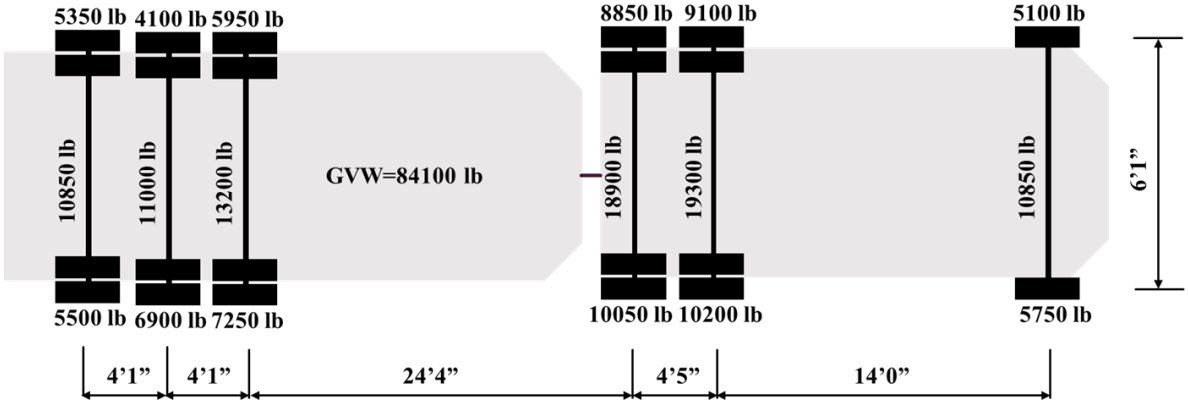

Figure 5.39. Bridge #3 Calibration Truck B Information.

5.4.3.2. Field Testing

The field calibration took place on November 8, 2021. A GoPro camera was set up to record the calibration test. A laptop was used to control the DAQs during the field test. The data was continuously reviewed to ensure sufficient data quality.

A total of 15 test runs were conducted with different speeds of approximately 60, 70, and 80 mph. All of the tests were conducted with normal traffic on both lanes, so no traffic control was required. This bridge also had two lanes of traffic. It was planned for the truck to drive along the center of the two lanes. Table 5.7 shows the summary of the tests conducted. Figure 5.40 and Figure 5.41 illustrate examples of test scenarios.

Table 5.7. Summary of Calibration Tests (Bridge #3).

Test Number	Truck Name	Truck Path	Speed (mph)
1	A	Outside Lane	60
2	B	Outside Lane	58
3	A	Outside Lane	66
4	B	Outside Lane	65
5	A	Outside Lane	70
6	B	Outside Lane	70
7	A	Inside Lane	60
8	B	Inside Lane	59
9	A	Inside Lane	59
10	B	Inside Lane	57
11	A	Inside Lane	64
12	B	Inside Lane	70
13	A	Inside Lane	68
14	B	Inside Lane	65
15	A&B	Side by Side	N/A

Figure 5.40. Truck A Passing the Outside Lane (Bridge #3).

Figure 5.41. Truck B Passing the Inside Lane (Bridge #3).

5.5. B-WIM Deployment Summary

The B-WIM systems for the three bridges were successfully developed, installed, calibrated, and recorded for roughly one month at each site. From this task, significant information about the different instrumentation approaches for successful B-WIM data acquisition was learned. Axle detection was explored using: (a) vertical strain gauges at the beam ends, (b) strain gauges mounted to the bottom surface of the deck, (c) LVDTs at the bearings (measuring vertical displacement), and (d) accelerometers at the bearings. To measure the truck axle and gross weights, the instrumentation included: (a) mid-span strain gauges along each beam, (b) strain gauge rosettes at the beam ends, and (c) LVDTs at the bearings. Detailed quantification of accuracy was performed in the subsequent task, which is explained in Section 6.

Many logistical conclusions have been made because of the three bridge field studies. First, the installation time of the B-WIM systems was within one day for a crew of four people using a ladder. Removal of the system was achieved in a few hours. Secondly, the installation of the strain gauge rosettes was found to be easier than the deck strain gauges. This was due to the relatively high ladder work needed for the deck gauges. Another logistical item was conducting the calibration tests without traffic control. Performing calibration tests with truck speeds in the flow of conventional traffic worked very well. This avoids the cost of traffic control, the inconvenience to the traveling public, and improves safety. Finally, the reusable (nondestructive) B-WIM sensors and DAQ selected for the study have proven to be sufficiently robust to withstand all weather conditions and could be easily moved from bride to bridge. The

long-term durability of B-WIM systems should be relatively better than pavement WIM systems, based on the performance of long-term structural monitoring systems utilizing similar equipment.

6. LIVE LOAD DATA ANALYSIS AND VALIDATION

6.1. Overview

The live load truck data recorded from the B-WIM systems were processed to determine the information for each truck crossing the bridge. The truck weight and axle information included gross vehicle weight, individual axle weights, number of axles, axle spacing, truck average speed, and vehicle (truck) classification. Algorithms developed from the previous tasks were utilized to obtain the above truck information. The data analysis methodologies are presented, followed by the results from Bridge #1, Bridge #2, and Bridge #3.

A validation study was conducted by comparing the B-WIM results with independent WIM data. The initial plan was to utilize traffic data from a nearby permanent WIM station as the primary basis for validating the B-WIM system. However, the Bryan permanent WIM station LW554 on SH 6 was under maintenance during the B-WIM data collection period. As a result, the research team (led by Lubinda Walubita) installed portable WIM units near Bridge #1 (both lanes) and Bridge #2 (outside lane only) specifically for the B-WIM validation study. The results of these validation studies are also presented in this section.

6.2. Data Analysis Methodologies

6.2.1. Introduction

The data recorded by the B-WIM systems were collected and processed to determine the information for each truck crossing the bridge. Several algorithms were utilized to obtain the truck information. These algorithms include lane detection, axle detection, GVW calculation, axle weight calculation, and truck classification. Calibration tests for Bridge #1 will be used as examples to demonstrate the algorithms in the following sections.

6.2.2. Assumptions

There were several assumptions made as part of the data processing. The B-WIM methods employed assumed that the instrumented span behaves as simply supported. It was also assumed that the truck loads could be modeled as a group of concentrated forces moving across the structure at a constant speed. For side-by-side trucks, it was also assumed that both vehicles had the same constant speed. The bridge and truck dynamics were not explicitly modeled and were primarily removed through data filtering techniques to obtain the static content. In addition, it was assumed that the trucks were within the striped traffic lanes.

6.2.3. Lane Detection Methodology

Lane detection is the first step of the B-WIM data processing. It is vital to accurately determine the lane of the crossing truck so that the correct corresponding “axle detection” sensors can be picked for further analysis. The strain gauges installed at the midspan were utilized for lane detection. Similar to the idea of distribution factors, when

the truck passes midspan, the strains for each girder can be obtained. For Bridge #1, if Girder #1, Girder #2, and Girder #3 show greater strain magnitude than the rest of the girders, the truck path can be determined as the inside lane (or left lane) and vice versa. Figure 6.1 shows an example of the strain magnitudes of each girder when the calibration truck traveled on the outside lane (or right lane). Each data point represents the strain magnitude of each girder at a specific time. G1 to G6 represents Girder #1 to Girder #6. It is obvious that girders under the outside lane have a greater response. This methodology only works for the single truck passing condition; side-by-side cases will be identified as special configurations (discussed further in Section 6.2.7).

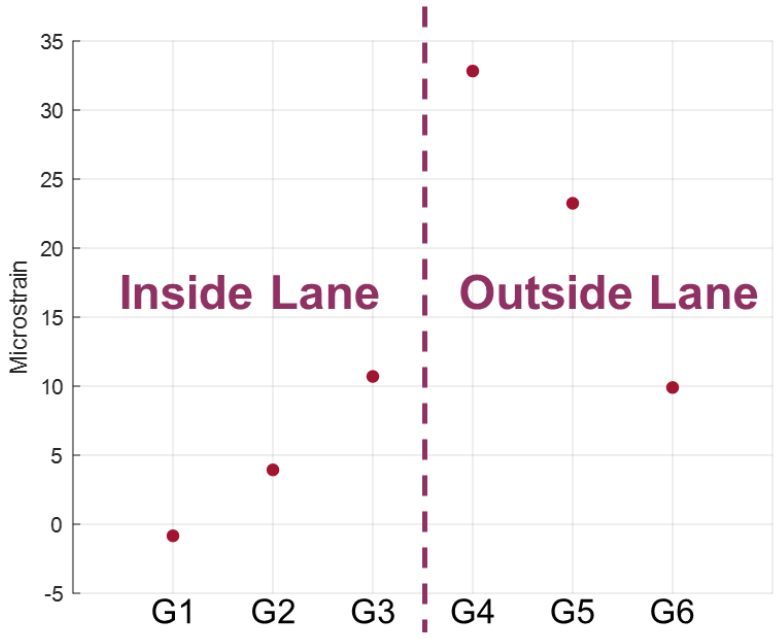

Figure 6.1. Midspan Strain Response When a Truck Passes along the Outside Lane.

6.2.4. Axle Detection Information

The axle information herein includes the axle number, axle spacing, and average speed. An important step in data processing is to identify the peaks (or spikes) in the axle detection data. These peaks depict the instance that an axle is right above the gauge, which is critical information for the B-WIM algorithms. The primary axle detection sensors utilized were the strain gauges installed underneath the deck at the quarter span. The LVDTs (Bridge #1 and Bridge #2) and the vertical gauge of the strain rosette were also explored as alternative options.

6.2.4.1. Strain Gauge (Quarter Span)

Data from the axle detection strain gauges were processed with a low-pass filter. A low-pass filter allows signals below a cutoff frequency (passband) and attenuates signals above the cutoff frequency (stopband). By removing some frequencies, the filter creates a smoothing effect. In other words, the filter produces slow changes in output values to make it easier to see trends and boost the overall signal-to-noise ratio with minimal signal degradation. The cutoff frequency was set as 1.0 Hz.

There were two methodologies used to process the axle detection strain data. The first method was to use the filtered data directly. This method has been widely used for strain-based B-WIM (Kalin et al. 2006; Lydon et al. 2017; Wu et al. 2020; Yu et al. 2016). Take Test #14 as an example. Figure 6.2 shows the axle detection sensors installed underneath the bridge deck, which clearly show the corresponding peaks when each axle of Truck A passed the bridge. However, this method has difficulty detecting peaks when the response is low. Figure 6.3 shows the time history of the axle detection

gauge on the north side quarter span in Test #12 (Truck B with six axles). It is hard to tell the difference between the peaks for real axles and noise.

The second method was to use the second derivative of the measured data (Christenson et al. 2011; Wang et al. 2019). In general, each negative peak in the plot of strain second derivatives depicts the instance an axle is right above the strain gauge. As shown in Figure 6.4, this method can overcome the difficulties that are encountered in the first method. However, this method has its limitations. It was found that when the truck was traveling on the bridge at crawling speeds, the second derivative method could not accurately detect the corresponding peaks. Figure 6.5a and Figure 6.5b shows the time history data and second derivative data of Test #1, respectively.

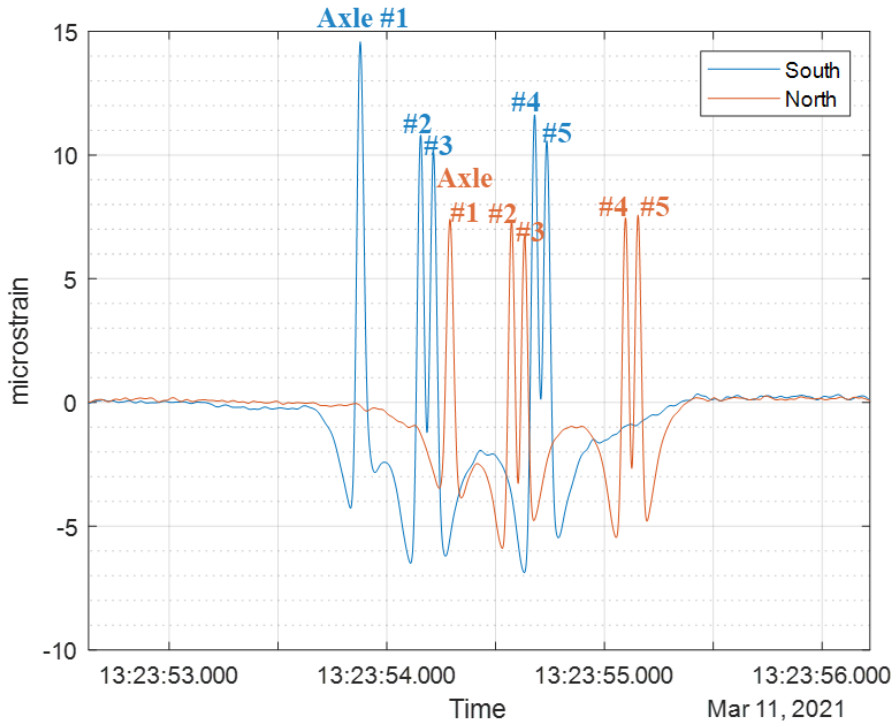

Figure 6.2. Axle Detection Strain Gauge Data (Test #14).

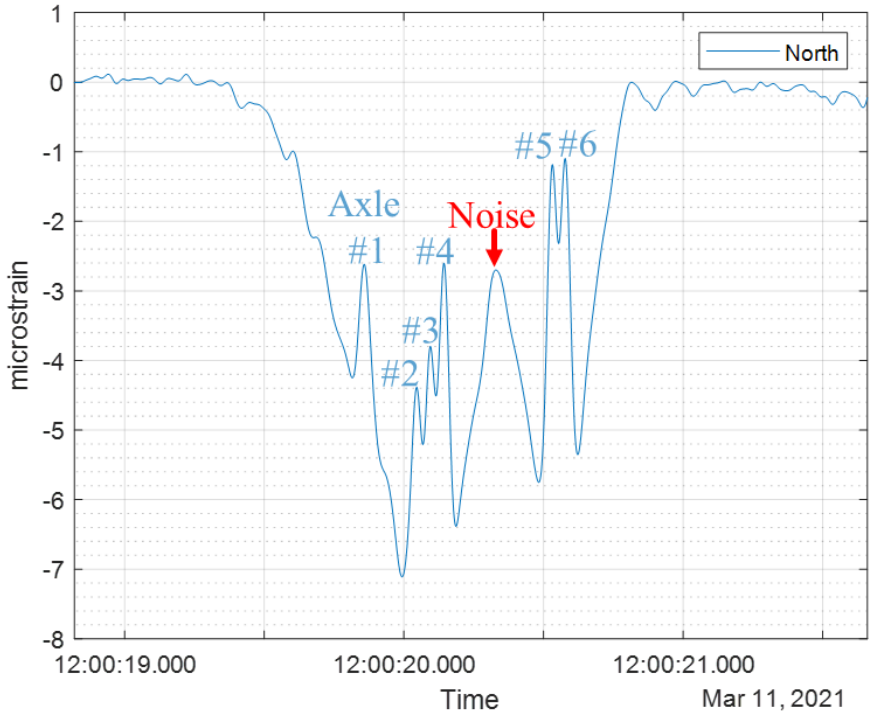

Figure 6.3. North Side Axle Detection Strain Gauge Data (Test #12).

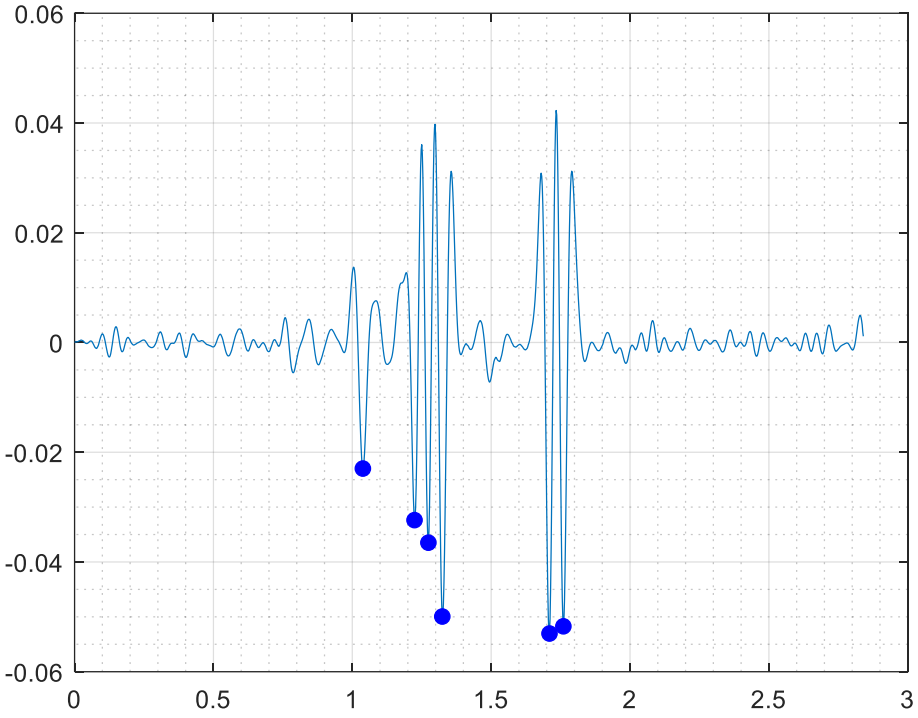

Figure 6.4. Second Derivative of North Side Axle Detection Strain Gauge Data (Test #12).

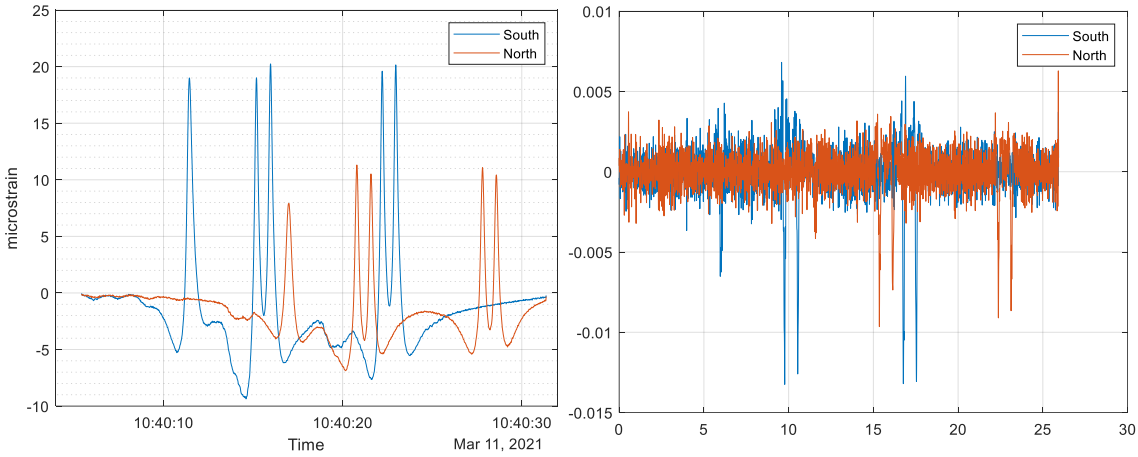

(a) Time History Data (b) Second Derivative Data

Figure 6.5. Strain Gauge Time History Data and Second Derivative Data (Test #1).

The second derivative method was used for obtaining axle information. Each spike (or peak) in the plotted data indicates a truck axle passing the strain gauge, where the axle numbers are obtained directly by counting the number of peaks. The average speed of the truck is determined as the speed of the first axle from Eq. (3.1), where l is the distance between the south and north strain gauges (30.5 ft for Bridge #1). The time difference of each axle passing over the south or north end of the strain gauges is provided in the second derivative data as well. The product of time difference and the calculated average speed provides the truck's axle spacing d_n, as given by Eq. (3.2).

6.2.4.2. Strain Rosette (Vertical Gauge)

Lydon et al. (2017) found that utilizing the measurement of vertical strain at the beam supports demonstrated success as an alternative axle detection method. The full strain rosette was installed to detect truck weights, but the vertical gauge within the rosette was used to explore the accuracy as an axle detection method.

Taking Test #15 as an example, Truck A (i.e., five-axle calibration truck) passed the bridge with a speed of 70 mph. Figure 6.6 shows the time history data of the vertical gauge. Each negative spike (or peak) in the time history data represents a passing axle. However, in some cases (Test #17), the time history data cannot clearly show the corresponding peaks, as shown in Figure 6.7a. It was found that taking the first derivative of the time history data would clearly show the peaks. Therefore, the first derivative method was used to process the vertical strain data. Figure 6.7b shows the first derivative data of the vertical gauge.

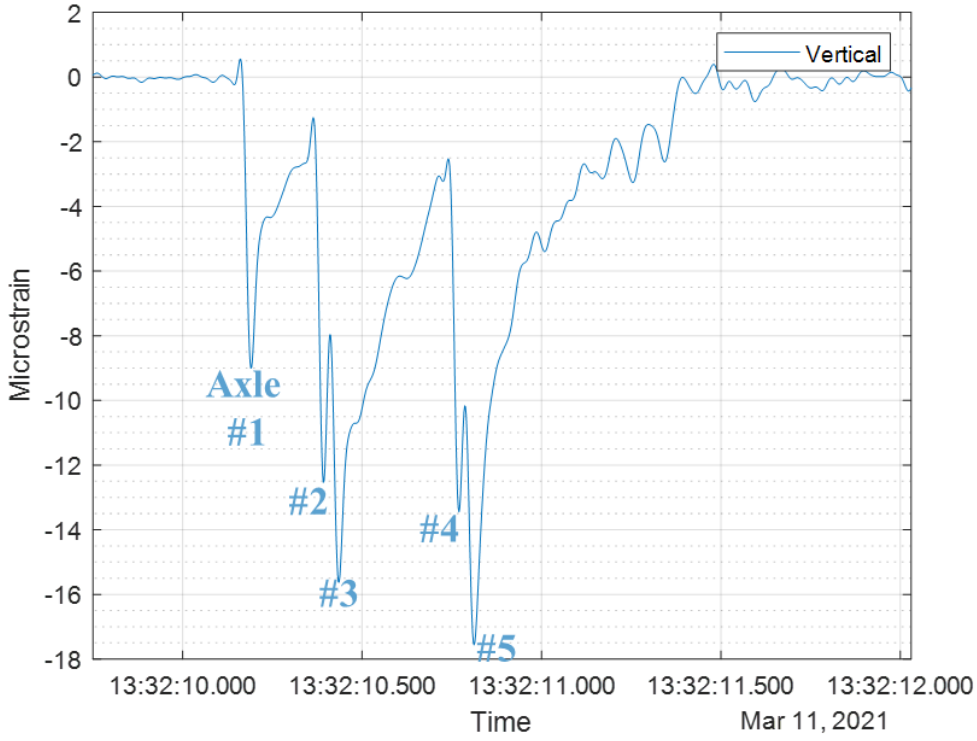

Figure 6.6. Time History of the Vertical Gauge (Test #15).

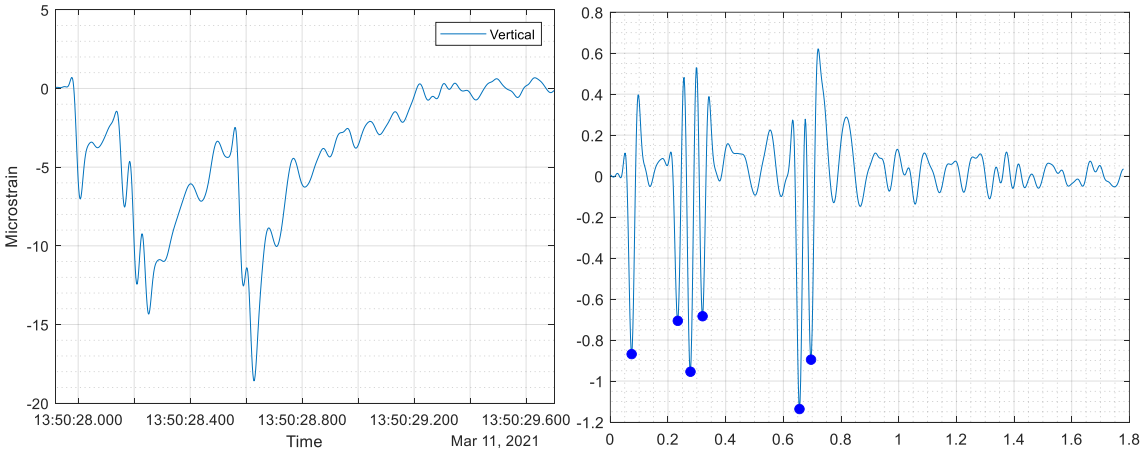

(a) Time History Data (b) First Derivative Data

Figure 6.7. Time History and First Derivative of the Vertical Gauge (Test #17).

6.2.4.3. LVDT

The LVDT axle detection utilized the vertical displacement of the bearing pad. Since the time history data (Truck A, 50 mph) shown in Figure 6.8a cannot provide clear peaks, the first derivative method was used, as shown in Figure 6.8b. However, when the truck passed the bridge at a higher speed, it was found that the corresponding LVDT data were not able to show clear peaks for axle detection. Figure 6.9 shows the time history and first derivative of the LVDT data for Test #18 (Truck B, 70 mph). The bearing pads being relatively old could be the reason for this issue.

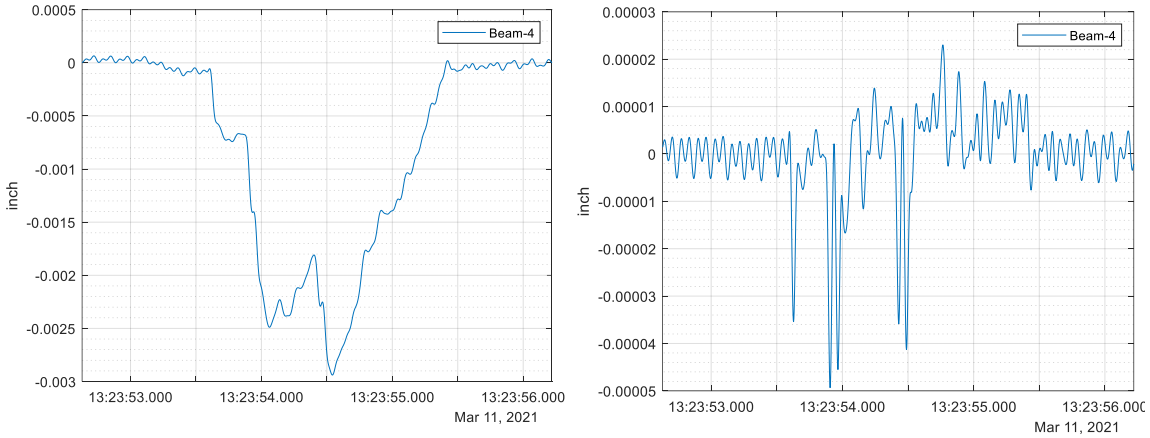

(a) Time History Data (b) First Derivative Data

Figure 6.8. Time History and First Derivative of the LVDT (Test #14).

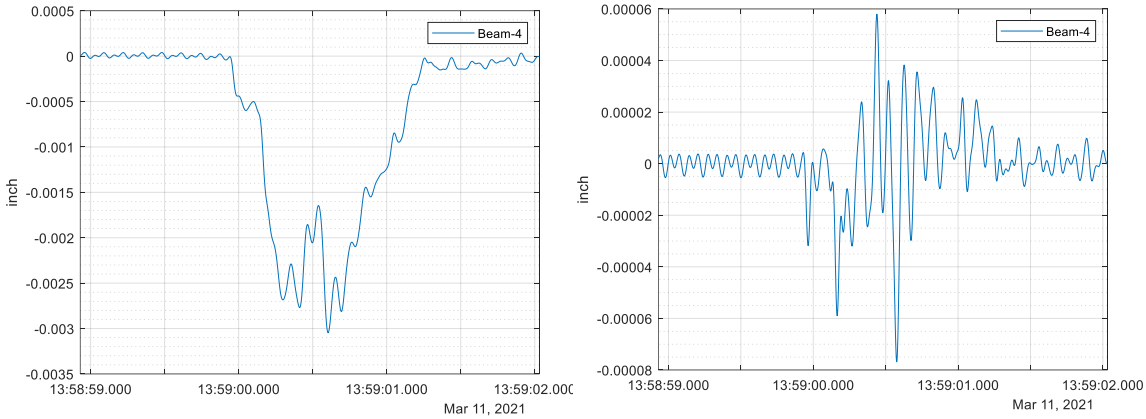

(a) Time History Data (b) First Derivative Data

Figure 6.9. Time History and First Derivative of the LVDT (Test #18).

6.2.5. GVW Calculation

The area method (previously discussed in Section 3.6.2) was applied to determine the gross vehicle weight information (Ojio and Yamada 2002). The data processed were from the weighing sensors (i.e., midspan strain gauges, strain rosette, and LVDTs). The axle information required in the gross weight calculations was obtained from the algorithms in the previous section.

6.2.5.1. Strain Gauges (Mid-span)

The area method is based on the principle that the area under the time history response curve is proportional to GVW. By combining the sum of the strain area from all of the weighing sensors at the midspan as well as considering the speed effect with an adjustment coefficient α, the weight of the truck can be calculated with Eq. (3.6) to Eq. (3.8). Figure 6.10 shows an example of the induced strain area from a truck passing event.

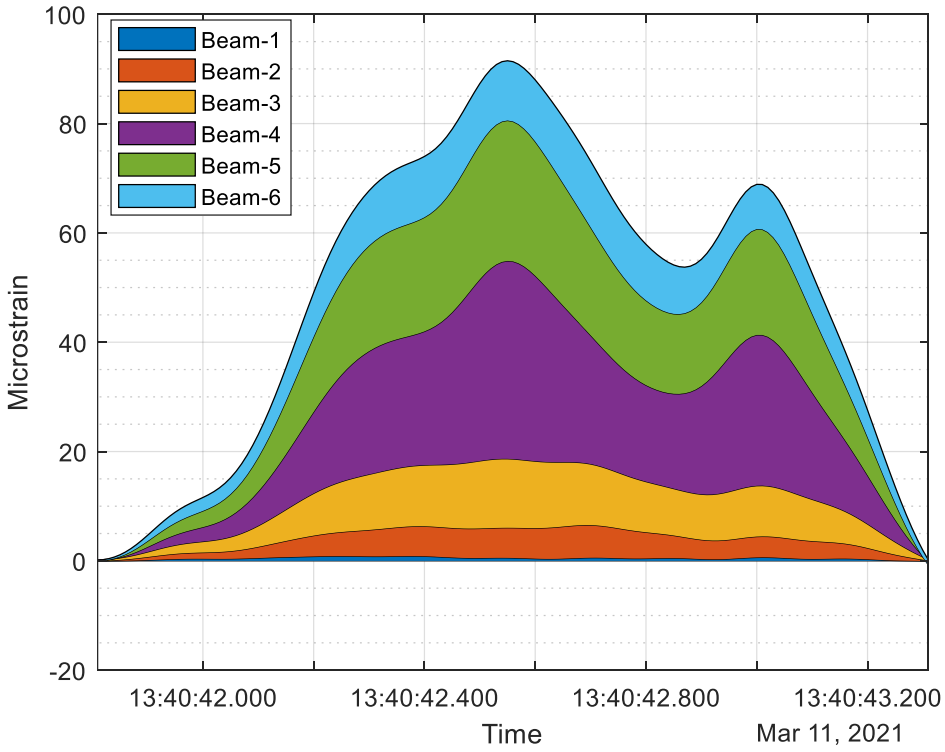

Figure 6.10. Example Areas of Strain Induced in a Test.

6.2.5.2. Strain Rosette (Shear)

The responses from the three strain gauges that make up the rosette were processed and converted to shear strain for GVW calculation purposes. The shear strain can be determined by Eq. (6.1):

$$\gamma_{xy} = 2\gamma_2 - \gamma_1 - \gamma_3 \qquad (6.1)$$

where γ_{xy} is the converted shear strain, γ_1 is the strain from the vertical gauge, γ_2 is the strain from the diagonal gauge, and γ_3 is the strain from the horizontal gauge.

Figure 6.11 shows an example of an induced shear strain area in a truck passing event.

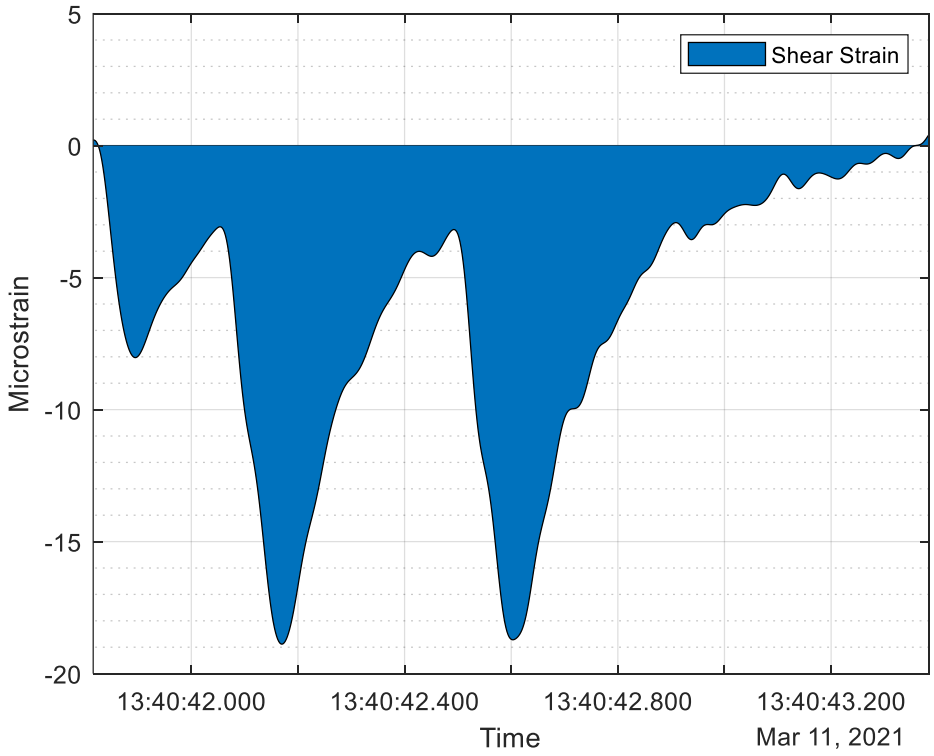

Figure 6.11. Example Area of Shear Strain Induced in a Test.

6.2.5.3. LVDT

Similar to the strain data, the area method was applied to the LVDT data. Eq. (3.6) to Eq. (3.8) were followed to determine the GVW of an unknown truck. The area herein is changed to the sum of the area of the displacements from all the bearing pads. Figure 6.12 shows an example of the induced displacement areas in a truck passing event.

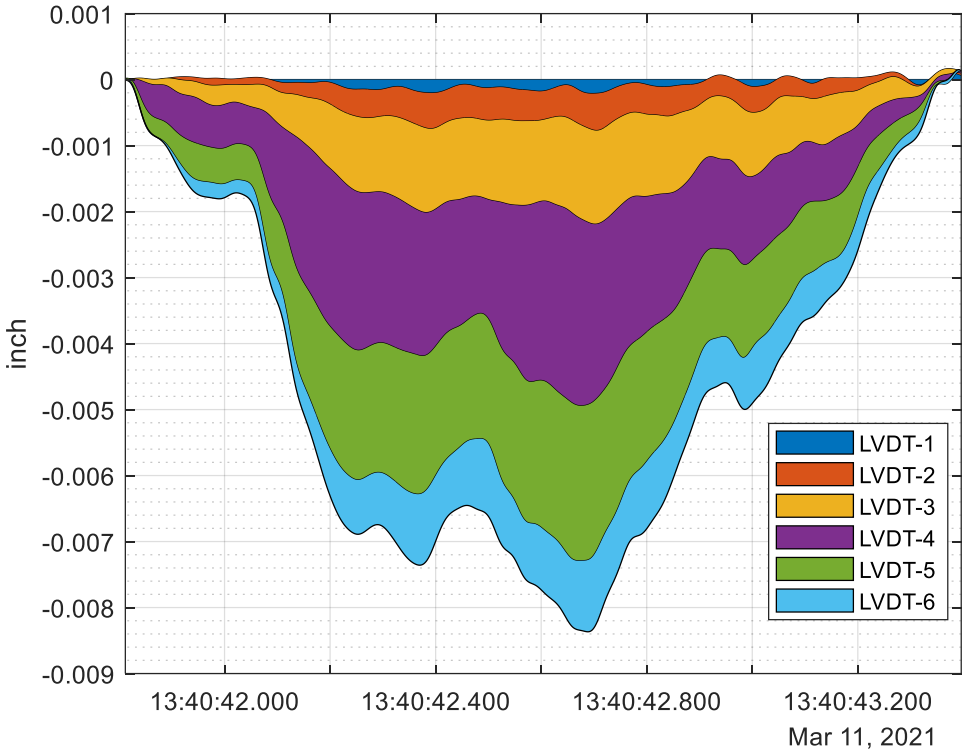

Figure 6.12. Example Area of Displacements Induced in a Test.

6.2.6. Axle Weight Calculation

6.2.6.1. Axle Weight Measurements Using Deck Strain Gauges

The axle weights are relative to the magnitudes of the negative peaks of the second derivative of the strain as each axle passes over the midspan. However, the strain from the midspan gauges did not provide clear peaks. The data from axle detection strain gauges were used to obtain the axle weights as an exploration. Subsequently, the GVW is distributed by the negative peak values of the second derivative, as shown in Eq. (6.2):

$$P_n = \left[\frac{\frac{d^2\varepsilon}{dt^2}(n)}{\sum_{i=1}^{n} \frac{d^2\varepsilon}{dt^2}(i)} \right] \times GVW \tag{6.2}$$

where P_n is the axle weight and $\mathcal{E}$ is the response from strain gauge magnitude. Therefore, the identification accuracy of axle weight is affected by the calculation accuracy of GVW and the negative peak values of the second derivative.

6.2.6.2. Axle Group Weight Measurements Using Strain Rosettes

The strain rosette installed near the bridge support measured the shear strain response. This measurement method was utilized as an alternative to using load cells with the reaction force method (refer to Section 3.6.2 for further details on the methodology). This method uses the shear influence line of a simply supported bridge. The axle weights can be calculated using the influence line. It was found that the theoretical shear influence line cannot accurately calculate individual axle weights. Therefore, the axles were divided into axle groups as the front axle and the tandems for calculation. According to the Texas Transportation Code, "A Tandem Axle is defined as two or more consecutive axles spaced 40 inches apart and not more than 96 inches apart." This definition allows for what is known as "Tridems," or a three-axle unit, but also includes the variable spacing of axles that is common on the rear tandem axle on the trailer portion of many tractor-trailers.

The shear can be calculated according to Eq. (6.1). The shear response of each axle group can be found in the peaks, as shown in Figure 6.13. The influence ordinates of the instance when the front axle reaches the support and the instance when the first

tandem group reaches the support can be calculated based on the magnitude of the first two peaks. The influence ordinate at the other end of the bridge support is zero. After a curve fitting with these three points, a new influence line for the axle groups can be obtained. Figure 6.14 shows and example from Bridge #1. This influence line is utilized to identify the weight of individual axles. For tandem axles, the individual axle weights within the tandem are assumed to be of equal magnitude. The same assumption was also applied to tridem and quad axle groups.

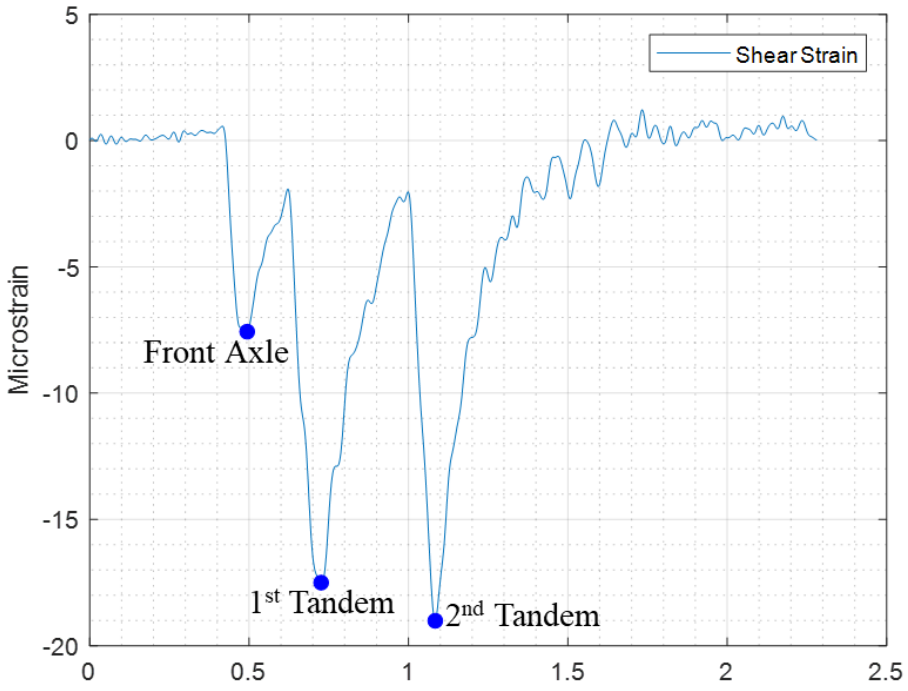

Figure 6.13. Shear Response of the Axle Groups.

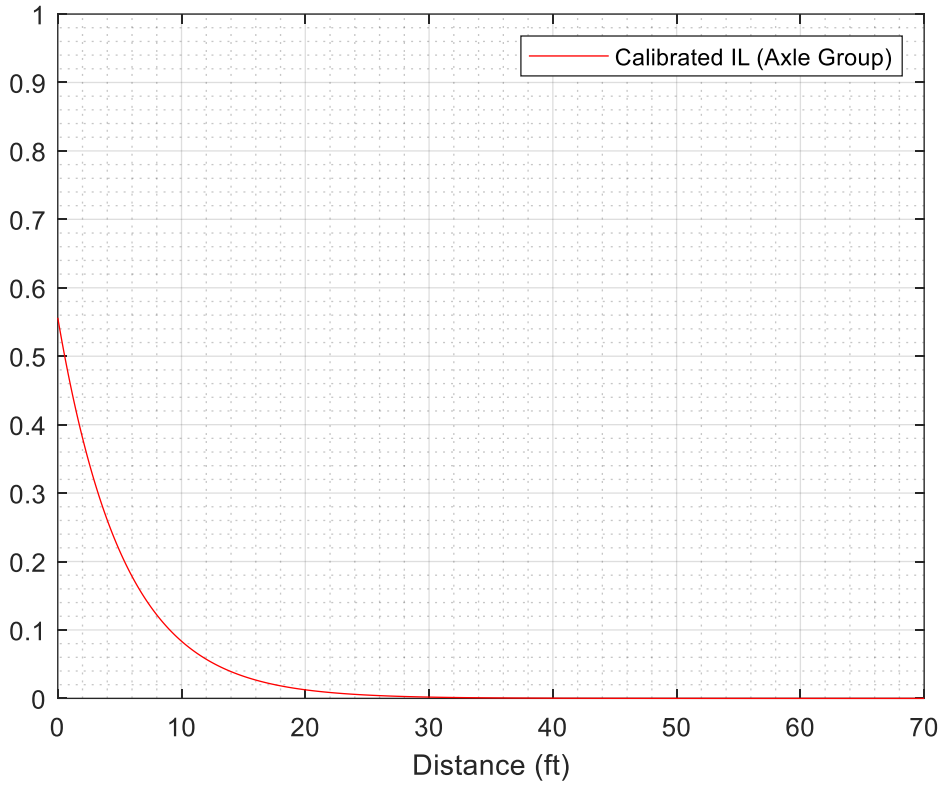

Figure 6.14. Influence Line for Axle Groups.

6.2.7. Side-by-Side Configuration Detection and GVW Calculation

The algorithms demonstrated above were based on single truck passing configurations. While relatively infrequent, trucks may simultaneously occur on a bridge span in adjacent lanes. Figure 6.15 and Figure 6.16 show example configurations of staggered trucks and side-by-side trucks with their midspan strain gauge response, respectively. These configurations can be identified automatically and processed thereafter.

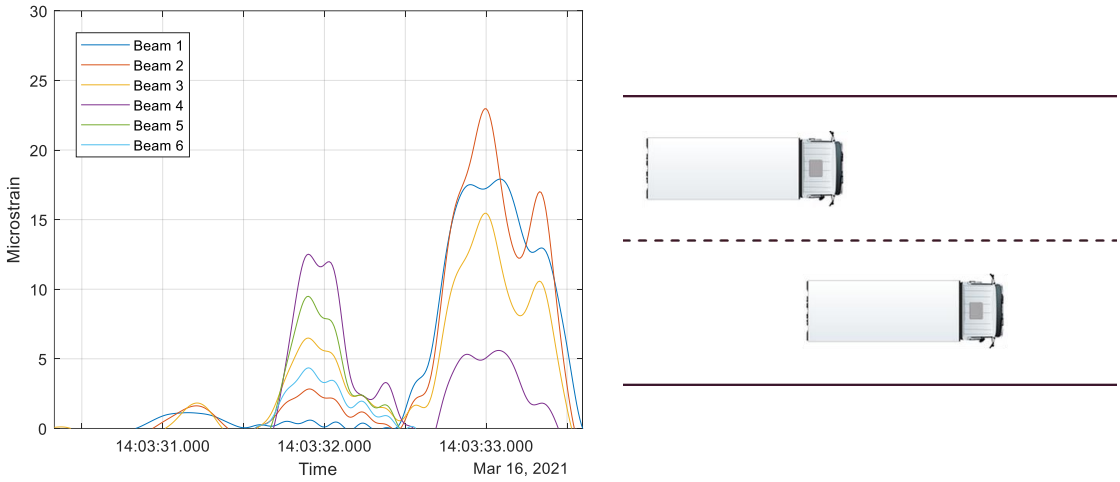

Figure 6.15. Staggered Configuration.

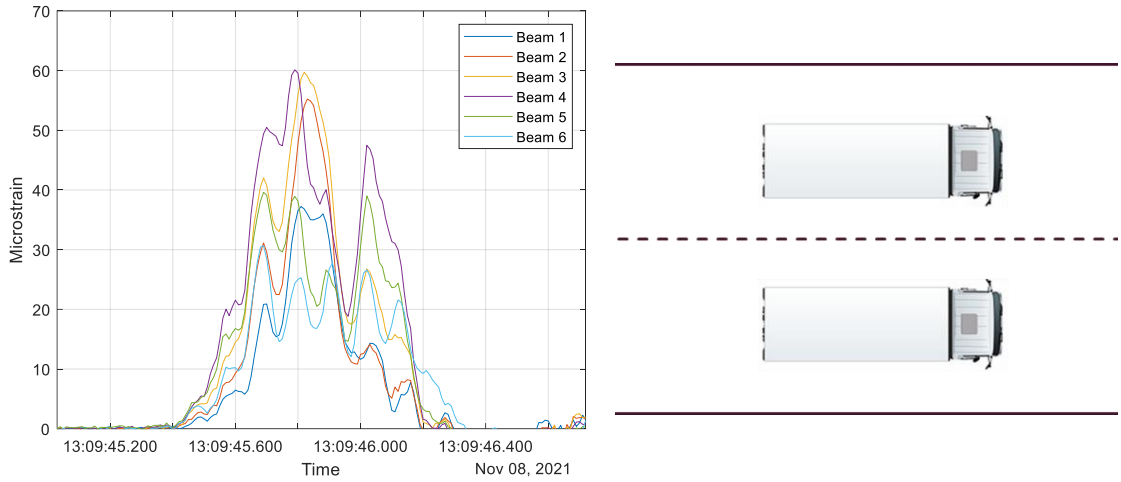

Figure 6.16. Side-by-Side Configuration.

The data recorded by the midspan strain gauges were used to identify the side-by-side configurations. The distribution ratios of the induced strain areas were calculated and compared to determine the configurations. The distribution ratios were calculated with Eq. (6.3). Figure 6.17 shows the distribution of different configurations. It was found that the difference between the left lane and right lane in side-by-side or staggered

configurations is smaller than 25 percent. Therefore, this number can be used as a threshold for the side-by-side case detection.

$$Distribution\% = \left(A_i \Big/ \sum_{1}^{n} A_i \right) \times 100\% \qquad (6.3)$$

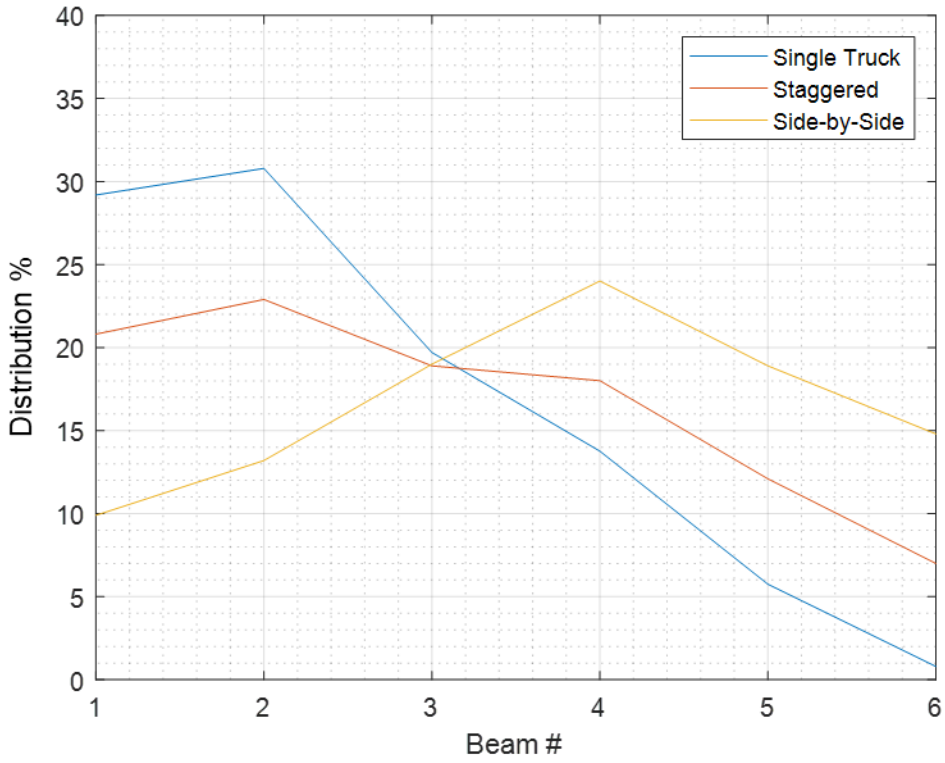

Figure 6.17. Multiple Trucks Present Configurations.

The individual GVW of the side-by-side trucks can be obtained by utilizing the area method and midspan distribution factors. For example, consider Truck A travels on the inside lane, while Truck B travels on the outside lane. The combined GVW (GVW_{total}) of the two trucks can be obtained by the area method introduced in the previous section. The midspan strain distribution factor for this truck passing event

(DF_n) can be determined by Eq. (6.3), where n is the beam number. By conducting calibration tests, the distribution factors when the calibration truck passes the inside lane (DFI_n) and the outside lane (DFO_n) can be calculated. Using the n^{th} beam, two equations can be constructed, as shown in Eq. (6.4) and Eq. (6.5). The gross weight of each truck (GVW_A and GVW_B) can be determined by solving the equations.

$$GVW_A + GVW_B = GVW_{total} \tag{6.4}$$

$$DFI_n \cdot GVW_A + DFO_n \cdot GVW_B = DF_n \cdot GVW_{total} \tag{6.5}$$

Side-by-side tests were conducted for the Bridge #3 calibration tests. The accuracies of the above algorithms are explored in the data processing section of this chapter.

6.2.8. Vehicle Classification

FHWA developed a standardized vehicle classification system known as the FHWA 13-category classification rule (TxDOT 2013). The FHWA classification system is shown in Figure 6.18. However, the FHWA definitions are based on vehicle characteristics that can be easily identified visually but that cannot be computed on the basis of the axle number, weight, and axle spacings. Therefore, this vehicle classification was not utilized to classify vehicles using the B-WIM system data.

In 2003, the Traffic Expert Task Group (ETG) of the FHWA Long-Term Pavement Performance (LTPP) project developed a new set of rules for classifying vehicles based on sensor outputs available from WIM systems. In 2006, the LTPP

project adopted the Traffic ETG recommendation that this ruleset be used at Specific Pavement Study Transportation Pooled Fund Study WIM scale sites in those states that were willing to adopt these rules (Hallenbeck et al. 2014). It uses a combination of four variables to classify each vehicle:

- Number of axles on the vehicle.
- Spacing between those axles.
- Weight of the first axle on the vehicle.
- GVW of the vehicle.

Not all variables are used to define each class of vehicle. The LTPP rules are shown in Table 6.1.

For the B-WIM systems in this research study, the FHWA LTPP rules were primarily utilized. The axle number and axle spacing calculations were used for vehicle classification. Only vehicles with a GVW greater or equal to 20 kips were captured for further data processing.

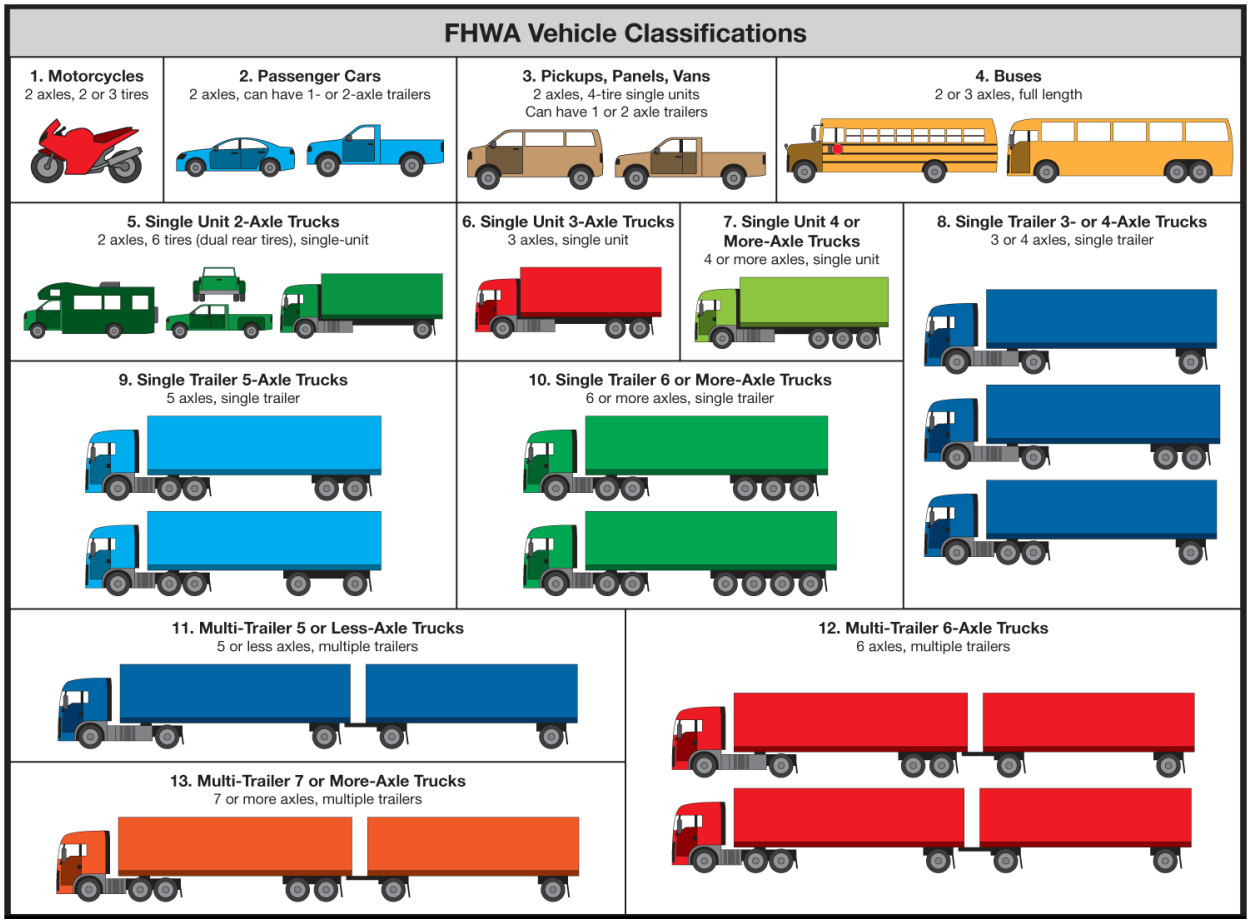

Figure 6.18. FHWA Vehicle Classifications (reprinted from TxDOT 2013).

Table 6.1. LTPP Classification Rules for SPS WIM Sites (reprinted from Hallenbeck et al. 2014).

Class	Vehicle Type	No. of Axles	Spacing between Axles 1 and 2 (ft)	Spacing between Axles 2 and 3 (ft)	Spacing between Axles 3 and 4 (ft)	Spacing between Axles 4 and 5 (ft)	Spacing between Axles 5 and 6 (ft)	Spacing between Axles 6 and 7 (ft)	Spacing between Axles 7 and 8 (ft)	Spacing between Axles 8 and 9 (ft)	Gross Weight Min–Max (Kips)	Axle 1 Weight Min (Kips)[1]
1	Motorcycle	2	1.00–5.99	—	—	—	—	—	—	—	0.10–3.00	—
2	Passenger Car		6.00–10.10	—	—	—	—	—	—	—	1.00–7.99	—
3	Other (Pickup/Van)		10.11–23.09	—	—	—	—	—	—	—	1.00–7.99	—
4	Bus		23.10–40.00	—	—	—	—	—	—	—	12.00 >	—
5	2D Single Unit		6.00–23.09	—	—	—	—	—	—	—	8.00 >	2.5
2	Car with 1 Axle Trailer	3	6.00–10.10	6.00–25.00	—	—	—	—	—	—	1.00–11.99	—
3	Other with 1-Axle Trailer		10.11–23.09	6.00–25.00	—	—	—	—	—	—	1.00–11.99	—
4	Bus		23.10–40.00	3.00–7.00	—	—	—	—	—	—	20.00 >	—
5	2D with 1-Axle Trailer		6.00–23.09	6.30–30.00	—	—	—	—	—	—	12.00–19.99	2.5
6	3-Axle Single Unit		6.00–23.09	2.50–6.29	—	—	—	—	—	—	12.00 >	3.5
8	Semi, 2S1		6.00–23.09	11.00–45.00		—	—	—	—	—	20.00 >	3.5
2	Car with 2-Axle Trailer	4	6.00–10.10	6.00–30.00	1.00–11.99	—	—	—	—	—	1.00–11.99	—
3	Other with 2-Axle Trailer		10.11–23.09	6.00–30.00	1.00–11.99	—	—	—	—	—	1.00–11.99	—
5	2D with 2-Axle Trailer		6.00–26.00	6.30–40.00	1.00–20.00	—	—	—	—	—	12.00–19.99	2.5
7	4-Axle Single Unit		6.00–23.09	2.50–6.29	2.50–12.99	—	—	—	—	—	12.00 >	3.5
8	Semi, 3S1		6.00–26.00	2.50–6.29	13.00–50.00	—	—	—	—	—	20.00 >	5.0
8	Semi, 2S2		6.00–26.00	8.00–45.00	2.50–20.00	—		—	—	—	20.00 >	3.5
3	Other with 3-Axle Trailer	5	10.11–23.09	6.00–25.00	1.00–11.99	1.00–11.99	—	—	—	—	1.00–11.99	—
5	2D with 3 Axle Trailer		6.00–23.09	6.30–35.00	1.00–25.00	1.00–11.99	—	—	—	—	12.00–19.99	2.5
7	5-Axle Single Unit		6.00–23.09	2.50–6.29	2.50–6.29	2.50–6.30	—	—	—	—	12.00 >	3.5
9	Semi, 3S2		6.00–30.00	2.50–6.29	6.30–65.00	2.50–11.99	—	—	—	—	20.00 >	5.0
9	Truck + Full Trailer (3–2)		6.00–30.00	2.50–6.29	6.30–50.00	12.00–27.00	—	—	—	—	20.00>	3.5
9	Semi, 2S3		6.00–30.00	16.00–45.00	2.50–6.30	2.50–6.30	—	—	—	—	20.00 >	3.5
11	Semi + Full Trailer, 2S12		6.00–30.00	11.00–26.00	6.00–20.00	11.00–26.00	—	—	—	—	20.00 >	3.5
10	Semi, 3S3	6	6.00–26.00	2.50–6.30	6.10–50.00	2.50–11.99	2.50–10.99	—	—	—	20.00 >	5.0
12	Semi + Full Trailer, 3S12		6.00–26.00	2.50–6.30	11.00–26.00	6.00–24.00	11.00–26.00	—	—	—	20.00 >	5.0
13	7-Axle Multi-trailers	7	6.00–45.00	3.00–45.00	3.00–45.00	3.00–45.00	3.00–45.00	3.00–45.00	—	—	20.00 >	5.0
13	8-Axle Multi-trailers	8	6.00–45.00	3.00–45.00	3.00–45.00	3.00–45.00	3.00–45.00	3.00–45.00	3.00–45.00	—	20.00 >	5.0
13	9-Axle Multi-trailer	9	6.00–45.00	3.00–45.00	3.00–45.00	3.00–45.00	3.00–45.00	3.00–45.00	3.00–45.00	3.00–45.00	20.00 >	5.0

6.3. Calibration Test Results

6.3.1. Bridge #1

6.3.1.1. Introduction

The results from 17 calibration tests were processed and summarized in this section, including lane detection, axle number, axle spacing, speed, GVW, axle weight, and vehicle (truck) classification. The three crawl speed tests were not included since their primary purpose was for bridge assessment and to further justify the minimum speed required for B-WIM data processing. The results obtained from the 17 B-WIM calibration tests were then compared with the measured results of the calibration trucks. Though Truck A and Truck B were the same truck with two different axle configurations, the tests conducted included different truck paths and speeds. The results comparison was to explore the repeatability and accuracy of the algorithms.

6.3.1.2. Lane Detection Results

To evaluate the lane detection performance, the accuracy was defined as the ratio between the number of the correctly detected passing lanes and the real passing lanes. For the 17 calibration tests, the B-WIM system was able to detect the truck lanes with an accuracy of 100 percent.

6.3.1.3. Axle Information Results

The axle information results were first evaluated using percent error calculated using Eq. (3.3). The results were then summarized as percent accuracy since this is a standard WIM approach, as shown in Eq. (3.21). The strain gauges installed underneath the south

side quarter span were able to accurately obtain all the axle numbers correctly (i.e., 100 percent accuracy). However, the strain gauges underneath the north side quarter span got one test's axle number wrong, resulting in an accuracy of 94.1 percent. Both south and north sides were able to obtain the peak of the front axle of each truck, which was used to calculate truck speeds with an accuracy of 98.4 percent. Axle spacings were then calculated based on the algorithms illustrated in the previous sections with the second derivative method. Compared with the manually measured value, the average accuracy was 95.4 percent. Table 6.2 summarizes the axle information from the strain gauges underneath the quarter spans.

Table 6.2. Axle Information Detection Accuracy (Quarter Span Strain Gauges).

Parameters	Accuracy
Axle Number	100%
Average Speed	98.4%
Axle Spacing	95.4%

The strain rosette could only detect trucks passing the outside lane due to the installed location. The vertical gauge was able to capture the axle number correctly (i.e., 100 percent accuracy). Since only one side was instrumented with the strain rosette, vehicle speed could not be calculated. Speeds from the quarter span strain gauge calculation results were used with the rosette to calculate the axle spacings. The vertical gauge was able to provide an accuracy of 92.5 percent for axle spacing.

The LVDTs could not provide clear peaks for axle information detection purposes. The accuracy of the axle number detection was 40.0 percent. Due to the low accuracy of axle number detection, the axle spacings were not calculated.

Axle information detection accuracies of the quarter span strain gauges, strain rosette, and LVDTs are summarized in Table 6.3.

Table 6.3. Accuracy of Axle Information Detection Summary (Bridge #1).

Sensor Type	Axle Number Accuracy	Speed Accuracy	Axle Spacing Accuracy
Strain Gauge	100%	98.4%	95.4%
Strain Rosette	100%	N/A	92.5%
LVDT	40.0%	N/A	N/A

6.3.1.4. GVW Results

Each single calibration vehicle test was used to calculate the truck GVWs of the remaining tests. For example, the midspan strain areas and speed of Test #1 were used as the baseline to calculate the GVWs for the rest of the tests, which provided 16 data points. Then Test #2 was used as the baseline to get another 16 data points, etc. The errors of the calculated GVW from the midspan strain gauges are shown in Figure 6.19. The mean value of the errors is 0.8 percent, with a standard deviation of 12.6 percent. Figure 6.20 shows the CDF of the errors. From Eq. (3.21), the average of the GVW accuracy from the midspan strain gauges is 90.4 percent.

The histogram of errors of the calculated GVW (outside lane trucks only) from the strain rosette (shear) are shown in Figure 6.21. The mean value of the errors is 0.9

percent, with a standard deviation of 13.5 percent. Figure 6.22 shows the CDF of the errors. The average of the GVW accuracy from strain rosette is 89.8 percent.

The histogram of the calculated GVW errors from LVDTs are shown in Figure 6.23. The mean value of the errors is 1.1 percent, with a standard deviation of 15.2 percent. Figure 6.24 shows the CDF of the errors. The average GVW accuracy from LVDTs is 88.5 percent.

The GVW calculation accuracies of the midspan strain gauges, strain rosette, and LVDTs in comparison to the manual static scale measurements are summarized in Table 6.4.

Table 6.4. Accuracy of GVW Calculation Summary (Bridge #1).

Sensor Type	Accuracy
Strain Gauge (Midspan)	90.4%
Strain Rosette (Outside lane only)	89.8%
LVDT	88.5%

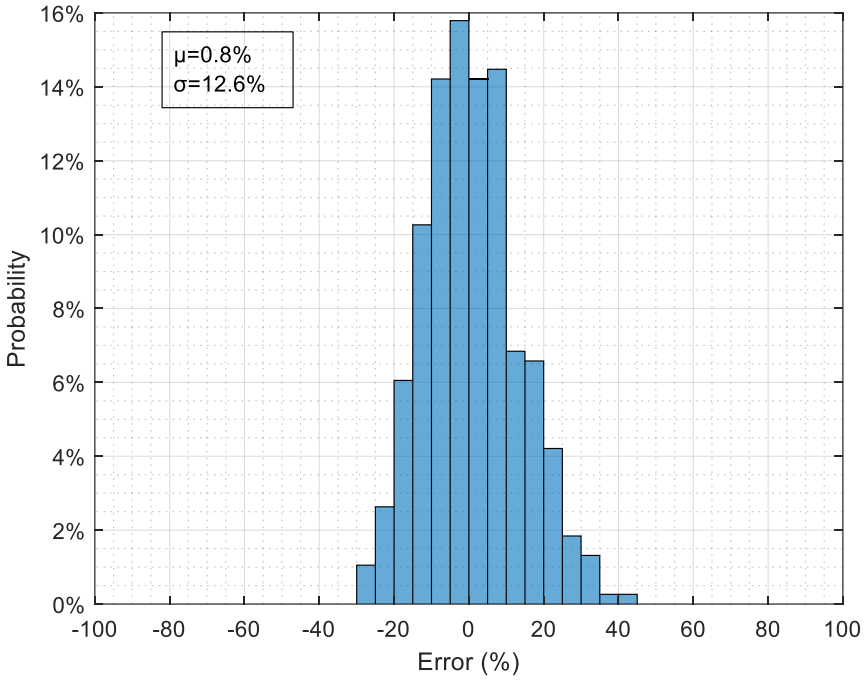

Figure 6.19. Histogram of GVW by Area Method (Midspan Strain Gauges).

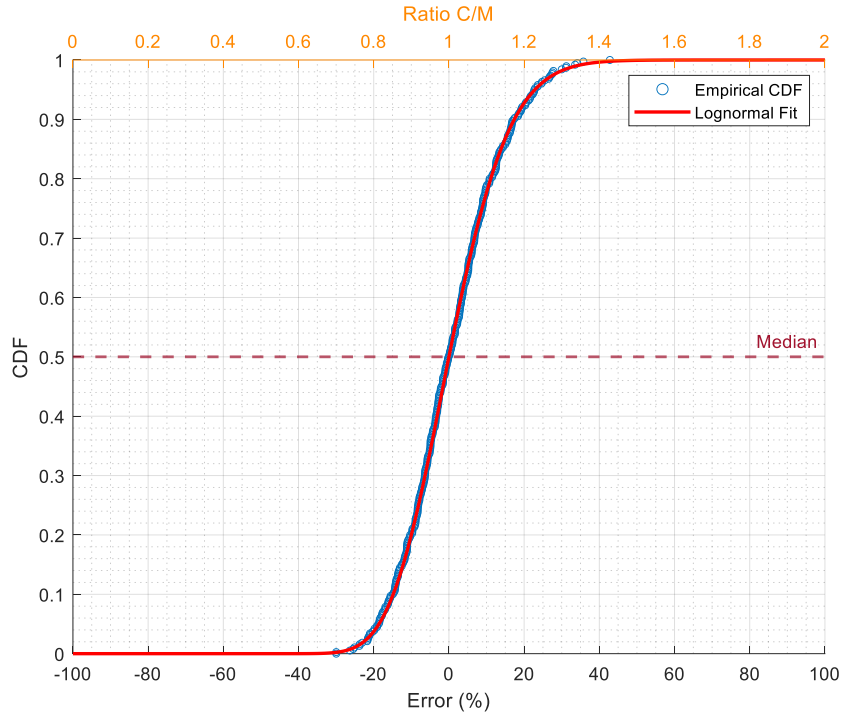

Figure 6.20. CDF of GVW Errors by Area Method (Midspan Strain Gauges).

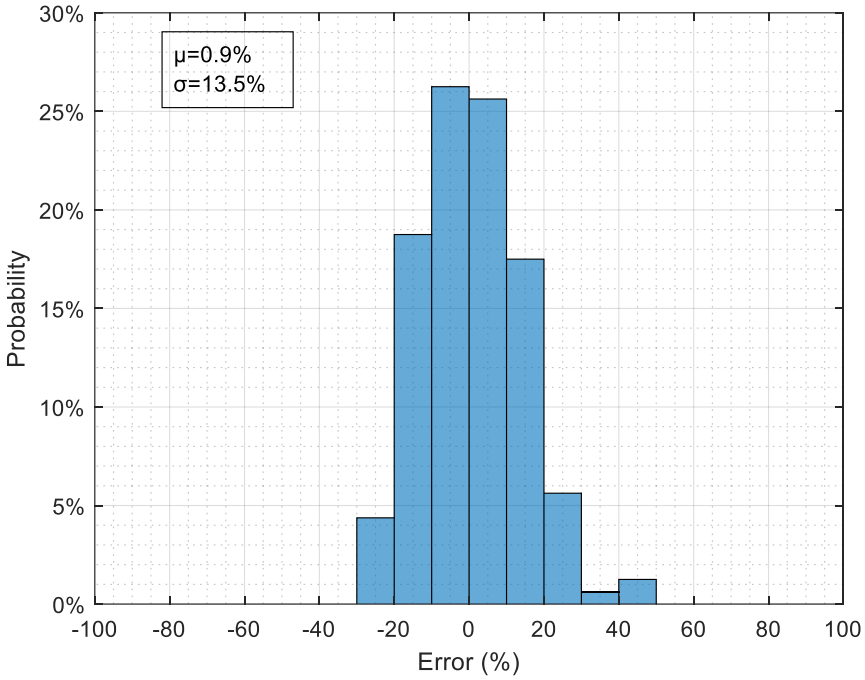

Figure 6.21. Errors of GVW by Area Method (Strain Rosette).

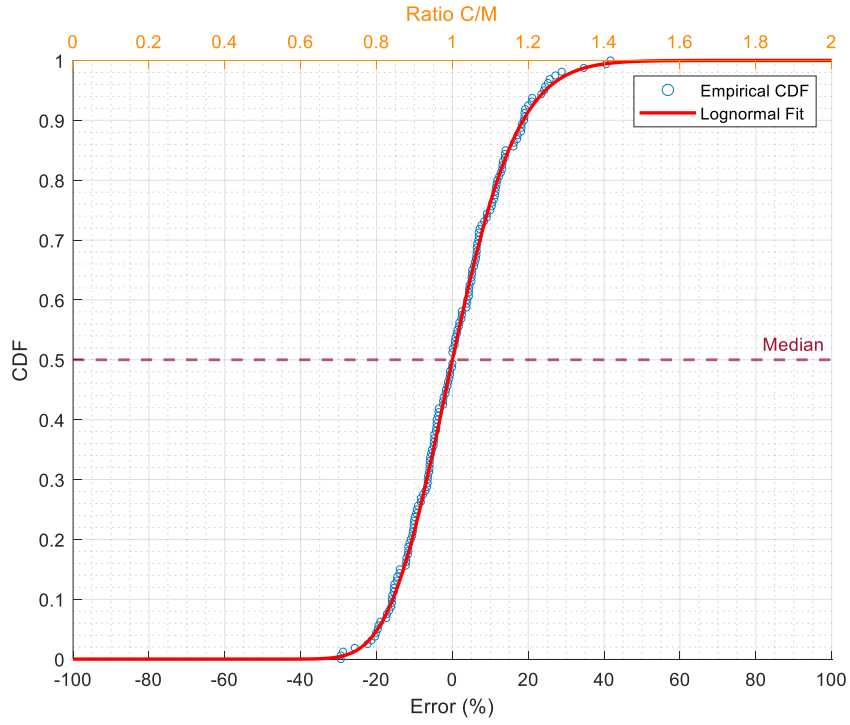

Figure 6.22. Histogram and CDF of GVW Errors by Area Method (Strain Rosette).

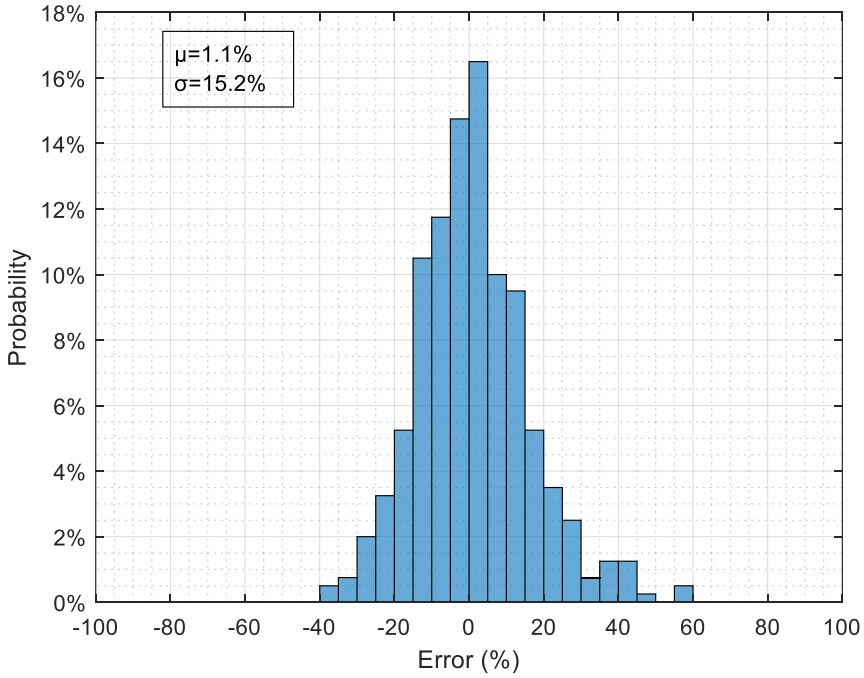

Figure 6.23. Errors of GVW by Area Method (LVDTs).

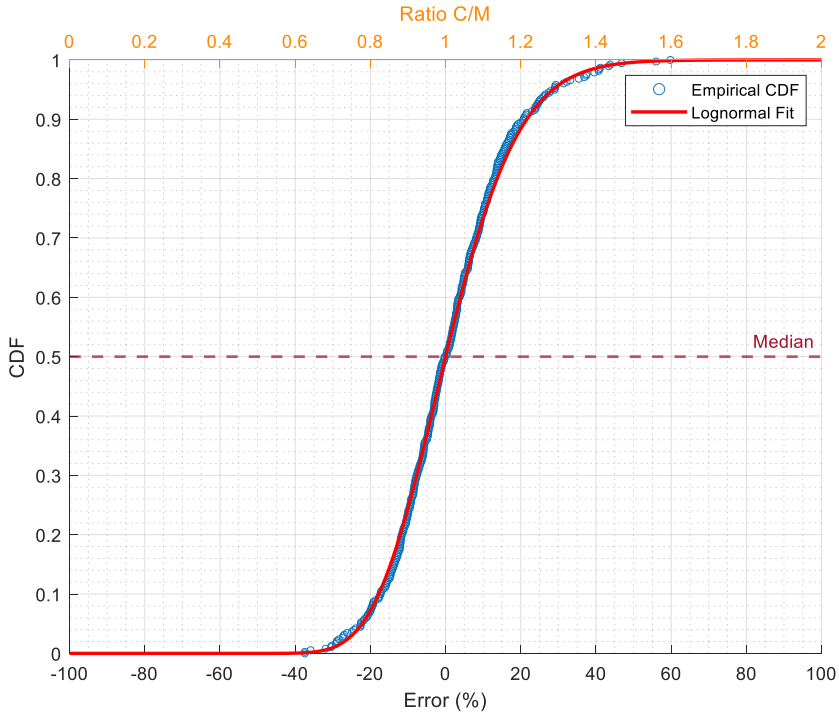

Figure 6.24. Histogram and CDF of GVW Errors by Area Method (LVDTs).

6.3.1.5. Axle Weight Results

Individual axle weights are calculated by utilizing the axle detection strain gauges. This method cannot be used for low-speed (i.e., < 15 mph) tests, so Test 1 to Test 6 are excluded. The average accuracy of the individual axle weights is 90.0 percent. Figure 6.25 shows the histogram of individual axle weights error.

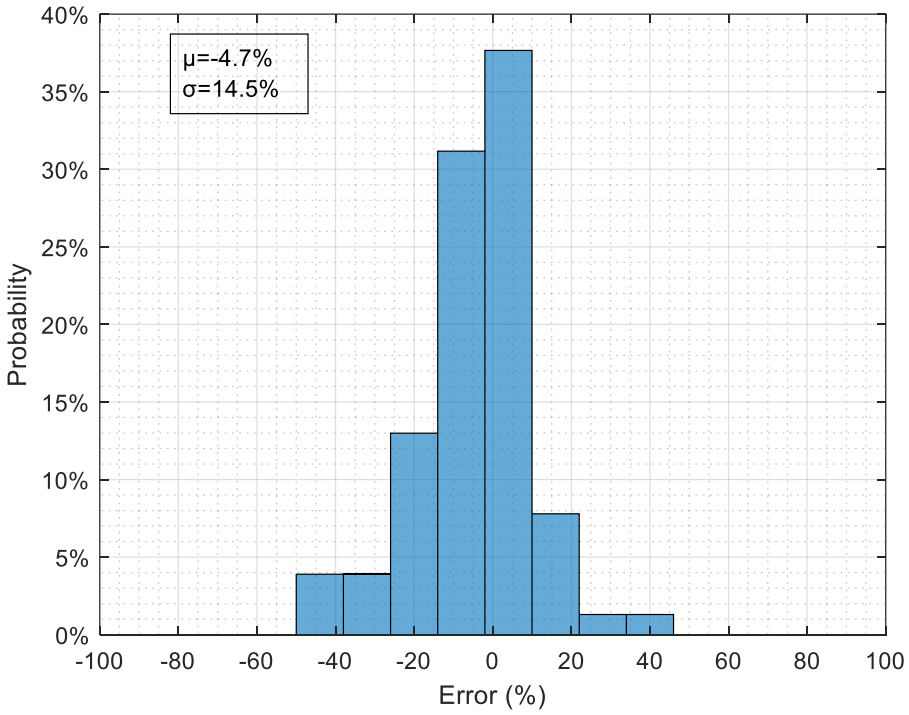

Figure 6.25. Errors of Individual Axle Weight Calculation (Bridge #1 Calibration Test).

Axle group weights are calculated by the strain rosette (shear) for outside lane trucks only. This method uses the influence line of the shear force for a simply supported bridge. The axle weights can be calculated using the influence line. The GVW can then be calculated by summing the axle weights.

Shear data from the 10 calibration tests with trucks passing the outside lane were utilized for axle group weight calculations. It was found that the average accuracy of the axle group weight is 93.6 percent, and the average accuracy of the GVW is 95.6 percent. Table 6.5 summarizes the results of the axle group weight calculations.

Table 6.5. Axle Group Weight Calculation Summary (Strain Rosette).

Test Number	Front Axle (kips)	Error	1st Tandem (kips)	Error	2nd Tandem (kips)	Error	GVW	Error
4	14.4	−1.4%	34.1	1.3%	32.3	0.9%	80.9	0.8%
5	15.0	2.7%	32.4	−3.7%	31.9	−0.3%	79.3	−1.2%
6	15.0	2.7%	31.9	−5.2%	31.6	−1.3%	78.5	−2.2%
14	15.3	4.8%	36.2	7.6%	34.9	9.1%	86.3	7.5%
15	13.6	−6.8%	31.4	−6.7%	34.2	6.9%	79.1	−1.4%
16	14.6	0.0%	33.7	0.1%	33.6	5.0%	81.9	2.1%
17	10.8	−8.5%	31.2	−14.2%	33.7	6.8%	75.7	−5.0%
18	12.9	9.3%	37.6	3.4%	41.3	30.9%	91.8	15.2%
19	11.4	−3.4%	35.6	−2.1%	37.4	18.5%	84.4	5.9%
20	11.9	0.8%	33.3	−8.4%	37.0	17.3%	82.1	3.0%

6.3.1.6. Vehicle (Truck) Classification Results

According to the LTPP rules in Table 6.1, the five-axle Truck A fits in the "Class 9, Semi 3S2" category based on the axle spacing. However, when the axle was released, the six-axle Truck B could not be categorized since the axle spacing between axle 3 and axle 4, and the axle spacing between axle 4 and axle 5 was out of range based on the LTPP rule. According to the FHWA vehicle classification category, Truck B met the description of "single trailer 6 or more axles." Therefore, it was categorized as truck Class 10.

6.3.2. Bridge #2

6.3.2.1. Introduction

The results from eight calibration tests for the Bridge #2 B-WIM system were processed and summarized in this section, including lane detection, axle number, axle spacing, speed, GVW, and vehicle classification. The results obtained from the calibration tests were then compared with the measured results of the calibration truck.

6.3.2.2. Lane Detection Results

Since this bridge has five beams, the left and right lane response comparison was based on Beam #1 to Beam #3 and Beam #3 to Beam #5, respectively. For the eight calibration tests, the B-WIM system was able to detect the truck passing lanes with an accuracy of 100 percent.

6.3.2.3. Axle Information Results

The vertical gauge of the strain rosettes installed near the south and north end supports was utilized for axle detection. The vertical gauges at the south end were able to accurately capture axle numbers from Test #1 to Test #6 but only detected four axles in Test #7 and Test #8, which resulted in an accuracy of 75.0 percent. The vertical gauges at the north end only got three tests' axle numbers correctly, resulting in an accuracy of 37.5 percent. The reason for this reduction in accuracy is due to the fact that the truck was traveling along the span before it reached the north-end vertical gauge. The peak in response is less pronounced for the exit end compared to the entry end.

Both the south and north end vertical gauges were able to capture the peak of the front axle of each truck, which was used to calculate truck speeds and had an average accuracy of 98.0 percent. Axle spacings were then calculated based on the detected speed. Compared with the tape measured values, the average accuracy was 91.5 percent. Since Test #7 and Test #8 only detected four axles instead of five axles, the axle spacing between the last two axles was treated as zero, which significantly reduced the average accuracy of axle spacing calculation. If those two tests were not counted in the axle spacing comparison, the average accuracy would be 97.7 percent. Therefore, two strain gauges were installed underneath the bridge deck after the calibration tests for better axle detection.

Since the bearing pads on Bridge #2 were much newer compared with Bridge #1, the LVDTs provided better axle detection results. The accuracy of the axle number detection was 87.5 percent due to the inaccurate axle number detection in Test #7. The average accuracy of axle spacing detection was 93.1 percent.

Axle information detection accuracies of the strain rosette (vertical strain) and LVDTs are summarized in Table 6.6.

Table 6.6. Accuracy of Axle Information Detection Summary (Bridge #2).

Sensor Type	Axle Number Accuracy	Speed Accuracy	Axle Spacing Accuracy
Strain Rosette	75.0%	98.0%	91.5%
LVDT	87.5%	N/A	93.1%

6.3.2.4. GVW Calculation Results

Each single truck test was used to calculate the truck GVWs of the remaining tests. The errors of the calculated GVW from the midspan strain gauges are shown in Figure 6.26. The mean value of the errors is 0.8 percent, with a standard deviation of 12.9 percent. Figure 6.27 shows the histogram with a CDF of the errors. The average GVW accuracy from midspan strain gauges is 90.3 percent.

The histogram of errors of the calculated GVW from the strain rosette is shown in Figure 6.28. The mean value of the errors is 5.8 percent, with a standard deviation of 36.2 percent. Figure 6.29 shows the CDF of the errors. The average of GVW accuracy from strain rosette is 73.2 percent.

The histogram of errors of the calculated GVW from LVDTs is shown in Figure 6.30. The mean value of the errors is 0.1 percent, with a standard deviation of 4.4 percent. Figure 6.31 shows the CDF of the errors. The average GVW accuracy from LVDTs is 96.8 percent.

The GVW calculation accuracies of the midspan strain gauges, strain rosette, and LVDTs in comparison to the manual static scale measurements are summarized in Table 6.7.

Table 6.7. Accuracy of GVW Calculation Summary (Bridge #2).

Sensor Type	Accuracy
Strain Gauge (Midspan)	90.3%
Strain Rosette	73.2%
LVDT	96.8%

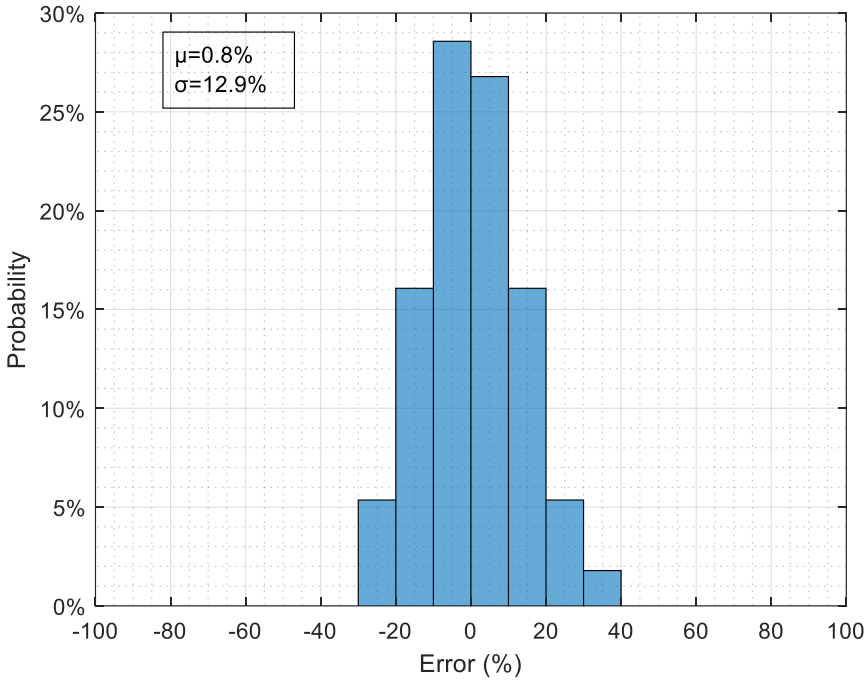

Figure 6.26. Errors of GVW by Area Method (Midspan Strain Gauges).

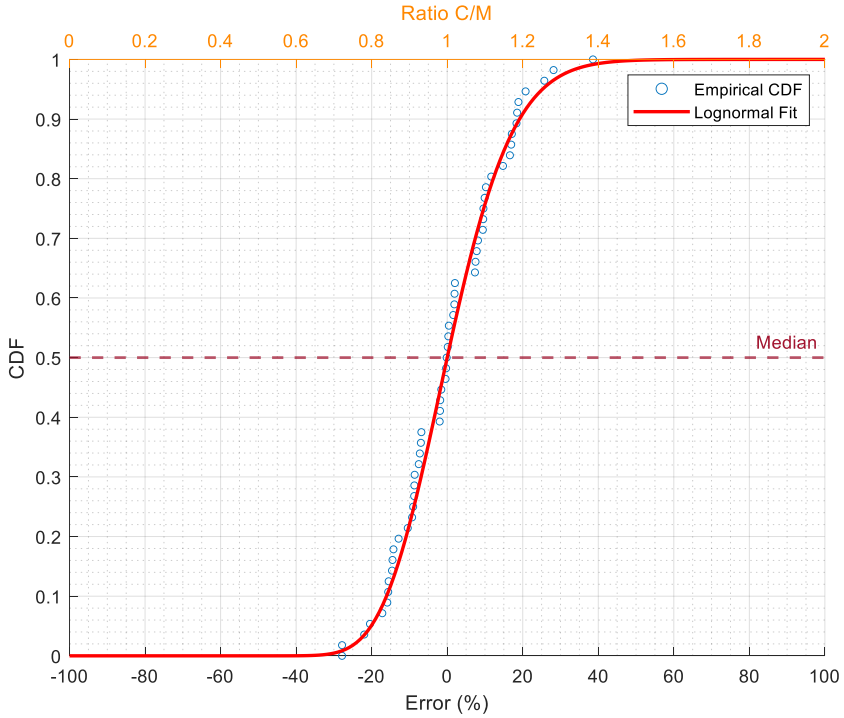

Figure 6.27. CDF of GVW Errors by Area Method (Midspan Strain Gauges).

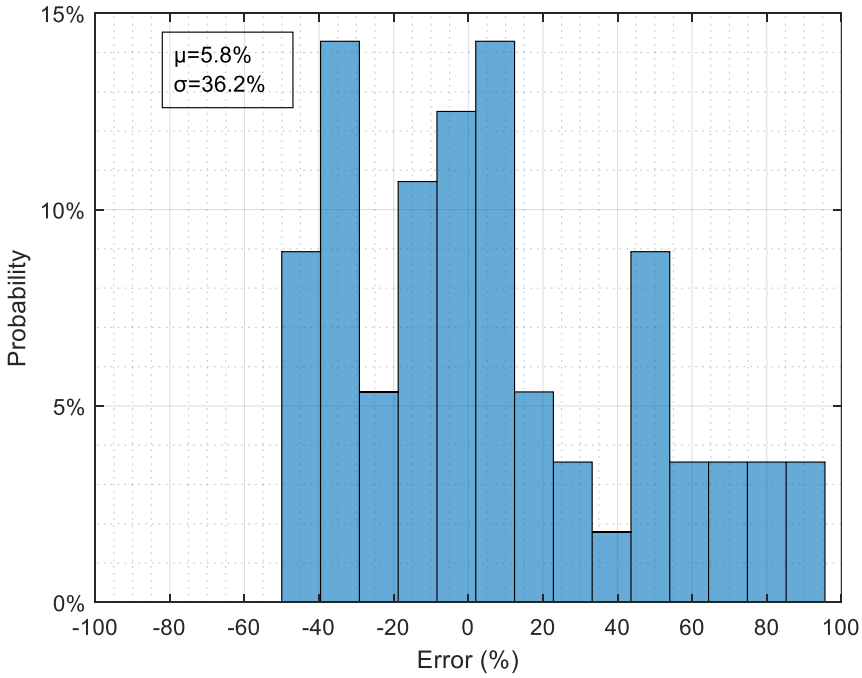

Figure 6.28. Histogram of GVW Errors by Area Method (Strain Rosette).

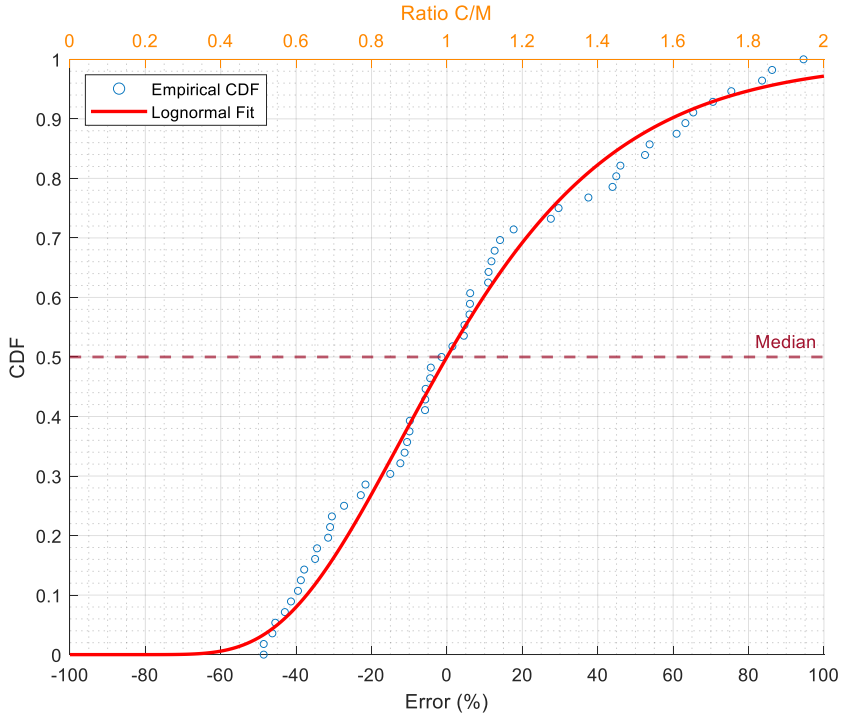

Figure 6.29. CDF of GVW Errors by Area Method (Strain Rosette).

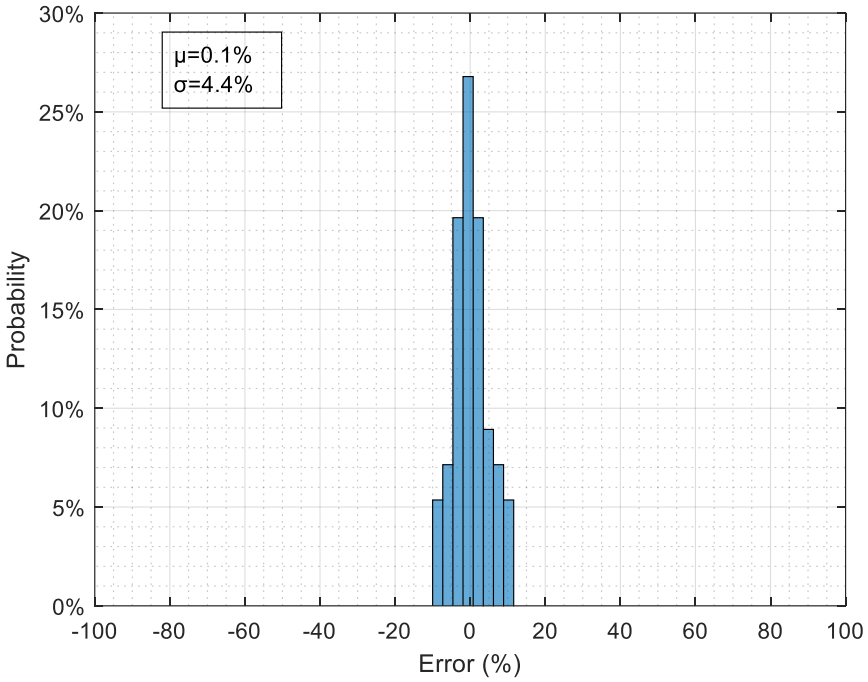

Figure 6.30. Histogram of GVW Errors by Area Method (LVDT).

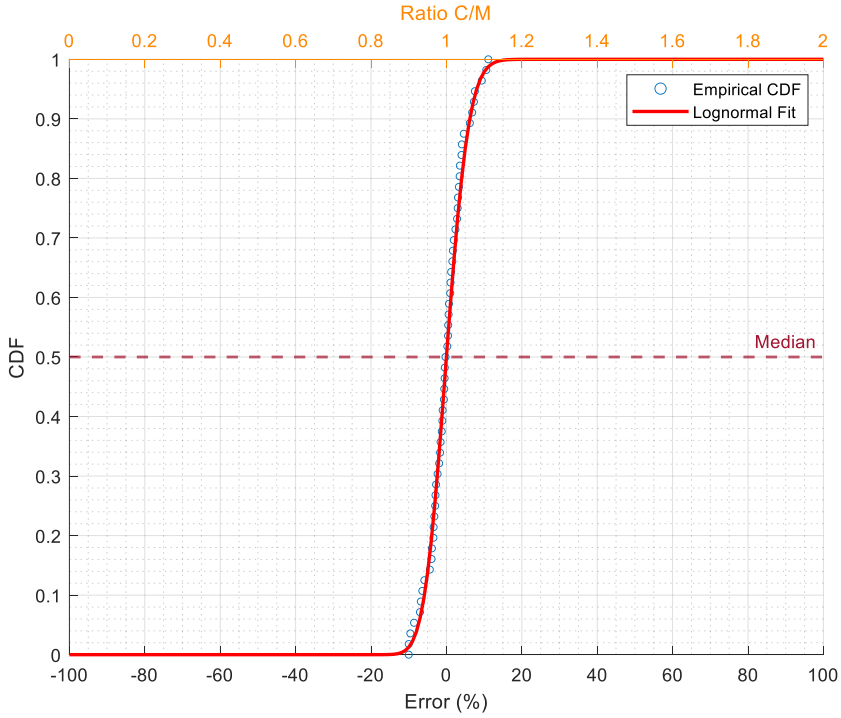

Figure 6.31. CDF of GVW Errors by Area Method (LVDT).

6.3.2.5. Vehicle (Truck) Classification Results

According to the LTPP rules in Table 6.1, the five-axle calibration truck fits in the "Class 9, Semi 3S2" category based on the axle spacing.

6.3.3. Bridge #3

6.3.3.1. Introduction

The results from the 15 calibration tests for the Bridge #3 B-WIM system were processed and summarized in this section, including lane detection, axle number, axle spacing, speed, GVW, and vehicle classification. The results obtained from the calibration tests were then compared with the measured results of the calibration trucks. Though there are two vertical gauges installed on the beams of the second span, they will be named "South side vertical gauges" for convenience. Test #15 was conducted with two calibration trucks for the exploration of the side-by-side configuration.

6.3.3.2. Lane Detection Results

The B-WIM system was able to detect all the trucks crossing the bridge, which included the multiple truck cases in Test #7 and Test #11. The calibration tests were conducted within normal traffic (i.e., no lane closure). Therefore, other trucks crossed the bridge simultaneously with the calibration trucks. The side-by-side configuration with both calibration trucks (conducted in Test #15) was also detected. For the rest of the calibration tests, the B-WIM system was able to detect the truck passing lanes with an accuracy of 100 percent.

6.3.3.3. Axle Information Results

The vertical gauge of the strain rosettes was installed 3.0 ft from the north end center of the bearing, and the south side vertical gauges were utilized for axle detection. The vertical gauges near the north end were only able to accurately capture axle numbers for those tests when the calibration trucks passed the bridge on the outside lane, which resulted in an overall accuracy of 46.7 percent (100 percent for outside lane tests). The vertical gauges at the south end had much better accuracy than the north end; the south side vertical gauges were able to capture truck axle numbers on both lanes with an accuracy of 92.8 percent.

The strain gauges installed underneath the bridge deck were able to capture accurate axle numbers for the calibration truck travelling through both lanes. The average accuracy for axle number detection from the strain gauges underneath the bridge deck was 100 percent.

There are several methods to calculate the speed of the truck since multiple axle detection sensors were installed. The first combination was to use the north and south side vertical gauges. The second combination was to use the north side vertical gauges and the strain gauges underneath the bridge deck (i.e., deck gauges). The third combination was to use the deck gauges and the south side vertical gauges. Since the axle number detection results were inaccurate on the inside lane tests for the north side vertical gauges, the truck speeds were calculated for outside lane tests only for the combinations with north side vertical gauges. The accuracies of the speed detection for the three combinations are summarized in Table 6.8. In a future implementation, this

would be identified during the calibration process, and refinements would be made to the instrumentation prior to finalizing the B-WIM system.

Table 6.8. Speed Detection Accuracy (Bridge #3).

Sensor Combination	Accuracy
North and South Vertical Gauge	97.6% (Outside lane only)
North Vertical Gauge and Deck Gauge	85.5% (Outside lane only)
Deck Gauge and South Vertical Gauge	97.8% (Both lanes)

The axle spacings were then calculated with speed obtained from the deck gauges and vertical gauges. Compared with the tape measured values, the accuracies are shown in Table 6.9.

Table 6.9. Axle Spacing Accuracy (Bridge #3).

Sensor Type	Accuracy
North Vertical Gauge	84.8% (Outside lane only)
Deck Gauge	96.0%
South Vertical Gauge	87.2%

6.3.3.4. GVW Calculation Results

Test results were utilized for comparison with the measured weights for the trucks. Each single-truck test was used to calculate the truck GVWs of the remaining tests. The histogram of errors of the calculated GVW from the midspan strain gauges is shown in Figure 6.32. The mean value of the errors is 6.3 percent, with a standard deviation of

19.2 percent. Figure 6.33 shows the CDF of the errors. The average GVW accuracy from midspan strain gauges is 86.0 percent.

The histogram of calculated GVW errors from the strain rosette is shown in Figure 6.34. The mean value of the errors is −1.2 percent, with a standard deviation of 25.5 percent. Figure 6.35 shows the CDF of the errors. The average of the GVW accuracy from strain rosette is 78.8 percent.

The GVW calculation accuracies of the midspan strain gauges and strain rosette in comparison to the manual static scale measurements are summarized in Table 6.7.

Table 6.10. Accuracy of GVW Calculation Summary (Bridge #3).

Sensor Type	Accuracy
Strain Gauge (Midspan)	86.0%
Strain Rosette	78.8%

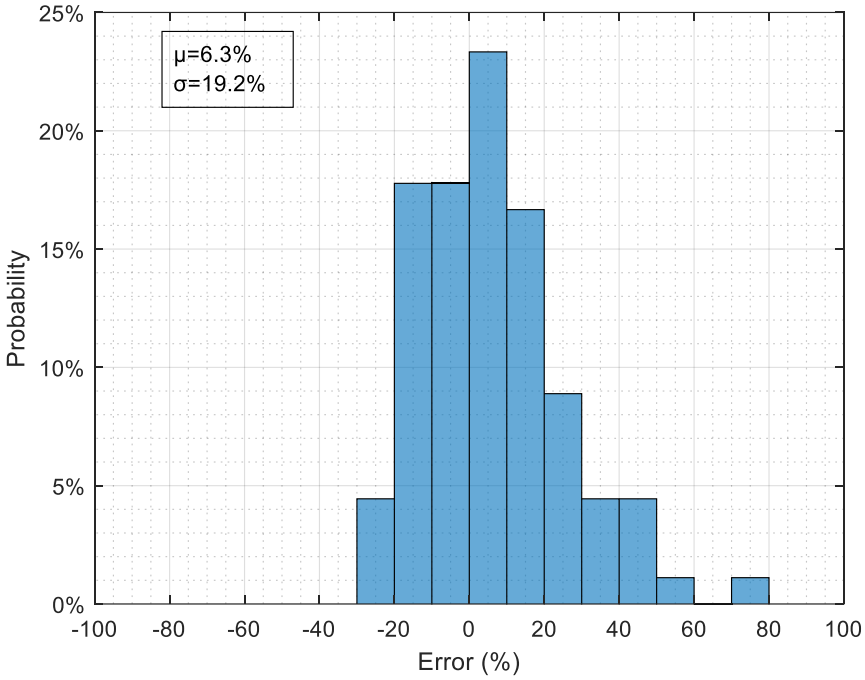

Figure 6.32. Histogram of GVW Errors by Area Method (Midspan Strain Gauges).

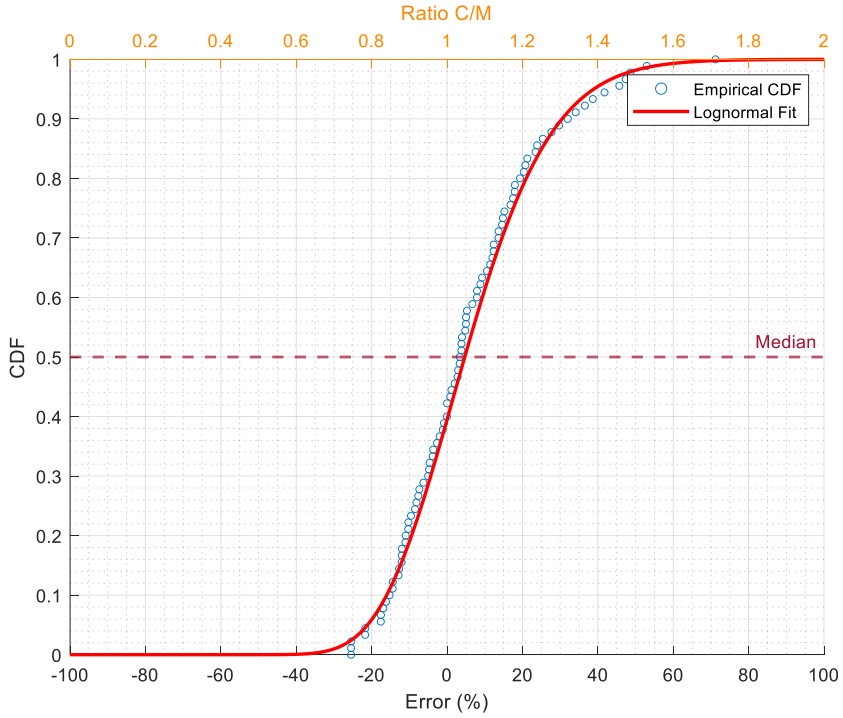

Figure 6.33. CDF of GVW Errors by Area Method (Midspan Strain Gauges).

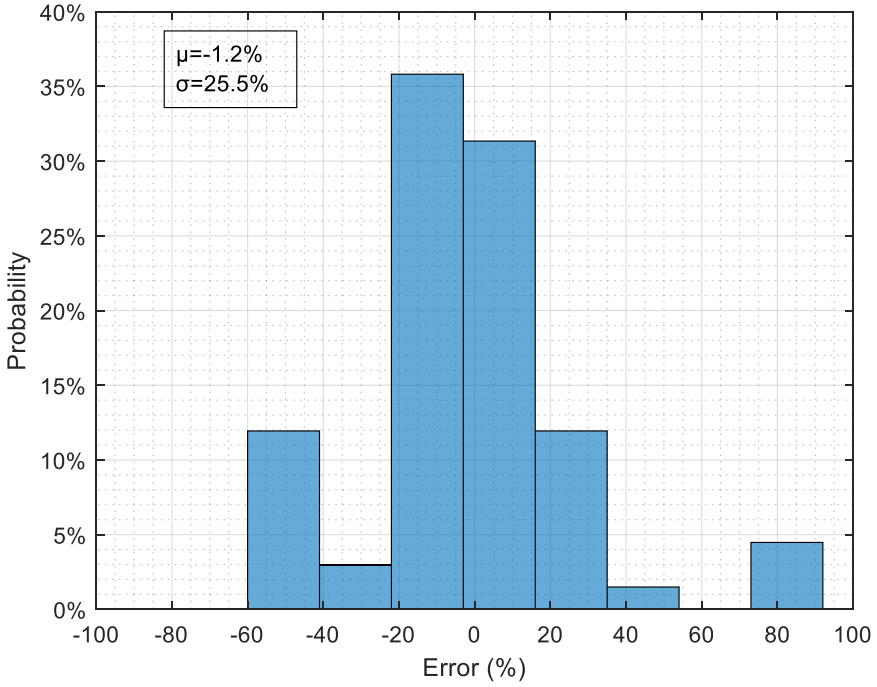

Figure 6.34. Histogram of GVW Errors by Area Method (Strain Rosette).

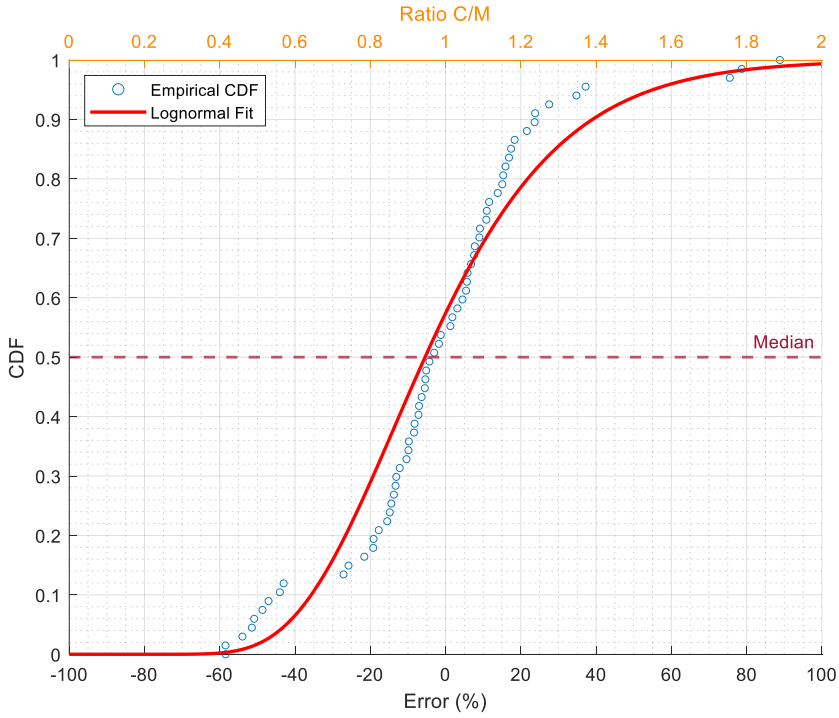

Figure 6.35. CDF of GVW Errors by Area Method (Strain Rosette).

6.3.3.5. Side-by-Side Configuration Exploration

One side-by-side configuration was conducted during the calibration test. Truck A traveled on the inside lane while Truck B travelled on the outside lane and passed the bridge at the same time. The midspan distribution factors were calculated and summarized in Table 6.11. This includes the cases when: (a) one truck passes the outside lane while nothing is on the inside lane (*DFO*), (b) one truck passes the inside lane while nothing is on the outside lane (*DFI*), and (c) the side-by-side case (*DF*).

The gross weight of the combination of the two trucks was calculated by the area method as 130.3 kips. The calculated weight for each truck was determined by using the constructed equations, Eq. (6.4) and Eq. (6.5), of each beam; the average accuracies after comparing with the manually measured weights are shown in Table 6.12. It was found that using the constructed equation from Beam #5 gave the most accurate results. It was decided to use Beam #5 for solving the side-by-side case of Bridge #3 when analyzing the live load data.

Table 6.11. Midspan Distribution Factors Summary.

Configuration	Distribution Factor (%)					
	Beam 1	**Beam 2**	**Beam 3**	**Beam 4**	**Beam 5**	**Beam 6**
DFO	4.3%	10.3%	18.3%	26.9%	22.5%	17.8%
DFI	21.5%	23.3%	23.9%	19.2%	9.0%	3.1%
DF	11.0%	14.7%	19.9%	23.9%	17.5%	13.2%

Table 6.12. GVW Calculation of Each Truck and Accuracy.

Truck	GVW (kips)					
	Beam 1	**Beam 2**	**Beam 3**	**Beam 4**	**Beam 5**	**Beam 6**
A	50.7	43.6	36.2	51.4	48.4	40.7
B	79.6	86.7	94.1	80.0	81.9	89.7
Average Accuracy	95.2%	93.4%	81.2%	94.1%	98.5%	88.5%

6.3.3.6. Vehicle (Truck) Classification Results

According to the LTPP rules in Table 6.1, the three-axle calibration of Truck A fits in the "Class 6, 3-Axle Single Unit" category based on the axle spacing. The six-axle calibration of Truck B fits in the "Class 10, Semi, 3S3" category based on the axle spacing.

6.4. Live Load Data Analysis

6.4.1. Introduction

After the calibration tests, the B-WIM systems recorded data using a specified trigger threshold to capture trucks with weights greater than 20.0 kips. The live load data of each bridge were collected and processed to determine information for each truck crossing the bridge. Several two-hour datasets were selected to show the performance of the B-WIM systems.

6.4.2. Bridge #1 Live Load Data Analysis

A total of 1,200 truck counts from different dates and times were utilized for live load analysis of Bridge #1, as summarized in Table 6.13. There were 374 truck counts on the inside lane and 826 counts on the outside lane.

Table 6.13. B-WIM Data Summary for Bridge Evaluation (Bridge #1).

Date	Time Range	Number of Truck Passing Events (≥ 20 kips)	Number of Truck Passing Event/Hour
3-11-2021 Thursday	11:02 a.m. to 2:17 p.m.	434	144
3-16-2021 Tuesday	1:11 p.m.to 3:11 p.m.	284	142
3-18-2021 Thursday	4:00 a.m.to 6:00 a.m.	139	69
3-19-2021 Friday	8:00 p.m.to 10:00 p.m.	77	38
3-20-2021 Saturday	9:02 a.m.to 11:02 a.m.	146	73
3-21-2021 Sunday	4:00 p.m.to 6:00 p.m.	85	42
4-10-2021 Saturday	6:02 p.m.to 8:02 p.m.	35	17

The average α value (calculated in Eq. (3.7)) from the calibration tests was 17.51. This value was used with the area method to calculate the GVWs. The average midspan distributions were calculated. From Beam #1 to Beam #6, the *DFI* of the inside lane was 27.8 percent, 29.8 percent, 21.5 percent, 15.4 percent, 5.4 percent, and 0.6 percent, respectively. The *DFO* of the outside lane was 2.2 percent, 7.8 percent, 15.9 percent, 35.5 percent, 25.9 percent, and 13.5 percent, respectively. Although there were no side-

by-side calibration tests conducted, the results from the single truck calibration tests were used with the equations presented earlier (using Beam #2) to evaluate the side-by-side configurations.

The majority of the trucks that passed in the selected dataset were Class 9 (about 72.0 percent), as shown in Figure 6.36, which is typical for most Texas highways (Prakoso 2022; Walubita et al. 2021; Zhang et al. 2022). The GVW of each truck was calculated based on the area method. The distribution of GVW is shown in Figure 6.37. The distribution of the truck average speed is shown in Figure 6.38. The individual axle weight of each truck was calculated using the strain gauges installed underneath the bridge deck. Figure 6.39a and Figure 6.39b show the distribution of the single axle weight and tandem axle weight, respectively. The tridem and quad axle weights were also calculated; due to the small sample size, the distributions are not plotted.

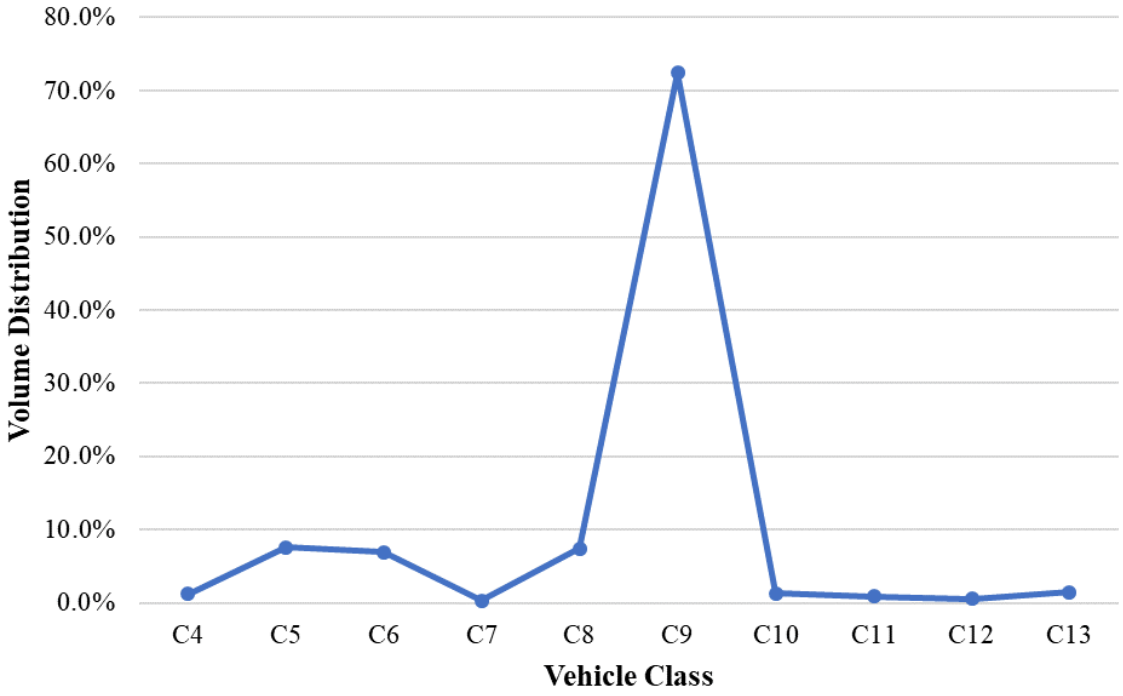

Figure 6.36. Vehicle (Truck) Classification Distribution (Bridge #1).

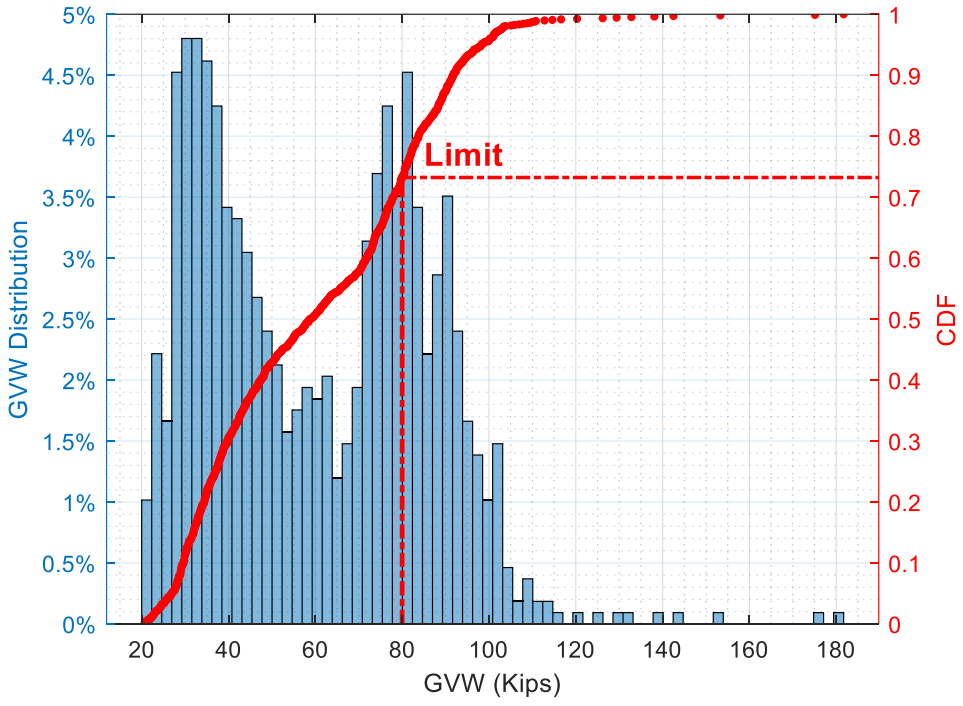

Figure 6.37. Vehicle (Truck) GVW Distribution (Bridge #1).

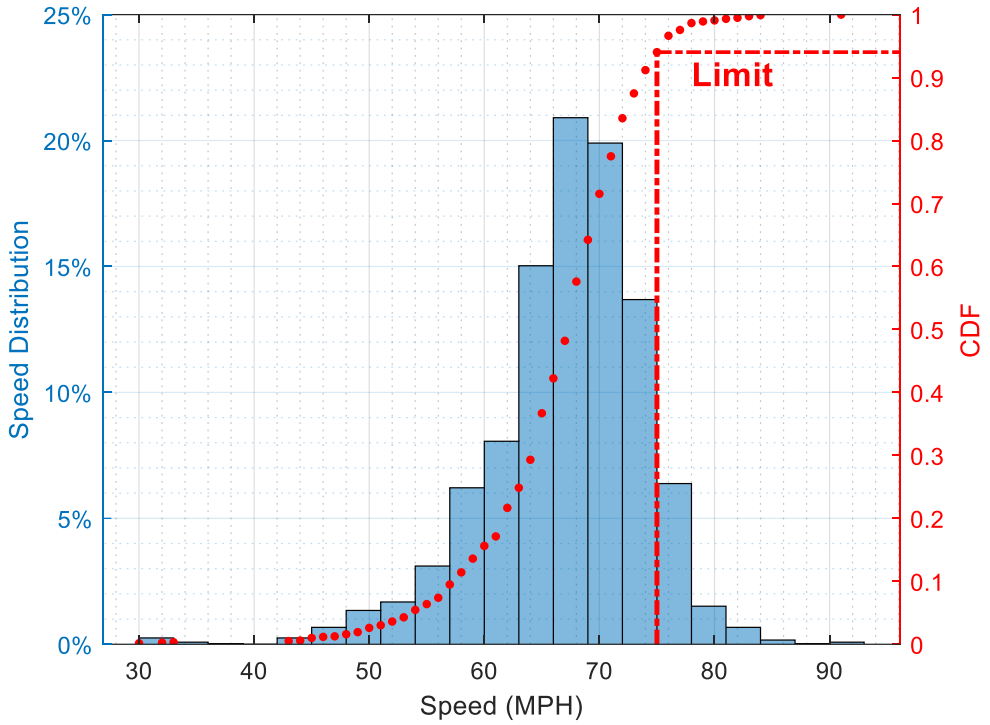

Figure 6.38. Truck Speed Distribution (Bridge #1).

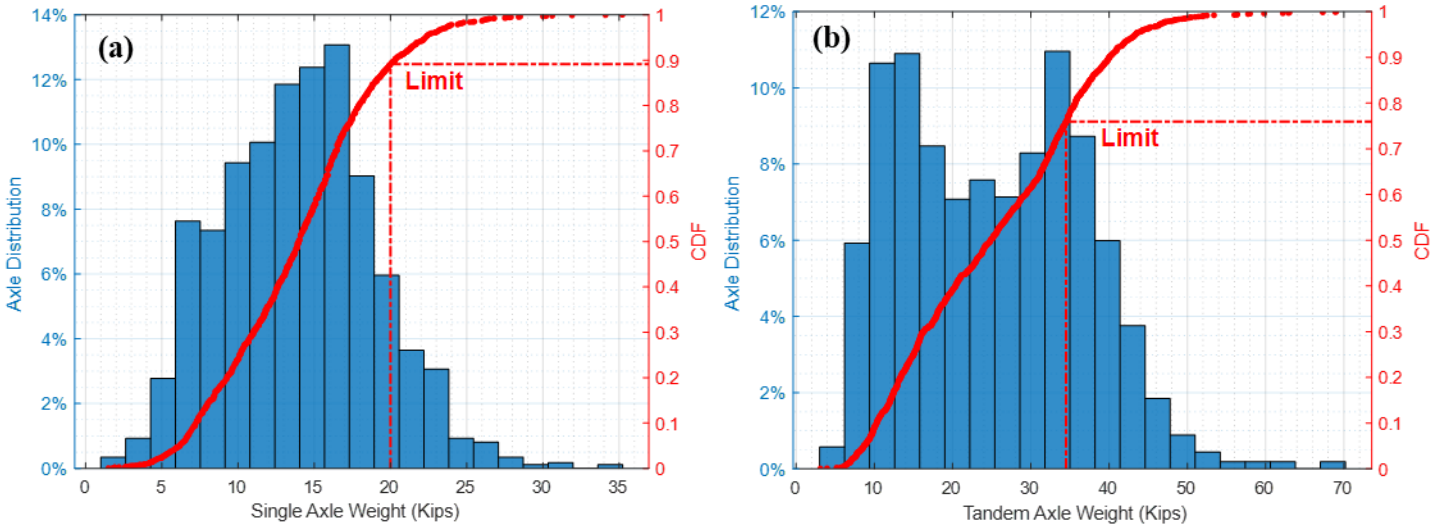

Figure 6.39. Truck Single and Tandem Axle Weight Distributions (Bridge #1).

The GVW distribution had a mean of 60.3 kips with a standard deviation of 26.5 kips. A bimodal relationship, as shown in Figure 6.37, was observed for the GVW distributions. The bimodal distributions are indicative of the dominance of two specific truck load groups—35 and 80 kips for Bridge #1. A significant number of trucks were over the maximum truck GVW limit of 80 kips on both lanes (approximately 26 percent). The data shown are only for trucks, which are defined as vehicles with a weight greater than 20 kips.

The single axle weight distribution had a mean of 13.9 kips and a standard deviation of 5.0 kips. Most of the single axle weights were within the limit of 20 kips. A few trucks had the single axle overloaded (about 10 percent). The tandem axle weight distribution had a mean of 25.2 kips and a standard deviation of 11.6 kips. There were 24 percent of the tandem axles that were over the weight limit (i.e., 34 kips). The tridem axle weight distribution had a mean of 46.0 kips and a standard deviation of 17.0 kips. Among the tridem axles, 43.7 percent were over the weight limit of 42 kips. The B-WIM system detected a total of seven quad axles in the dataset, with a mean of 46.3 kips and a standard deviation of 16.4 kips. Three of them were over the weight limit of 50 kips, which made the rate 42.8 percent of quad axles. Although not exactly on the same locational spot as the B-WIM, similar weight statistics were also recorded with the portable WIM measurements.

Table 6.14 summarizes the mean and standard deviation of the GVW, truck speed, axle number, wheelbase, and axle weights.

Table 6.14. GVW and Axle Information Summary (Bridge #1).

Truck Information	Mean	Standard Deviation	Legal Limits
GVW (kips)	60.3	26.5	80 kips
Speed (mph)	66.7	6.8	75 mph
Number of Axles	4.6	1.0	N/A
Wheelbase (ft)	51.2	15.3	N/A
Single Axle Weight (kips)	13.9	5.0	20 kips
Tandem Axle Weight (kips)	25.2	11.6	34 kips
Tridem Axle Weight (kips)	46.0	17.0	42 kips
Quad Axle Weight (kips)	46.3	16.4	50 kips

6.4.3. Bridge #2 Live Load Data Analysis

A total of 650 truck counts from different dates and times were utilized for the live load analysis of Bridge #2, as summarized in Table 6.15. There were 96 truck counts on the inside lane and 554 counts on the outside lane.

Table 6.15. B-WIM Data Summary for Bridge Evaluation (Bridge #2).

Date	Time Range	Number of Truck Passing Events (≥ 20 kips)	Number of Truck Passing Event/Hour
7-19-2021 Monday	6:00 a.m. to 8:00 a.m.	143	71
8-6-2021 Friday	1:18 p.m.to 3:18 p.m.	182	91
9-1-2021 Wednesday	7:00 a.m.to 9:00 a.m.	166	83
9-2-2021 Thursday	2:00 p.m.to 4:00 p.m.	159	79

The average α value from the calibration tests was 33.29. This value was used with the area method to calculate the GVWs. The average midspan distributions were calculated. From Beam #1 to Beam #5, the *DFI* of the inside lane was 28.8 percent, 47.4 percent, 15.5 percent, 6.7 percent, and 1.6 percent, respectively. The *DFO* of the outside lane was 4.3 percent, 17.2 percent, 26.5 percent, 40.6 percent, and 11.5 percent, respectively. Although there were no side-by-side calibration tests conducted, the results from the single truck calibration tests were used with the equations presented earlier (using Beam #4) to evaluate the side-by-side configurations.

As is typical of most Texas highways, the majority of the trucks that passed in the selected dataset were Class 9 (i.e., about 77.0 percent), as shown in Figure 6.40. The GVW of each truck was calculated based on the area method. The distribution of GVW is shown in Figure 6.41. The distribution of truck speed is shown in Figure 6.42. The individual axle weight of each truck was calculated using the strain gauges installed underneath the bridge deck. Figure 6.43a and Figure 6.43b show the distribution of the single axle weight and tandem axle weight, respectively.

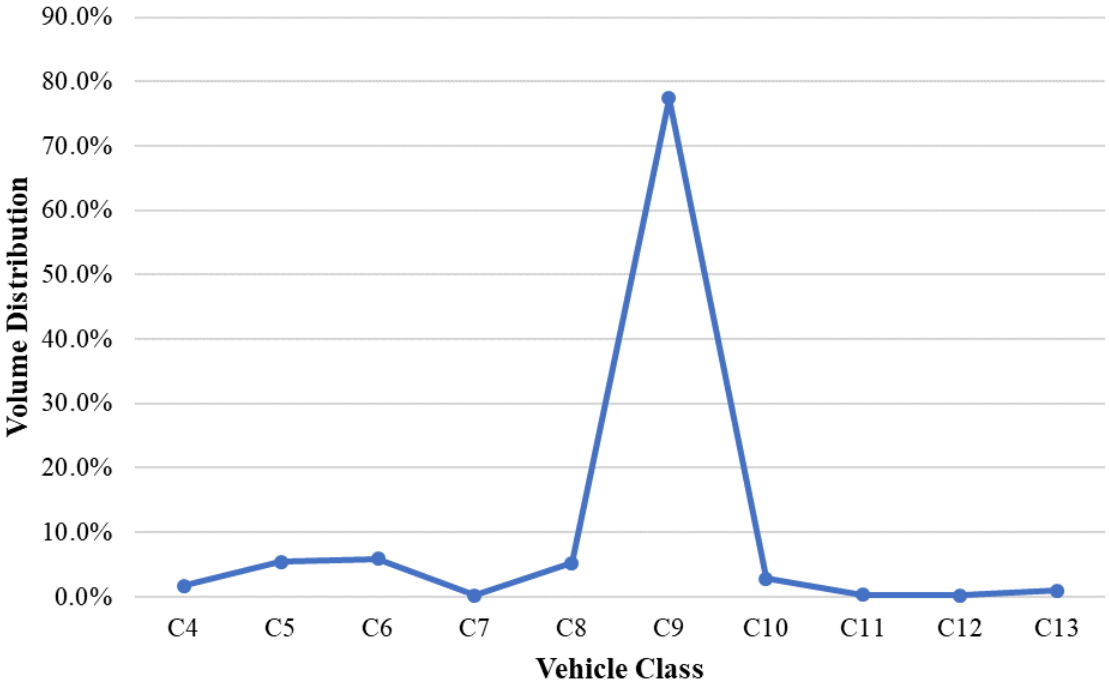

Figure 6.40. Truck Classification Distribution (Bridge #2).

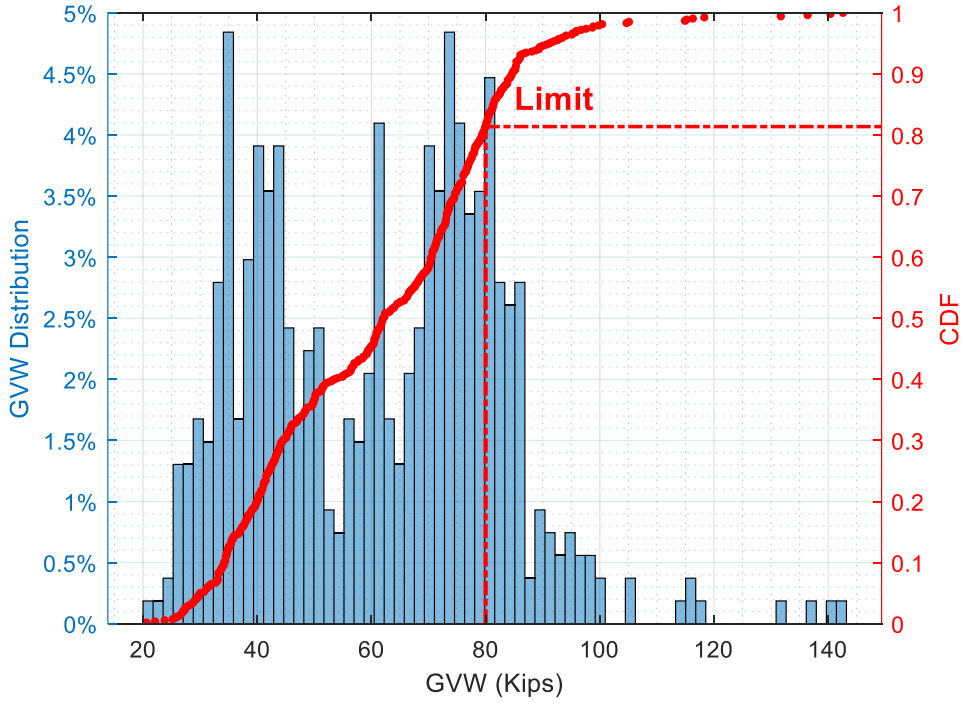

Figure 6.41. Truck GVW Distribution (Bridge #2).

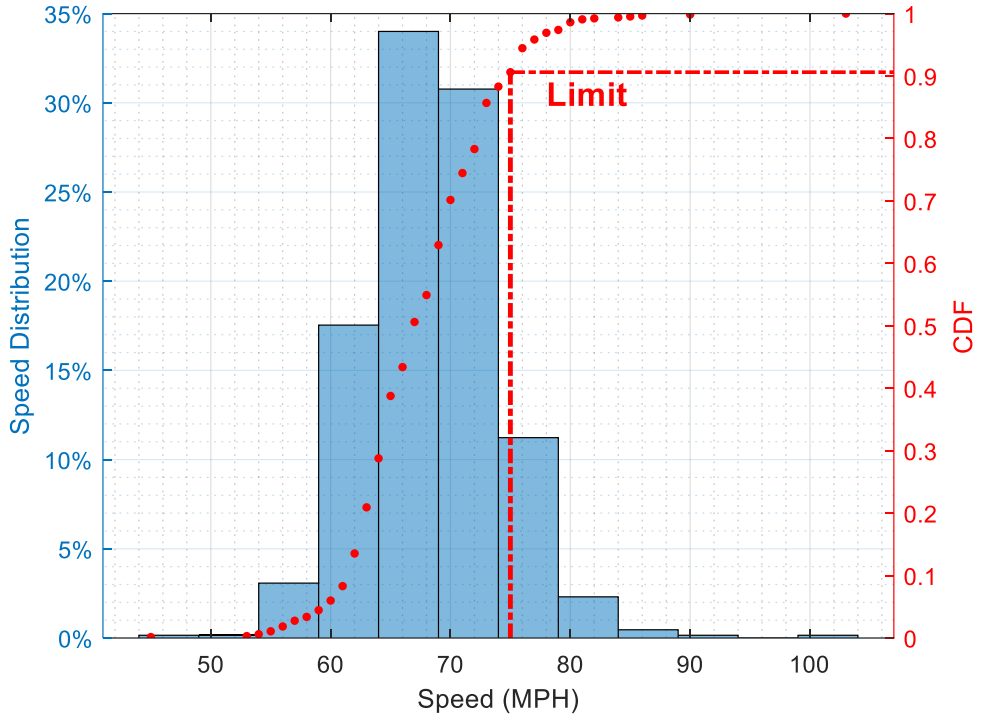

Figure 6.42. Truck Speed Distribution (Bridge #2).

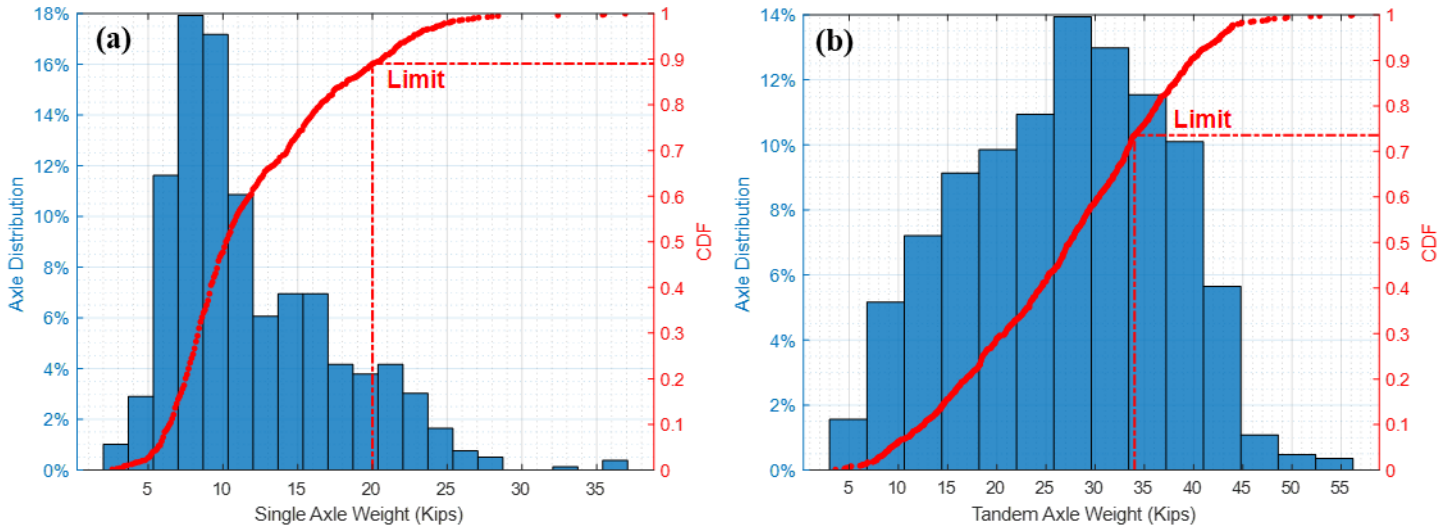

Figure 6.43. Truck Single and Tandem Axle Weight Distributions (Bridge #2).

The GVW distribution had a mean of 61.1 kips with a standard deviation of 21.1 kips. The distribution also shows a bimodal relationship. The bimodal distributions are indicative of the dominance of two specific truck load groups—40 and 75 kips for Bridge #2. About 20 percent of the trucks are over the maximum truck GVW limit of 80 kips on both lanes.

The single axle weight distribution had a mean of 12.0 kips and a standard deviation of 5.5 kips. The majority of the single axle weights were within the limit (i.e., 11.1 percent overweight). The tandem axle weight distribution had a mean of 26.8 kips and a standard deviation of 12.0 kips. There were 26.4 percent of the tandem axles that were over the weight limit. The tridem axle weight distribution had a mean of 31.9 kips and a standard deviation of 19.3 kips. Among the tridem axles, 35.3 percent were over the weight limit. The B-WIM system on Bridge #2 detected a total of five quad axles in the dataset, with a mean of 59.0 kips and a standard deviation of 19.3 kips. Four of these quad axles were over the weight limit. Like Bridge #1, similar weight trends were also reported with the portable WIM measurements.

Table 6.16 summarizes the mean and standard deviation of GVW, truck speed, axle number, wheelbase, and axle weights.

Table 6.16. GVW and Axle Information Summary (Bridge #2).

Truck Information	Mean	Standard Deviation	Legal Limits
GVW (kips)	61.2	21.0	80 kips
Speed (mph)	67.9	5.6	75 mph
Number of Axles	4.7	0.9	N/A
Wheelbase (ft)	53.8	13.8	N/A
Single Axle Weight (kips)	12.0	5.5	20 kips
Tandem Axle Weight (kips)	25.2	10.3	34 kips
Tridem Axle Weight (kips)	31.9	19.3	42 kips
Quad Axle Weight (kips)	59.0	19.3	50 kips

6.4.4. Bridge #3 Live Load Data Analysis

A total of 1,546 truck counts from different dates and times were utilized for live load analysis of Bridge #3, as summarized in Table 6.17. There were 301 truck counts on the left lane and 1,245 counts on the right lane.

Table 6.17. B-WIM Data Summary for Bridge Evaluation (Bridge #3).

Date	Time Range	Number of Truck Passing Events (≥ 20 Kips)	Number of Truck Passing Event/Hour
11-8-2021 Monday	10:39 a.m. to 12:39 p.m.	733	366
11-19-2021 Friday	7:00 p.m. to 9:00 p.m.	294	147
11-24-2021 Wednesday	7:00 a.m. to 9:00 a.m.	519	259

The average α value from the Bridge #3 calibration tests was 17.25. This value was used with the area method to calculate the GVWs. Based on the side-by-side calibration test result, Beam #5 was used for evaluating side-by-side configurations.

Like the previous bridges and as typical of Texas highways, most of the trucks that passed during the two-hour window were Class 9 (i.e., about 81.0 percent), as shown in Figure 6.44. The GVW of each truck was calculated based on the area method. The distribution of the GVW is shown in Figure 6.45. The distribution of truck speed is shown in Figure 6.46. Figure 6.47a and Figure 6.47b show the distribution of the single axle weight and tandem axle weight, respectively.

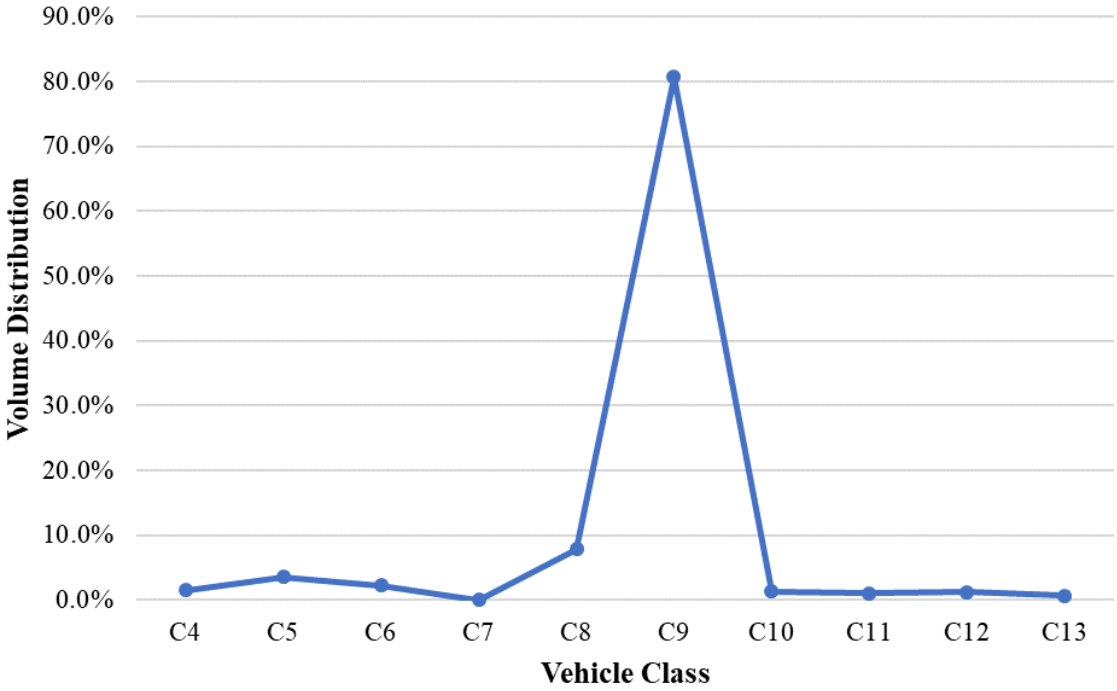

Figure 6.44. Truck Classification Distribution (Bridge #3).

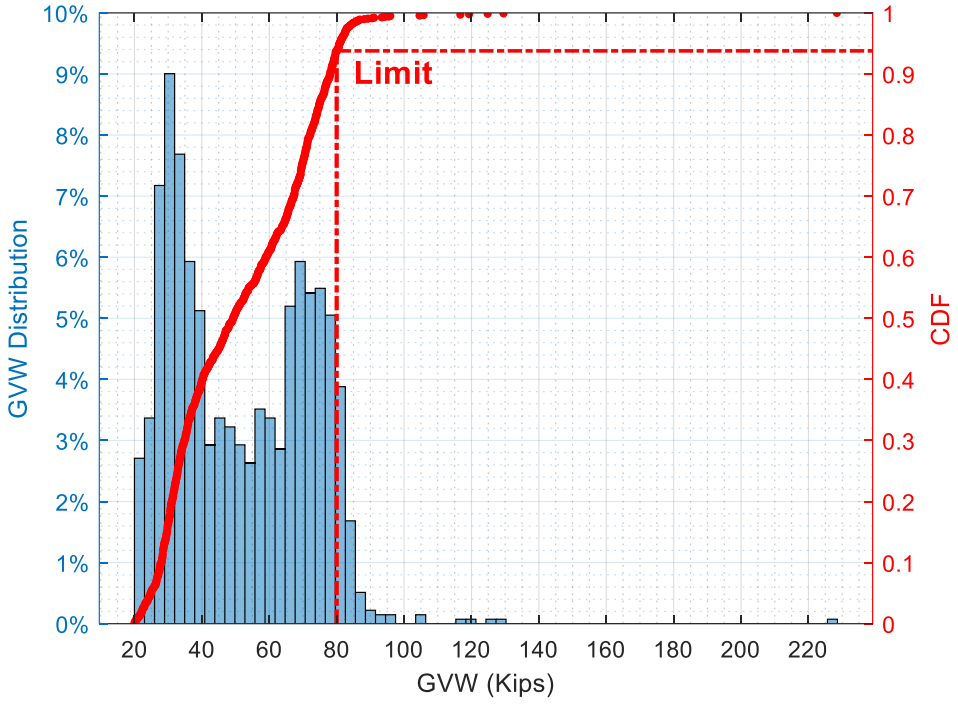

Figure 6.45. Truck GVW Distribution (Bridge #3).

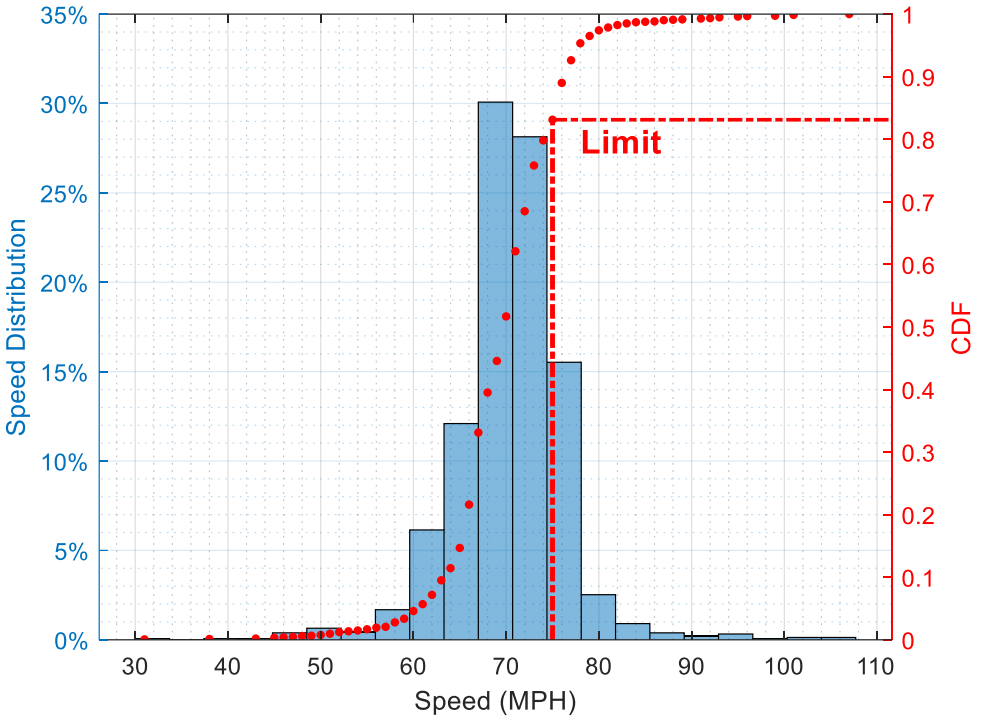

Figure 6.46. Truck Speed Distribution (Bridge #3).

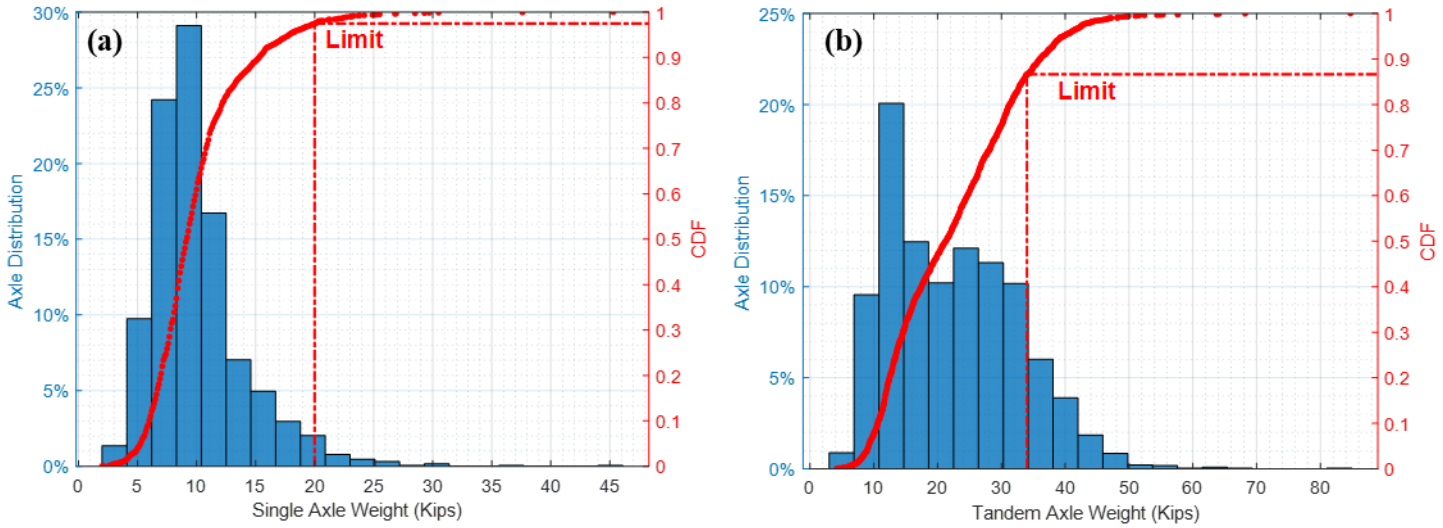

Figure 6.47. Truck Single and Tandem Axle Weight Distributions (Bridge #3).

The GVW distribution had a mean of 53.2 kips with a standard deviation of 22.7 kips. The distribution also shows a bimodal relationship. The bimodal distributions are indicative of the dominance of two specific truck load groups—32 and 70 kips for Bridge #3. About 7 percent of the trucks are over the maximum truck GVW limit of 80 kips on both lanes.

The single axle weight distribution had a mean of 10.0 kips and a standard deviation of 4.0 kips. Only 2.5 percent of the single axles were overweight. The tandem axle weight distribution had a mean of 22.3 kips and a standard deviation of 10.1 kips. There were 13.3 percent of the tandem axles that were over the weight limit. The tridem axle weight distribution had a mean of 37.8 kips and a standard deviation of 16.5 kips. Among the tridem axles, 35.3 percent were over the weight limit. During the time windows of the dataset, there were no trucks with quad axles.

Table 6.18 summarizes the mean and standard deviation of GVW, truck speed, axle number, wheelbase, and axle weights.

Table 6.18. GVW and Axle Information Summary (Bridge #3).

Truck Information	Mean	Standard Deviation	Legal Limits
GVW (kips)	51.6	20.4	80 kips
Speed (mph)	70.1	6.2	75 mph
Number of Axles	4.8	0.8	N/A
Wheelbase (ft)	57.0	12.2	N/A
Single Axle Weight (kips)	10.0	4.0	20 kips
Tandem Axle Weight (kips)	22.3	10.1	34 kips
Tridem Axle Weight (kips)	37.8	16.5	42 kips
Quad Axle Weight (kips)	None measured		50 kips

6.5. B-WIM Validation Study

6.5.1. Introduction

The live load analysis results from the B-WIM systems were compared with the installed p-WIM systems for validation studies. The p-WIM station near Bridge #1 was deployed on both lanes, while the p-WIM near Bridge #2 was only installed in the outside lane. There were no WIM stations nearby for Bridge #3. Therefore, results from both lanes of the Bridge #1 B-WIM system were compared with the p-WIM. Only the outside lane results were compared for Bridge #2. No comparison was made for Bridge #3.

6.5.2. Bridge #1 Validation Study

The two-hour dataset between 1:11 p.m. and 3:11 p.m. on March 16, 2021, was processed from both the B-WIM system and the p-WIM system. The number of passing trucks, truck classification distribution, GVW distribution, and front axle weight were

compared for the validation study. While the p-WIM measures all the vehicle classes, only the truck data (i.e., Class 4 and higher) were extracted and used for comparative analysis with the B-WIM's truck traffic data. As previously mentioned, the B-WIM developed in this study is primarily for truck detection/measurements, namely Class 4 and higher.

Table 6.19 illustrates the number of trucks recorded by the two systems in the two lanes within the two-hour time window. The B-WIM initially captured fewer vehicles since there was a threshold set to only capture trucks rather than cars. After the filter (GVW > 20.0 kips) was applied to both datasets, the number of trucks recorded by the two systems was relatively close. The B-WIM system had a 4.6 percent difference in the number of recorded trucks. The difference might be caused by the GVW calculation errors on both systems near the threshold range (20.0 kips); some of the side-by-side cases might not have been detected in the B-WIM system due to the large weight difference between the two trucks and their lateral positions.

Table 6.19. Comparison of the Number of Trucks (March 16, 2021).

System	Total Two-Hour Truck Count in Two Lanes	
	No Condition	GVW > 20 kips
B-WIM	316	284
p-WIM	345	298

Figure 6.48 shows the GVW distribution comparison between the two systems. The GVW calculated from the midspan strain gauges, average truck speed, number of

axles, and wheelbase obtained from the quarter span strain gauges were compared with the p-WIM. The mean and standard deviation of each result are summarized in Table 6.20. The average GVWs from the B-WIM and p-WIM are 59.2 kips and 57.9 kips, respectively, with a difference of 2.2 percent. The average differences in speed, axle number, and wheelbase are all within 6.0 percent. There is a 22.3 percent difference between the mean of the front axle weight of the two systems. The truck class distribution is shown in Figure 6.49, and the B-WIM has a similar truck class distribution compared with the p-WIM.

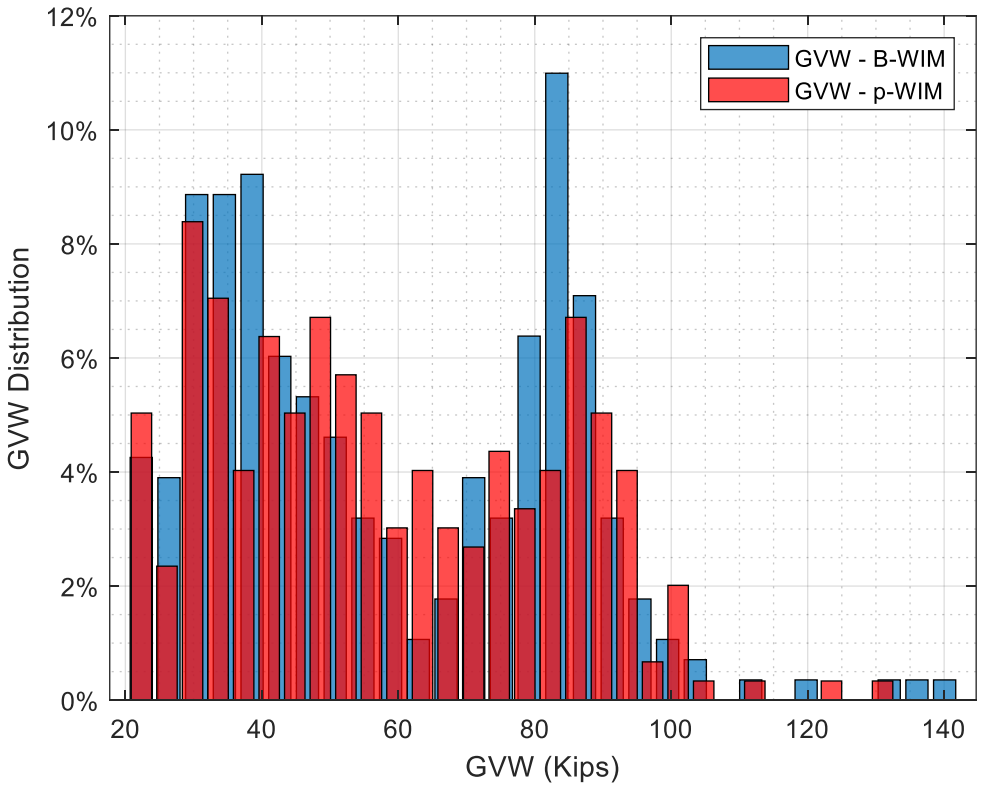

Figure 6.48. GVW Distribution Comparison (March 16, 2021).

Table 6.20. GVW and Axle Information Comparison (March 16, 2021).

System	GVW (kips)		Average Speed (mph)		Number of Axles		Wheelbase (ft)		Front Axle (kips)	
	Mean	Std Dev	Mean	Std Dev	Mean	Std Dev	Mean	Std Dev	Mean	Std Dev
B-WIM	59.2	25.6	69.8	4.3	4.5	1.0	54.4	24.6	13.4	3.3
p-WIM	57.9	23.7	70.8	4.5	4.5	1.0	51.2	14.7	10.4	2.6
Percentage Difference	2.2%		1.4%		1.1%		5.8%		22.3%	

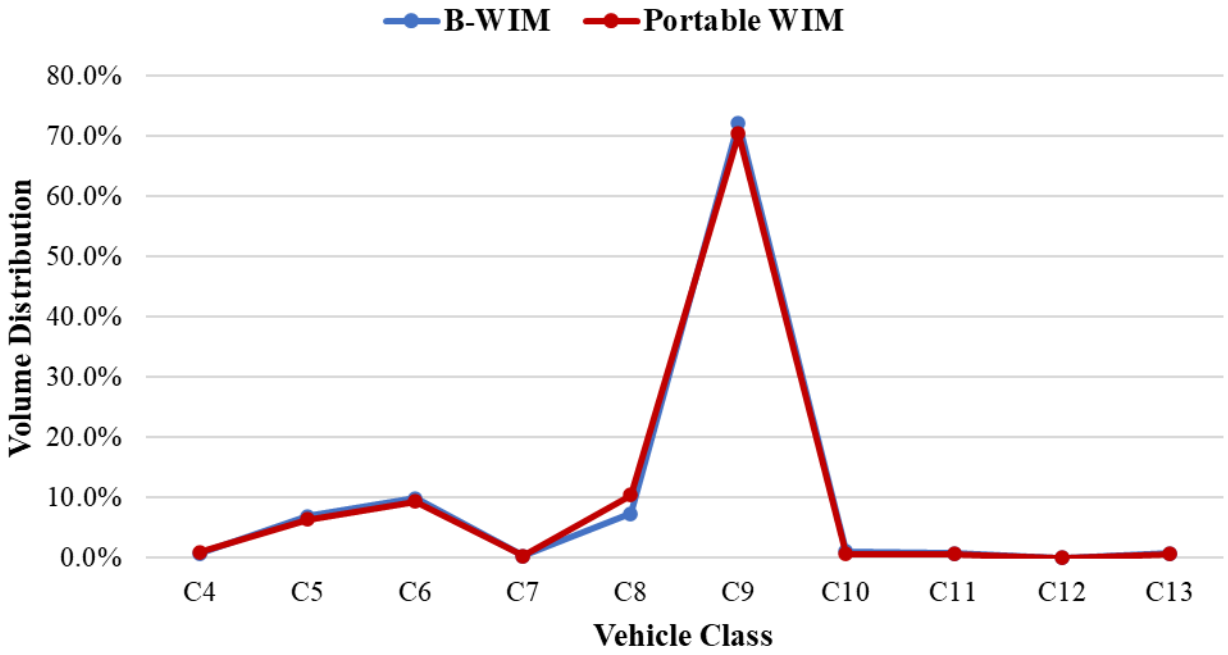

Figure 6.49. Vehicle Classification Distribution Comparison (March 16, 2021).

Another two-hour dataset between 9:02 a.m. and 11:02 a.m. on March 20, 2021, was processed from both the B-WIM system and the p-WIM system. The number of the

passing trucks, truck classification distribution, and GVW distribution were compared for the validation study.

Table 6.21 illustrates the number of trucks recorded by the two systems in two lanes within the two-hour time window. The B-WIM initially captured fewer vehicles since there was a threshold set to only capture trucks rather than cars. After the filter (GVW > 20.0 kips) was applied to both datasets, the number of trucks recorded by the two systems was almost same. Again, the difference might be caused by the GVW calculation errors on both systems near the threshold range (i.e., 20.0 kips).

Table 6.21. Comparison of the Number of Trucks (March 20, 2021).

System	Total Two-Hour Truck Count in Two Lanes	
	No Condition	GVW > 20 kips
B-WIM	151	146
p-WIM	187	145

Figure 6.52 shows the GVW distribution comparison between the two systems. The GVW calculated from the midspan strain gauges, average speed, number of axles, and wheelbase obtained from the quarter span strain gauges was compared with the p-WIM. The mean and standard deviation of each result are summarized in Table 6.22. The average GVWs of the B-WIM and p-WIM are 61.7 kips and 53.8 kips, respectively, with a difference of 12.8 percent. The average differences in truck speed, axle number, and wheelbase are all within 4.0 percent. The mean of the front axle weight has a difference of about 23.0 percent.

The truck class distribution is shown in Figure 6.55 and, like before, the B-WIM has a similar truck class distribution compared with the p-WIM except for some differences between the Class 5.

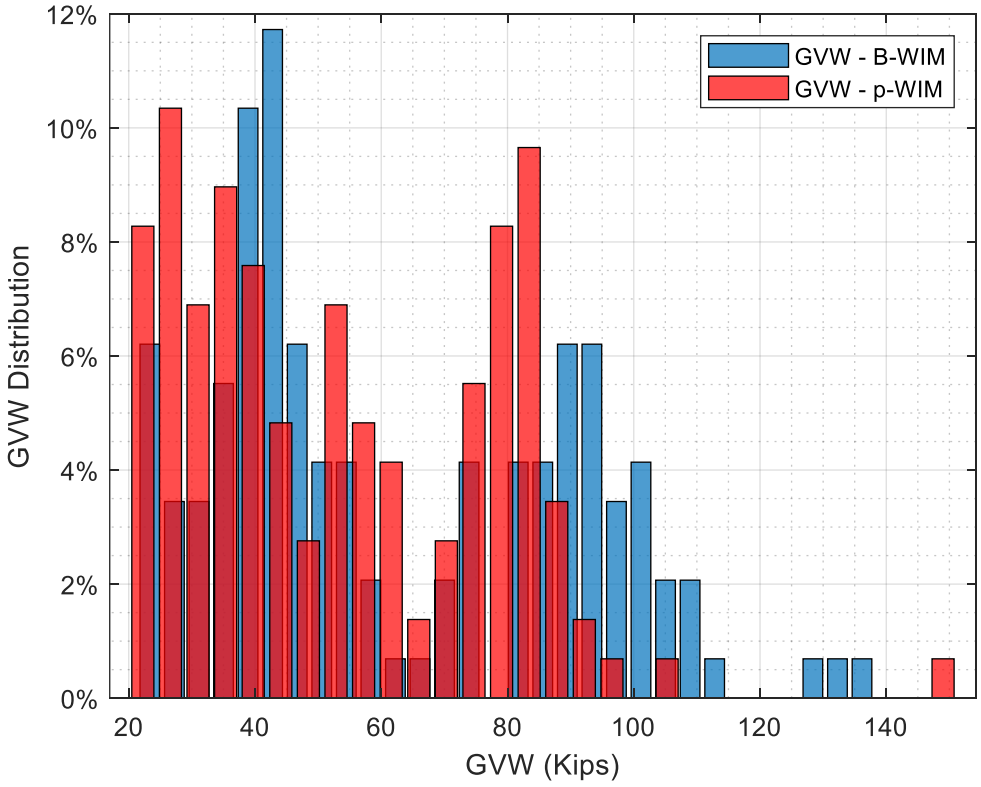

Figure 6.50. GVW Distribution Comparison (March 20, 2021).

Table 6.22. GVW and Axle Information Comparison (March 20, 2021).

System	GVW (kips)		Average Speed (mph)		Number of Axles		Wheelbase (ft)		Front Axle (kips)	
	Mean	Std Dev	Mean	Std Dev	Mean	Std Dev	Mean	Std Dev	Mean	Std Dev
B-WIM	61.7	28.6	70.0	5.1	4.3	1.2	50.3	20.6	13.0	7.6
p-WIM	53.8	24.1	71.5	5.5	4.5	1.1	50.1	15.6	10.0	2.6
Percentage Difference	12.8%		1.4%		3.6%		0.4%		23.0%	

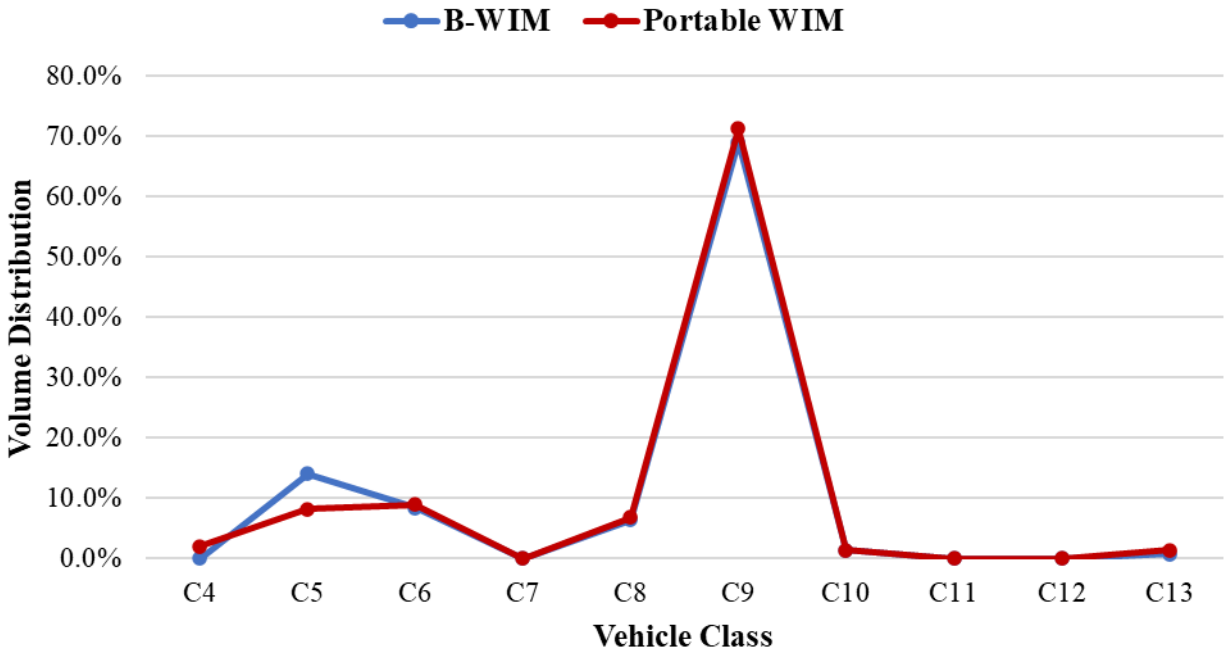

Figure 6.51. Vehicle Classification Distribution Comparison (March 20, 2021).

Based on the outcomes of the two validation studies on Bridge #1 (SH 6), it was found that the B-WIM system had close results when compared with the p-WIM system for GVW, average speed, number of axles, and wheelbase. However, there was around a

20 percent difference in the truck front axle calculation results. B-WIM calculated higher front axle weight on average. This could have been due to the cumulative errors when distributing the axle weights from the calculated GVW in the B-WIM system.

6.5.3. Bridge #2 Validation Study

Since the p-WIM was only deployed on the outside lane near Bridge #2, the inside lane results were excluded when conducting the validation study for the Bridge #2 B-WIM system. The two-hour dataset between 6:00 a.m. and 8:00 a.m. on July 19, 2021, was processed from both the B-WIM system and the p-WIM system. The number of passing trucks, truck classification distribution, GVW distribution, and front axle weight were compared for the validation study.

The B-WIM captured 135 trucks crossing the outside lane, while the p-WIM recorded 169 trucks with GVW over 20.0 kips—a difference of about 25 percent. After further analysis, it was found that the B-WIM system recorded less two-axle and three-axle trucks. Several causes are considered to have attributed to this. Firstly, when a lightweight truck is following too closely to a much heavier truck, the midspan response of the lighter weight truck in the B-WIM system was probably considered as noise in the truck passing event processing. Secondly, there were likely side-by-side cases, with potentially one truck being heavier than the other. Thirdly, there was about 0.4 miles distance between the p-WIM site and the bridge. Therefore, some trucks might have changed lanes before entering the bridge. Lastly, the systematic errors generated when calculating the GVW near the threshold could also have been a contributing factor.

Figure 6.52 shows the GVW distribution comparison between the two systems. The GVW calculated from the midspan strain gauges, average truck speed, number of axles, and wheelbase obtained from the quarter span strain gauges were compared with the p-WIM. The mean and standard deviation of each result are summarized in Table 6.23. The average GVWs from the B-WIM and p-WIM are 63.4 kips and 58.5 kips, respectively, with a difference of 7.7 percent. The average differences in speed, axle number, and wheelbase are all within 5.0 percent. Both systems had a similar mean value of front axle weight, with a difference of 1.9 percent. The numbers of trucks in each vehicle class are shown in Figure 6.55, the B-WIM has a close vehicle class distribution compared with the p-WIM.

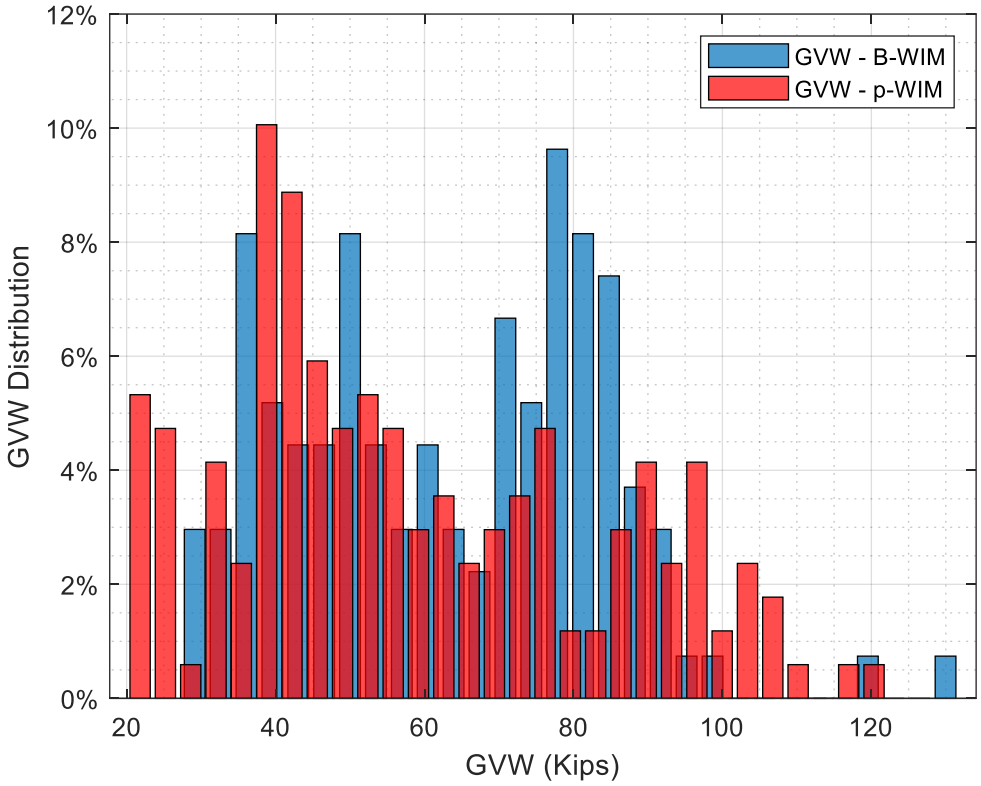

Figure 6.52. GVW Distribution Comparison (Outside Lane July 19, 2021).

Table 6.23. GVW and Axle Information Comparison (Outside Lane July 19, 2021).

System	GVW (kips)		Average Speed (mph)		Number of Axles		Wheelbase (ft)		Front Axle (kips)	
	Mean	Std Dev	Mean	Std Dev	Mean	Std Dev	Mean	Std Dev	Mean	Std Dev
B-WIM	63.4	21.0	66.8	4.6	4.7	0.9	53.6	13.5	9.9	2.9
p-WIM	58.5	24.7	69.7	4.4	4.6	0.9	51.4	13.9	10.1	3.3
Percentage Difference	7.7%		4.2%		2.1%		4.1%		1.9%	

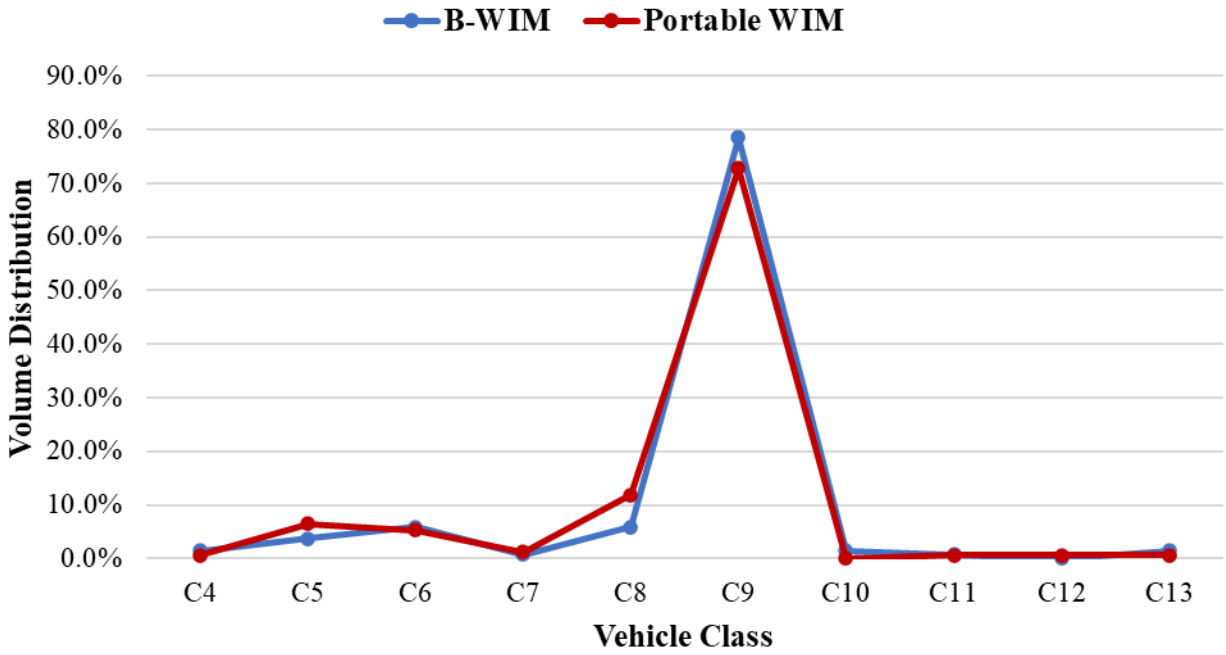

Figure 6.53. Vehicle Classification Distribution Comparison (July 19, 2021).

Another two-hour dataset between 1:18 p.m. and 3:18 p.m. on August 6, 2021, was processed from both the B-WIM and p-WIM systems. The number of passing trucks, truck classification distribution, GVW distribution, and front axle weight were compared for the validation study.

The B-WIM captured 145 trucks crossing the outside lane, while the p-WIM recorded 208 trucks with GVW over 20.0 kips. Figure 6.54 shows the GVW distribution comparison between the two systems. The GVWs calculated from the midspan strain gauges, average speed, number of axles, and wheelbase obtained from the quarter span strain gauges were compared with the p-WIM. The mean and standard deviation of each result are summarized in Table 6.24. The average GVWs from the B-WIM and p-WIM are 61.6 kips and 54.5 kips, respectively, with a difference of 11.5 percent. The average

differences in truck speed, axle number, and wheelbase are all within 5.0 percent. There is a difference of 14.0 percent between the mean of the front axle weight of both systems. The number of trucks in each class category is shown in Figure 6.55.

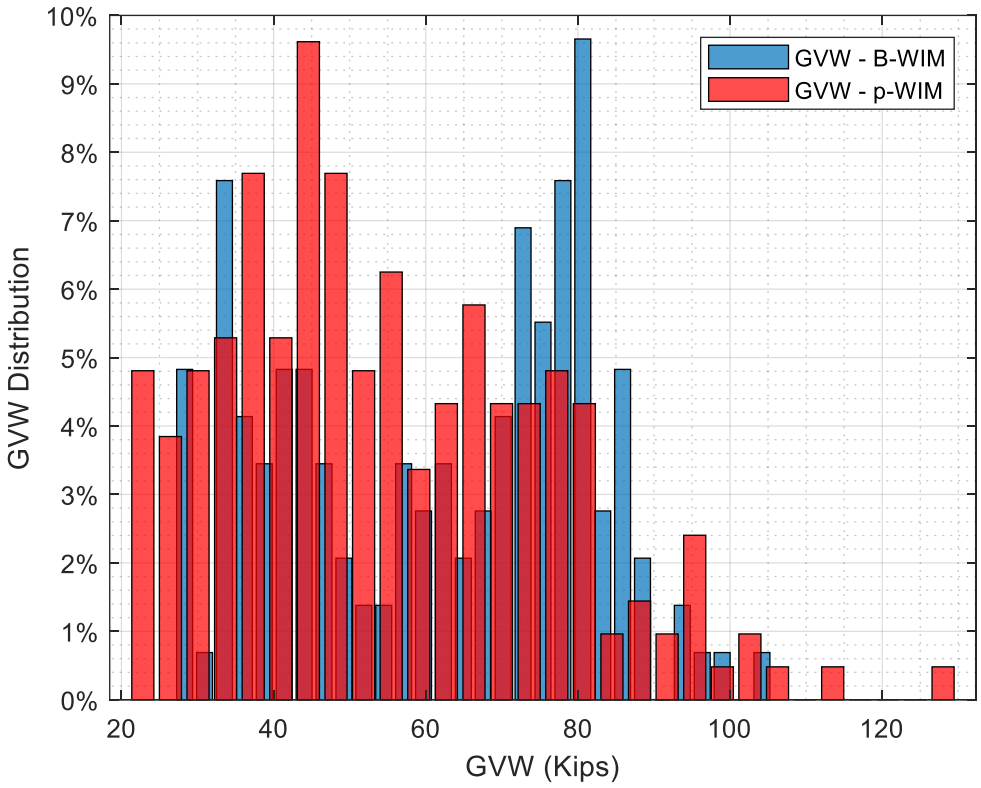

Figure 6.54. GVW Distribution Comparison (Outside Lane August 6, 2021).

Table 6.24. GVW and Axle Information Comparison (Outside Lane August 6, 2021).

System	GVW (kips)		Average Speed (mph)		Number of Axles		Wheelbase (ft)		Front Axle (kips)	
	Mean	Std Dev	Mean	Std Dev	Mean	Std Dev	Mean	Std Dev	Mean	Std Dev
B-WIM	61.6	19.9	66.8	4.6	4.8	0.9	55.7	13.0	9.2	2.3
p-WIM	54.5	21.0	69.1	6.1	4.7	1.0	53.0	13.8	10.7	3.5
Percentage Difference	11.5%		3.3%		2.1%		4.8%		14.0%	

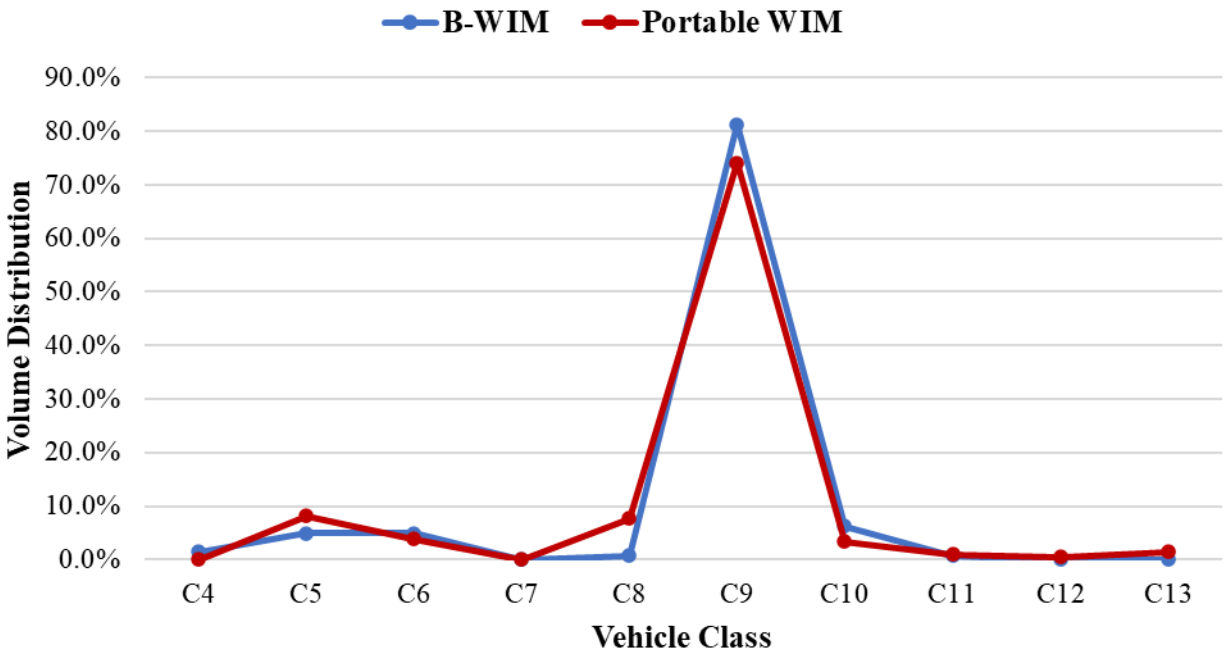

Figure 6.55. Vehicle Classification Distribution Comparison (Outside Lane August 6, 2021).

The Bridge #2 validation study found close results for GVW, average speed, number of axles, and wheelbase. In addition, compared with Bridge #1, B-WIM on Bridge #2 had closer axle weight calculation results to the p-WIM system. However, for

the Bridge #2 validation study the number of detected trucks was less for the B-WIM system than the p-WIM system. This might be because of relatively significant weight differences for the side-by-side cases. In addition, trucks may have changed lanes before entering the bridge. (The p-WIM was installed well before the bridge in the outside lane only.) Therefore, a portion of the trucks were only captured on the p-WIM system. Nonetheless, the overall average difference was less than 15 percent, which is statistically considered very satisfactory for field studies of this nature.

6.6. Live Load Data Analysis and Validation Study Summary

6.6.1. Overview

In this task, the first objective was to process the live load data recorded from three B-WIM systems to determine the passing trucks' gross weights, axle weights, axle numbers, axle spacings, speeds, and classification category. The algorithms utilized for this data processing were primarily developed in a previous research task. The data processing began with the calibration test performed at each site. The accuracy of the axle detection and weight calculation algorithms for multiple types of sensors were evaluated based on the calibration test results. In addition, several two-hour windows of data after the calibration runs were processed, and the information for each truck crossing the bridges was determined.

The second objective of this task was to validate the B-WIM results through comparison with the independent p-WIM data. The research team (led by Lubinda Walubita) had installed p-WIM stations near Bridge #1 (both lanes) and Bridge #2

(outside lane only), specifically for the B-WIM validation study. Overall, the validation studies showed relatively similar results, which were quantified for each truck criteria.

6.6.2. Axle Detection Information

Axle detection identifies the specific point in time when truck axles cross specific points on the bridge. This information allows for the calculation of the number of axles, axle speed, and axle spacing. Axle detection is arguably the most critical part of the B-WIM data processing since the information is utilized to determine other truck characteristics. At the start of the axle detection algorithm, the truck lane needs to be determined. It was found that the midspan strain gauges can be used for lane detection by comparing the distribution factors on the beams. Calibration tests and validation studies showed high accuracy of lane detection with this methodology. In addition, side-by-side configurations can be reliably detected using the distribution factors of each beam.

Three sensor approaches were explored for axle detection, including the vertical strain gauge of the strain rosettes, LVDTs measuring the vertical deformation of the bearings, and strain gauge installed on the underside of the bridge deck. Each approach has advantages and disadvantages, which are briefly conveyed below. Future systems should consider a combination of these sensor approaches for a redundant solution.

Firstly, the vertical strain gauge of the strain rosette can be used to reliably measure axle numbers by taking the first derivative of the data. The accuracy of the axle number detection is influenced by the location of the strain rosette. The vertical strain gauges installed near the center of the bearing line had better axle number detection results (i.e., 100 percent in Bridge #1 calibration tests, 75.0 percent in Bridge #2

calibration tests) than those installed away from the bearing pad (i.e., 92.8 percent in Bridge #3 calibration tests). The vertical strain gauges installed at the bridge support where the trucks enter the bridge had more accurate results than those installed at the bridge support where the trucks leave the bridge.

Secondly, the LVDTs did not accurately measure the axle numbers at high speeds in the Bridge #1 calibration tests. The accuracy was 40.0 percent. This may be due to the age of the bearing pads of Bridge #1. The bearing pads of Bridge #2 were newer than those in Bridge #1. The accuracy for axle number detection was significantly improved (i.e., 87.5 percent). For Bridge #3, LVDTs were not utilized since steel bearings were present.

Finally, strain gauges on the underside of the bridge deck near the quarter span can be used to satisfactorily measure the axle numbers, axle speed, and axle spacing accurately by the second derivative method. However, this method cannot be used when the truck passes the bridge at speeds slower than 15 mph.

6.6.3. Weight Calculation

The B-WIM weight calculation includes the GVW and the individual axle weights. The methodology utilized in the algorithm for GVW is the area method, which was applied to the midspan strain gauges, LVDTs, and strain rosettes. As part of this methodology, side-by-side cases needed to be addressed. The approach was to utilize the beam distribution factors identified in the calibration process, which has produced reasonable results. Of the three sensor approaches, each one has its advantages and disadvantages. Overall, the midspan strain gauges were shown to be the most accurate, with the strain

rosettes not far behind. The LVDT approach can yield accurate data if the bearings are suitable. Again, future B-WIM systems should consider multiple methods in parallel to increase the reliability of the data.

Various axle weight calculation methods were explored. The shear response from the strain rosette showed peaks from the axle groups and was used to calculate the axle group weight. The second derivative of the data of strain gauges underneath the bridge deck was utilized to calculate the individual axle weights. Results from the calibration tests showed reasonable accuracy of the deck gauges; this method was used for live load data analysis since it was more straightforward.

Two-hour data time windows from two of the B-WIM systems were selected and compared with the corresponding p-WIM data. It was found that for around 300 trucks in Bridge #1, the average GVWs from both systems had a difference of only 2.2 percent. The average differences in speed, axle number, and wheelbase were all within 6.0 percent. The front axle weight had a higher difference of about 23.0 percent. For Bridge #2, the GVW differences were within 8.0 percent, and the rest of the differences of truck properties are within 5.0 percent. However, fewer trucks were detected by the B-WIM systems compared with the p-WIM. This was likely due to lightweight trucks following close to a much heavier truck, where the light truck was treated as noise. Another possibility is that a lightweight truck was adjacent to a heavy truck, and the lightweight was ignored. Overall, the comparison between the B-WIM and p-WIM results were relatively consistent and produced similar conclusions about the trucks traveling on the highways/bridges studied. With an overall average difference of less than 15 percent

between the two systems, the validation results obtained were deemed satisfactory and statistically acceptable for field studies of this nature.

6.6.4. Vehicle (Truck) Classification

The B-WIM system can reliably identify the truck classifications if the axle detection information is accurate. The results from the B-WIM calibration tests were accurate. In addition, the truck classification results were essentially the same for the Bridge #1 and Bridge #2 validation study between the B-WIM and p-WIM systems.

7. BRIDGE EVALUATION AND LOAD RATING

7.1. Overview

Historically, evaluation of the bridge itself has not been a requirement for B-WIM systems. However, B-WIM systems have the potential secondary benefit of providing refined bridge information since their setups typically have included strain gauges on each beam along one cross section of the bridge. Bridge information such as the live load DF and percentage of the composite action (with supplemental strain gauges) can be obtained from the B-WIM system. This information can be valuable to bridge engineers to perform a new load rating or update the existing bridge ratings.

This section presents the work performed to develop a methodology for evaluating a bridge and calculating a load rating using the B-WIM system. B-WIM data from the three previously selected bridges were utilized for this task. The B-WIM system has incorporated algorithms for site-specific DFs and the determination of the composite actions for redefining the load ratings.

7.2. Methodology and Approach

7.2.1. Introduction

The bridge load rating algorithms were coded using MATLAB software for compatibility with the B-WIM software. This B-WIM code allows the user to input the bridge and rating vehicle information, and the code outputs an AASHTO LFR (AASHTO 2011) using line-girder analysis. LFR was selected by TxDOT over Load and

Resistance Factor Rating so that the results would be compatible with their existing ratings. The bridge load rating code was designed for prestressed concrete and steel multi-girder bridges. The general bridge input requirements include girder spacing, span length, and the number of lanes. There are 10 notional trucks that calculate the live load demands used for the desired load rating. These notional trucks include the HS20, HS15, H20, H15, SU4, SU5, SU6, SU7, EV2, and EV3 (TxDOT 2020). In addition, the code is setup such that actual trucks (not notional) captured from the B-WIM data can be load rated.

7.2.2. Prestress Concrete Bridges

For prestressed concrete bridges, the user must adjust the following inputs: span length, number of lanes, girder type, design truck, miscellaneous dead load, thickness of the slab, thickness of the overlay, girder spacing, concrete material properties, and steel strand material properties. The commonly used beam types are A, B, C, IV, VI, VI(MOD), 48, 54, 60, 66, and 72, or the user can define the beam properties. Concrete properties can be found on the construction drawings or approximated based on the year the bridge was constructed. The prestressing steel strand layout is used to find the eccentricity at midspan. If the value is known, it can be directly entered. The program then takes the inputted values and runs them through the AASHTO LFR equations. These include the dead load moment, design section properties, prestress losses, flexural strength, and allowable moments.

The program output is the bridge load rating based on the desired notional truck. After the code is run, an inventory and operating rating will be displayed. For the

inventory rating, the allowable stress rating includes the concrete tension, concrete compression, and prestressed tension—all based on the service moments. The strength ratings are also calculated. The lowest strength or allowable stress rating will control the inventory rating. The operating rating is controlled by either the strength or allowable prestress tension rating.

7.2.3. Steel Girder Bridges

For steel girder bridges, the user must adjust the following inputs: span length, number of lanes, design truck, miscellaneous dead load, cover plate dimensions, girder dimensions, rolled section properties, material properties, and composite action. Recommended steel and concrete slab properties can be approximated based on the year the bridge was constructed, or exact values can be found on the construction drawings. If the bridge experiences composite action, the composite section is used for the calculations.

The program then takes the inputted values and runs them through the AASHTO LFR equations. These include the dead load moment, design section properties, composite and non-composite calculations, allowable moments, and serviceability checks. The inventory and operating load ratings are output for the bridge configuration. The inventory and operating ratings are the lesser of the strength and serviceability ratings.

7.2.4. Distribution Factors

The load ratings are performed using line-girder analysis. Therefore, DFs are required. These factors provide a percentage of the live loading that is carried by a single beam. This can be from a single truck or multiple trucks side-by-side. To determine the live load DFs, strain gauges should be installed on every beam of a bridge cross-section. Therefore, the "weight" strain gauges from the B-WIM system work well for DFs.

During a truck passing event, varying strains will be seen transversely through the cross-section as the live load passes over the structure. To evaluate the beam response, the transverse distribution of strains for each girder at a given time can be used to find the live load DFs, as shown in Eq. (3.19), assuming the section modulus to be the same for all beams. These DFs are per lane and not per wheel line.

7.2.4.1. One-Lane Loaded Distribution Factors

A graphical example of the lateral live load distribution for a one-lane loaded case is shown in Figure 7.1. The midspan strain responses from the truck passing event are plotted for each beam at a given instant (shown with the dashed vertical line). It can be seen that the DF for this case is roughly 0.40 based on Eq. (3.19), and the controlling beam is Beam #4.

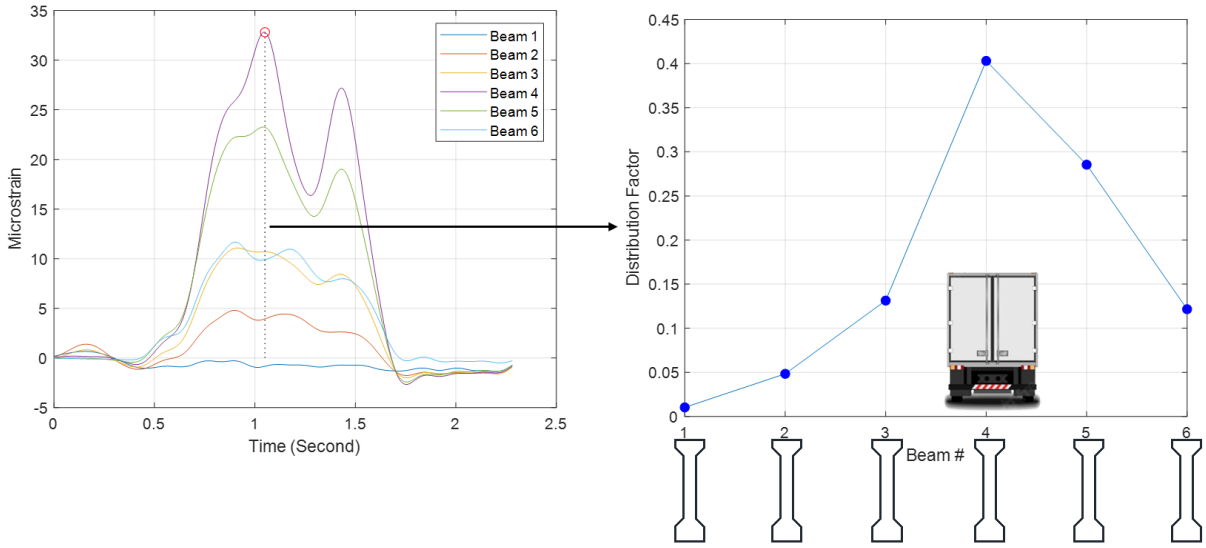

Figure 7.1. Distribution Factor Example for a One-Lane Loaded Case.

7.2.4.2. Two-Lane Loaded Distribution Factors

The DFs for two-lane loaded cases can be obtained with two side-by-side trucks on the bridge that are of similar weight and configuration. The other approach is using the superposition method. Figure 7.2a and Figure 7.2b use the superposition method. These figures show the DFs calculated for the same truck passing the bridge on the left and right lanes with the same speed. The results are then summed up for each beam, and the DF for this specific two-lane loaded case is 0.54, as shown in Figure 7.3.

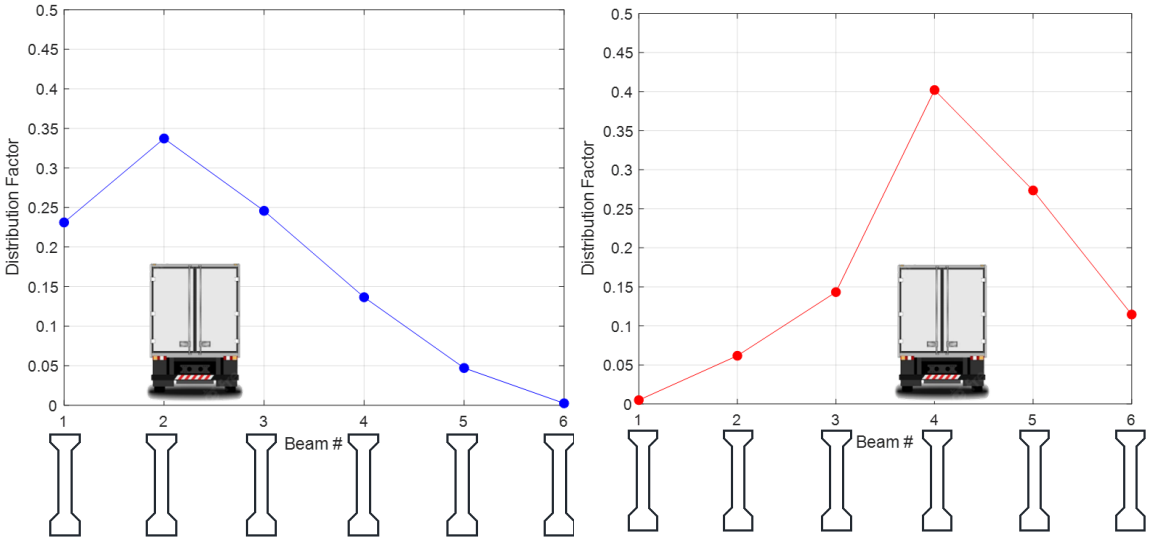

(a) Truck Passing Left Lane (b) Truck Passing Right Lane

Figure 7.2. Examples of Distribution Factors of Single Truck Passing Event.

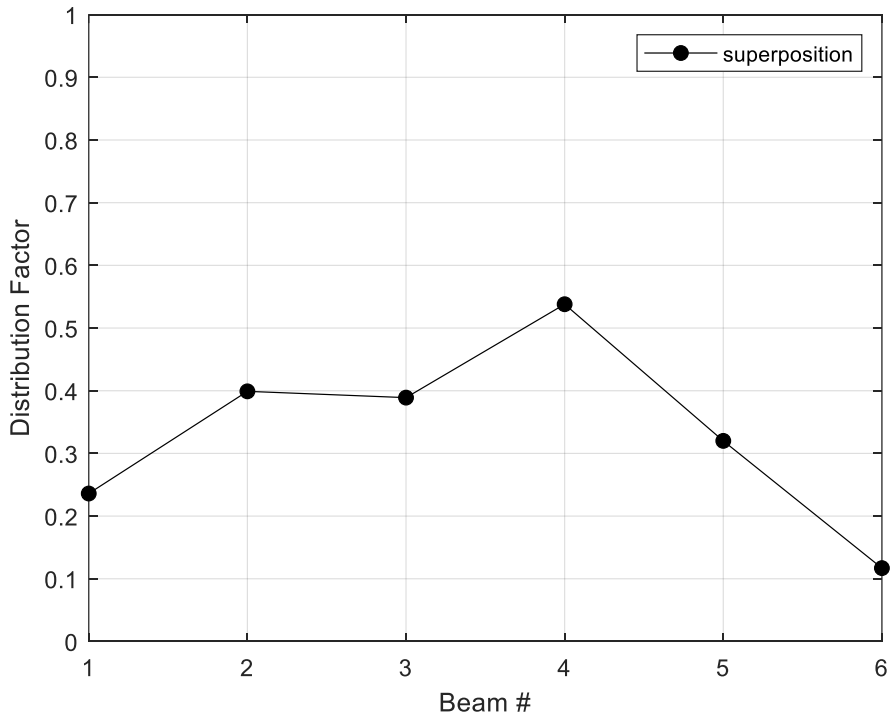

Figure 7.3. Distribution Factor Example for a Two-Lane Loaded Case.

7.2.4.3. Distribution Factors Using B-WIM Live Load Data

Controlled load tests are the most common method for identifying DFs (Chajes et al. 1997); however, many applications using ambient live load data have been successful. (Yarnold and Wilson 2015)) were able to field identify the DFs for a steel girder bridge using vibrating wire strain gauges to measure the ambient traffic response. DFs can be calculated for each truck over a number of weeks, months, or even years and then combined to determine the appropriate DFs.

For example, assume a B-WIM system recorded M_L number of single truck passing events on the left lane and M_R number of single truck passing events on the right lane for a two-lane bridge with N beams during a specific time range. The DFs of each beam can be calculated by Eq. (3.19). An $M_L \times N$ matrix and an $M_R \times N$ matrix can be constructed for left and right lane passing trucks, respectively. The data can be analyzed statistically, and the DFs of the one-lane loaded cases can be determined by using the mean values or a higher percentile (95th percentile selected for this study). To obtain the DFs for two-lane loaded cases, the matrix constructed for both lanes needs to be combined. Take the first row from the left lane matrix and sum them up with each row of the right lane matrix to result in an $M_R \times N$ dataset. Then take the second row from the left lane matrix and repeat the same step. Another $M_R \times N$ dataset is obtained, which results in a $2M_R \times N$ dataset. Repeat the step till the last row of the left lane matrix. In the end, a matrix with $M_L \times M_R$ rows and N columns can be constructed. Using statistical analysis, the DFs for two-lane loaded cases can be determined.

The above methods will be demonstrated with recorded B-WIM data in the Case Study Section (Section 7.4) for the three selected bridges.

7.2.5. Composite Action

The level of composite action refers to the continuity of the beams with the deck slab. Fully composite behavior indicates 100 percent continuity; thus, the beams deform with the deck. Non-composite behavior is the opposite. The composite behavior may be uncertain due to the loss of as-built plans, long-term degradation of an originally designed fully composite bridge, or even a bridge that was designed as non-composite but had other mechanisms to behave as partial or even fully composite (Barker et al. 1999; Chajes et al. 1997; James and Yarnold 2017; Jauregui 1999). As a result of this uncertainty, field measurements can help determine the composite behavior of the bridge.

The conventional approach to field determining the level of composite action is to measure the longitudinal strain response at multiple positions along with the height of a beam cross-section. These measurements are then utilized to identify the neutral axis (i.e., location of zero strain), assuming a linear strain profile. Figure 7.4 illustrates an example data set from a separate study (Yarnold et al. 2018). The strain values shown are for different positions of the truck driving across the bridge. Then, assuming a linear strain profile, the measured strains were projected to the field to determine the neutral axis, which was at the bottom of the deck slab. This is an example of fully composite behavior.

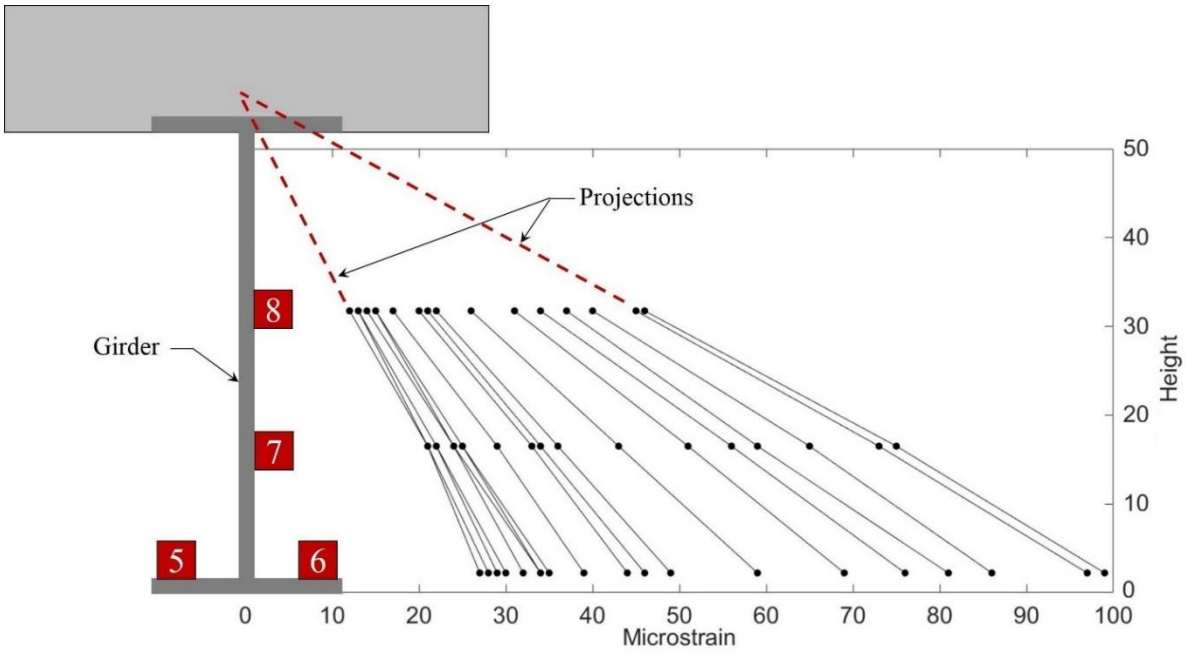

Figure 7.4. Example of Strain Measurements to Determine the Level of Composite Action (reprinted from Yarnold et al. 2018).

7.3. Code Validation

The B-WIM bridge load rating code was validated to ensure its accuracy with the AASHTO LFR standards. The approach for the validation was to compare the newly developed code results with the well-established TxDOT Load Rating Spreadsheet. This spreadsheet has been used by TxDOT for over 20 years and has been well vetted. The TxDOT spreadsheet was not used in this study because of integration challenges with the primary B-WIM code. In addition, flexibility for the expansion of the bridge assessment calculations was desired.

The AASHTO specification requires different equations to be applied depending on the outcome of previously defined variables. To ensure that the MATLAB code would calculate the correct equation, different input variables were explored. These

variables included girder type/size, girder spacing, slab thickness, span length, and material properties. The intermediate calculations were checked along with the final load ratings.

Table 7.1 shows a sample of the validation process. This illustration includes a steel girder bridge that is 30 ft long, a 6-inch slab, 7 ft girder spacing, 33 ksi steel yield strength, and 2.5 ksi concrete compression strength. The bridge is rated for the SU4 design truck and does not have composite action. As seen in the table, the TxDOT spreadsheet values and the values produced by the code are similar. After changing multiple input variables and getting similar values, the code proved to be outputting correctly. A summary of the prestressed beam and steel girder load rating code validation is provided in Table 7.2 and Table 7.3, respectively.

Table 7.1. Sample of the Validation Process.

	Example Value	**Code Value**	**Percent Difference**
Live Load Moment (k-ft)	136.8	136.9	0.04%
Impact Factor	0.30	0.30	0.00%
Distribution Factor	1.27	1.27	0.00%
Dead Load Moment (k-ft)	66.8	66.8	0.00%
Plastic Section Modulus (in^3)	160.2	160.3	0.06%
Minimum Elastic Modulus (in^3)	140.5	140.5	0.00%
Capacity (k-ft)	801.2	801.3	0.01%
Inventory Rating	1.31	1.31	0.00%
Operating Rating	2.19	2.19	0.00%

Table 7.2. Prestress Girder Validation Results.

	Bridge A	Bridge B	Bridge C	Bridge D
Length (ft)	80	80	55	30
Beam Type	IV	IV	IV	A
Girder Spacing (ft)	8.5	6	7.5	9
Number of Prestress Strands	32	24	22	32
Design Truck	HS20	HS20	HS20	H20
Inventory LFR	1.75	1.76	2.61	5.29
Operating LFR	2.92	2.93	4.36	8.83
Inventory Percent Difference	0.37%	0.42%	0.99%	5.27%
Operating Percent Difference	0.37%	0.42%	0.99%	5.27%

Table 7.3. Steel Girder Validation Results.

	Bridge A	Bridge B	Bridge C	Bridge D
Length (ft)	90	70	30	30
Beam Type	W21x68	W21x68	W21x68	W21x68
Girder Spacing (ft)	9	8	7	7
Slab Thickness (in)	6	7.5	6	6
Composite Action	Yes	No	No	Yes
Design Truck	H-20	HS20	SU-4	EV-2
Inventory LFR	1.31	0.80	1.31	—
Operating LFR	2.19	1.33	2.19	3.56
Inventory Percent Difference	1.15%	0.98%	0.02%	—
Operating Percent Difference	1.13%	0.37%	0.19%	0.67%

7.4. Refined Notional Load Ratings for the TxDOT Bridges

7.4.1. Introduction

Presented below are the bridge load rating case studies for the three selected in-service bridges. The newly developed B-WIM code calculated DFs using the original B-WIM data for all three bridges. The first two bridges were comprised of prestressed concrete beams. The last bridge was a steel multi-girder bridge. For the steel bridge, an additional bridge evaluation code was included to study the composite action (with supplemental

gauges at the web location) since no shear studs were provided. Each bridge and the load rating results from notional trucks are summarized separately below.

7.4.2. Bridge #1

7.4.2.1. Introduction

Bridge #1 is a prestressed concrete I-beam simple span bridge on SH 6, Bryan District. Details and cross-section views can be found in Section 4 and Section 5. The bridge superstructure is comprised of six 54-inch-deep prestressed concrete beams. The beams are spaced 7.5 ft apart and have a compressive strength of 5.0 ksi (initial release compressive strength of 4.0 ksi). The slab is 7.5 inches thick with an assumed compressive strength of 4.0 ksi. The prestressing strands are ½ inch, grade 270 steel. There are 18 stands, and the eccentricity at midspan is 21.53 inches. This bridge has an overlay with a thickness estimate of 1.5 inches.

7.4.2.2. Distribution Factors for Bridge #1

The B-WIM data shown in Table 6.13 was used to determine the refined DFs. The DFs of each beam were calculated and summarized in a box and whisker plot (i.e., box plot). The box plot displays the five-number summary of a set of data, including the minimum, first quartile, median, third quartile, and maximum. Figure 7.5 and Figure 7.6 show box plots and their mean values of left lane trucks and right lane trucks, respectively. On each box, the central mark indicates the median, and the bottom and top edges of the box indicate the 25th and 75th percentiles, respectively. The whiskers extend to the most

extreme data points not considered outliers, and the outliers are plotted individually using the "+" marker symbol.

In Figure 7.6, it is visually evident that Beam #4 had the largest average DF for the one-lane loaded case. Figure 7.7 shows the histogram of calculated Beam #4 DFs, and Figure 7.8 shows the CDF of the DFs. The mean value is 0.38 with a standard deviation of 0.02, and the 95th percentile value is 0.41. As a comparison, the DF calculated using the AASHTO LFR method for the interior beam with one lane loaded is 0.54 (see Figure 7.7). This shows the conservative DF approach for the AASHTO LFR method, which has been consistently shown in prior studies.

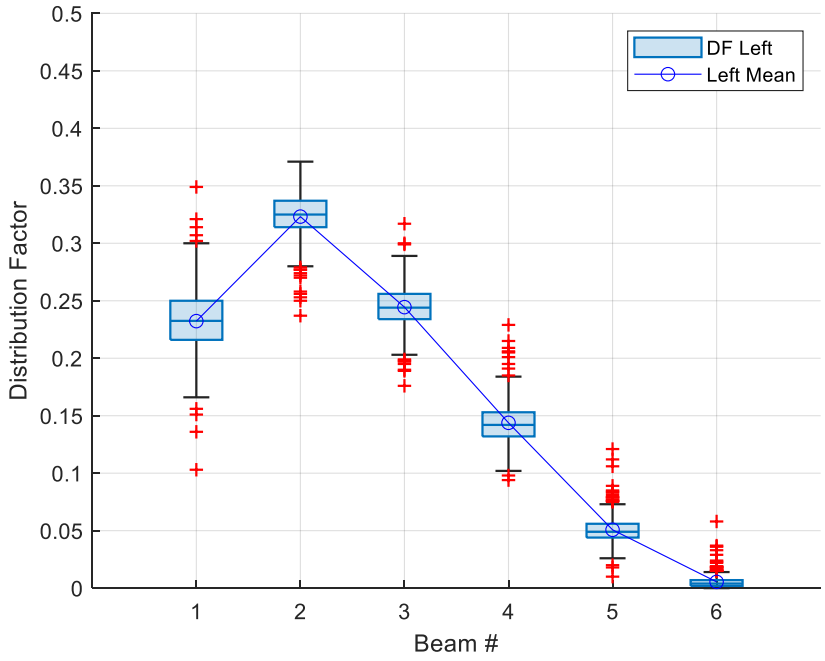

Figure 7.5. Box Plot of DFs on Left Lane Truck Passing Events (Bridge #1).

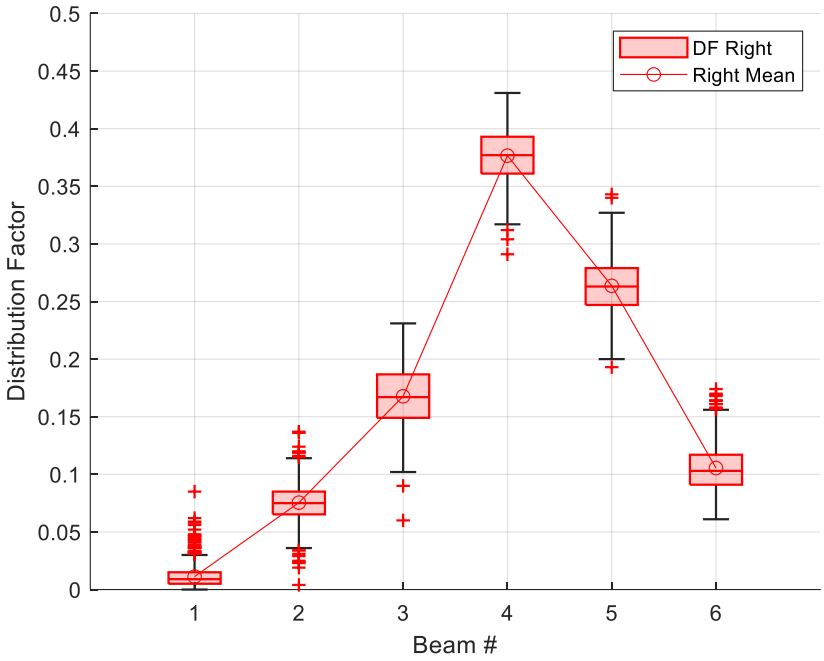

Figure 7.6. Box Plot of DFs on Right Lane Truck Passing Events (Bridge #1).

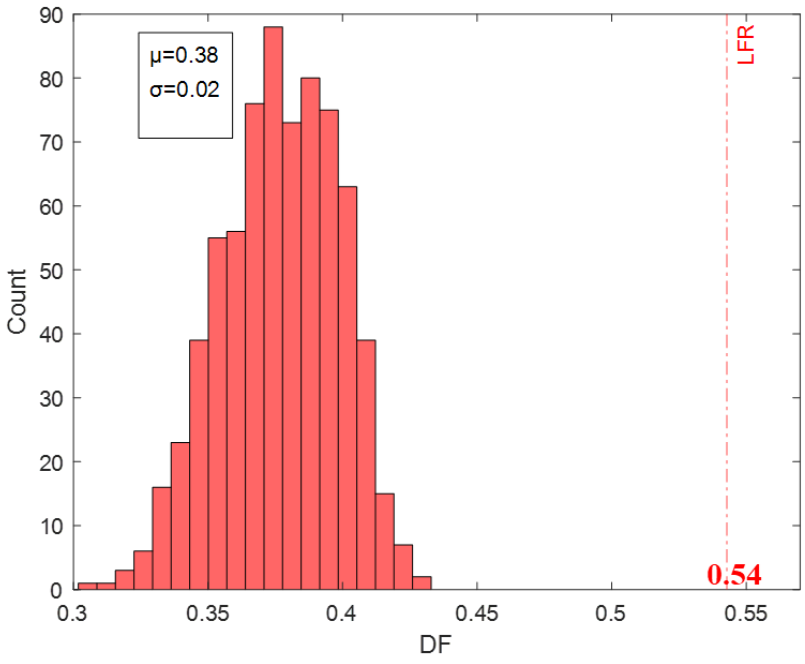

Figure 7.7. Histogram of Beam #4 DFs for One-Lane Loaded (Bridge #1).

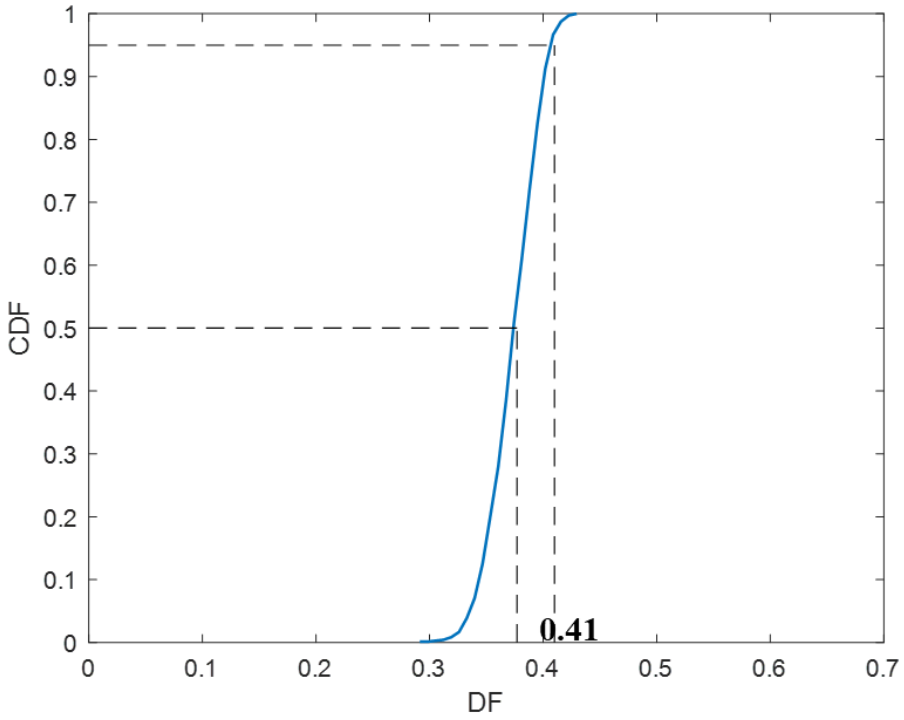

Figure 7.8. CDF of Beam #4 DFs for One-Lane Loaded (Bridge #1).

To determine the two-lane loaded DFs, the left lane DFs and right lane DFs were summed up with a total of 240,146 combinations. Figure 7.9 demonstrates the box plot of the combined DFs for each beam, and Figure 7.10 shows the mean combined DFs. Summing up the mean DF of each beam, the total is 1.99. Figure 7.11 shows the histogram and CDF of the controlling beam (Beam #4) DFs. The mean value for two-lanes loaded is 0.52 with a standard deviation of 0.03, and the 95th percentile value is 0.57. This is the controlling field identified DF for Bridge #1. As a comparison, the DF calculated with the AASHTO LFR method for the interior beam with two-lane loaded is 0.69 (see Figure 7.11).

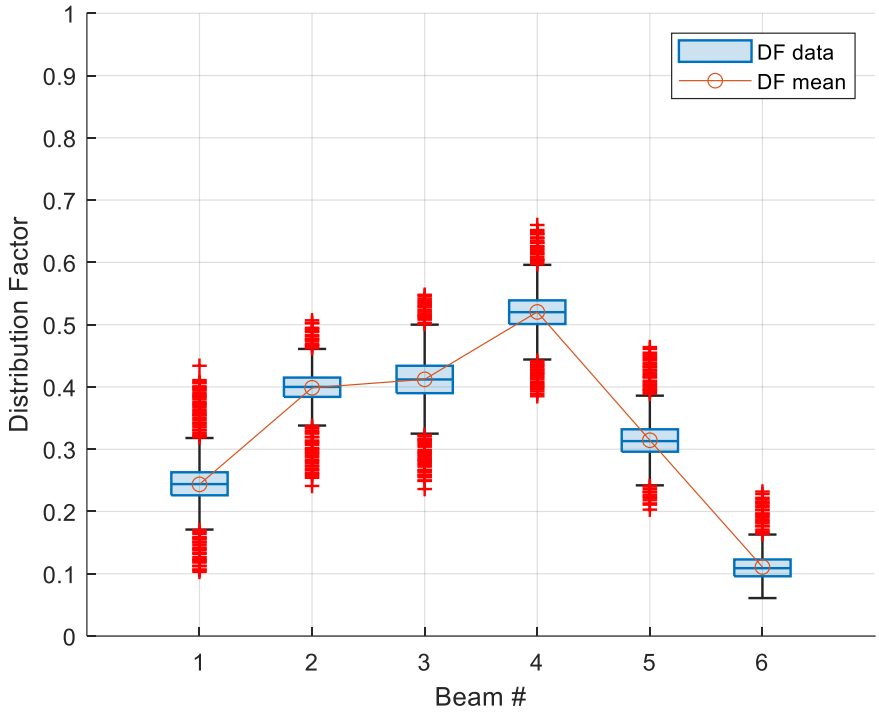

Figure 7.9. Box Plot of DFs of Two-Lane Loaded Cases (Bridge #1).

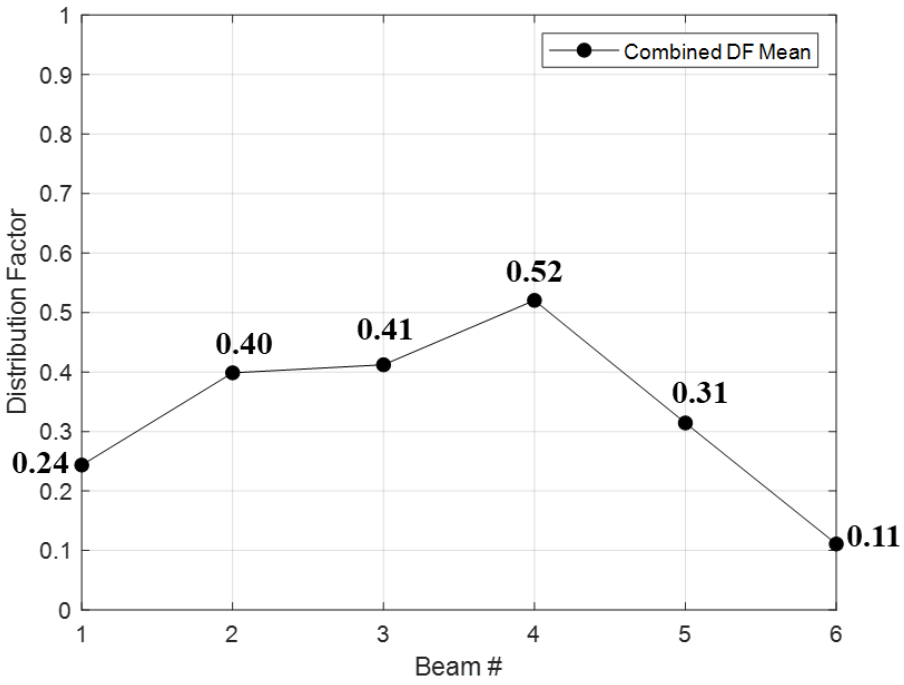

Figure 7.10. Mean DF of Each Beam of Two-Lane Loaded Cases (Bridge #1).

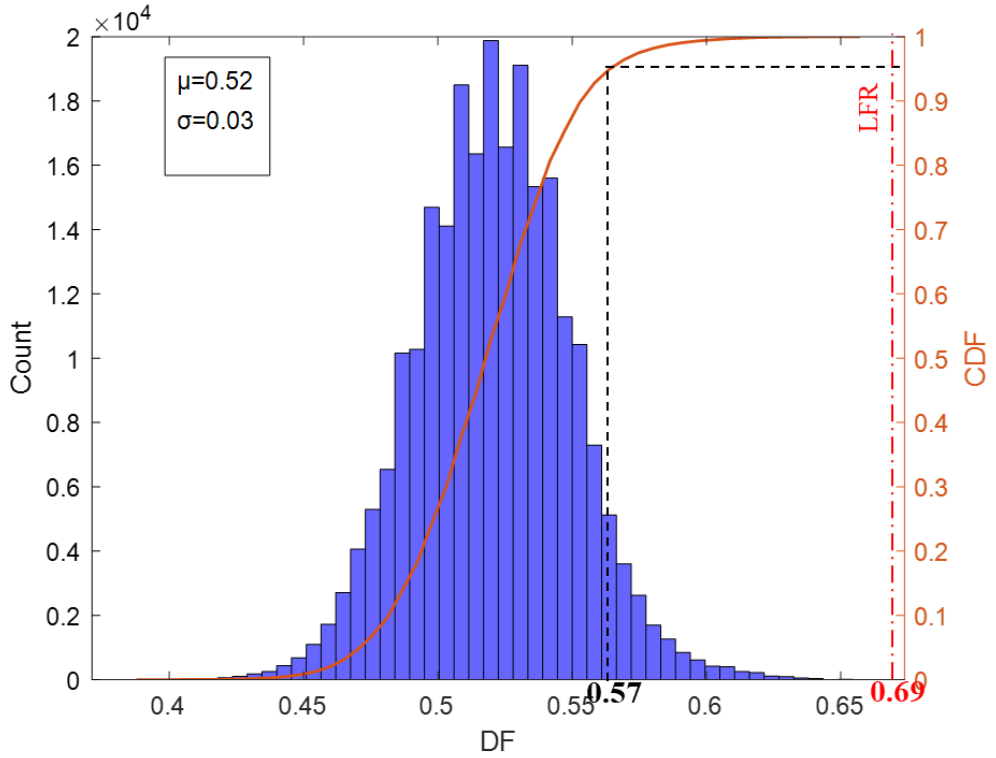

Figure 7.11. Histogram and CDF of Beam #4 Two-Lane Loaded Combined DFs (Bridge #1).

7.4.2.3. Load Rating for Bridge #1

The multi-lane DF of 0.57 was inputted into the B-WIM load rating code. Compared to the AASHTO LFR DF of 0.69, the B-WIM factors were improved for Bridge #1. Table 7.4 shows inventory LFRs for the rating trucks. As expected, with the refined DF, the ratings increased. For example, the HS20 rating increased by nearly 20 percent. Similarly, Table 7.5 shows the operating LFRs. The ratings for this particular bridge prior to the B-WIM system were adequate. This effort was to show the additional advantages of a B-WIM system outside of the truck-traffic data measurements.

Table 7.4. Bridge #1 Inventory Load Factor Rating.

Truck	Without B-WIM	With B-WIM
HS20	1.34	1.60
H20	1.87	2.23
SU4	1.64	1.93
SU5	1.48	1.74
SU6	1.33	1.57
SU7	1.22	1.44

Table 7.5. Bridge #1 Operating Load Factor Rating.

Truck	Without B-WIM	With B-WIM
HS20	2.24	2.68
H20	3.12	3.74
SU4	2.75	3.23
SU5	2.49	2.92
SU6	2.23	2.62
SU7	2.05	2.41
EV2	2.68	3.15
EV3	1.76	2.07

7.4.3. Bridge #2

7.4.3.1. Introduction

Bridge #2 is a prestressed concrete I-beam bridge that was built in 2010 on SH 6, Bryan District. Details and cross-section views can be found in Section 4 and Section 5. The bridge superstructure is comprised of six prestressed type IV I-beams. The girders are spaced 8.5 ft apart and have a compressive strength of 5.0 ksi (initial release compressive strength of 4.0 ksi). The slab is 8 inches thick with a compressive strength of 4.0 ksi. The prestressing strands are ½ inch, grade 270 steel. There are 20 strands, and the eccentricity at midspan is 21.93 inches.

7.4.3.2. Distribution Factors for Bridge #2

The B-WIM data shown in Table 6.15 was used to determine the refined DFs. The DFs of each beam were calculated. Figure 7.12 and Figure 7.13 show box plots and their mean values of left lane trucks and right lane trucks, respectively. Beam #2 had the largest average DF for the one-lane loaded case. Figure 7.14 shows the histogram of calculated Beam #2 DFs, and Figure 7.15 shows the CDF of the DFs. The mean value is 0.51 with a standard deviation of 0.04, and the 95th percentile value is 0.57. As a comparison, the DF calculated with the AASHTO LFR method for the interior beam with one lane loaded is 0.61 (see Figure 7.14).

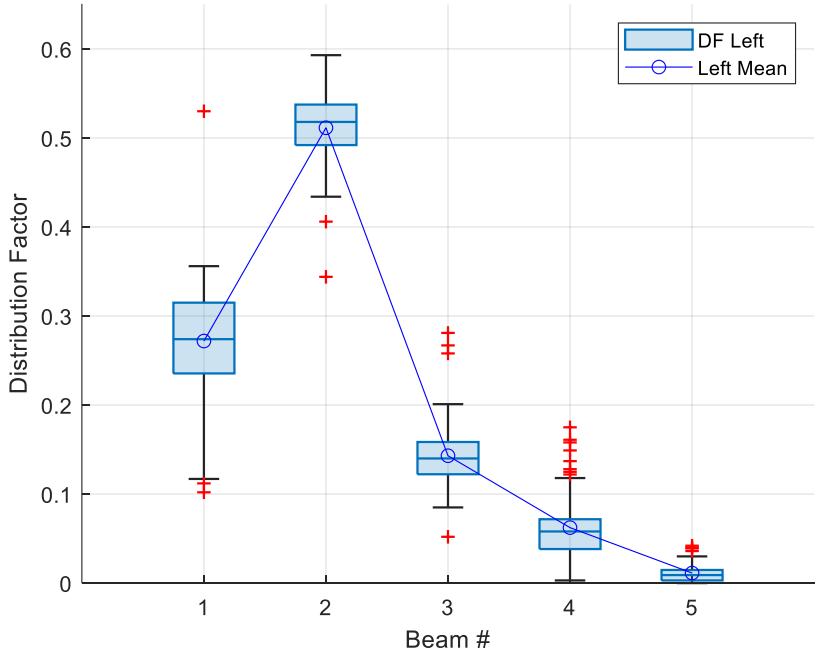

Figure 7.12. Box Plot of DFs on Left Lane Truck Passing Events (Bridge #2).

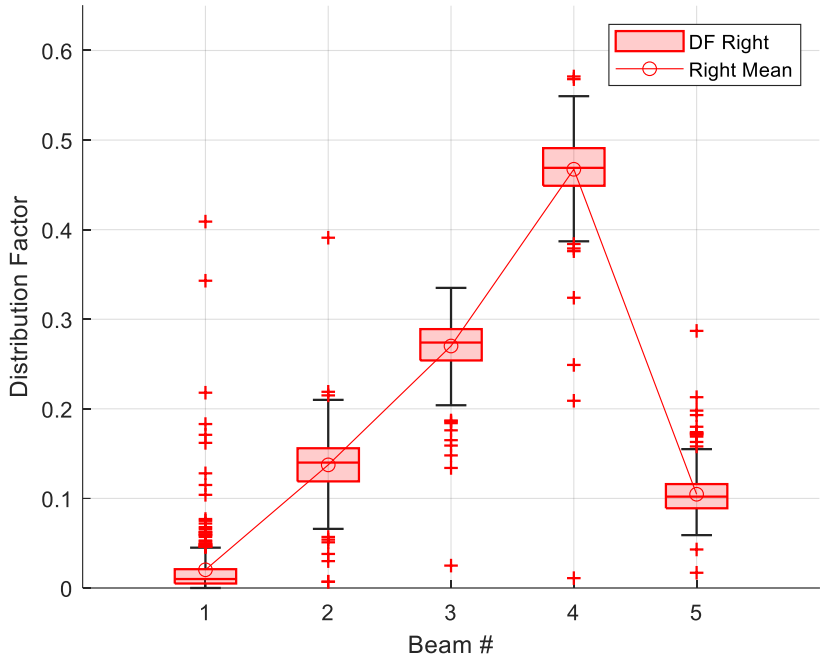

Figure 7.13. Box Plot of DFs on Right Lane Truck Passing Events (Bridge #2).

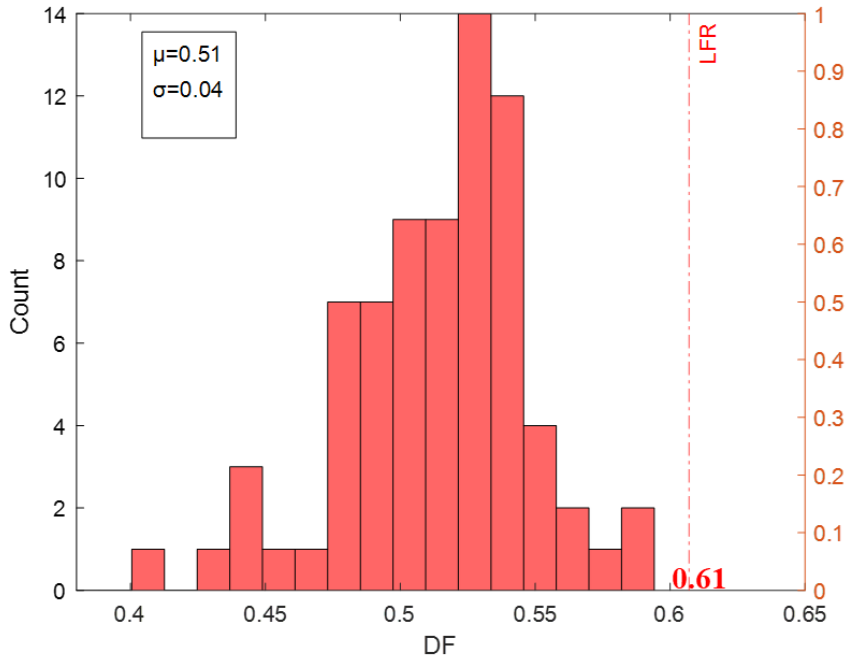

Figure 7.14. Histogram of Beam #2 DFs for One-Lane Loaded (Bridge #2).

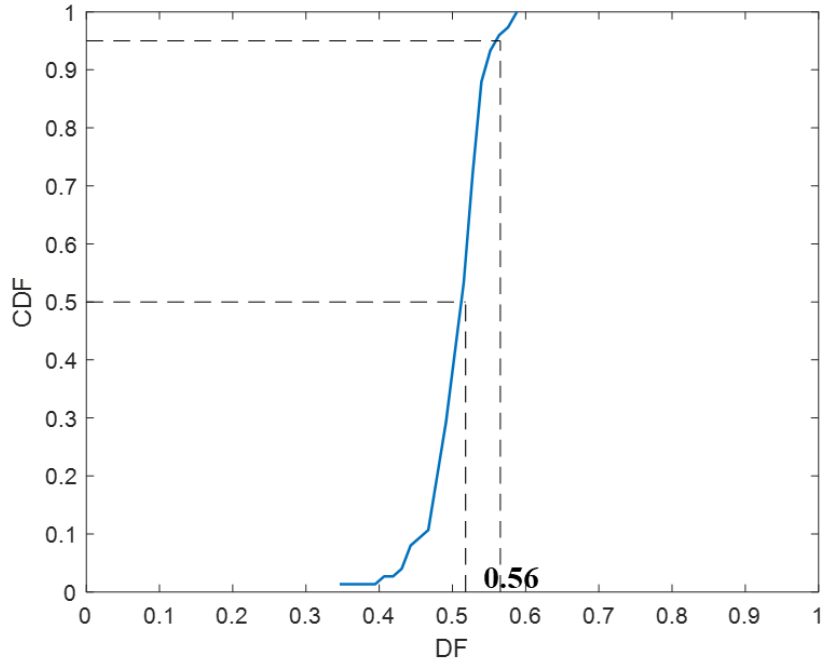

Figure 7.15. CDF of Beam #2 DFs for One-Lane Loaded (Bridge #2).

To determine the two-lane loaded DF, the left lane DFs and right lane DFs were summed up with a total of 34,350 combinations. Figure 7.16 demonstrates the box plot of the combined DFs for each beam, and Figure 7.17 shows the mean combined DFs. Summing up the mean DF of each beam, the total is 1.99. Figure 7.18 shows the histogram and CDF of the controlling beam (Beam #2) DFs. The mean value is 0.65 with a standard deviation of 0.05, and the 95th percentile value is 0.72. The DF calculated with the LFR method for the interior beam with two-lane loaded is 0.77 (see Figure 7.18).

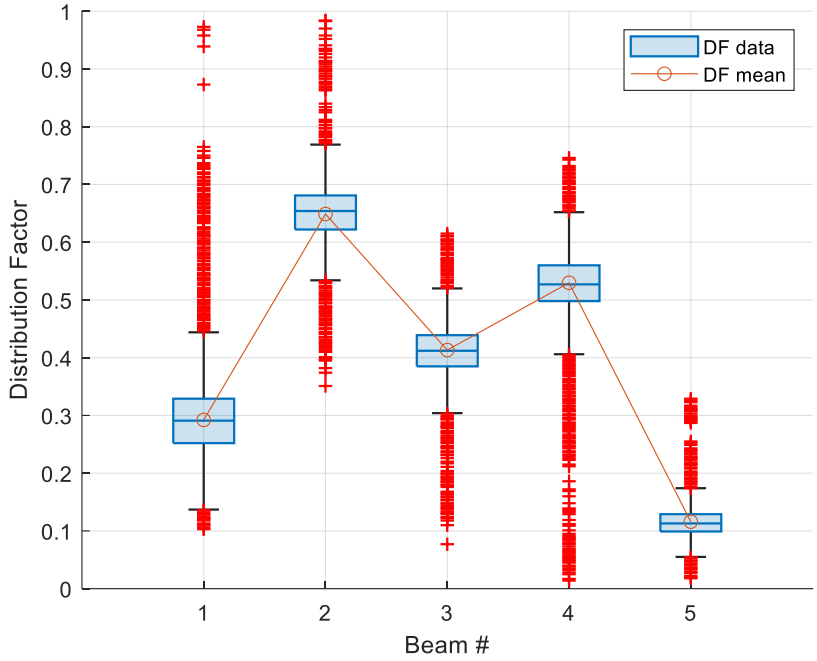

Figure 7.16. Box Plot of DFs of Two-Lane Loaded Cases (Bridge #2).

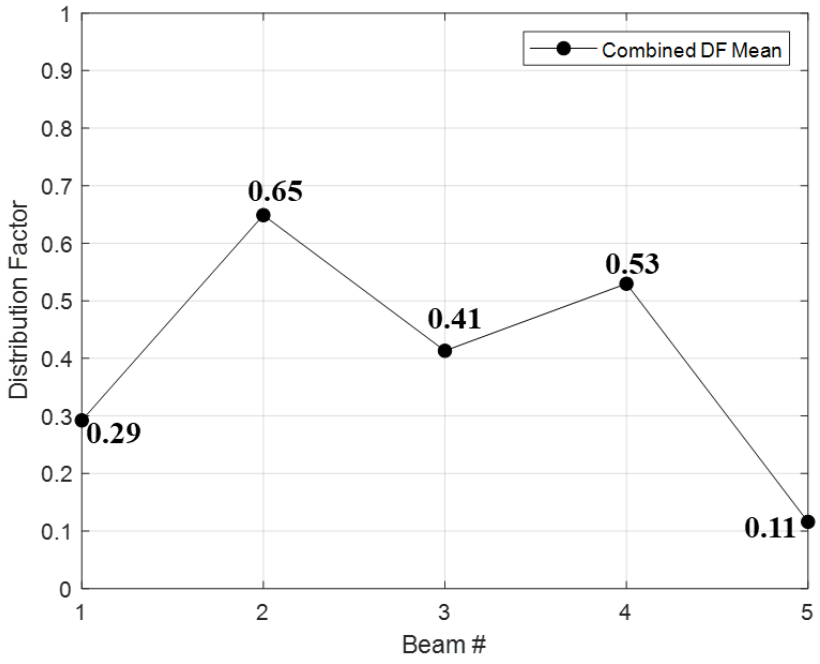

Figure 7.17. Mean DF of Each Beam of Two-Lane Loaded Cases (Bridge #2).

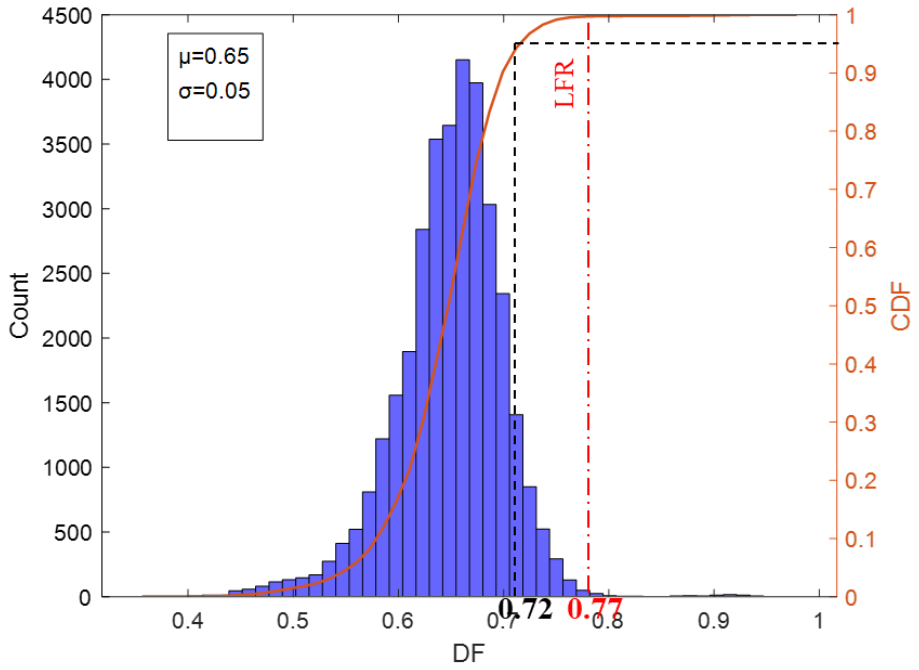

Figure 7.18. Histogram and CDF of Beam #2 Two-Lane Loaded Combined DFs (Bridge #2).

7.4.3.3. Load Rating for Bridge #2

The load ratings for Bridge #2 are summarized in Table 7.6 and Table 7.7. The Bridge #2 DF was refined from 0.77 to 0.72. This decrease led to an increase in both the inventory and operating LFR. The increase in load ratings was not as significant as Bridge #1 but still yielded helpful information.

Table 7.6. Bridge #2 Inventory Load Factor Rating.

Truck	Without B-WIM	With B-WIM
HS20	1.07	1.14
H20	1.46	1.55
SU4	1.32	1.48
SU5	1.19	1.24
SU6	1.08	1.14
SU7	0.98	1.02

Table 7.7. Bridge #2 Operating Load Factor Rating.

Truck	Without B-WIM	With B-WIM
HS20	1.87	2.00
H20	2.56	2.73
SU4	2.31	2.43
SU5	2.09	2.19
SU6	1.87	1.97
SU7	1.71	1.80
EV2	2.25	2.36
EV3	1.48	1.56

7.4.4. Bridge #3

Bridge #3 is a steel rolled I-beam bridge on IH 35 (Wichita Falls District) that was built in 1948 and rehabilitated in 1985. Details and cross-section views can be found in Section 4 and Section 5. The bridge superstructure is comprised of two W36×150 exterior girders and four W36×170 interior girders. The exterior girders are spaced 7.0 ft apart and have a yield strength of 33 ksi. The interior girders are spaced 8.0 ft apart and have a yield strength of 33 ksi. The slab is 17.375 inches thick with a compressive strength of 2.5 ksi. The relatively thick deck is due to a rehabilitation project where the roadway alignment was raised. Figure 7.19 illustrates the retrofitted cross-section with the additional topping slab and dowel connection. The bridge was not designed as composite between the steel beams and the original concrete deck.

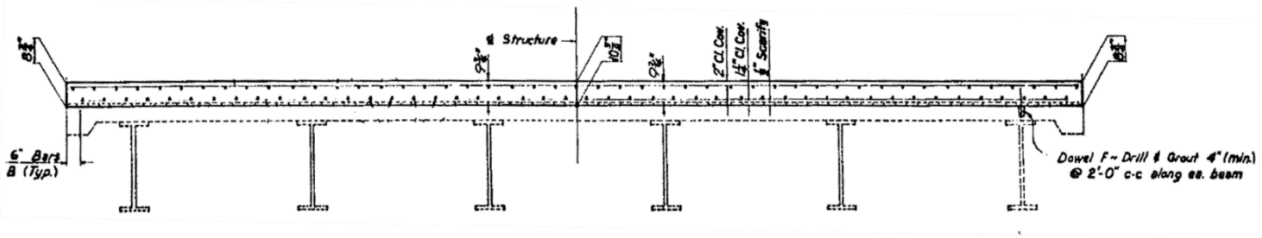

Figure 7.19. Retrofit Cross Section of Bridge #3.

7.4.4.1. Distribution Factors and Composite Action for Bridge #3

The B-WIM data shown in Table 6.17 was used to determine the refined DFs. The DFs of each beam were calculated. Figure 7.20 and Figure 7.21 show box plots and their mean values of left lane trucks and right lane trucks, respectively. Beam #4 had the largest average DF for the one-lane loaded case. Figure 7.22 shows the histogram of calculated Beam #4 DFs, and Figure 7.23 shows the CDF of the DFs. The mean value is 0.31 with a standard deviation of 0.02, and the 95th percentile value is 0.33. As a comparison, the DF calculated by the LFR method for the interior beam with one lane loaded is 0.57 (see Figure 7.22).

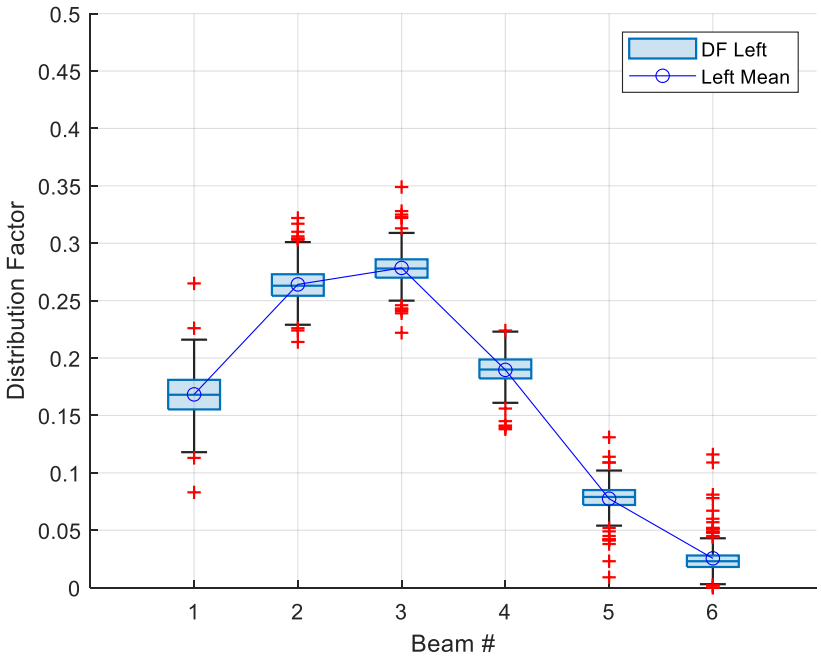

Figure 7.20. Box Plot of DFs on Left Lane Truck Passing Events (Bridge #3).

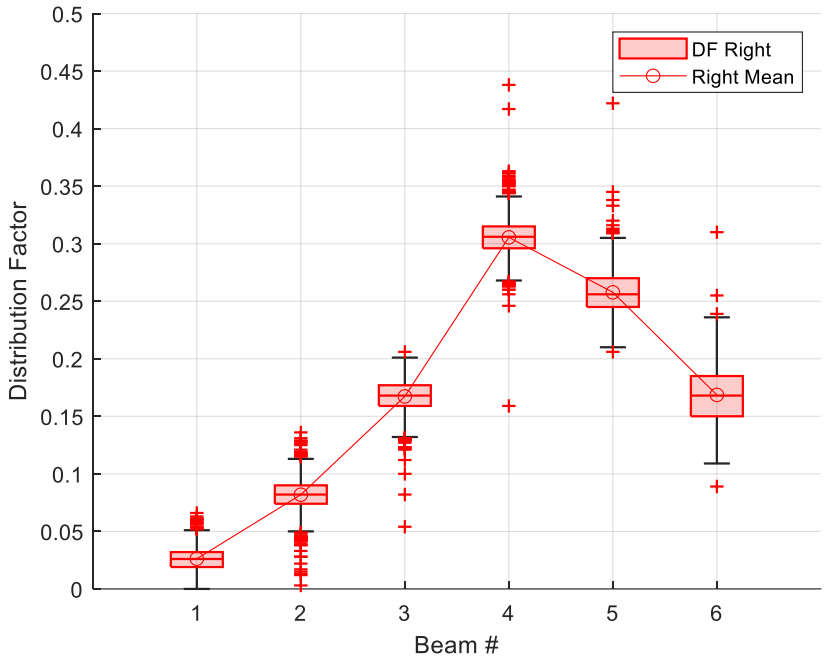

Figure 7.21. Box Plot of DFs on Right Lane Truck Passing Events (Bridge #3).

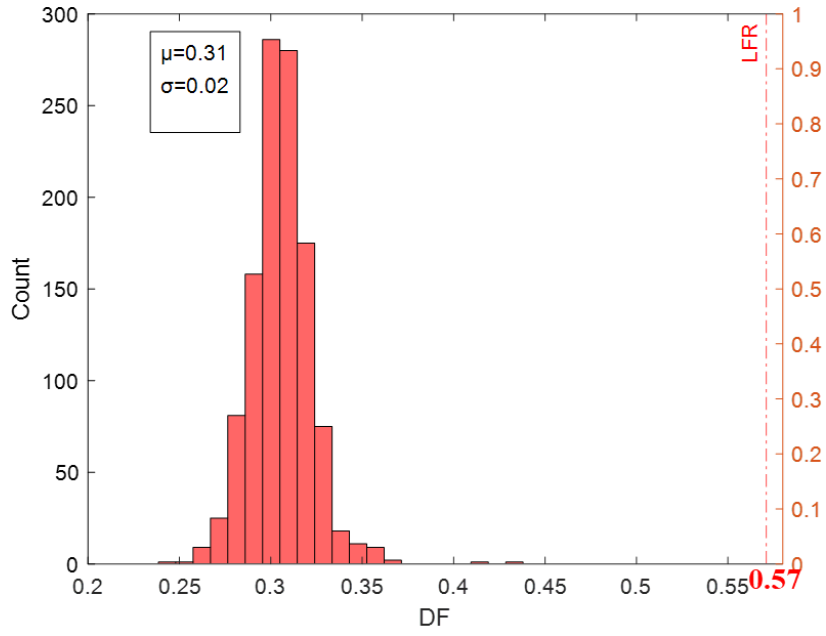

Figure 7.22. Histogram of Beam #4 DFs for One-Lane Loaded (Bridge #3).

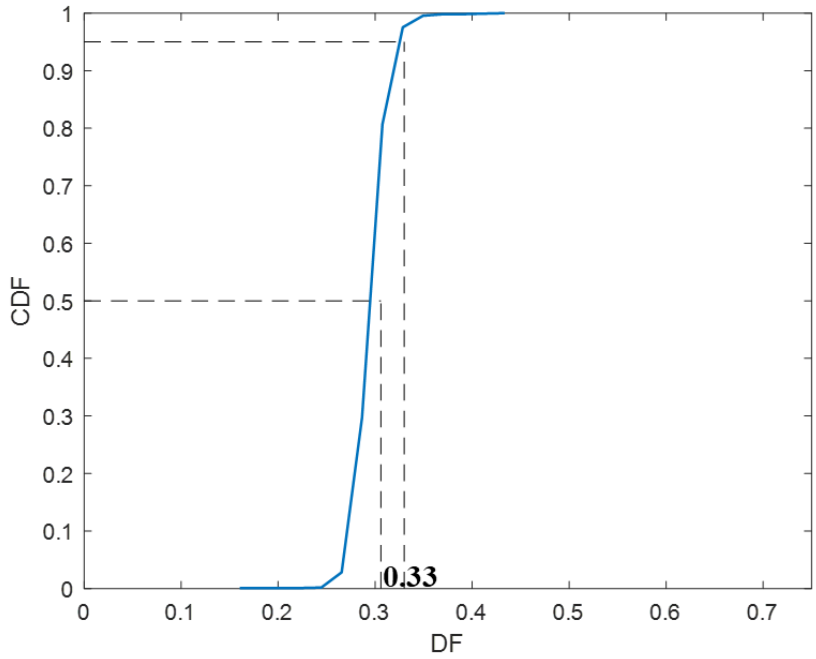

Figure 7.23. CDF of Beam #4 DFs for One-Lane Loaded (Bridge #3).

To determine the two-lane loaded DF, the left lane DFs and right lane DFs were summed up with a total of 252,882 combinations. Figure 7.24 demonstrates the box plot of the combined DFs for each beam, and Figure 7.25 shows the mean combined DFs. Summing up the mean DF of each beam, the total is 1.99. Figure 7.26 shows the histogram and CDF of the controlling beam (Beam 4) DFs. The mean value is 0.50 with a standard deviation of 0.02, and the 95th percentile value is 0.53. The DF calculated by the LFR method for the interior beam with two lanes loaded is 0.73 (see Figure 7.26). This relatively significant difference may be attributed to the unusually significant deck slab thickness, which is doing a better job distributing the load laterally. Another possible cause may be the torsional stiffness reduction due to the concrete cracking. This is explored in Appendix A with theoretical derivation of live load distribution factors.

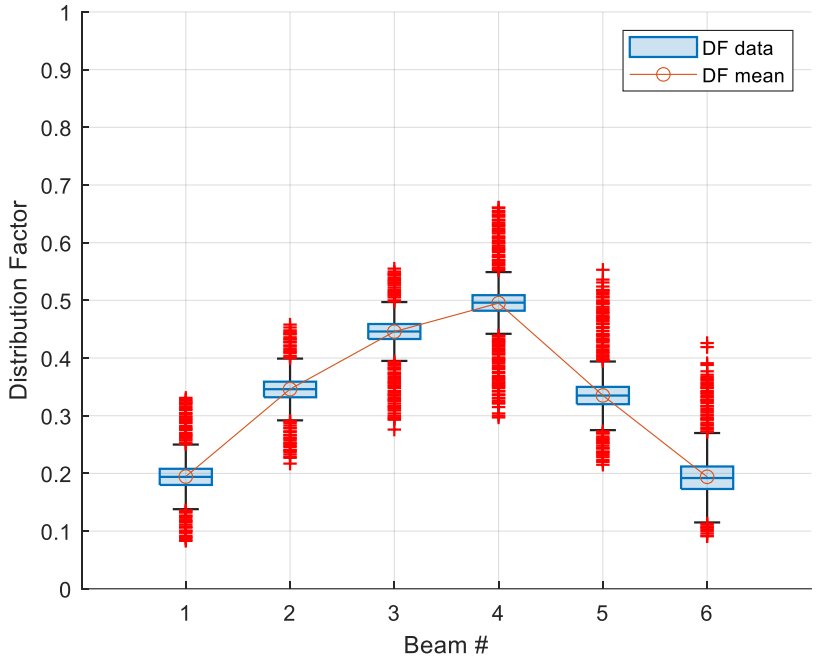

Figure 7.24. Box Plot of DFs of Two-Lane Loaded Cases (Bridge #3).

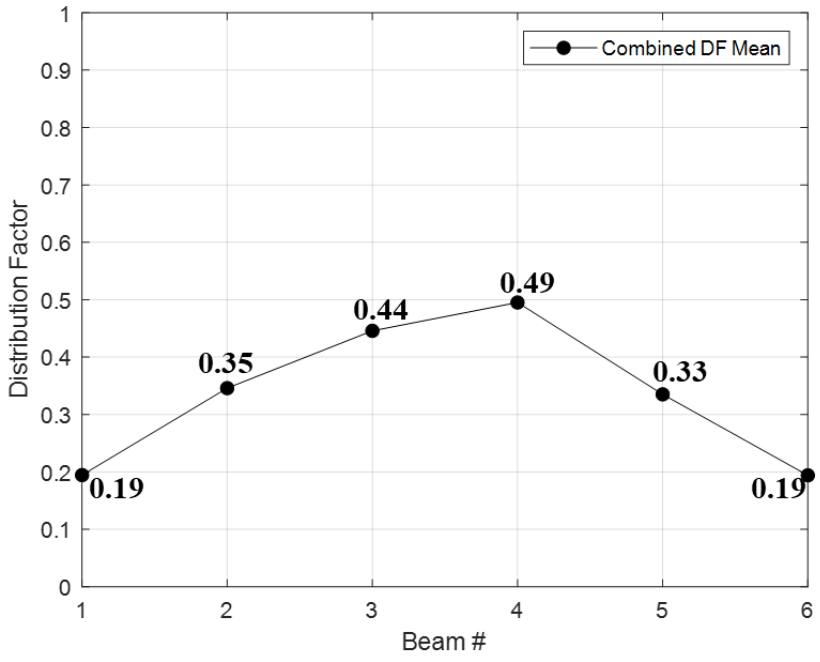

Figure 7.25. Mean DF of Each Beam of Two-Lane Loaded Cases (Bridge #3).

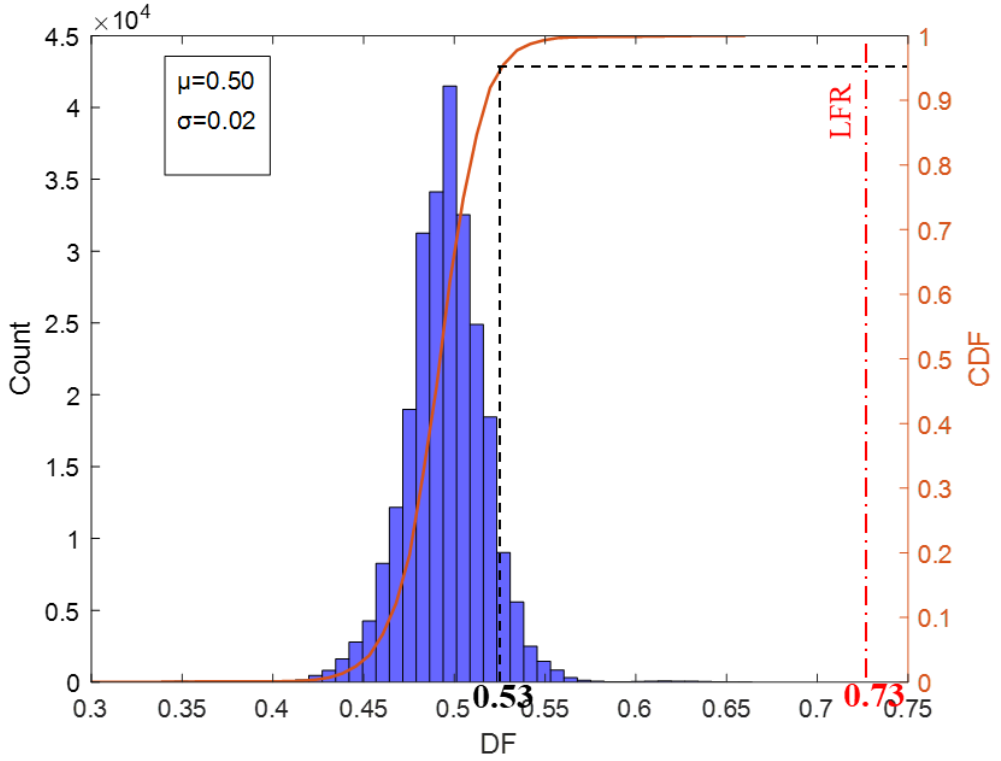

Figure 7.26. Histogram and CDF of Beam #4 Two-Lane Loaded Combined DFs (Bridge #3).

To determine the level of composite action, Beam #3 and Beam #4 were instrumented with supplemental strain gauges near mid-height. The interior steel beam has an overall depth of 36.16 inches. One strain gauge was installed at the center of the bottom flange. The other strain gauge was instrumented at 17.1 inches from the bottom surface of the bottom flange. Figure 7.27 shows the configuration of Beam #4 and sensor locations.

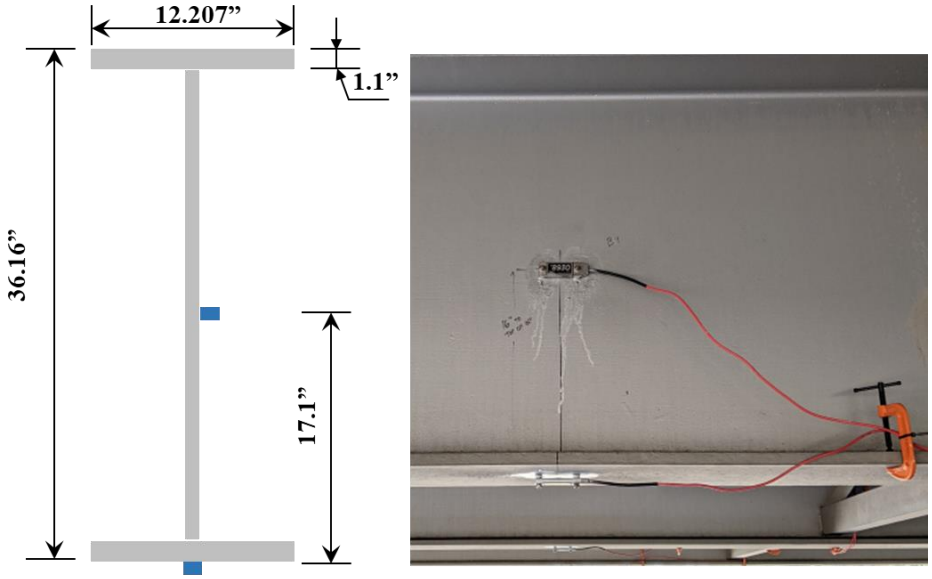

Figure 7.27. Configuration of the Interior Beam for Composite Action Analysis.

The bridge deck was retrofitted with a thickness of 17.375 inches. The elastic neutral axis (ENA) was calculated to be 38.6 inches from the bottom surface line of the bottom flange (for pure bending). The plastic neutral axis (PNA) was located 45.5 inches from the bottom surface line of the bottom flange (for pure bending). Figure 7.28 shows the locations of the ENA and PNA for interior beams. The ENA and PNA are actually lower due to the axial force induced from the relatively stiff original bearings.

The data from the 15 calibration tests were utilized for preliminary composite action analysis. A zeroing algorithm was implemented in the post-processing phase, so only the relative strain measurements were used for each truck event. Figure 7.29 shows the neutral axis calculation for Beam #3 and Beam #4 based on the 15 calibration tests. It was found that as the truck weight went up, the calculated neutral axis moved downward.

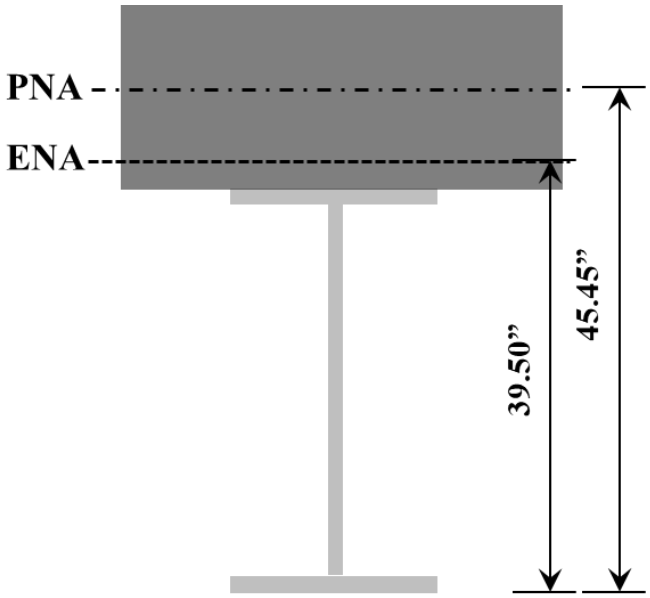

Figure 7.28. Location of the Elastic and Plastic Neutral Axis of the Interior Beams.

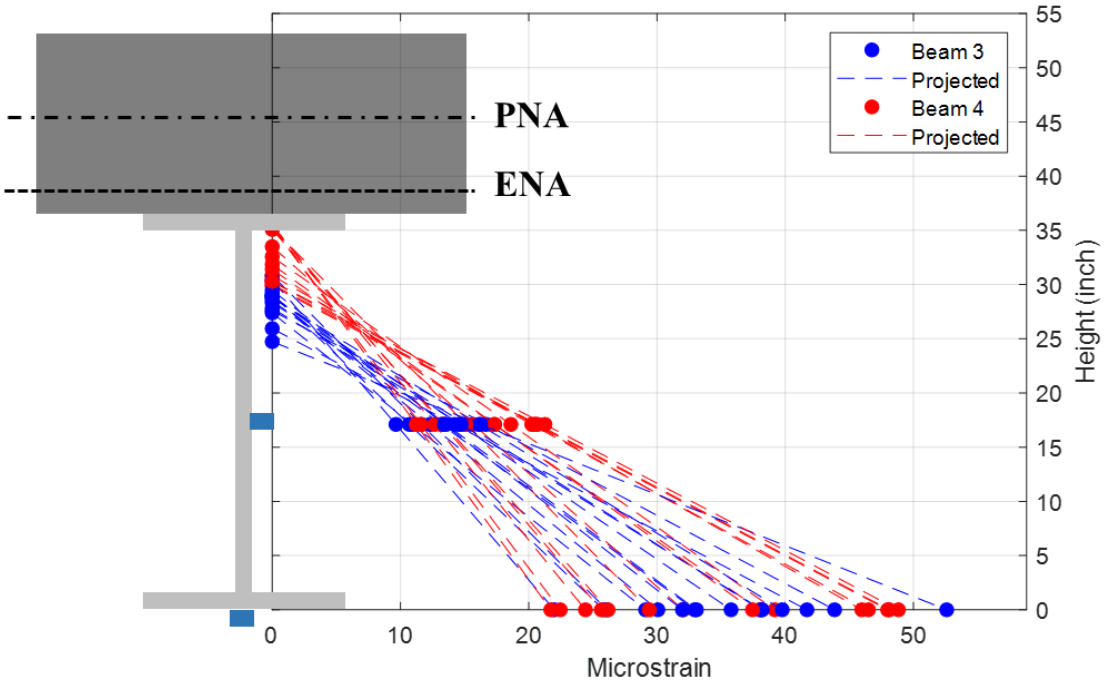

Figure 7.29. Neutral Axis Calculation of the 15 Calibration Tests.

The conventional approach for the identification of the neutral axis using ambient truck traffic is to plot the strain gauge profiles during a significant truck event. Then these lines are projected to find the vertical axis intercept. However, the results from a single truck event are deceiving and do not illustrate the variability of the field-identified neutral axis. To comprehensively evaluate the composite nature of the structure, a set of ambient data was utilized. A total of 439 trucks passed the right lane. The neutral axis was projected for all truck events at Beam #4. The objective was to quantitatively determine the distribution of the neutral axis location and the variability in composite action. This variability can come from many areas, such as the dynamic amplification of different types of trucks traveling at different speeds. In addition, the axial component varies based on the weight of the trucks.

Figure 7.30 provides a histogram of the neutral axis locations. The data indicate a mean neutral axis location of 35.0 inches with a standard deviation of 2.8 inches. The results indicate at least partially composite behavior under truck loading. Figure 7.31 provides the calculated neutral axis compared to the strain profile for each truck event. The neutral axis lowers when the strain magnitude increases due to heavier trucks, as expected. The bridge is essentially fully composite to a relatively high load level because there are other mechanisms at play. The bearings are original from 1948 and likely do not move under live loading. This induces an axial force into the beam, which moves the ENA downward.

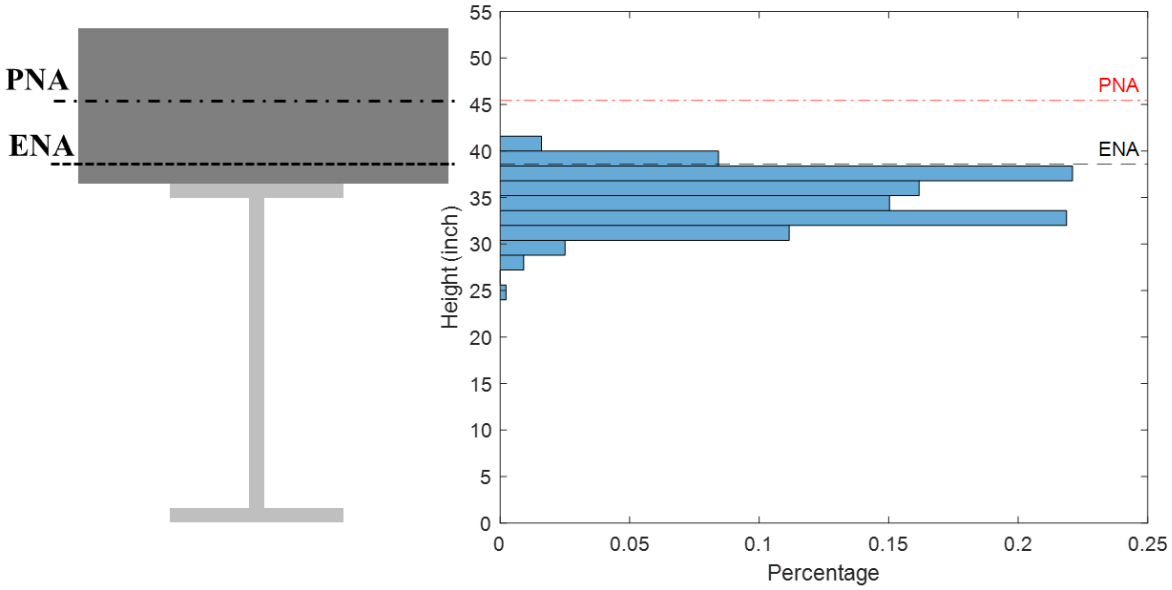

Figure 7.30. Histogram of Apparent Neutral Axis Locations.

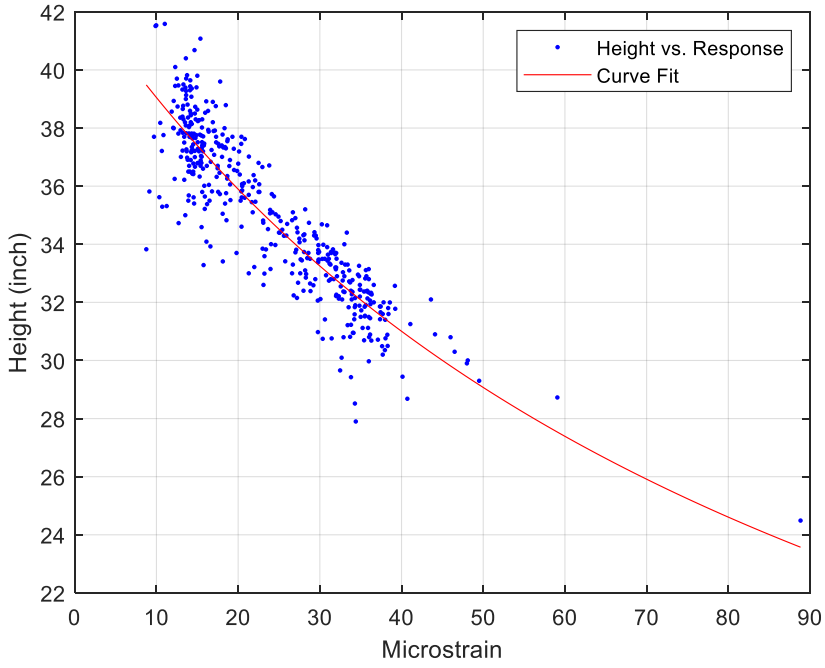

Figure 7.31. Field-Measured Apparent Neutral Axis versus Strain Response.

7.4.4.2. Load Rating for Bridge #3

Like Bridge #1 and #2, Bridge #3 load rating utilized a refined field-identified DF. However, composite action was also analyzed. Table 7.8 and Table 7.9 show the outputs of the redefined LFR with respect to updating the DF, composite action, or both. The interior beam is presented because it controls over the exterior beam (despite a smaller beam size).

The Bridge #3 load rating results show more variation than the prior bridges. First, the load rating increase is relatively significant just from the field-refined DF. The HS20 ratings increased by roughly 50 percent. The percentage increase is higher than usual, which can be attributed to the substantial deck thickness stiffening the structure and shedding the load laterally more than conventional bridges. The load rating increase for composite action is even more significant than that from the refined DFs. This is typically a significant increase but further enhanced due to the thick deck slab. The operating ratings are all greater than 1.0 with only the refined DFs. Therefore, the additional benefit from composite action (even partial) only improves the situation. Overall, the B-WIM evaluation indicates that Bridge #3 is performing much better for supporting vertical loading than the original load ratings indicate.

Table 7.8. Bridge #3 Inventory (Interior Beam) Load Factor Rating.

Truck	Without B-WIM	B-WIM with refined DF	B-WIM with redefined composite action	B-WIM with redefined composite action and DF
HS20	0.73	1.10	1.89	2.72
H20	1.01	1.52	2.62	3.77
SU4	0.83	1.25	2.15	3.09
SU5	0.77	1.15	1.98	2.85
SU6	0.69	1.04	1.79	2.57
SU7	0.64	0.97	1.66	2.39

Table 7.9. Bridge #3 Operating (Interior Beam) LFR.

Truck	Without B-WIM	B-WIM with refined DF	B-WIM with redefined composite action	B-WIM with redefined composite action and DF
HS20	1.22	1.83	3.15	4.53
H20	1.69	2.54	4.36	6.28
SU4	1.39	2.08	3.58	5.15
SU5	1.28	1.92	3.30	4.75
SU6	1.15	1.73	2.98	4.29
SU7	1.07	1.61	2.77	3.99
EV2	1.37	2.05	3.53	5.09
EV3	0.90	1.35	2.32	3.35

7.5. Load Ratings for Actual Trucks Captured from the B-WIM Systems

An additional benefit of bridge evaluation utilizing a B-WIM system is that actual trucks can be load rated. As a result, several heavy trucks from the B-WIM live load data analysis were selected for load rating of each bridge. Table 7.10 to Table 7.12 summarizes the axle and weight information of the selected trucks. Only single truck events were evaluated for this supplemental study. Also, the results provided in this section are valid for the duration the B-WIM system was deployed.

Table 7.10. Trucks Selected from Live Load Data (Bridge #1).

Truck	Axle Weight (kips)									Axle Spacing (ft)							
	1	2	3	4	5	6	7	8	9	1 to 2	2 to 3	3 to 4	4 to 5	5 to 6	6 to 7	7 to 8	8 to 9
1	10.2	22.6	22.0	8.1	7.1	11.0	11.0	16.8	7.9	25.3	5.0	26.8	4.8	27.3	4.5	14.3	16.7
2	16.5	11.9	30.0	30.2	24.8	21.6	23.2	16.8		15.3	4.7	4.7	35.0	4.7	4.7	14.0	
3	15.6	14.1	26.2	28.5	23.2	20.5	25.2			18.2	4.5	4.7	35.8	4.9	4.7		
4	19.6	24.3	22.6	23.1	22.6	30.3				20.1	4.6	36.5	4.6	4.6			
5	18.8	24.5	22.3	27.4	31.5					21.1	4.8	32.1	10.1				
6	28.4	21.5	16.6	21.8						22.1	4.7	4.7					
7	13.5	26.9	24.1							21.4	4.4						
8	20.0	34.1								25.9							

Table 7.11. Trucks Selected from Live Load Data (Bridge #2).

Truck	Axle Weight (kips)									Axle Spacing (ft)							
	1	2	3	4	5	6	7	8	9	1 to 2	2 to 3	3 to 4	4 to 5	5 to 6	6 to 7	7 to 8	8 to 9
1	12.4	28.8	24.2	15.3	13.2	14.4	15.0	18.2		17.6	5.4	30.6	5.4	5.2	5.4	5.4	
2	6.5	24.8	20.2	20.1	25.6	17.9	21.3			18.6	5.1	4.9	34.2	4.8	4.8		
3	6.3	14.1	12.8	20.1	18.4	23.4				20.5	5.5	34.4	5.1	8.8			
4	25.1	25.0	22.6	19.8	23.8					16.3	5.4	29.6	5.0				
5	7.8	21.2	22.1	20.7						13.1	4.8	19.5					
6	9.1	24.3	20.6							19.7	5.0						
7	9.3	36.9								26.4							

Table 7.12. Trucks Selected from Live Load Data (Bridge #3).

Truck	Axle Weight (kips)									Axle Spacing (ft)							
	1	2	3	4	5	6	7	8	9	1 to 2	2 to 3	3 to 4	4 to 5	5 to 6	6 to 7	7 to 8	8 to 9
1	14.9	21.3	20.5	18.2	17.8	15.0	21.9			17.5	5.9	5.7	42.4	5.7	5.7		
2	50.9	33.8	63.4	11.3	24.6	9	35.3			5.0	11.5	6.1	6.9	6.1	4.8		
3	14.5	19.0	14.8	24.2	11.7	20.4				20.8	5.7	35.4	4.6	5.0			
4	16.2	32.9	35.3	17.1	17.8					17.7	4.9	35.3	4.5				
5	17.2	21.3	24.8	30.1						5.9	16.9	4.8					
6	17.7	36.3	27.8							22.8	5.0						
7	17.2	45.3								26.8							

The axle spacings and weights in Table 7.10 to Table 7.12 above were put into a 2D structural analysis software (qBridge) to determine the maximum moment due to live load. The field-identified distribution factors from the case studies were used for this analysis. Table 7-13 through Table 7.15 show the live load moment as well as the inventory and operating ratings based on actual trucks captured from the B-WIM system (defined above).

Table 7.13. Bridge #1 Moment and LFR—Axle Weight and Spacing.

Truck	Number of Axles	GVW (kips)	Moment (kip-ft)	Inventory LFR	Operating LFR
1	9	116.6	793.0	1.96	3.27
2	8	175.1	1286.0	1.21	2.02
3	7	153.3	1201.0	1.29	2.16
4	6	142.5	1207.0	1.29	2.15
5	5	124.6	938.0	1.65	2.76
6	4	88.4	1291.0	1.20	2.01
7	3	64.5	932.0	1.67	2.78
8	2	54.1	705.0	2.20	3.68

Table 7.14. Bridge #2 Moment and LFR—Axle Weight and Spacing.

Truck	Number of Axles	GVW (kips)	Moment (kip-ft)	Inventory LFR	Operating LFR
1	8	141.5	1172.0	1.03	1.81
2	7	136.4	1152.0	1.05	1.84
3	6	95.1	1006.0	1.20	2.10
4	5	116.3	1098.0	1.10	1.93
5	4	71.8	1022.0	1.18	2.07
6	3	54.1	812.0	1.49	2.61
7	2	46.1	744.0	1.62	2.84

Table 7.15. Bridge #3 Moment and LFR—Axle Weight and Spacing.

Truck	Number of Axles	GVW (kips)	Moment (kip-ft)	Inventory LFR—Non-Composite	Operating LFR—Non-Composite	Inventory LFR—Composite	Operating LFR—Composite
1	7	129.5	655.0	1.00	1.67	2.48	4.14
2	7	228.4	1538.0	0.43	0.71	1.06	1.76
3	6	104.6	597.0	1.10	1.83	2.72	4.54
4	5	119.3	824.0	0.80	1.33	1.97	3.29
5	4	93.4	737.0	0.89	1.48	2.21	3.68
6	3	81.8	754.0	0.87	1.45	2.16	3.59
7	2	62.4	562.0	1.17	1.95	2.89	4.82

These B-WIM load rating results provide some general findings. First, as expected, the total number of axles does not play a major role in the LFRs since the bridges are relatively short. The axle weight and axle spacings have a larger influence on the LFRs. As the weight of the axles increase (or spacing of the axles decreases), the

moment increases and the LFR decreases. The results from the first two bridges produced load ratings all above 1.0, which indicates little concern for overload issues. All but one of the non-composite operating load ratings for the third bridge were above 1.0. The Truck 2 was captured during the calibration test as a crane truck (see Figure 7.32). This truck had a GVW of 228 kips with 7 axles (total wheelbase 40 ft). The load ratings with this truck are conservative because the data indicate composite action is present. In the composite state the load ratings are well above 1.0. Overall, substantial trucks above the legal load limits were captured with the B-WIM system and load rated. This is a unique capability of a B-WIM system.

Figure 7.32. Heavy Crane Truck Passing Bridge #3.

7.6. Further Research on Bridge #3

7.6.1. Introduction

Bridge #3 was not designed as composite between the steel beams and the original concrete deck. However, the field test data indicated that the bridge was at least partially composite. Certain factors contributed to this, such as the axial force induced from the relatively stiff original bearings, and the concrete deck after the rehabilitation project. In this section, a finite element model of the Bridge #3 was built and calibrated based on the field test results. Finite element analysis sensitivity studies were conducted to quantify the influence of two factors, axial stiffness induced from the bearings and the concrete modulus of the deck slab, on the apparent neutral axis location.

7.6.2. Finite Element Model

7.6.2.1. Model Description

The finite element model was created utilizing Strand7 software. Strand7 has fully integrated visual environment combined with a suite of powerful solvers that give functionality in a single application.

The 3D finite element superstructure model was developed according to details from the as-built and rehabilitation drawings. Four-node shell elements (Quad4 designation in Strand7) were used to represent the bridge deck slab and barriers. Since the thickness of the bridge deck was not uniformly distributed, the thickness of the bridge deck plate element was calculated as 16.31 inches by taking the average of the maximum and minimum values of the deck thickness according to the drawings. Two-node beam elements (Beam2 designation in Strand7) were utilized to model the steel

girders. Rigid links were used to attach the girders to the deck slab, the concrete barriers to the deck slab, and the girders to the bearings. All the elements were divided into a mesh with 1.0 ft length. Figure 7.33 shows the finite element model of the Bridge #3.

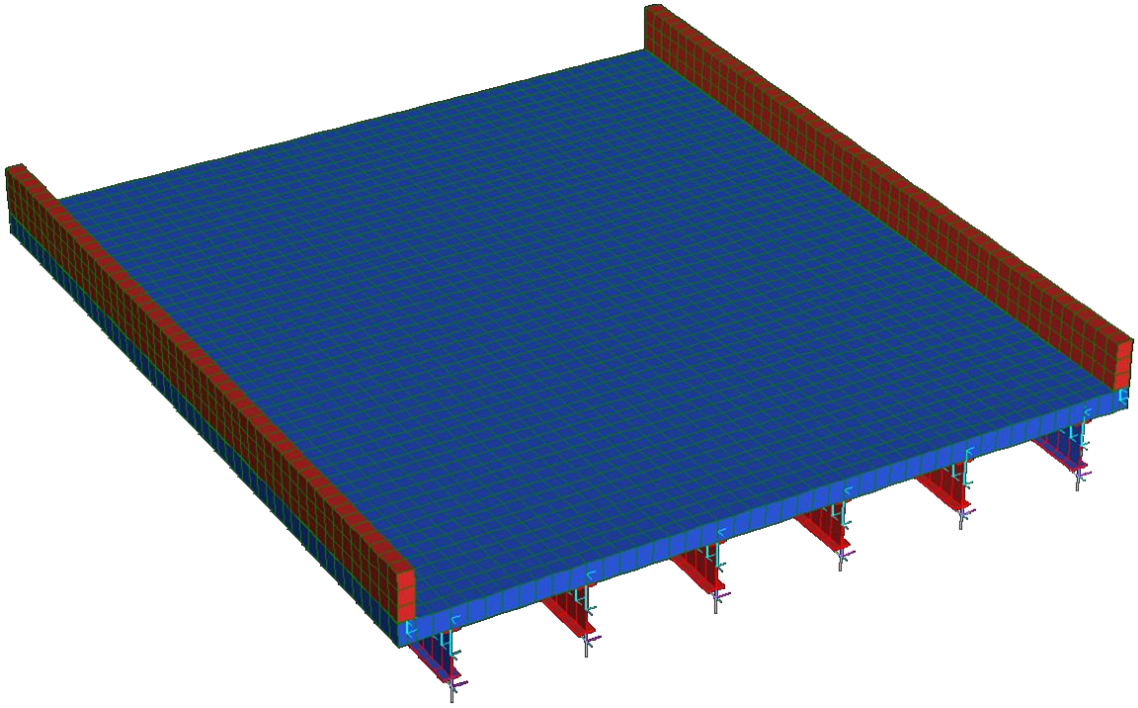

Figure 7.33. Finite Element Model of Bridge #3.

7.6.2.2. Material Properties

Standard material properties were assigned to the structural steel. The stiffness (modulus) is of importance since it affects the apparent neutral axis location. Table 7.16 summarizes the assigned properties of the finite element model. In this study, the modulus of concrete was explored as an unknown parameter and was varied from 1000 ksi to 5000 ksi during the model updating process. This is discussed further in Section 7.6.3.

Table 7.16. Material Properties of the Finite Element Model.

Parameter	Steel	Concrete
Modulus of Elasticity (ksi)	29000	2000 to 5000
Poisson's Ratio	0.25	0.2

7.6.2.3. Boundary conditions

Boundary conditions indicate the global supports of the superstructure model and how the model is restrained from movement. Nodal restraints at both ends of the superstructure were applied. The south end of the bridge was restrained in all three translational degrees of freedom while the rotational restraints were released (pinned support conditions). The north end supports (where the vehicles enter the bridge) were restrained as roller supports. A translational stiffness was applied in the longitudinal direction to simulate the axial stiffness induced from the old steel bearings. The boundary condition and the added translational stiffness of the north ends are shown in Figure 7.34. The added longitudinal stiffness is also treated as an unknown parameter varying from 0 to 10,000 kip/ft. This is discussed further in Section 7.6.3.

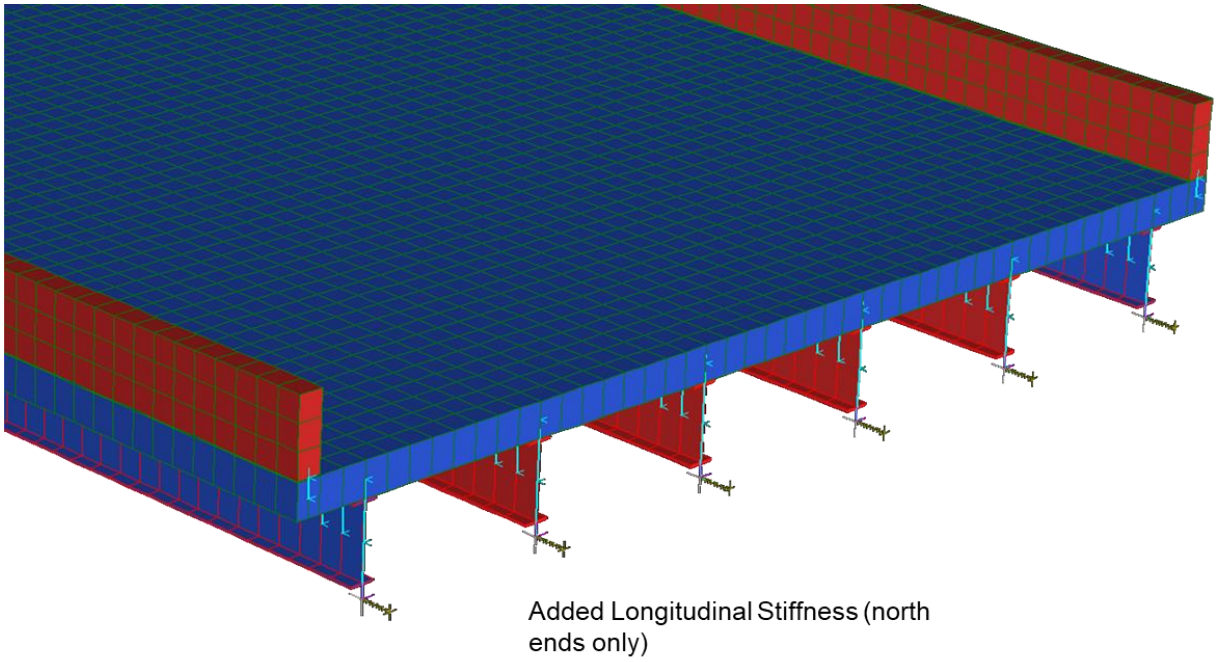

Figure 7.34. Boundary Conditions of the North End

7.6.2.4. Loading

Truck loads were defined utilizing the load path function in Strand7. The Bridge #3 calibration truck A was used to simulate the truck loads. The wheel loads of the truck were modeled as point loads and the lateral position of the trucks were modeled as passing the bridge along the center of the lane. Figure 7.35 shows the load path on the outside lane of the bridge. Figure 7.36 Shows an example of the deformed shape of the girders under the trucks loads on the outside lane. Girder #4 (counting from the left) had the maximum deformation under outside loads as observed from the field tests.

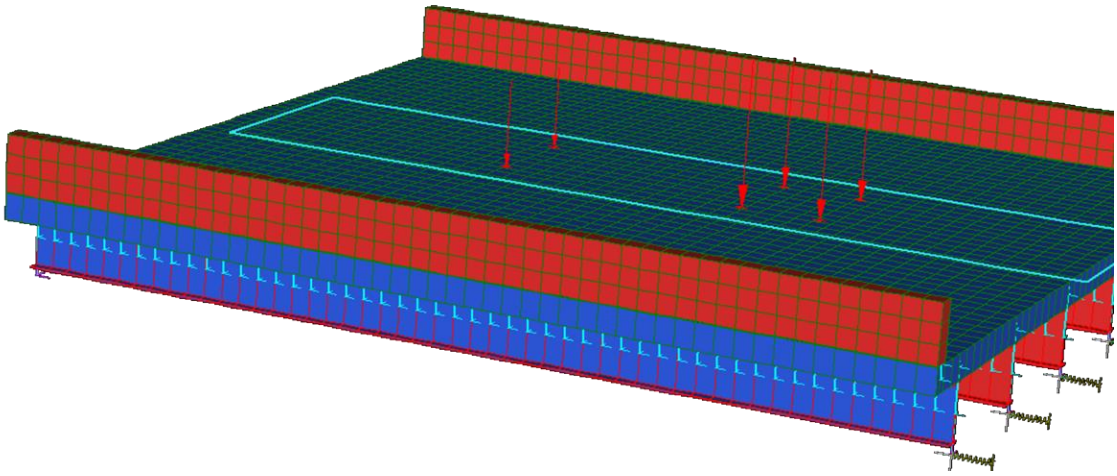

Figure 7.35. Truck Loads on the Outside Lane.

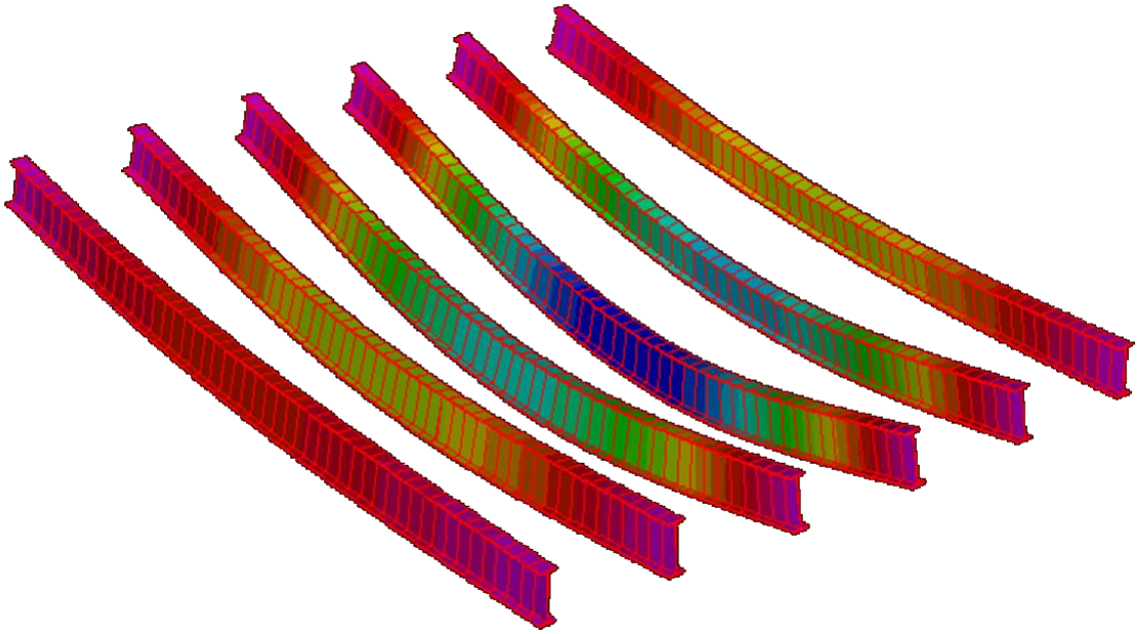

Figure 7.36. Example of Deformed Girders Under Outside Lane Load.

7.6.3. Model Calibration

The finite element model was checked and screened for errors. However, to adequately represent the real structure, and understand the influence of unknown parameters, validating the numerical model with the field test results is necessary. The process of model calibration involves reconciling differences between finite element analysis and field test results. The two unknown parameters, concrete modulus and support longitudinal stiffness were varied to calibrate the finite element model. The field B-WIM calibration Test #1 was utilized to calibrate the finite element model. Since the apparent neutral axis locations of the girders were the main factor for investigations. The strain results of the Girder #3 and Girder #4 from the finite element analysis and the field measured results were compared, since only these two girders had strain gauges installed on the web. The objective function used referred to as the square root sum of squares, and was constructed as Eq. (7.1).

$$Objective\ Function = \sqrt{\sum_{1}^{2}\left(\mu_{F_i} - \mu_{M_i}\right)^2 + \sum_{1}^{2}\left(\omega_{F_i} - \omega_{M_i}\right)^2} \qquad (7.1)$$

where the μ_F is the girder bottom flange strain response from the finite element analysis, μ_M is the girder bottom flange strain response from the field measured result, ω_F is the girder web strain response from the finite element analysis, ω_M is the girder web strain response from the field measured result. Since only Girder #3 and Girder #4 had strain gauges installed on the web, the numbers 1 and 2 indicate the strain response of Girder #3 and Girder #4, respectively.

The concrete modulus was varied from 1000 ksi to 5000 ksi with a 500 ksi increment, while the longitudinal stiffness was varied from 0 to 10000 kip/ft with a 1000

kip/ft increment. In addition, a set of simulations were conducted with a very large value of the translational stiffness to investigate a fully restrained condition. Table 7.17 summarizes the objective function values for the combination of concrete modulus and translational stiffness.

Table 7.17. Objective Function Results Summary.

Longitudinal Stiffness (kip/ft)	Concrete Modulus (ksi)								
	1000	1500	2000	2500	3000	3500	4000	4500	5000
0	24.54	17.81	13.54	10.60	8.66	7.61	7.37	7.78	8.58
1000	21.67	15.27	11.32	8.78	7.36	6.95	7.32	8.17	9.25
2000	19.28	13.16	9.52	7.41	6.59	6.80	7.65	8.78	10.02
3000	17.26	11.39	8.08	6.47	6.28	7.02	8.19	9.50	10.82
4000	15.55	9.92	6.97	5.94	6.35	7.47	8.84	10.24	11.61
5000	14.10	8.70	6.16	5.75	6.66	8.04	9.52	10.97	12.36
6000	12.86	7.71	5.66	5.85	7.11	8.66	10.20	11.68	13.07
7000	11.80	6.94	5.43	6.13	7.64	9.28	10.86	12.35	13.73
8000	10.92	6.37	5.42	6.53	8.20	9.89	11.49	12.97	14.35
9000	10.18	5.99	5.58	6.99	8.76	10.49	12.09	13.56	14.93
10000	9.57	5.78	5.86	7.48	9.31	11.05	12.65	14.12	15.47
99999999	21.33	22.84	24.38	25.76	26.98	28.08	29.07	29.98	30.82

The objective function values are plotted as shown in Figure 7.37. It was found that when the concrete modulus was approximately 2000 ksi and the longitudinal stiffness is 8000 kip/ft, the objective function had the minimum value. The strain response of this combination was compared with the field measured results of Girder #3 and Girder #4 as shown in Table 7.18. The average difference was -2.8 percent between the finite element analysis and field measured results. The comparison of results showed the reasonable agreement between the finite element analysis and selected field test. The

selected concrete modulus and longitudinal stiffness were utilized for sensitivity studies and are discussed further in Section 7.6.4.

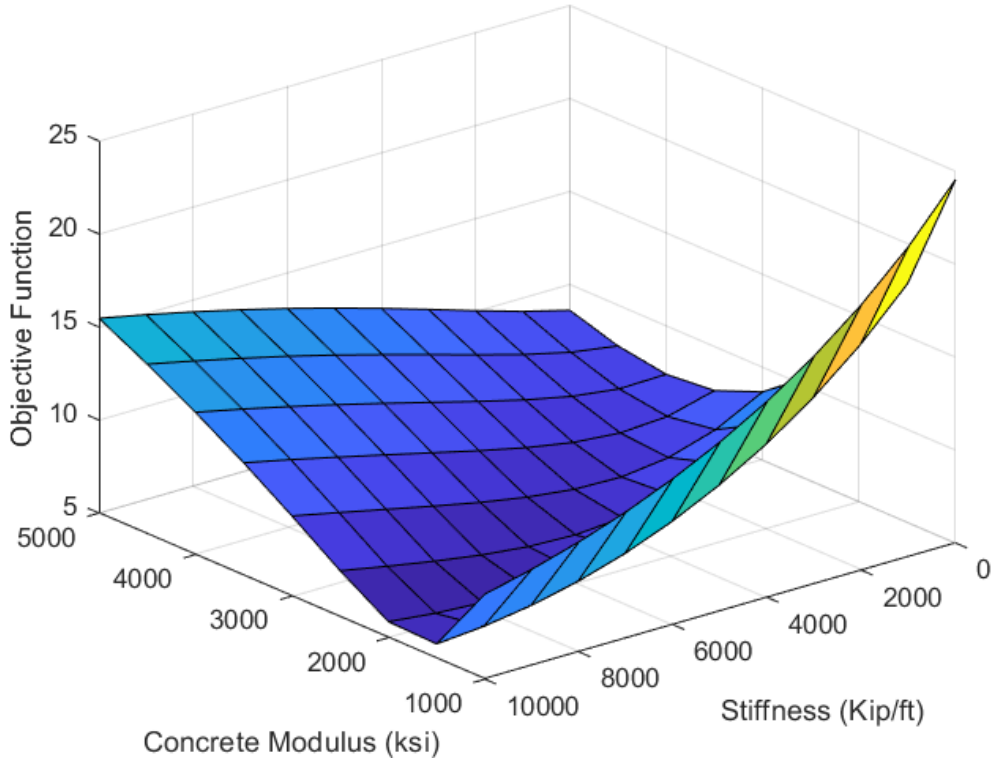

Figure 7.37. Objective Function Values versus the Two Parameters.

Table 7.18. Strain Response Comparison (2000 ksi Modulus, 8000 kip/ft Stiffness).

Method	Strain Response (Microstrain)			
	Girder #3	**Girder #4**	**Web #3**	**Web #4**
Field Measured	34	50	13	20
Finite Element Analysis	30	50	13	24
Percent Difference	11%	0%	-1%	-21%

7.6.4. Neutral Axis Study with the Parameters

7.6.4.1. Introduction

The finite element model was calibrated with a reasonable agreement on the results compared with field test. To evaluate how the two parameters, concrete modulus and longitudinal stiffness influence the neutral axis location of the girders, simulations were conducted as sensitivity studies.

Theoretically, the elastic neutral axis location of the composite cross section moves up when the concrete modulus becomes larger. This is illustrated in Figure 7.38. For the composite material the composite section becomes transformed section. This method transforms the concrete material into an amount of steel that has the same effect as the concrete for analysis purpose as shown in Eq. (7.2):

$$n = \frac{E_2}{E_1} \tag{7.2}$$

where n is the modular ratio, E_2 is the elastic modulus of the concrete material, E_1 is the elastic modulus of steel material.

The elastic neutral axis can be calculated using Eq. (7.3):

$$Y = \frac{\sum_i A_i y_i}{\sum_i A_i} \tag{7.3}$$

where Y is the elastic neutral axis of the composite cross section measured from the bottom of the bottom flange, A_i is the area for different material sections, and y_i is the center of gravity for different material sections measured from the bottom of the bottom flange.

The area of the transformed concrete section can be calculated as shown in Eq. (7.4):

$$A_1 = \frac{b_E}{n} h_1 = \frac{b_E h_1 E_1}{E_2} = A_c \frac{E_1}{E_2} \tag{7.4}$$

where Ac is the area of the untransformed concrete section.

The elastic neutral axis of the composite cross section is calculated as Eq. (7.5):

$$Y = \frac{A_c \frac{E_1}{E_2} y_1 + A_2 y_2}{A_c \frac{E_1}{E_2} + A_2} = \frac{E_1 A_c y_1 + E_2 A_2 y_2}{E_1 A_c + E_2 A_2} \tag{7.5}$$

To evaluate the relationship between the elastic neutral axis location and the concrete modulus, the derivative of the above equation is shown in Eq. (7.6):

$$Y' = \frac{A_c A_2 E_2 \left(y_1 - y_2 \right)}{\left(A_c E_1 + A_2 E_2 \right)^2} \tag{7.6}$$

Since y_1 is larger than y_2, the above equation has a positive result. The sign of the derivative indicates that the neural axis location is increasing when the concrete modulus is getting bigger, as shown in Figure 7.39.

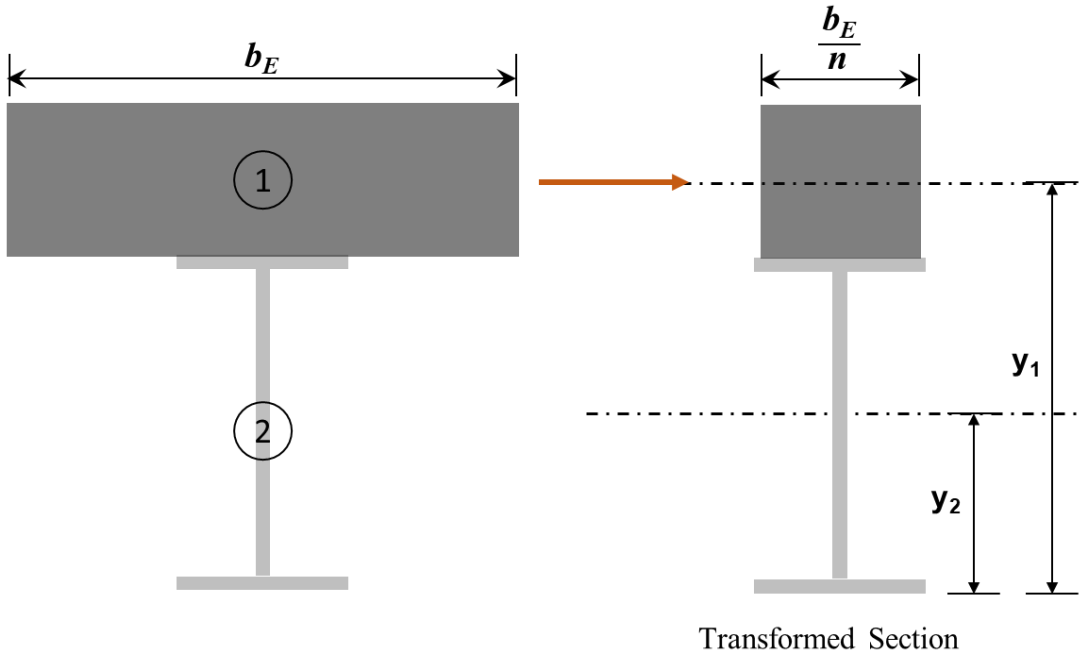

Figure 7.38. Transformed Cross Section.

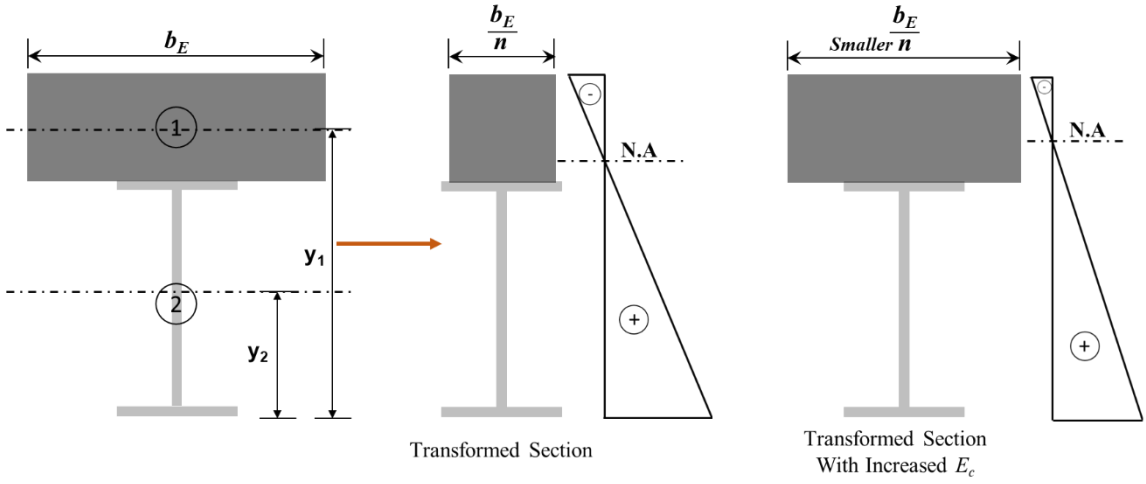

Figure 7.39. Elastic Neutral Axis Moves Up with Increased Concrete Modulus.

The plastic neutral axis location of the composite action also has the similar trend. This is illustrated in Figure 7.40. The compression stress depth can be determined by Eq. (7.7).

$$a = \frac{A_s F_y}{0.85 f_c^{'} b_e} \qquad (7.7)$$

where a is the stress block depth, A_s is the steel tension area, F_y is the steel yield stress, f_c' is the concrete strength, and b_e is the effective slab width. When the concrete modulus becomes larger, the concrete strength and effective width becomes bigger, thus decreases the stress block depth and makes the neutral axis move up, as shown in Figure 7.40.

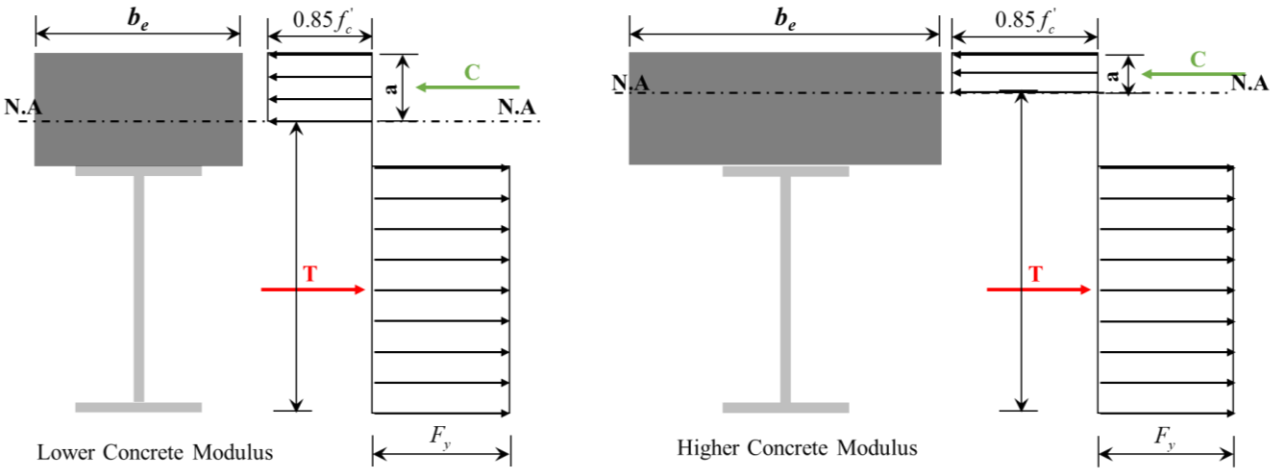

Figure 7.40. Neutral Axis Influenced by the Concrete Modulus

The boundary condition of the bridge north end is illustrated in Figure 7.41. The axial stiffness induced from the bearings can be treated as a longitudinal spring with a stiffness k. The apparent neutral axis of the cross section moves down when the longitudinal stiffness increases as shown in Figure 7.42. The flexural bending is the positive bending moment induced from the truck loading. The axial compression is the restoring longitudinal force from the spring, it also induces a negative bending moment since the force location is below the beam center of gravity. Increasing the truck loading

will increase the longitudinal force from the spring, the combined effect moves the apparent neutral axis further down.

Figure 7.41. Boundary Condition Illustration.

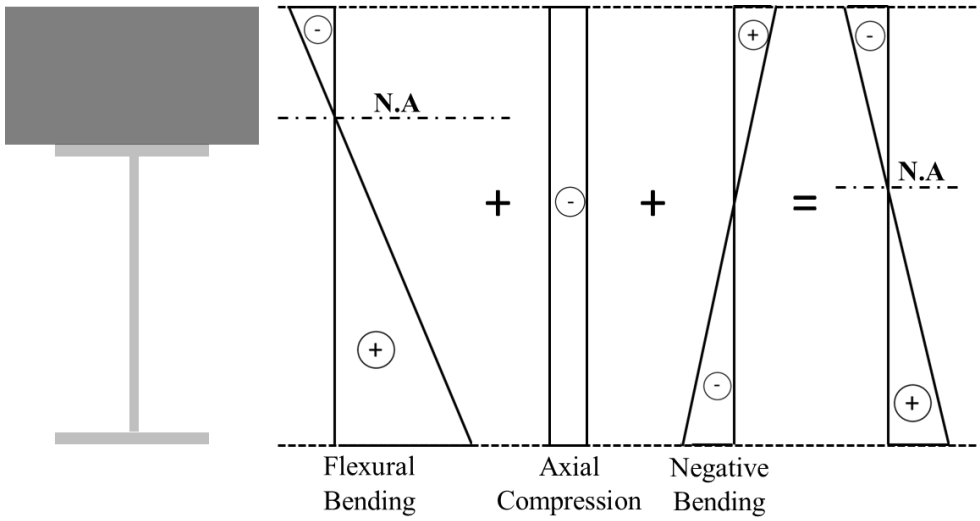

Figure 7.42. Neutral Axis Location Influenced by the Longitudinal Stiffness.

Detailed derivation of the apparent neutral axis location calculation can be found in Appendix B. It also summarizes the details of the theoretical derivation of the apparent neutral axis location under different load cases and concrete modulus.

In the following sections, each of the parameters are evaluated with single degree of freedom sensitivity studies. When evaluating the concrete modulus, the longitudinal stiffness remains at a constant 8000 kip/ft. When evaluating the longitudinal stiffness, the concrete modulus remains at a constant 2000 ksi.

7.6.4.2. Sensitivity Study of the Concrete Modulus

To evaluate the influence of the concrete modulus on the apparent neutral axis location sensitivity studies were performed. Several finite element analyses were conducted with concrete modulus varied from 1000 ksi to 5000 ksi, with a 250 ksi increment while the longitudinal support stiffness was 8000 kip/ft. The apparent neutral axis locations of Girder #3 and Girder #4 were calculated by using the maximum strain responses from the top and bottom flanges. As shown in Figure 7.43, it was found that when the concrete modulus becomes larger, the apparent neutral axis moves up. This correlates with the theory. It was also found that the increasing rate of the apparent neutral axis location became smaller when the concrete modulus increased from 1000 to 2750 (the rate changed from 6% to 2%). After 3000 ksi, the rate remains 1% when the modulus increases for both girders.

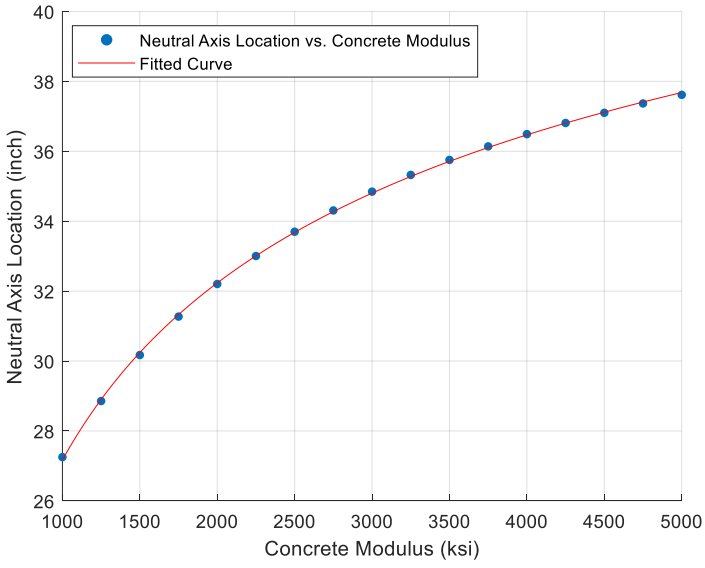

(a) Girder #3 Apparent Neutral Axis Location

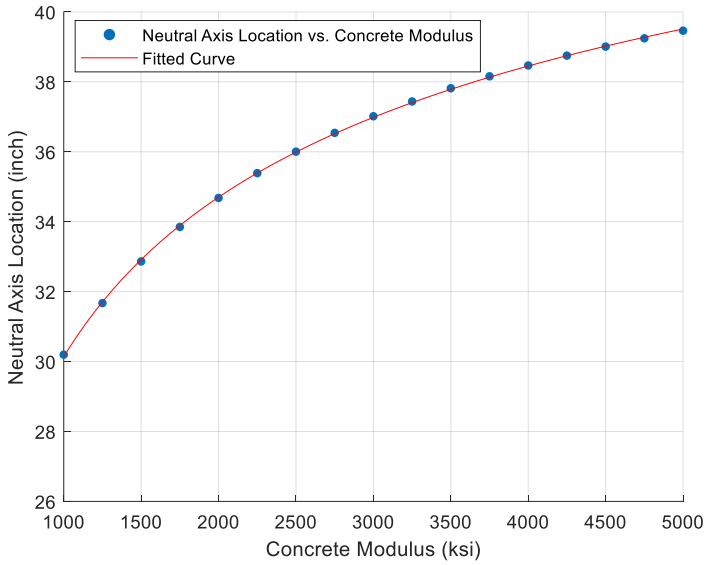

(b) Girder #4 Apparent Neutral Axis Location

Figure 7.43 Apparent Neutral Axis Location versus Concrete Modulus.

7.6.4.3. Sensitivity Study of the Added Longitudinal Stiffness

The apparent neutral axis locations of Girder #3 and Girder #4 were calculated with the longitudinal support stiffness varied from 0 to 25000 kip/ft while the concrete modulus remained 2000 ksi. Again. the maximum strain response from the top and bottom flanges were utilized to project the apparent neutral axis location. As shown in Figure 7.44, it was found that when the longitudinal stiffness increases, the apparent neutral axis moves down. It was also found that the influence rate of the longitudinal stiffness tends to be smaller as the stiffness becomes larger.

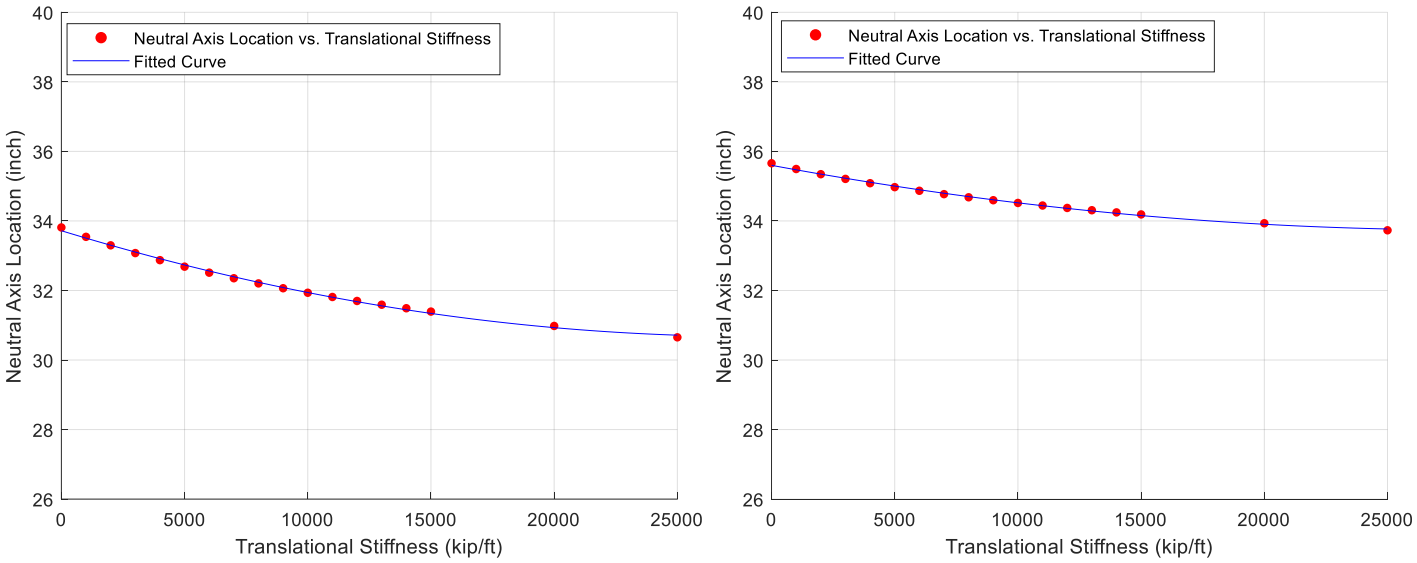

(a) Girder #3 Apparent Neutral Axis Location (b) Girder #4 Apparent Neutral Axis Location

Figure 7.44. Apparent Neutral Axis Location versus Longitudinal Stiffness.

7.7. Bridge Evaluation Summary

This section provides an overview of the methodology for bridge evaluation and load rating within a B-WIM system. This methodology was evaluated through three in-service bridges that were instrumented for B-WIM purposes (see previous chapters).

Since these B-WIM setups included strain gauges across the bridge cross section near the midspan, the live load DFs could be reliably obtained. The DFs calculated for one-lane and two-lane loaded cases were compared with the results from the AASHTO LFR method. The B-WIM system of the steel bridge (Bridge #3) had supplemental strain gauges installed along with the web of two beams. The neutral axis of the beams was calculated by utilizing the live load data for composite action studies. Several overall conclusions can be drawn:

- The DFs obtained from the live load data were consistently smaller than the results from the AASHTO LFR method for both one-lane and two-lane load cases.
- Bridge load rating factors were increased due to the refined DFs obtained from the B-WIM results. The increase in HS20 ratings was roughly 20 percent, 7 percent, and 50 percent for Bridges #1–3, respectively, only implementing the distribution improvement.
- Bridge #3 composite action assessment based on live load data indicated that the bridge was fully composite for in-service loading and at least partially composite for relatively high load levels. This could substantially increase the load ratings if needed.
- An additional benefit of bridge evaluation utilizing a B-WIM system is that actual trucks can be load rated aside from notional rating vehicles. This provides an assessment of the in-service performance.

- B-WIM data has the potential to reduce the uncertainty of existing bridge behavior using many of the already developed field testing approaches. This study incorporated those for DFs and composite action. Others could be implemented, such as stress ranges for fatigue-sensitive details, dynamic amplification, etc.

8. B-WIM GUIDELINES FOR FUTURE IMPLEMENTATION

8.1. Overview

Utilizing the findings from the previous tasks, particularly the findings from the literature, the testbed bridge, and the three in-service bridges, technical guidelines for B-WIM systems were developed. The guidelines were developed to help readers understand more thoroughly the deployment of B-WIM systems and their operation for truck-traffic data collection. The guidelines cover and describe the following aspects:

- B-WIM system components.
- Bridge selection criteria for B-WIM.
- B-WIM deployment.
- B-WIM data retrieval, processing, analysis, and interpretation.

8.2. B-WIM System Components

8.2.1. Introduction

A B-WIM system components usually consist of a DAQ, a remote communication system (optional), a power supply system, and sensors. The sensors can be divided into two main categories: axle-detecting sensors and weighing sensors. The main components needed for the installation of a B-WIM system on a bridge are introduced in the following subsections.

8.2.2. Data Acquisition System

The DAQ is the heart of the B-WIM system components. The selection of the DAQ is critical for the success of the project. It must be able to capture reliable measurements in severe environmental conditions. Other considerations for selection of the DAQ include the number and type of sensors it can measure, the measurement sampling rate capabilities, the resolution it can provide for measurements, the data storage capacity, and the cost.

8.2.3. Axle Detecting Sensors

Strain gauges are recommended as the primary axle detecting sensors. They can be installed underneath the bridge deck near the quarter span or installed on the web of beams near the bridge ends for this purpose.

LVDTs can also be used as axle detecting sensors if the bridge has relatively new bearing pads. Comprehensive calibration and data quality checks are recommended if LVDTs are utilized for axle detection.

8.2.4. Weighing Sensors

Strain gauges are recommended as the primary weighing sensors. The preferred location is along the bottom flange of each beam near midspan. The measured flexural response of the bridge span can be used to calculate the GVW. The same strain gauges can also be constructed as a three-strain gauge rosette and installed near the end of the beams to get the shear response and obtain the GVW.

8.2.5. Power supply

The recommended power supply for the DAQ is a battery charged with a solar panel. The battery must be sized such that it can sufficiently power the system through the evening and during days with cloud cover.

The solar panel must be adequately sized to sufficiently charge the battery throughout the length of the study. A common location for mounting is the wing walls. A charge controller is typically needed to regulate the voltage and current received from the solar panel to charge the battery safely and keep the battery from overcharging. In addition, the controller regulates the output voltage from the battery to the DAQ so that it is provided a stable voltage.

8.2.6. Enclosure

Enclosures are designed to protect a DAQ's most sensitive components from elements such as dust, water, sunlight, or pollutants. The enclosure can house DAQs, communication peripheral, power supply, and appropriate sensors. The enclosure can be locked for security against theft. There is typically a hole for cable management so that the cables from the sensors can be inserted and the enclosure can be closed without damaging the cables.

8.3. Bridge Selection Criteria for B-WIM Systems

8.3.1. Introduction

Selecting bridges for B-WIM applications is critical before heading to the field and starting the deployment. Nearly all bridges could be utilized for B-WIM. However, certain bridges are better candidates since they will provide higher accuracy data, simplify the data processing, and reduce the field work required.

The primary recommended selection criteria for a B-WIM system application are bridge type, span length, pavement surface roughness, carriageway type, and underside access. Other selection considerations are geographical location, bridge skew, and road geometry.

An array of resources is available to obtain this bridge information. NBI data and Assetwise can be very beneficial to obtain bridge parameters. Google Maps and Google Street View are useful tools that can be used to check and study the bridge site. Additionally, conducting a site survey in person is also helpful since the Google Map may not be up to date or may not provide sufficient perspective.

8.3.2. Bridge Type

An array of bridges has been studied for B-WIM. This includes prior studies in the literature and the bridges studied as part of this research study. One prestressed concrete slab beam bridge, two prestressed concrete I-beam bridges, and one steel I-beam bridge were instrumented with B-WIM systems and evaluated. As shown earlier, the B-WIM systems on these bridges were able to capture truck information with reasonable accuracies. All of them are spread multi-girder type bridges since the weighing sensors

need to be installed underneath the beam across the width of the bridge and the bridge deck needs to be accessible for the installation of axle detection sensors. Therefore, slab beam bridges and beam-deck bridges are suitable types for B-WIM. In addition, literature indicates that box girder bridges and orthotropic deck bridges are also acceptable for B-WIM. Bridge type criteria to avoid are curved bridges or bridges with significant skews. These types of bridges produce more complex data sets that reduce accuracy of the B-WIM results.

8.3.3. Span Type and Length

Simple span bridges are recommended for B-WIM applications. Continuous bridges can be utilized for B-WIM. However, simple spans essentially eliminate the influence of the adjacent spans, which simplifies the B-WIM algorithms and increases the accuracy of the results. As a result, the bridges tested in this study were simple span bridges.

The length of the span is an important criterion as well. Relatively short span lengths are preferred since they reduce the likelihood of vehicles on the bridge back-to-back. Short spans minimize varying vehicle speed on the bridge. In addition, short span lengths reduce the contribution from vehicles entering or leaving the bridge, which reduces the error of weight calculation and axle detection. However, the span should have enough length to place axle detection sensors at each end for speed measurement. Therefore, the ideal span length is 30 to 80 ft based on the literature and the field testing results in this study. However, spans up to 125 ft would also be sufficient.

8.3.4. Carriageway Type

The carriageway type is another selection criteria that is recommended to simplify the B-WIM data processing and increase the accuracy of the results. If at all possible it is best to select a bridge with the least number of lanes and with one-way traffic. The three in-service bridges deployed with B-WIM systems in this study had two traffic lanes and one-way traffic direction. This was selected to reduce the possibility of side-by-side cases compared with more lanes or two directions.

8.3.5. Pavement Roughness

Pavement unevenness can be an obstacle to achieving accurate B-WIM results due to dynamic amplification of the measurements. The pavement-to-bridge transition should be relatively smooth to minimize this effect. The spans selected for the three in-service bridges were the spans at the abutment. The pavement surface roughness was particularly important.

8.3.6. Underside Access

One advantage of B-WIM (over pavement WIM) is that the installation process can avoid traffic control, which increases safety. It is preferred to have underside access that allows for installation within one day that does not disrupt traffic. Therefore, dry ground with a vertical clearance less than 20 ft is desirable. Utilizing a snooper truck is not preferred since it requires lane closures but can be utilized if needed.

8.3.7. Other Considerations

To weigh vehicles travelling at a uniform speed, the bridge should be away from any area with frequent lane changes, acceleration, or deceleration. Therefore, it is best to avoid a bridge near an on- or off-ramp. Also, B-WIM systems are predominantly focused on trucks, namely Class 4 vehicles and higher. Urban city bridges with the majority of vehicles comprised of small cars may not be effective for B-WIM applications.

8.3.8. Bridge Selection Criteria Summary

Table 8.1 summarizes the recommended bridge selection criteria for B-WIM systems to produced accurate results. These criteria are based on the literature and the bridges tested in this research study. The criteria can be improved with future research.

Table 8.1. Bridge Selection Criteria Summary.

Selection Criteria	Recommendation
Bridge Type	Straight spread multi-girder bridges (no skew)
Span Type	Simple span
Length	30 to 80 ft (can go up to 125 ft if needed)
Traffic Direction	One-way with minimal lanes
Pavement Roughness	Even and smooth
Underside Access	Favorable

8.4. B-WIM System Deployment

8.4.1. Preparations

After a bridge is selected for B-WIM deployment and before the installation procedures, a document containing a sensor layout (i.e., type of sensors, location of the sensors on the bridge), equipment list, and sampling rate for B-WIM installation should be made. There are different schematic plans for installing a B-WIM system. The design of the B-WIM system for the selected bridge is subjected to the bridge site and the budget.

Inspection of the main B-WIM system components before installation is required to ensure each component, including the data acquisition system, sensors, cell modem (if applied), and batteries, function properly.

8.4.2. B-WIM System Calibration

8.4.2.1. Introduction

The calibration of a B-WIM system is essential for obtaining accurate weighing results and ensuring the performance of the system. The sensors used in a B-WIM system are usually factory calibrated. However, the bridge response measured by a B-WIM system should be related to the truck loads crossing the bridge. The purpose of the calibration test is to find the relationship between the structural response and the crossing loads.

8.4.2.2. Calibration Test Truck Selection

Axle and weight information of the test trucks will be measured before the calibration test so that the selected trucks can be used as reference vehicles. There are several considerations when selecting the test trucks for B-WIM calibration test:

- The test trucks should represent heavy truck types that are most frequently observed at the bridge site. If resources permit, the use of more than one truck will better represent the dynamic loading conditions encountered at the bridge site (e.g., a five-axle tractor trailer and three-axle dump truck).
- The test trucks should be loaded at or near full load capacity but not exceeding the state's weight limitations.
- The test trucks must have a working speedometer and be able to reach the required test speeds.
- The loads should be non-shifting so the load distribution on each axle will not change during the calibration test.

8.4.2.3. Test Truck Speed Selection

The test truck's speed when passing the bridge should be as close as possible to the dominant heavy trucks at the bridge site. Testing with different speeds is recommended to minimize error dependency on speed. For example, if the posted speed limit is 70 mph, the speeds for the test trucks can be selected as 50 mph, 60 mph, and 70 mph.

8.4.2.4. Calibration Test Operation

Before starting the calibration test, the test trucks need to be loaded and their axle and weight information should be measured. The layout of each test truck should be documented, including axle spacing and axle weights. When conducting the calibration test, run each test truck according to the test plan. Since the calibration test is conducted without traffic control, there may be other heavy trucks passing the bridge with the

calibration truck simultaneously. In this case, the test run should be repeated. The operator can communicate with the drivers using two-way radios in case some of the tests need to be repeated or more tests are needed. Use a radar gun (or other speed measurement tools) to measure the test truck's speed while crossing the bridge for comparison with the B-WIM system results.

8.5. B-WIM System Data Processing

The logic of the data processing recommended from this study is shown in Figure 8.1. Algorithms explained in Section 3 and Section 6 are followed for the data processing and analysis. The retrieved B-WIM data are first divided into individual truck passing events. Each event includes either one truck passing the bridge or multiple trucks passing the bridge at the same time. Data from the midspan strain gauges are processed to calculate the distribution factors of each beam and detect whether it is a single truck passing or multiple trucks passing event. For a single truck event, data from the midspan strain gauge are used to detect which lane the truck is passing. Data from the corresponding axle detection sensors of the specific lane are selected and processed to obtain the number of axles, average speed, and axle spacing. The results from the axle information are then utilized to calculate the GVW of the truck. Axle weights are obtained by distributing GVW to each axle. The truck is classified once the truck information is determined.

For multiple trucks, especially side-by-side cases, data from the axle detection sensors of each lane are processed separately. The total weight of the trucks is calculated by the data from the midspan strain gauges. The weight of each truck is obtained by

distributing the total GVWs based on the calculated distribution factors. To address back-to-back truck cases, it is recommended to implement B-WIM on relatively short span bridges (as stated earlier). However, back-to-back cases can be separated by setting a maximum axle spacing threshold in the axle data processing algorithm.

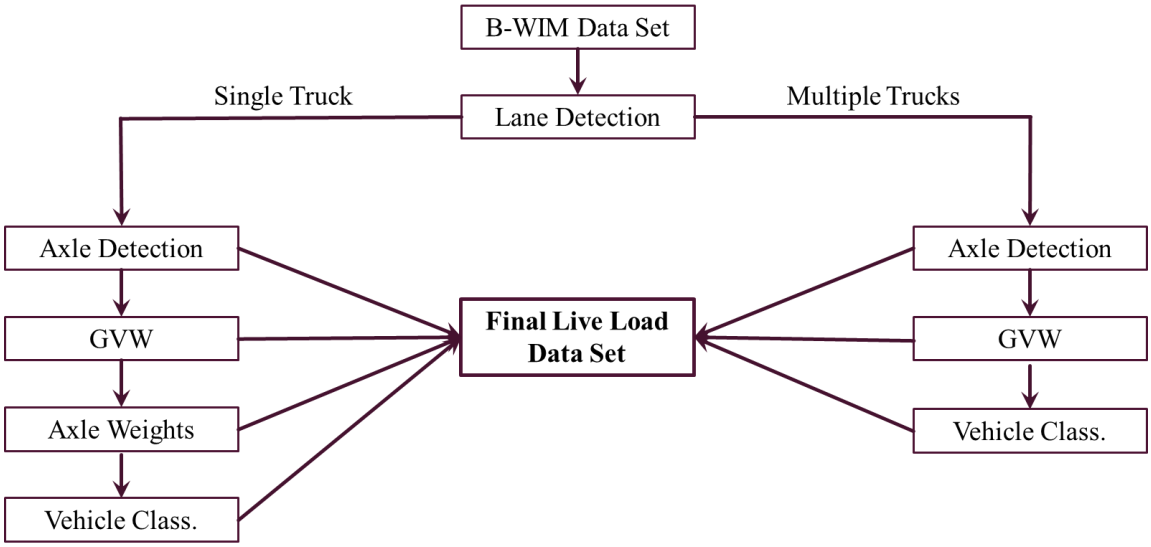

Figure 8.1. Data Processing Logic.

9. CONCLUSIONS, RECOMMENDATIONS AND FUTURE RESEARCH

9.1. Overview

B-WIM systems have been utilized as an alternative to pavement WIM systems for truck-traffic measurements. The primary objective of B-WIM is to instrument a bridge to obtain the axle information (i.e., weights, number, and spacings) and weight information (i.e., axle and gross) of trucks that cross the structure. A secondary objective of B-WIM is to evaluate the performance of the bridge itself. In this research study, methodologies for B-WIM systems were developed and quantitatively evaluated.

In this research study, the relevant literature and the current state of the practice were reviewed. A preliminary B-WIM system was developed and evaluated on a testbed bridge at the RELLIS campus. Thereafter, three in-service highway bridges in Texas were selected, and B-WIM systems for each bridge were developed and tested. Truck-traffic data were collected and utilized for live load analysis. Validation studies were conducted by comparing B-WIM results with nearby independent p-WIM systems. The three bridges were also evaluated with refined load ratings utilizing the B-WIM data. Finally, guidelines for future B-WIM implementation were drafted.

9.2. Conclusions

9.2.1. Preliminary B-WIM Development and Testing

A preliminary B-WIM system and data processing algorithms were developed and evaluated on the testbed bridge (i.e., RELLIS Bridge). The structure is a prestressed

concrete slab beam bridge. Four different types of sensors (i.e., strain gauges, load cells, displacement gauges, and accelerometers) were instrumented underneath the structure, and three trucks were used to conduct full-scale testing, with various speeds on three different paths. Truck information results obtained from different algorithms were compared with the known measured values (i.e., radar gun, measuring tape, and static scales) for their overall accuracy. The following conclusions were drawn based on the results of the preliminary B-WIM system testing.

9.2.1.1. Axle Detection Findings from the Preliminary B-WIM System

1. The axle detection strain gauges installed underneath the bridge deck near both ends provided clear data peaks when each vehicle axle passed the bridge. The axle numbers were counted directly from the strain data. This was used for automated identification of the average speed and axle spacing. The results yielded relatively high accuracy (i.e., 97 percent and 96 percent, respectively).
2. The load cells installed at each bearing were used as axle detection and weight calculation sensors. Axle information was obtained by taking the second derivative of the data, which showed high accuracy (i.e., 97 percent accuracy for both average speed and axle spacing).
3. Taking the second derivative of the measured data from the deck strain gauges and load cells provided clear peaks. Each peak in the plot of second derivatives depicted the instance an axle was right above the sensor.
4. A low-pass filter was used to smooth the data and boost the overall signal-to-noise ratio with minimal signal degradation.

9.2.1.2. Weight Calculation Findings from the Preliminary B-WIM System

1. The weight detection strain gauges underneath the beams at midspan provided sufficient information to calculate the GVW using a modified area method algorithm. The research team took the spatial behavior of the bridge and the truck average speed into consideration. The calculated GVW results had an average accuracy of 92 percent. However, the axle weight was not able to be calculated from the weight sensors since the peaks were not distinct from the data. Axle detection sensor data were used to calculate the axle weights by taking the ratios of the peaks in the second derivative of the data, which produced an accuracy of 69 percent.
2. The load cells were used for the weight calculations. The GVW was calculated using the area method similar to the midspan strain gauges. Another algorithm, named the reaction force method, was also implemented. This method calculated the axle weights first based on the reaction force influence line, and then it calculated the GVW by summing the axle weights. The area and reaction force methods provided accuracies of 89 percent and 91 percent, respectively, for the GVW. As for the axle weight results, the reaction force method provided an accuracy of 87 percent.
3. The midspan strain gauges with a 200-Hz sampling rate could not indicate axle information. When using the area method for GVW calculations, the sampling frequency of the weighing sensors could be lower. Consequently, the computation time and data storage requirement could be reduced.

9.2.2. B-WIM Deployment on In-Service Bridges

The B-WIM systems for the three selected highway bridges were successfully developed, installed, calibrated, and recorded for roughly one month at each site. The three structures included a relatively old and new prestressed concrete I-beam bridge and a steel girder bridge. Significant information was learned about the different instrumentation approaches for successful B-WIM data acquisition. Axle detection was explored using (a) vertical strain gauges at the beam ends, (b) strain gauges mounted to the bottom surface of the deck, (c) LVDTs at the bearings (i.e., measuring vertical displacement), and (d) accelerometers at the bearings. To identify truck axle and gross weight, the studied instrumentation included (a) mid-span strain gauges along each beam, (b) strain gauge rosettes at the beam ends, and (c) LVDTs at the bearings. Detailed conclusions are discussed in the subsequent Section 9.2.3.

Many logistical conclusions have been made because of the three bridge field studies:

1. The installation time of the B-WIM system was within one day for a crew of four people using a ladder. Removal of the system was achieved in a few hours.
2. The installation of the strain gauge rosettes was easier than the deck strain gauges. This was due to relatively high ladder work needed for the deck gauges.
3. Calibration tests can be conducted without traffic control. Performing calibration tests with truck speeds in the flow of traffic worked well. This avoids the cost of traffic control, the inconvenience to the traveling public, and improves safety.

4. The reusable (nondestructive) B-WIM sensors and DAQ selected for the study have proven sufficiently robust to withstand all weather conditions. The long-term durability of B-WIM systems should be relatively better than pavement WIM systems based on long-term structural monitoring systems using the same equipment.

9.2.3. Live Load Data Analysis and Validation Findings

Live load data recorded from three B-WIM systems were processed to determine the passing trucks' gross weights, axle weights, axle numbers, axle spacings, average speeds, and vehicle classifications. Algorithms developed in Section 3 and Section 6 were utilized for data processing. The data processing began with the calibration test performed at each site. The accuracy of the axle detection and weight calculation algorithms for multiple types of sensors were evaluated based on the calibration test results. In addition, several two-hour windows of data after the calibration were processed, and the information for each truck crossing the bridges was determined. A validation study was conducted through the comparison between the B-WIM results and the independent p-WIM data.

9.2.3.1. Axle Detection Findings from Calibration Tests

Axle detection identifies the specific point in time when truck axles cross specific points on the bridge. This information allows for the calculation of the number of axles, axle speed, and axle spacing. Axle detection is arguably the most critical part of the B-WIM data processing since the information is utilized to determine other truck characteristics.

Three sensor approaches were explored for axle detection, which included the vertical strain gauge of the strain rosettes, LVDTs measuring the vertical deformation of the bearings, and strain gauge installed on the underside of the bridge deck. Each approach has advantages and disadvantages, which are briefly discussed below. The following conclusions were drawn:

1. The truck passing lane needs to be determined at the start of the axle detection algorithm. It was found that the midspan strain gauges can be used for lane detection by comparing the distribution factors to the beams. Calibration tests and validation studies show the high accuracy of lane detection with this methodology. In addition, side-by-side configurations can be reliably detected using the distribution factors of each beam.
2. The vertical strain gauge of the strain rosette can be used to reliably measure axle numbers by taking the first derivative of the data. The accuracy of the axle number detection is influenced by the location of the strain rosette. The vertical strain gauges installed near the center of the bearing line had better axle number detection results (i.e., 100 percent in Bridge #1 calibration tests, 75.0 percent in Bridge #2 calibration tests, 92.8 percent in south vertical gauges of Bridge #3 calibration tests) than those installed away from the bearing pad (i.e., 46.7 percent in north vertical gauges of Bridge #3 calibration tests). The vertical strain gauges installed at the bridge support where the trucks enter the bridge had more accurate results than those installed at the bridge support where the trucks leave the bridge.

3. The LVDTs did not accurately measure axle numbers for high-speed truck passings in the Bridge #1 calibration tests. The accuracy was 40.0 percent. This may be due to the age of the bearing pads of Bridge #1. The bearing pads of Bridge #2 were newer than those in Bridge #1. The accuracy for axle number detection was significantly improved (i.e., 87.5 percent). For Bridge #3, LVDTs were not utilized since steel bearings were present.
4. Strain gauges on the underside of the bridge deck near the quarter span can be used to measure axle numbers, average speed, and axle spacing accurately by the second derivative method. However, this method cannot be used when the truck passes the bridge at speeds slower than 15 mph.

9.2.3.2. Weight Calculation Findings from Calibration Tests

The B-WIM weight calculation includes the GVW and the individual axle weights. The methodology utilized in the algorithm for GVW is the area method, which was applied to the midspan strain gauges, LVDTs, and strain rosettes. As part of this methodology, side-by-side cases were addressed utilizing the beam distribution factors identified in the calibration process, which has produced reasonable results. Following findings are observed:

1. Comparing the calibration tests GVW results from Bridge #1, #2, and #3, the midspan strain gauges were shown to be the most accurate (i.e., 90.4 percent, 90.3 percent, 86 percent, and respectively), with the strain rosettes not far behind (i.e., 89.8 percent,73.2 percent, and 78.8 percent, respectively). The LVDT

approach can yield accurate data as long as the bearings are suitable (i.e., 88.5 percent for Bridge #1 and 96.8 percent for Bridge #2).

2. Axle weight calculation methods were explored. The shear response from the strain rosette showed peaks from the axle groups and was used to calculate the axle group weight. The second derivative of the data of strain gauges underneath the bridge deck was utilized to calculate individual axle weights. Results from the calibration tests showed reasonable accuracy of the deck gauges, and this method was used for live load data analysis since it was more straightforward.

9.2.3.3. Validation Study Findings

The research team (led by Lubinda Walubita) installed p-WIM stations near Bridge #1 (both lanes) and Bridge #2 (outside lane only). Two-hour data time windows from two of the B-WIM systems were selected and compared with the corresponding p-WIM data, leading to the following conclusions.

1. It was found that for around 300 trucks in Bridge #1, the average GVWs from both systems had a difference of 2.2 percent. The average differences in speed, axle number, and wheelbase were all within 6.0 percent. The front axle weight had a higher difference of about 23.0 percent. For Bridge #2, the GVW differences were within 8.0 percent, and the rest of the differences of truck properties were within 5.0 percent. However, fewer trucks were detected by the B-WIM systems compared with the p-WIM. This was likely due to lightweight trucks following close to a much heavier truck, where the light truck was treated as noise. Another possibility is that a lightweight truck was adjacent to a heavy

truck and the lightweight was ignored. Overall, the comparison between the B-WIM and p-WIM results were relatively consistent and yielded similar conclusions.

2. The B-WIM system can reliably identify the vehicle classifications if the axle detection information is accurate. The vehicle classification results were essentially the same for the Bridge #1 and Bridge #2 validation studies between the B-WIM and p-WIM systems.

9.2.4. Bridge Evaluation and Load Rating Findings

The B-WIM data were utilized to perform refined load ratings using line-girder analysis. Live load DFs were reliably obtained since the B-WIM setups of the three bridges included strain gauges across the bridge cross section near the midspan. The DFs calculated for one-lane loaded and two-lane loaded cases were compared with the results from the AASHTO LFR method. The B-WIM system for the steel bridge (i.e., Bridge #3) had supplemental strain gauges installed along with the web of two beams. The neutral axis of the beams was calculated utilizing the live load data for composite action studies. The methodology for bridge evaluation and load rating within a B-WIM system was developed and evaluated through the three bridges. Several overall conclusions can be drawn:

1. The DFs obtained from the live load data were consistently smaller than the results from the AASHTO LFR method for both one-lane load and two-lane load cases.

2. Bridge load rating factors were increased due to the refined DFs obtained from the B-WIM results. The increase in HS20 ratings was roughly 20 percent, 7 percent, and 50 percent for Bridges 1–3, respectively, only implementing the distribution improvement.
3. The Bridge #3 composite action assessment based on live load data indicated that the bridge was fully composite for in-service loading and at least partially composite for relatively high load levels. This could substantially increase the load ratings if needed.
4. An additional benefit of bridge evaluation utilizing a B-WIM system is that actual trucks can be load rated, aside from notional rating vehicles. This provides an assessment of the in-service performance.
5. B-WIM data has the potential to reduce the uncertainty of existing bridge behavior using many of the already developed field testing approaches. This study incorporated those for DFs and composite action. Others could be implemented, such as stress ranges for fatigue-sensitive details, dynamic amplification, etc.

9.3. Recommendations

9.3.1. B-WIM System and p-WIM System Comparison

Based on the literature and field testing, a comparison between the B-WIM and p-WIM systems are summarized in Table 9.1.

Table 9.1. WIM Systems Comparison.

Item	B-WIM	Portable WIM	Permanent WIM
Installation Time and Manpower	Less than one day; 4 people.	Less than 1.5 hours; 2 to 3 people.	Roughly 8 hours; 4 to 5 people
Traffic Control for Installation	No (unless poor underside access)	Yes	Yes
Traffic Control for Calibration	No	No	No
Traffic Data Measures	○ Trucks only ○ Truck speed ○ Number of axles ○ Axle spacing ○ Truck type/classification, namely Class 4 and higher ○ GVW ○ Individual axle weight	○ All vehicle types ○ Vehicle speed ○ Number of axles ○ Axle spacing ○ Wheelbase ○ Vehicle classification ○ GVW ○ Individual axle weight	
Advantages	○ High accuracy for GVW and axle detection. ○ Durable system (underneath the bridge) ○ Provides bridge evaluation data ○ Cost effective ○ No trenching, cutting, or damage to the pavement ○ Reusable system	○ Consistent weight measurements ○ Data accuracy comparable to permanent WIM ○ Portable and can be installed nearly on any highway site on any pavement type ○ Cost-effective ○ No trenching, cutting, or damage to the pavement	○ High accuracy ○ Consistent weight measurements. ○ Have more commercial systems available
Challenges/Concerns	○ Axle weight accuracy is lower ○ Current expertise is limited ○ Measures only trucks ○ Still needs long-term evaluation	○ Dynamic effects may influence the measurement results ○ Sensors under direct truck load, less durable	○ High deployment and maintenance costs ○ Installation typically requires cutting the pavement and building a concrete slab ○ Limited to certain highways

9.3.2. Bridge Selection Recommendations for B-WIM Applications

B-WIM could be applied on most bridges. However, certain bridges are better candidates since they will provide higher accuracy data, simplify the data processing, and reduce the field work required. The primary recommended selection criteria for a B-WIM application are bridge type, span length, pavement surface roughness, carriageway type, and underside access. Other selection considerations are geographical location, bridge skew, and road geometry. The following are the recommended selection criteria:

1. *Bridge Type.* Straight spread multi-girder type bridges, including slab beam bridges, beam-deck box girder bridges, and orthotropic deck bridges.
2. *Span Type.* Simple span bridges are recommended for B-WIM applications. Continuous deck slabs (e.g., link slab) are not an issue for B-WIM systems.
3. *Span Length.* Relatively short span lengths are preferred with the ideal span length around 30 to 80 ft. Spans up to 125 ft are acceptable.
4. *Carriageway Type.* It is best to select a bridge with the least number of lanes and with one-way traffic.
5. *Pavement Roughness.* The pavement-to-bridge transition should be relatively smooth. The roadway surface should be in good condition.
6. *Underside Access.* It is preferred to have underside access that allows for installation within one day that does not disrupt traffic. Therefore, dry ground with a vertical clearance less than 20 ft is desirable.
7. *Traffic Spectrum.* The traffic on the bridge should be more than 15 mph and include an appreciable percentage of trucks greater than 20 kips.

9.3.3. B-WIM Method Recommendations

9.3.3.1. Axle Detection Sensors and Data Processing Algorithm Recommendations

To accurately detect axle information of the passing trucks, strain gauges are recommended to be installed on the underside of the bridge deck near the quarter span of both ends. Each traffic lane requires two strain gauges installed under the lane. It is recommended to set a high sampling rate (at least 500 Hz) for the axle detection sensors. A higher sampling rate helps reveal the axle numbers of the crossing trucks, especially when the truck has closely spaced axles and passes the bridge at high speed. However, data storage capacity and data computation resources need to be taken into consideration. The second derivative method is recommended to process the data from deck strain gauges.

The vertical strain gauge of the strain rosette is also recommended to reliably measure axle numbers by taking the first derivative of the data. The vertical strain gauge is recommended to be installed at the bridge support where the trucks enter the bridge for better accuracy. Axle detection results from the vertical strain gauges can be combined with the deck strain gauge results for a redundant system to obtain reliable axle information of the passing trucks.

For newly constructed bridges or bridges under rehabilitation projects, load cells can be a good approach for axle detection sensors. It is recommended to install the load cells for all bearings at both ends of the bridge. Utilizing the second derivative method for data processing can achieve accurate axle information.

9.3.3.2. Weight Calculation Sensors and Data Processing Algorithm Recommendations

Strain gauges are recommended to be installed under the beams at the midspan location across the structure. The midspan strain gauges are necessary for a B-WIM system and have the following functions:

1. Truck passing lane detection for selection of the corresponding axle detection sensors.
2. Side-by-side case detection.
3. GVW calculation based on the strain response induced at midspan.
4. Distribution factor calculation for bridge load rating.

The area method is the recommended algorithm for GVW calculation. This method is relatively simple and straightforward since the average speed of the passing truck is calculated in the axle detection step. Based on the calibration test results, GVW of the unknown trucks can be obtained by comparing the induced strain area of the passing trucks with the calibration truck. The axle weight of the truck can be obtained using the second derivative results from the deck strain gauges.

For newly constructed bridges or bridges under rehabilitation process, load cells at the bearings are a good alternative for weight calculation sensors. The reaction force method is recommended to process the load cell data for obtaining the axle weights and GVW of passing trucks. Relatively good accuracies can be achieved with this approach.

9.4. Future Research

Following the research study conducted and presented herein, an implementation research project could be conducted in the future. However, certain improvements need to be made and certain research questions need to be addressed before the B-WIM system can be implemented in highway bridges. They are identified below as future research areas.

9.4.1. Data Processing Techniques

Data processing is the first and the most important step after the field measured data is collected. Improvement made in this step can increase the accuracies of the truck characterization procedures. Data processing time can be saved, which is important if real-time analysis is the goal. In the data processing of this study, the central differences were used for obtaining the second derivatives. This method may not be the most accurate way to differentiate the data. Other methods, such as adaptive step size or a higher-order numerical differentiation scheme, and wavelet analysis should be evaluated and compared. This can be done utilizing the existing field measured data or from numerical simulations.

9.4.2. Axle Detection Accuracy

In the peak detection process, there could be cases where noise in the measurement produces sharp changes as the peaks are similar to the passing axles. This can be improved through enhanced filtering methods or by adding the physical meaning to the data processing algorithm. For example, adding the minimum and maximum axle

spacing limitation when picking peaks. In addition, higher sampling rates should be explored for axle detection sensors. In this study the axle detection sensors were sampled at 500 Hz due to the limitation of the equipment capacity. A 1000 Hz sampling rate should be evaluated through full-scale field testing if equipment permits. Higher sampling rates may help identify those axles that are very close to each other and passing the bridge with high speeds. Other types of sensors can be evaluated for axle detection purpose if funding permits in full-scale field testing. Accelerometers should be evaluated as an alternative option for axle detection. They can also be utilized for bridge health monitoring if installed in multiple locations under the bridge. A camera-based technology can be explored for axle detection utilizing computer vision related algorithms, it can also detect side-by-side cases and used as traffic monitoring purpose.

9.4.3. Axle weight calculation accuracy.

The accuracy of obtaining the GVWs using the B-WIM approach was relatively high in this research study. However, it remained as a challenge to accurately calculating the axle weights of the passing trucks. Using load cells in B-WIM systems has the potential to provide accurate axle weight results. However, it requires more full-scale field testing on the in-service bridges. Logistically the use of load cells can be challenging for existing bridges. The best situation is to have load cells installed during the construction of a new bridge or during bearing replacement. The axle weight accuracies may be improved through enhanced data processing and axle detection methods. In addition, load cell alternatives should be focused as a research objective such as LVDTs and strain rosettes. If funding is sufficient, LVDTs can be installed at the bearings of each girder at

both ends. Newer bridges are preferred since it showed more displacement. For older bridges, more sensitive LVDTs or other types of displacement sensors should be used. Strain rosette can also be utilized as an alternative, it is suggested to conduct numerical simulations to determine the best locations for the strain rosette before implementing field testing.

9.4.4. Multiple Vehicles Presence

The bridges selected in this study were short span bridges. The muti-vehicle scenarios especially side-by-side cases are rare but remained as a challenge when happened. Utilizing the distribution factors and area method gave reasonable results on estimating the GVWs of the side-by-side trucks, however the sample size was small since only few side-by-side tests were conducted. More side-by-side tests should be conducted and different algorithms can be developed, such as using the influence surface or using signal decoupling algorithms. In addition, bridges that have lanes with opposite directions are wroth being studied for B-WIM applications. It is suggested to start with a two-lane bridge with opposite directions to reduce the complexity. Down-scale lab testing can be conducted to evaluate the accuracy of the axle detection and weight calculation algorithms before conducting a full-scale field test.

9.4.5. Vehicles with Non-Constant Speed

In this study, the vehicles were considered to have constant speeds when passing the bridges. In reality, vehicles may accelerate or decelerate when passing the bridge. This would induce a longitudinal force and influence the measured strain response. Numerical

simulations should be conducted with changing speeds to explore how it will influence the B-WIM results. The weight calculation algorithm may be adjusted based on the simulation results. If funding permits, a full-scale experimental testing would be beneficial to conduct on a closed bridge.

9.4.6. Dual-Purpose B-WIM Applications

In this study, the B-WIM results were used for live load analysis and bridge evaluation. More research can be focused on incorporating B-WIM systems into structural health monitoring systems to extend their applications and may reduce the cost of structural health monitoring systems. With appropriately modified sensor installation designs, more bridge information such as damage detection or dynamic behavior can be evaluated.

9.4.7. Application on Bridges with Long Span Length

Using B-WIM on long span bridges has rarely been studied. Several challenges need to be overcome for this topic. (1) Dynamic effect increased by the bridge due to the longer span length. (2) Higher chances of multiple vehicle presence problem. (3) Vehicles may change speed when passing the bridge. More sensors may need to be installed along the bridge to solve these challenges.

9.4.8. Application on Other Types of Bridges

In this research study, slab girder bridges were studied for B-WIM applications. Different types of bridges, such as truss bridge or arch bridge, should be studied for the

accuracy and feasibility of B-WIM application. Numerical simulations are suggested to find the appropriate sensor locations before conducting field test.

9.4.9. Life Cycle Cost-Benefit study

This future study can evaluate the benefits of deploying B-WIM technologies financially. This study can be conducted by: (1) Comparing the cost of B-WIM systems with other WIM systems. (2) Estimating the maintenance cost caused by overweight vehicles. (3) Estimating the cost saved by implementing B-WIM systems that removes those overweighted vehicles.

9.4.10. B-WIM for Overweight Truck Enforcement

B-WIM results can be used to pre-select overweight trucks from traffic flow for static weighing. The pre-selection can help the weigh crews to operate more efficiently. Research can focus on real-time data processing and real-time communication with enforcement (or develop a camera and ticketing system).

REFERENCES

AASHTO 2011. "The manual for bridge evaluation."

Abercrombie, R., Beshears, D., Scudiere, M., Coats, J., Sheldon, F., Brumbaugh, C., Hart, E., and McKay, R. 2005. "Weigh-in-motion research and development activities at the Oak Ridge National Laboratory." In *Proc., International Conference on Weigh-In-Motion, 4th, 2005, Taipei, Taiwan*.

ASTM 2009. "Standard Specification for Highway Weigh-In-Motion (WIM) Systems with User Requirements and Test Methods E 1318-09." *2007 Annual Book of ASTM Standards. Edited by ASTM Committee E17-52 on Traffic Monitoring. ASTM International, USA*.

Barker, M. G., Imhoff, C., McDaniel, W., and Frederick, T. 1999. "Field testing and load rating procedures for steel girder bridges."Rep. No. RDT 99-004.

Bushman, R., and Pratt, A. J. 1998. "Weigh in motion technology–economics and performance." In *Proc., Presentation on the North American Travel Monitoring Exhibition and Conference (NATMEC). Charlotte, North Carolina*.

Chajes, M. J., Mertz, D. R., and Commander, B. 1997. "Experimental load rating of a posted bridge." *Journal of Bridge Engineering*, 2(1): 1–10.

Chatterjee, P., OBrien, E., Li, Y., and González, A. 2006. "Wavelet domain analysis for identification of vehicle axles from bridge measurements." *Computers & structures*, 84(28): 1792–1801.

Chen, S.-Z., Wu, G., and Feng, D.-C. 2019. "Development of a bridge weigh-in-motion method considering the presence of multiple vehicles." *Engineering Structures*, 191: 724–739.

Chen, S.-Z., Wu, G., Feng, D.-C., and Zhang, L. 2018. "Development of a bridge weigh-in-motion system based on long-gauge fiber Bragg grating sensors." *Journal of Bridge Engineering*, 23(9): 04018063.

Christenson, R., Bakulski, S., and McDonnell, A.-M. H. 2011. "Establishment of a dual-purpose bridge health monitoring and weigh-in-motion system for a steel girder bridge."Rep. No. 11-1598.

Dahlberg, J., Lu, P., Freeseman, K., and Phares, B. 2018. "Development of Rural Road Bridge Weigh-in-Motion System to Assess Weight and Configuration of Farm-to-Market Vehicles."

Deesomsuk, T., and Pinkaew, T. 2010. "Evaluation of effectiveness of vehicle weight estimations using bridge weigh-in-motion." *The IES Journal Part A: Civil & Structural Engineering*, 3(2): 96–110.

Faruk, A. N., Liu, W., Lee, S. I., Naik, B., Chen, D. H., and Walubita, L. F. 2016. "Traffic volume and load data measurement using a portable weigh in motion system: A case study." *International Journal of Pavement Research and Technology*, 9(3): 202–213.

FHWA 2018. "Weigh-in-motion pocket guide."Rep. No. FHWA-PL-18-015, Department of Transportation, Federal Highway Administration, Office of Highway Policy Information, Washington, DC.

Fitzgerald, P. C., Sevillano, E., OBrien, E. J., and Malekjafarian, A. 2017. "Bridge weigh-in-motion using a moving force identification algorithm." *Procedia engineering*, 199: 2955–2960.

González, A., and OBrien, E. J. 1998. "The development of a dynamic bridge weigh-in-motion algorithm." In *Proc., Pre-proceedings of 2nd European Conference on Weigh-in-Motion of Road Vehicles*, 445–452.

González, A., Rowley, C., and OBrien, E. J. 2008. "A general solution to the identification of moving vehicle forces on a bridge." *International journal for numerical methods in engineering*, 75(3): 335–354.

González, I. 2011. "Study and application of modern bridge monitoring techniques." Doctoral dissertation, KTH Royal Institute of Technology.

Guo, T., Frangopol, D. M., and Chen, Y. 2012. "Fatigue reliability assessment of steel bridge details integrating weigh-in-motion data and probabilistic finite element analysis." *Computers & Structures*, 112: 245–257.

Hallenbeck, M. E., Selezneva, O. I., and Quinley, R. 2014. "Verification, refinement, and applicability of long-term pavement performance vehicle classification rules."Rep. No. FHWA-HRT-13-091, United States. Federal Highway Administration. Office of Infrastructure Research and Development.

Hallenbeck, M. E., and Weinblatt, H. (2004). *Equipment for collecting traffic load data*, Transportation Research Board.

He, W., Ling, T., OBrien, E. J., and Deng, L. 2019. "Virtual Axle Method for Bridge Weigh-in-Motion Systems Requiring No Axle Detector." *Journal of Bridge Engineering*, 24(9): 04019086.

Helmi, K., Taylor, T., and Ansari, F. 2015. "Shear force–based method and application for real-time monitoring of moving vehicle weights on bridges." *Journal of Intelligent Material Systems and Structures*, 26(5): 505–516.

Hopkins, R. 1952. "Weighing vehicles in motion." *Highway Research Board Bulletin*(50).

Ieng, S.-S. 2014. "Bridge influence line estimation for bridge weigh-in-motion system." *Journal of Computing in Civil Engineering*, 29(1): 06014006.

IRD (2019). "IRD DAW300PC." <http://www.i4t.nl/productinfo/IRD/DAW300/DAW300PC_0309.pdf>. (October 23, 2019).

IRD (2019). "Single Load Cell WIM (Weigh-In-Motion) Scale." <https://www.irdinc.com/pcategory/wim-scales--sensors/single-load-cell-wim-weighinmotion-scale.html.>. (October 19, 2019).

Jacob, B., Ieng, S. S., and Schmidt, F. 2012. "Bridge weigh-in-motion on steel orthotropic decks and application to bridge assessment." In *Proc., Transportation Research Board 91th Annual Meeting*.

Jacob, B., and O'Brien, E. J. 2005. "Weigh-in-motion: Recent developments in Europe." In *Proc., Fourth International Conference on Weigh-In-Motion (ICWIM4), Taipei, Taiwan, National Taiwan University*.

James, E. D., and Yarnold, M. T. 2017. "Rapid evaluation of a steel girder bridge: case study." *Journal of Bridge Engineering*, 22(12): 1–9.

Jauregui, D. V. (1999). *Measurement-based evaluation of noncomposite steel girder bridges*, The University of Texas at Austin.

Jian, X., Xia, Y., Lozano-Galant, J. A., and Sun, L. 2019. "Traffic Sensing Methodology Combining Influence Line Theory and Computer Vision Techniques for Girder Bridges." *Journal of Sensors*, 2019.

Kalhori, H., Makki Alamdari, M., Zhu, X., and Samali, B. 2018. "Nothing-on-road axle detection strategies in bridge-weigh-in-motion for a cable-stayed bridge: case study." *Journal of Bridge Engineering*, 23(8): 05018006.

Kalin, J., Žnidarič, A., and Lavrič, I. 2006. "Practical implementation of nothing-on-the-road bridge weigh-in-motion system." In *Proc., International symposium on heavy vehicle weights and dimensions*.

Kara De Maeijer, P., Luyckx, G., Vuye, C., Voet, E., Vanlanduit, S., Braspenninckx, J., Stevens, N., and De Wolf, J. 2019. "Fiber Optics Sensors in Asphalt Pavement: State-of-the-Art Review." *Infrastructures*, 4(2): 36.

Kim, B. H., Park, M. S., Park, H.-G., Bae, I. H., Kim, S. J., and Yeo, K. S. (2011). "Evaluating Axle Loads of Moving Vehicle Using Bridge Deck Plate Responses." *Dynamics of Civil Structures, Volume 4*, Springer, 263–270.

Kim, S., Lee, J., Park, M.-S., and Jo, B.-W. 2009. "Vehicle signal analysis using artificial neural networks for a bridge weigh-in-motion system." *Sensors*, 9(10): 7943–7956.

Kineo (2019). "System of weighing portable Cet 10 - Measurement and control - System of weighing ", <https://www.interempresas.net/Measure/Companies-

Products/Product-System-of-weighing-portable-Cet-10-70440.html>. (October 19, 2019).

Klein, L. A., Mills, M. K., and Gibson, D. R. 2006. "Traffic detector handbook: Volume I."Rep. No. FHWA-HRT-06-108, Turner-Fairbank Highway Research Center.

Kolev, V., Christenson, R. E., Motaref, S., and Jang, S. 2016. "Development and evaluation of a dual purpose bridge health monitoring and weigh-in-motion system for a steel girder bridge: phase two."Rep. No. CT-2271-F-15-10, University of Connecticut.

Kumar, R., Schultz, A., and Hourdos, J. 2018. "Enriched Sensor Data for Enhanced Bridge Weigh-in-Motion (eBWIM) Applications."Rep. No. CTS 18-23, University of Minnesota.

Kwon, T. M. 2012. "Development of a Weigh-Pad-Based Portable Weigh-In-Motion System."Rep. No. MN/RC 2012-38

Lai, X., Aktan, A., Grimmelsman, K., Mazzotti, M., and Bartoli, I. (2019). *Highway Bridge Weigh-in-motion via Moving Load Identification*.

Lansdell, A., Song, W., and Dixon, B. 2017. "Development and testing of a bridge weigh-in-motion method considering nonconstant vehicle speed." *Engineering Structures*, 152: 709–726.

Lechner, B., Lieschnegg, M., Mariani, O., Pircher, M., and Fuchs, A. 2010. "A wavelet-based bridge weigh-in-motion system." *International Journal on Smart Sensing & Intelligent Systems*, 3(4): 573–591.

Lydon, M., Robinson, D., Taylor, S., Amato, G., Brien, E. J., and Uddin, N. 2017. "Improved axle detection for bridge weigh-in-motion systems using fiber optic sensors." *Journal of Civil Structural Health Monitoring*, 7(3): 325–332.

McCall, B., and Vodrazka Jr, W. C. 1997. "States' successful practices weigh-in-motion handbook."Rep. No. FHWA-PL-98-019, United States. Federal Highway Administration.

McNulty, P. 1999. "Testing of an Irish Bridge Weigh-in-Motion System." *MEngSc thesis, University College Dublin*.

Moses, F. 1979. "Weigh-in-motion system using instrumented bridges." *Transportation Engineering Journal of ASCE*, 105(3): 233–249.

O'Brien, E. J., Quilligan, M., and Karoumi, R. 2006. "Calculating an influence line from direct measurements." *Bridge Engineering, Proceedings of the Institution of Civil Engineers*, 159(BE1): 31–34.

O'Brien, E. J., Rowley, C., and González, A. 2009. "A regularised solution to the bridge weigh in motion equations." *International Journal of Heavy Vehicle Systems*, 16(3): 310–327.

O'Brien, E., Hajializadeh, D., Uddin, N., Robinson, D., and Opitz, R. 2012. "Strategies for axle detection in bridge weigh-in-motion systems." In *Proc., Proceedings of the international conference on weigh-in-motion (ICWIM 6)*, 79–88.

O'Brien, E. J., and Kealy, N. J. 1998. "Development of a novel bridge weigh-in-motion system." In *Proc., Proceedings of 5th International Symposium on Heavy Vehicle Weights and Dimensions*, 222–235.

Ojio, T., Carey, C., OBrien, E. J., Doherty, C., and Taylor, S. E. 2016. "Contactless bridge weigh-in-motion." *Journal of Bridge Engineering*, 21(7): 04016032.

Ojio, T., and Yamada, K. 2002. "Bridge weigh-in-motion systems using stringers of plate girder bridges." In *Proc., Third International Conference on Weigh-in-Motion (ICWIM3) Iowa State University, Ames*.

Ojio, T., and Yamada, K. 2005. "Bridge WIM by reaction force method." In *Proc., International Conference on Weigh-In-Motion, 4th, 2005, Taipei, Taiwan*.

Oskoui, E. A., Taylor, T., and Ansari, F. 2019. "Method and sensor for monitoring weight of trucks in motion based on bridge girder end rotations." *Structure and Infrastructure Engineering*, 16(3): 481–494.

Park, R., and Paulay, T. (1975). "Strength and Deformation of Members with Torsion." *Reinforced Concrete Structures*, 346-391.

Petersen, S., Hanson, Z., Janson, M., and Minge, E. 2015. "Portable Weigh-in-Motion System Evaluation."Rep. No. MN/RC 2015-03, Minnesota Department of Transportation.

Prakoso, A., Chunduri, H., and Walubita, LF. 2022. "Implementation of Portable Weigh-In-Motion (WIM) Technology on Texas Highways: Technical Report."Rep. No. FHWA/TX-21/5-6940-01-R1, Texas A&M Transportation Institute.

Quilligan, M. 2003. "Bridge Weigh-in-Motion: Development of a 2-D Multi-Vehicle Algorithm 'Licentiate Thesis." *Royal Institute of Technology, Stockholm, Sweden*.

Rahlwes, K. 1970. "Zur Torsionssteiffigkeit von Stahlbetonrechteckquerschnitten." *Beton und Slahlbetonball*, 65(9): 226–228.

Refai, H., Othman, A., and Tafish, H. 2014. "Portable weigh-in-motion for pavement design-phases 1 and 2."Rep. No. FHWA-OK-14-07, Oklahoma Department of Transportation Planning and Research Division.

Rowley, C., OBrien, E. J., González, A., and Žnidarič, A. 2009. "Experimental testing of a moving force identification bridge weigh-in-motion algorithm." *Experimental mechanics*, 49(5): 743–746.

Sekiya, H., Kubota, K., and Miki, C. 2017. "Simplified portable bridge weigh-in-motion system using accelerometers." *Journal of Bridge Engineering*, 23(1): 04017124.

Snyder, R., and Moses, F. 1985. "Application of in-motion weighing using instrumented bridges." *Transportation Research Record*, 1048: 83–88.

Terzioglu, T. 2015. "Behavior and design of spread prestressed concrete slab beam bridges." Doctoral dissertation, Texas A & M University.

TxDOT 2013. "Vehicle Classification Using FHWA 13-Category Scheme, Appendix A." *Traffic Recorder Instruction Manual: Vehicle Classification Using FHWA 13-Category Scheme*.

TxDOT 2020. "Bridge Load Rating Spreadsheet User Guide."

VPG (2011). "Load Cell Technology (Application Note)." *Document Number 11866*. (October 23 2022).

Wall, C. J., Christenson, R. E., McDonnell, A.-M. H., and Jamalipour, A. 2009. "A non-intrusive bridge weigh-in-motion system for a single span steel girder bridge using only strain measurements."Rep. No. CT-2251-3-09-5.

Walubita, L. F., Mahmoud, E., Fuentes, L., Komba, J. J., Teshale, E. Z., and Faruk, A. N. 2021. "Portable WIM systems: Comparison of sensor installation methods for site-specific traffic data measurements."

Wang, H., Zhu, Q., Li, J., Mao, J., Hu, S., and Zhao, X. 2019. "Identification of moving train loads on railway bridge based on strain monitoring." *Smart Struct. Syst*, 23(3): 263–278.

Wang, J., and Wu, M. 2004. "An overview of research on weigh-in-motion system." In *Proc., Fifth World Congress on Intelligent Control and Automation (IEEE Cat. No. 04EX788)*, IEEE, 5241–5244.

Wu, H., Zhao, H., Liu, J., and Hu, Z. 2020. "A filtering-based bridge weigh-in-motion system on a continuous multi-girder bridge considering the influence lines of different lanes." *Frontiers of Structural and Civil Engineering*, 14(5): 1232–1246.

Wu, S., and Law, S. 2010. "Moving force identification based on stochastic finite element model." *Engineering Structures*, 32(4): 1016–1027.

Yamaguchi, E., Kawamura, S.-i., Matuso, K., Matsuki, Y., and Naito, Y. 2009. "Bridge-Weigh-in-Motion by two-span continuous bridge with skew and heavy-truck flow in Fukuoka area, Japan." *Advances in Structural Engineering*, 12(1): 115–125.

Yarnold, M., Golecki, T., and Weidner, J. 2018. "Identification of composite action through truck load testing." *Frontiers in Built Environment*, 4: 74.

Yarnold, M., and Wilson, G. 2015. "Forensic investigation of the route 61 bridge." In *Proc., Structures Congress*, 309–321.

Yu, Y., Cai, C., and Deng, L. 2016. "State-of-the-art review on bridge weigh-in-motion technology." *Advances in Structural Engineering*, 19(9): 1514–1530.

Yu, Y., Cai, C., and Deng, L. 2017. "Vehicle axle identification using wavelet analysis of bridge global responses." *Journal of Vibration and Control*, 23(17): 2830–2840.

Zhang, J., Zhou, F., Hu, S., Mahmoud, E., and Walubita, L. F. 2022. "Development of Multiple-Choice Default Load Spectra Inputs Based on Road Types for the Texas Mechanistic-Empirical Flexible Pavement Design System." *Journal of Transportation Engineering, Part B: Pavements*, 148(2): 04022005.

Zhang, L., Zhao, H., OBrien, E. J., and Shao, X. 2019. "Virtual Monitoring of orthotropic steel deck using bridge weigh-in-motion algorithm: Case study." *Structural Health Monitoring*, 18(2): 610–620.

Zhao, H., Uddin, N., Shao, X., Zhu, P., and Tan, C. 2015. "Field-calibrated influence lines for improved axle weight identification with a bridge weigh-in-motion system." *Structure and Infrastructure Engineering*, 11(6): 721–743.

Zhao, Z., Uddin, N., and O'Brien, E. 2012. "Field verification of a filtered measured moment strain approach to the bridge weigh-in-motion algorithm." In *Proc., the international conference on weigh-in-motion (ICWIM 6)*, 63–78.

Znidaric, A., and Baumgartner, W. 1998. "Bridge weigh-in-motion systems-an overview." In *Proc., second European conference on weigh-in-motion of road vehicles, September 14–16, Portugal.*

.

Žnidaric, A., and Kulauzovic, B. 2018. "Innovative use of bridge-WIM as an efficient tool for optimized safety assessment of bridges." In *Proc., ARRB International Conference, 28th, 2018, Brisbane, Queensland, Australia*.

Žnidarič, A., Lavrič, I., Kalin, J., and Kreslin, M. 2012. "Using strips to mitigate the multiple-presence problem of BWIM systems." In *Proc., 6th International Conference on Weigh-In-Motion (ICWIM 6) International Society for Weigh-In-MotionInstitut Francais des Sciences et Technologies des Transports, de l'Aménagement et des Réseaux (IFSTARR) International Transport ForumForum of European National Highway Research Laboratories (FEHRL) Transportation Research BoardFederal Highway Administration*.

APPENDIX A

DERIVATION OF BRIDGE LIVE LOAD DISTRIBUTION FACTOR

A.1. General

This appendix presents a simplified derivation of live load distribution factors (LLDFs) from mechanics-based first principles. The LLDFs of example bridge and bridge #3 are calculated by this method and compared with AASHTO standards. This appendix supports material in Section 7.

A.2. Methodology

Consider a bridge that is divided into three lanes. Assume the deck is sufficiently stiff transversely to share the loads. When the left and middle lanes are loaded with trucks (wheel loads P), the deformation of the bridge span may be divided into two parts: (i) the vertical deformation caused by the total of the truck loads $\sum P$; (ii) the torsional deformation (since there is an eccentricity between the applied load and the center of the section) caused by the torsional moment $\sum Pe$. Figure A.1 illustrates the two deformation parts.

The vertical deformation Δ_S is calculated as:

$$\Delta_S = \frac{\sum PL^3}{48EI_{xx}} \tag{A.1}$$

where L = length of the bridge span; E = the Young's modulus of the span; and I_{xx} = the moment of inertia along the horizontal axis of the section.

The angle of twist θ can be calculated as:

$$\theta = \frac{\frac{T}{2}\frac{L}{2}}{GJ} = \frac{TL}{4GJ} \tag{A.2}$$

where T = the tortional moment; and G = the shear modulus where approximately G = $0.4E$; J = the torsional stiffness which is calculated as the sum of I_{xx} and I_y.

The deformation along the section is given by:

$$\Delta_T = \frac{\sum PexL}{1.6E\left(I_{xx} + I_y\right)} \tag{A.3}$$

where e = the distance from the load to the center of the section; x = the lateral distance from the center of the section to a specified point; and I_y = moment of inertia along the vertical axis of the section.

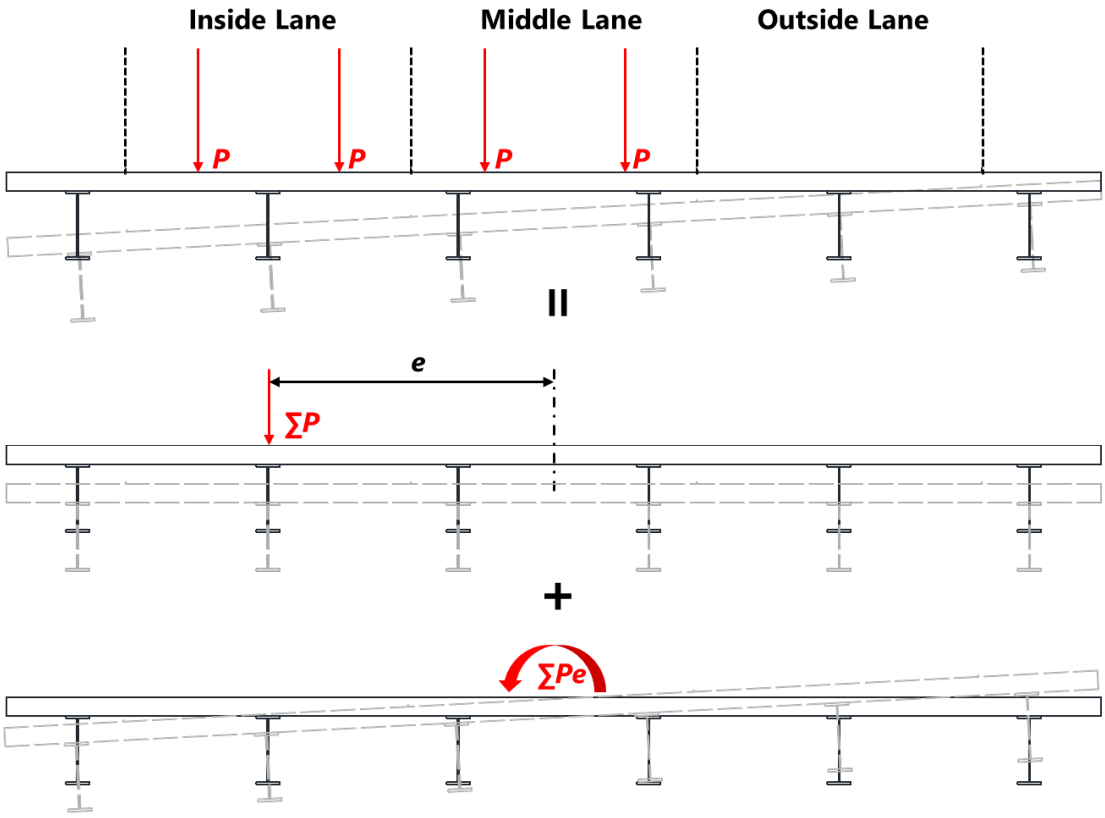

Figure A.1. Bridge Deformation Under Eccentric Loads.

Combining the deflections of the total deformation is obtained from:

$$\Delta_e = \Delta_S + \Delta_T \tag{A.4}$$

Therefore, the live load distribution factor is calculated as:

$$LLDF = \frac{\Delta_e}{\Delta_S} = 1 + \frac{\Delta_T}{\Delta_S} = 1 + \frac{30\left(\frac{e}{L}\right)\left(\frac{x}{L}\right)}{1 + I_y / I_{xx}} \tag{A.5}$$

Concrete might be cracked over time. Park and Paulay (1975) derived the torsional stiffness of reinforce concrete where diagonal cracking was taken into account and Rahlwes (1970) compared theoretical torsional stiffness of concrete section on the cracked and uncracked state. The torsional stiffness between cracked and uncracked

concrete was about 0.1. A torsional stiffness reduction factor Ψ is introduced into Eq. (A.5) to evaluate the live load distribution factor under different concrete deck slab cracking states:

$$LLDF = 1 + \frac{30\left(\frac{e}{L}\right)\left(\frac{x}{L}\right)}{1 + \Psi\left(I_y / I_{xx}\right)} \tag{A.6}$$

Ψ=1: Fully uncracked

Ψ=0.1: Probable cracked torsional stiffness reduction ratio

Ψ=0: Highly cracked

A.3. Example Bridge

Consider the bridge presented in Figure A.2. For example, the bridge has a span length L =110 ft and a width d = 46 ft with a deck thickness t = 8.5 inch. A total of 6 TX-54 girders are equally spaced, such that beam spacing S = 8 ft. The section properties of the deck and girder are calculated in Table A.1.

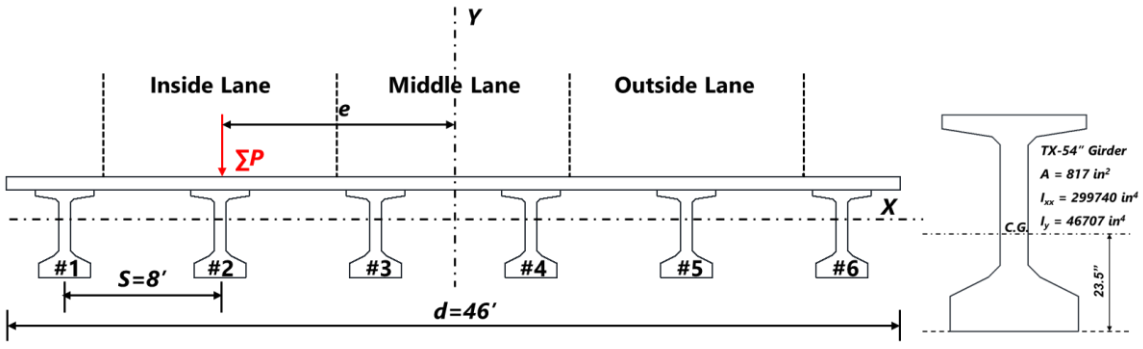

Figure A.2. Example Bridge Cross Section.

Table A.1. Summary of Section Properties along Horizontal Axis (Example Bridge).

Part	*n*	*d/n* (*in*)	*t* (*in*)	*A* (in^2)	*y* (*in*)	*Ay* (in^3)	$y - y_b$ (*in*)	$A(y - y_b)^2$ (in^4)	I_{ox} (in^4)
Deck	1.46	378	8.5	3214	58.2	187055	21	1417374	19349
6×Girder	N/A	N/A	N/A	4902	23.5	115197	-13.7	920056	1798440
					y_b=37.2				I_{xx}=4155220

In Table A.1, *n* = modular ratio; *d/n* = transformed deck width; *t* = deck thickness; *A* = part area; *y* = part center of gravity along the horizontal axis; y_b = neutral axis along the horizontal axis of the section; and I_{ox} = part moment of inertia along horizontal axis.

The neutral axis along the horizontal axis of the section is calculated as:

$$y_b = \frac{\sum Ay}{\sum A} = 37.2\ in \tag{A.7}$$

The moment of inertia along the horizontal axis of the deck slab is obtained by:

$$I_{dx} = \frac{(d/n)t^3}{12} = 19349\ in^4 \tag{A.8}$$

The moment of inertia along the horizontal axis is calculated as:

$$I_{xx} = I_{dx} + A_d e_d^2 + I_{gx} + A_{gx} e_g^2 = 4155220\ in^4 \tag{A.9}$$

Table A.2 summarizes the calculation of section properties along the vertical axis. The moment of inertia along the vertical axis of the deck slab is obtained by:

$$I_{dy} = \frac{(t/n)d^3}{12} = 81295027\ in^4 \tag{A.10}$$

The moment of inertia along the vertical axis is calculated as:

$$I_y = I_{dy} + A_d h_d^2 + I_{gy} + A_g h_g^2 = 213341029\ in^4 \tag{A.11}$$

Table A.2. Summary of Section Properties along Vertical Axis (Example Bridge).

Part	*n*	*t/n* (*in*)	*d* (*in*)	*A* (in^2)	*h* (*in*)	Ah^2 (in^4)	I_{oy} (in^4)
Deck	1.46	5.8	552	3214	0	0	81295027
2×Girders (3 and 4)				1634	48	3764736	93414
2×Girder (2 and 5)		N/A		1634	144	33882624	93414
2×Girder (1 and 6)				1634	240	94118400	93414
							Iy=213341029

In Table A.2, *t/n* = transformed deck thickness; *h* = part center of gravity along the vertical axis; and I_{oy} = part moment of inertia along vertical axis.

Since *e* = 12 ft, the live load distribution factor of different deck slab crack conditions can be calculated as:

$$LLDF_{\psi=1} = 1 + \frac{30(12/110)(12/110)}{1 + 213341029/4155220} = 1.01\ (wheel) \qquad \text{(A.12)}$$

$$LLDF_{\psi=0.1} = 1 + \frac{30(12/110)(12/110)}{1 + 0.1(213341029/4155220)} = 1.07\ (wheel) \qquad \text{(A.13)}$$

$$LLDF_{\psi=0} = 1 + \frac{30(12/110)(12/110)}{1 + 0} = 1.36\ (wheel) \qquad \text{(A.14)}$$

The calculated result is compared with AASHTO Standards. Using LFR method the live load distribution factor is calculated as:

$$LLDF_{LFR} = \frac{S}{6} = \frac{8}{6} = 1.33\ (wheel) \qquad \text{(A.15)}$$

According to LRFD method, the live load distribution factor is calculated as:

$$LLDF_{LRFD} = 0.075 + \left(\frac{S}{9.5}\right)^{0.6}\left(\frac{S}{L}\right)^{0.2}\left(\frac{K_g}{12Lt_s^3}\right)^{0.1} = 0.657\ (lane) = 1.31\ (wheel) \qquad \text{(A.16)}$$

A.4. Bridge #1 Live Load Distribution Factors

LLDF of the Bridge #1 was evaluated with the derived methodology. Figure A.3 shows the cross section of Bridge #1 with the eccentric load and the section properties along the horizontal axis are summarized in Table A.3. Bridge #1 has a span length L =70 ft and a width d = 44.25 ft with a deck thickness t = 7.5 inch. A total of six 54-inch prestressed concrete girders are with beam spacing S = 7.5 ft. The strengths of the concrete deck slab and concrete girder are 7.5 ksi and 4 ksi, respectively. The section properties of the deck and girder along the horizontal axis are calculated in Table A.3.

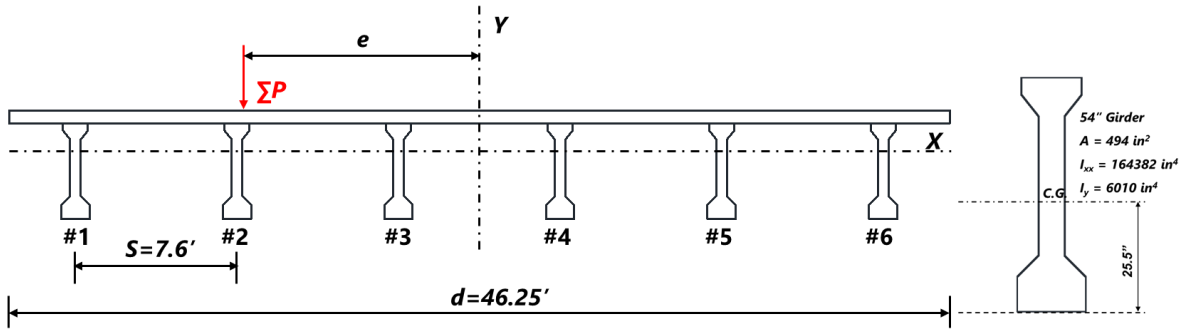

Figure A.3. Bridge #1 Cross Section.

Table A.3. Summary of Section Properties along Horizontal Axis (Bridge #1).

Part	n	d/n (in)	t (in)	A (in^2)	y (in)	Ay (in^3)	$y - y_b$ (in)	$A(y - y_b)^2$ (in^4)	I_{ox} (in^4)
Deck	1.37	387	7.5	2907	57.8	167879	16.3	772361	13605
6×Girder		N/A		2964	25.5	75582	-16	758784	986292
					y_b=41.5				I_{xx}=2531042

The neutral axis along the horizontal axis of the section is calculated as:

$$y_b = \frac{\sum Ay}{\sum A} = 41.5\ in \tag{A.17}$$

The moment of inertia along the horizontal axis of the deck slab is obtained by:

$$I_{dx} = \frac{(d/n)t^3}{12} = 13605\ in^4 \tag{A.18}$$

The moment of inertia along the x axis is calculated as:

$$I_{xx} = I_{dx} + A_d e_d^2 + I_{gx} + A_{gx} e_g^2 = 2531042\ in^4 \tag{A.19}$$

Table A.4 summarizes the calculation of section properties along the vertical axis. The moment of inertia along the vertical axis of the deck slab is obtained by:

$$I_{dy} = \frac{(t/n)d^3}{12} = 68303509\ in^4 \tag{A.20}$$

The moment of inertia along the vertical axis is calculated as:

$$I_y = I_{dy} + A_d h_d^2 + I_{gy} + A_g h_g^2 = 213341029\ in^4 \tag{A.21}$$

Table A.4. Summary of Section Properties along Vertical Axis (Bridge #1).

Part	***n***	***t/n*** *(in)*	***d*** *(in)*	***A*** *(in^2)*	***h*** *(in)*	***Ah²*** *(in^4)*	***I_{oy}*** *(in^4)*
Deck	1.37	5.5	531	2920	0	0	68303509
2×Girders (3 and 4)				988	45.6	2054408	12020
2×Girder (2 and 5)		N/A		988	136.8	18489669	12020
2×Girder (1 and 6)				988	228	51360192	12020
							Iy=140243838

Since e = 12 ft, the live load distribution factor of different deck slab crack conditions for the interior beam (x = 11.4 ft) can be calculated as:

$$LLDF_{\psi=1} = 1 + \frac{30(12/70)(11.4/70)}{1+140243838/2531042} = 1.01\ (wheel) \quad \text{(A.22)}$$

$$LLDF_{\psi=0.1} = 1 + \frac{30(12/70)(11.4/70)}{1+0.1(140243838/2531042)} = 1.13\ (wheel) \quad \text{(A.23)}$$

$$LLDF_{\psi=0} = 1 + \frac{30(12/70)(11.4/70)}{1+0} = 1.84\ (wheel) \quad \text{(A.24)}$$

The calculated result is compared with AASHTO Standards. Using LFR method the live load distribution factor is calculated as:

$$LLDF_{LFR} = \frac{S}{6} = \frac{7.5}{6} = 1.25\ (wheel) \quad \text{(A.25)}$$

According to LRFD method, the live load distribution factor is calculated as:

$$LLDF_{LRFD} = 0.075 + \left(\frac{S}{9.5}\right)^{0.6}\left(\frac{S}{L}\right)^{0.2}\left(\frac{K_g}{12Lt_s^3}\right)^{0.1} = 0.68\ (lane) = 1.36\ (wheel) \quad \text{(A.26)}$$

The field measured LLDF was 1.14 (wheel).

A.4. Bridge #3 Live Load Distribution Factors

The derived methodology was also utilized to evaluate the LLDF of Bridge #3. The field measured results showed lower DFs than the values calculated by AASHTO standards. One possible reason was that the concrete might be cracked over time. For Bridge #3, value of 0.1 was used as the ratio between stiffness of cracked and uncracked concrete. Thus, the thickness of the deck slab was treated as 10 percent of the original thickness.

Figure A.4 shows the cross section of Bridge #3 with the eccentric load and the section properties are summarized in Table A.5.

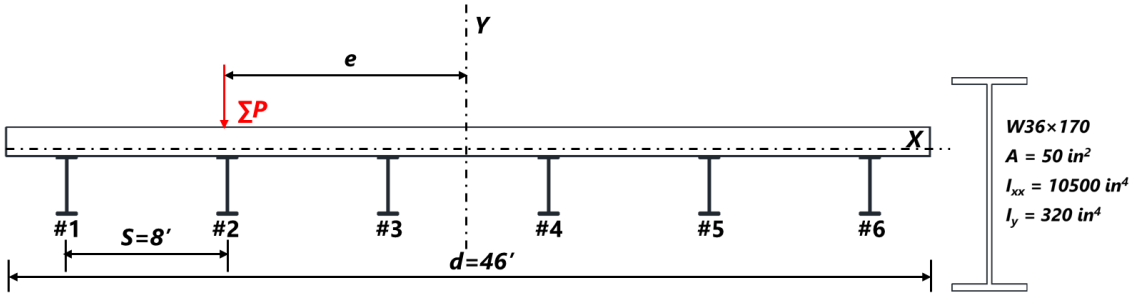

Figure A.4. Bridge #3 Cross Section.

Table A.5. Summary of Section Properties for Horizontal Axis (Bridge #3).

Part	***n***	***d/n*** *(in)*	***t*** *(in)*	***A*** *(in^2)*	***y*** *(in)*	***Ay*** *(in^3)*	***y - y_b*** *(in)*	***A(y - y_b)²*** *(in^4)*	***I_{ox}*** *(in^4)*
Deck	8.3	66.5	17.4	1155	44.8	51762	5.5	34939	29068
6×Girder		N/A		300	18.1	5430	-21.2	134832	63000
					y_b=39.3				I_{xx}=261839

The neutral axis of the section along the horizontal axis is calculated as:

$$y_b = \frac{\sum Ay}{\sum A} = 39.3\ in \tag{A.27}$$

The moment of inertia along the horizontal axis of the deck slab is obtained by:

$$I_{dx} = \frac{(d/n)t^3}{12} = 29068\ in^4 \tag{A.28}$$

The moment of inertia along the horizontal axis is calculated as:

$$I_{xx} = I_{dx} + A_d e_d^2 + I_{gx} + A_{gx} e_g^2 = 261839\ in^4 \tag{A.29}$$

Table A.6 summarizes the calculation of section properties along the vertical axis. The moment of inertia along the vertical axis of the deck slab is obtained by:

$$I_{dy} = \frac{(t/n)d^3}{12} = 29434406\ in^4 \quad \text{(A.30)}$$

The moment of inertia along the vertical axis is calculated as:

$$I_y = I_{dy} + A_d h_d^2 + I_{gy} + A_g h_g^2 = 37500326\ in^4 \quad \text{(A.31)}$$

Table A.6. Summary of Section Properties for Vertical Axis (Bridge #3).

Part	***n***	***t/n*** *(in)*	***d*** *(in)*	***A*** *(in^2)*	***h*** *(in)*	***Ah²*** *(in^4)*	***I_{oy}*** *(in^4)*
Deck	8.3	2.1	552	1159	0	0	29434406
2×Girders (3 and 4)				100	48	230400	640
2×Girder (2 and 5)		N/A		100	144	2073600	640
2×Girder (1 and 6)				100	240	5760000	640
							Iy=37500326

Since *e* = 12 ft, the live load distribution factor of different deck slab crack conditions can be calculated as:

$$LLDF_{\psi=1} = 1 + \frac{30(12/50)(12/50)}{1 + 37500326/261839} = 1.01\ (wheel) \quad \text{(A.32)}$$

$$LLDF_{\psi=0.1} = 1 + \frac{30(12/50)(12/50)}{1 + 0.1(37500326/261839)} = 1.11\ (wheel) \quad \text{(A.33)}$$

$$LLDF_{\psi=0} = 1 + \frac{30(12/50)(12/50)}{1 + 0} = 2.728\ (wheel) \quad \text{(A.34)}$$

The calculated result is compared with AASHTO Standards. Using LFR method the live load distribution factor is calculated as:

$$LLDF_{LFR} = \frac{S}{5.5} = \frac{8}{5.5} = 1.45\ (wheel) \tag{A.35}$$

According to LRFD method, the live load distribution factor is calculated as:

$$LLDF_{LRFD} = 0.075 + \left(\frac{S}{9.5}\right)^{0.6}\left(\frac{S}{L}\right)^{0.2}\left(\frac{K_g}{12Lt_s^3}\right)^{0.1} = 0.71\ (lane) = 1.42\ (wheel) \tag{A.36}$$

The field measured LLDF was 1.06 (wheel).

APPENDIX B

THEORETICAL ANALYSIS OF APPARENT NEUTRAL AXIS OF BRIDGE #3

B.1. General

This appendix presents the theoretical analyses of the change of the apparent neutral axis location influenced by deck stiffness and longitudinal stiffness from the stiff bearing. Concrete creep was considered when calculating the composite section properties and results were compared. The formulas of apparent neutral axis location were derived for different load types. This appendix supports material in Section 7.

B.2. Deck Stiffness

The concrete stiffness influences the modular ratio when calculating the composite section properties, thus changes the elastic neutral axis location. To calculate the theoretical elastic neutral axis location of Bridge #3, reasonable estimates need to be made to determine the concrete modulus of the deck. From engineering judgment, the probable strength of concrete can be estimated as 50 percent more than the original strength. The concrete modulus is considered as 3490 ksi.

The modular ratio n can be calculated as:

$$n = \frac{E_s}{E_c} = \frac{29000}{3490} = 8.3 \tag{B.1}$$

where E_s = the elastic modulus of steel; and E_c = the modulus of concrete.

The effective width of the deck slab was transformed as:

$$b_e = \frac{96}{n} = 11.55\ in \tag{B.2}$$

The elastic neutral axis can be calculated as:

$$y_b = \frac{\sum A\bar{y}}{\sum A} = 39.5\ in \tag{B.3}$$

However, concrete can alter shape if it is subjected to prolonged strain or stress. Take concrete creep into consideration, the modular ratio *n* was used as 20 to evaluate the elastic neutral axis location.

The effective width of the deck slab was transformed as:

$$b_e = \frac{96}{n} = 4.8\ in \tag{B.4}$$

The elastic neutral axis can be calculated as:

$$y_b = \frac{\sum A\bar{y}}{\sum A} = 34.8\ in \tag{B.5}$$

The composite sections of the two cases (without concrete creep and with concrete creep) are shown in Figure B.1. The properties of the composite sections of the two cases are calculated in Table B.1 and Table B.2, respectively.

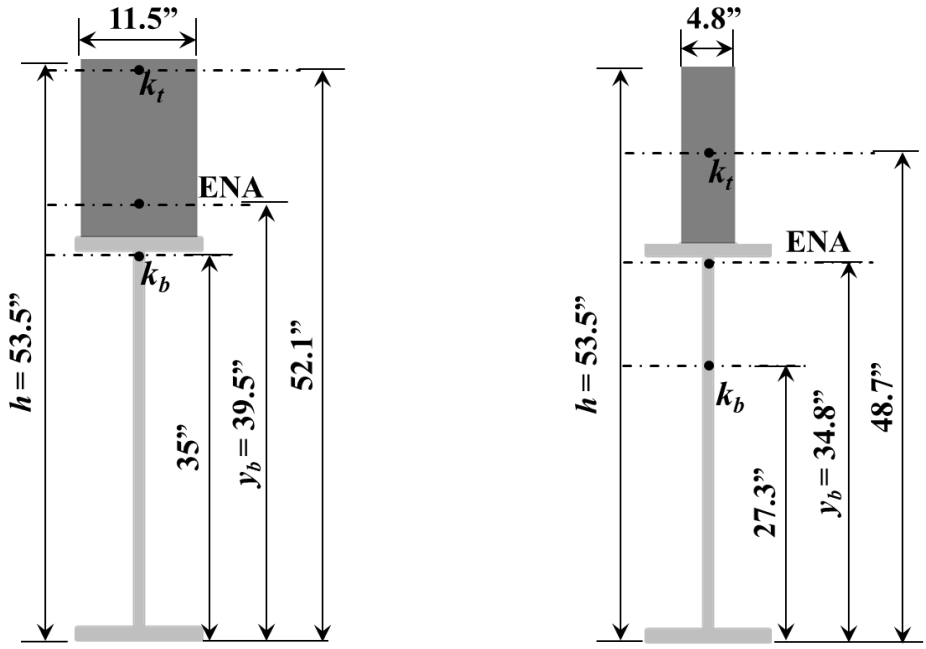

(a) Section Without Concrete Creep (b) Section With Concrete Creep

Figure B.1. Composite Sections of Bridge #3 for Two Concrete Cases.

Table B.1. Summary of Section Properties (Without Concrete Creep).

Part	***n***	***b_e*** *(in)*	***t*** *(in)*	***A*** *(in^2)*	***y*** *(in)*	***Ay*** *(in^3)*	***$y - y_b$*** *(in)*	***$A(y - y_b)^2$*** *(in^4)*	***I_{ox}*** *(in^4)*
Deck	8.3	11.5	17.4	201	44.8	9008	5.3	5646	5049
Girder	N/A	N/A	N/A	49.9	18.1	903	-21.4	22852	10500
					y_b=39.5				I_{xx}=44219

Table B.2. Summary of Section Properties (With Concrete Creep).

Part	***n***	***b_e*** *(in)*	***t*** *(in)*	***A*** *(in^2)*	***y*** *(in)*	***Ay*** *(in^3)*	***$y - y_b$*** *(in)*	***$A(y - y_b)^2$*** *(in^4)*	***I_{ox}*** *(in^4)*
Deck	20	4.8	17.4	83	44.8	3736	10	8300	2098
Girder	N/A	N/A	N/A	49.9	18.1	903	-16.7	13917	10500
					y_b=34.8				I_{xx}=34855

B.3. Longitudinal Stiffness

B.3.1. General

The relatively stiff original bearings may contribute to the change of apparent neutral axis location by inducing a longitudinal force. The bridge span can be treated as a simply supported beam with a longitudinal spring. However, in the extreme case where the bearings are stiff, the boundary condition changes to rigid. Three different load types, one centric load, point loads and distributed loads were theoretically evaluated for the calculation of apparent neutral axis location.

B.3.2. Centric Load

The truck load is treated as a centric load *P* on the center of beam. As shown in Figure B.2a, when the support is rigid, the fixed end moment can be calculated as:

$$M^F = \frac{PL}{8} \tag{B.6}$$

The longitudinal force *F* can be determined by:

$$F = \frac{PL}{8y_b} \tag{B.7}$$

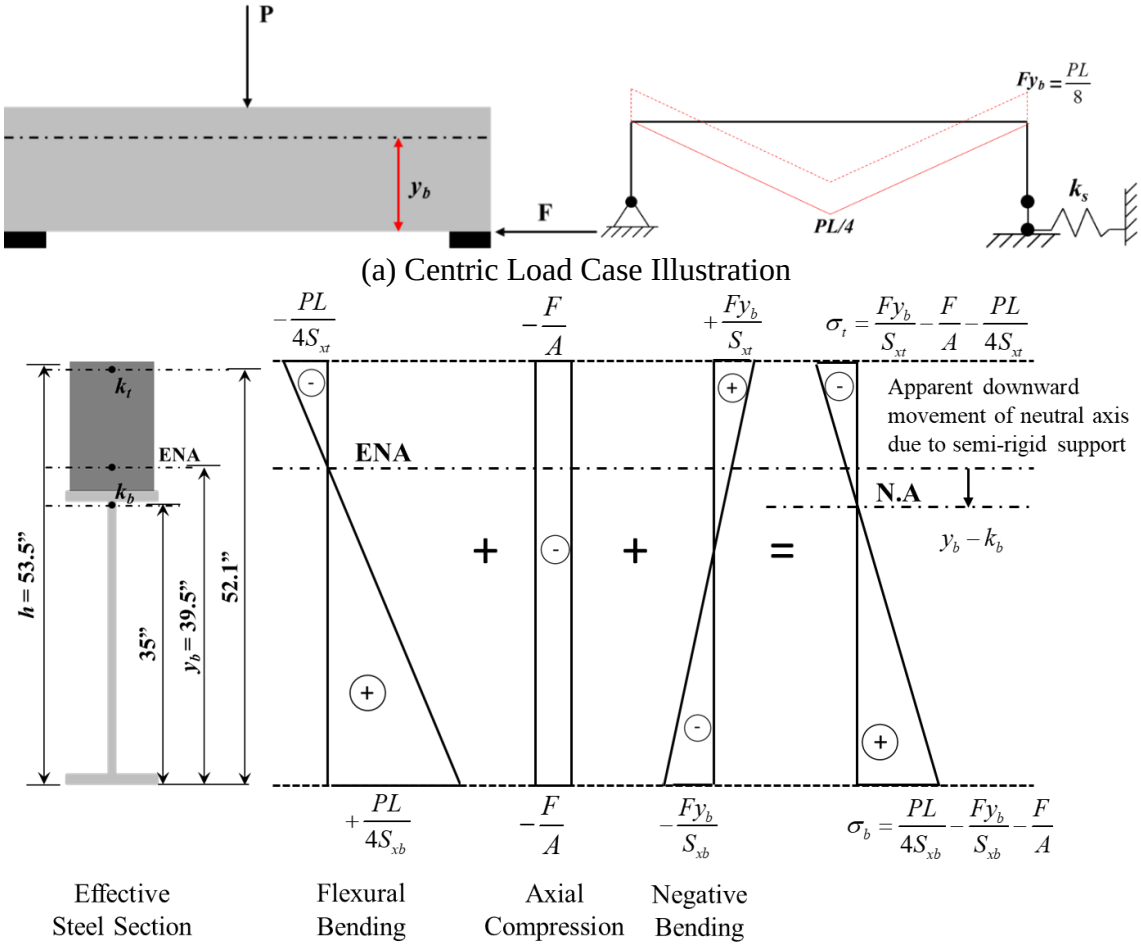

Figure B.2. Effect of Semi-Rigid Bearing Seats on a Simply Supported Concrete Slab on Steel Girder Span (Centric Load Without Concrete Creep Case).

From Figure B.2b, the sum of the two stresses is:

$$\sigma_b + |\sigma_t| = \frac{PL}{8S_{xb}} - \frac{PL}{8y_bA} + \frac{PL}{8y_bA} + \frac{PL}{8S_{xt}} = \frac{PL}{8}\left(\frac{1}{S_{xt}} + \frac{1}{S_{xb}}\right) \tag{B.8}$$

in which the section modulii can be determined by:

$$S_{xt} = k_tA = \frac{k_by_bA}{h - y_b} \tag{B.9}$$

$$S_{xb} = k_bA \tag{B.10}$$

where k_t and k_b = the kern points of top and bottom section, respectively. Utilizing Eq. (B.9) and Eq. (B.10), the bottom stress and the sum of the stresses can be simplified as:

$$\sigma_b = \frac{PL}{8}\frac{y_b - k_b}{k_b y_b A} \tag{B.11}$$

$$\sigma_b + |\sigma_t| = \frac{PL}{8}\left(\frac{h - y_b}{k_b y_b A} + \frac{y_b}{k_b y_b A}\right) = \frac{PL}{8}\frac{h}{k_b y_b A} \tag{B.12}$$

The apparent neutral axis location can be calculated as:

$$N.A = h\frac{\sigma_b}{\sigma_b + |\sigma_t|} = h\frac{\frac{PL}{8}\frac{y_b - k_b}{k_b y_b A}}{\frac{PL}{8}\frac{h}{k_b y_b A}} = y_b - k_b \tag{B.13}$$

B.3.2. Point Loads

The truck load is treated as point loads, *P/2* and *P/2* with a same distance *a* to the end of beam. As shown in Figure B.3a, when the support is rigid, the fixed end moment can be calculated as:

$$M^F = \frac{1}{2}P\frac{a(L-a)}{L} \tag{B.14}$$

The longitudinal force F can be determined by:

$$F = \frac{1}{2}P\frac{a(L-a)}{Ly_b} \tag{B.15}$$

From Figure B.3b, the sum of the two stresses is:

$$\sigma_b + |\sigma_t| = \frac{Pa^2}{2L}\left(\frac{1}{S_{xt}} + \frac{1}{S_{xb}}\right) \tag{B.16}$$

The bottom stress and the sum of the stresses can be simplified as:

$$\sigma_b = \frac{Pa^2(k_b + y_b) - PaLk_b}{2Ly_b Ak_b} \tag{B.17}$$

$$\sigma_b + |\sigma_t| = \frac{Pa^2}{2L}\frac{h}{k_b y_b A} \tag{B.18}$$

The apparent neutral axis location can be calculated as:

$$N.A = h\frac{\sigma_b}{\sigma_b + |\sigma_t|} = h\frac{\dfrac{Pa^2\left(k_b + y_b\right) - PaLk_b}{2Ly_bAk_b}}{\dfrac{Pa^2}{2L}\dfrac{h}{k_b y_b A}} = y_b - \left(\frac{L}{a} - 1\right)k_b \qquad \text{(B.19)}$$

where L is 50 ft and a is 22 ft, the apparent neutral axis can be calculated as:

$$N.A = y_b - \frac{14}{11}k_b \qquad \text{(B.20)}$$

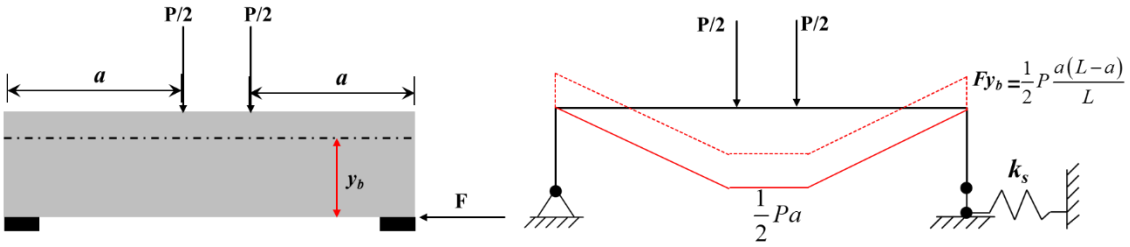

(a) Point Loads Case Illustration

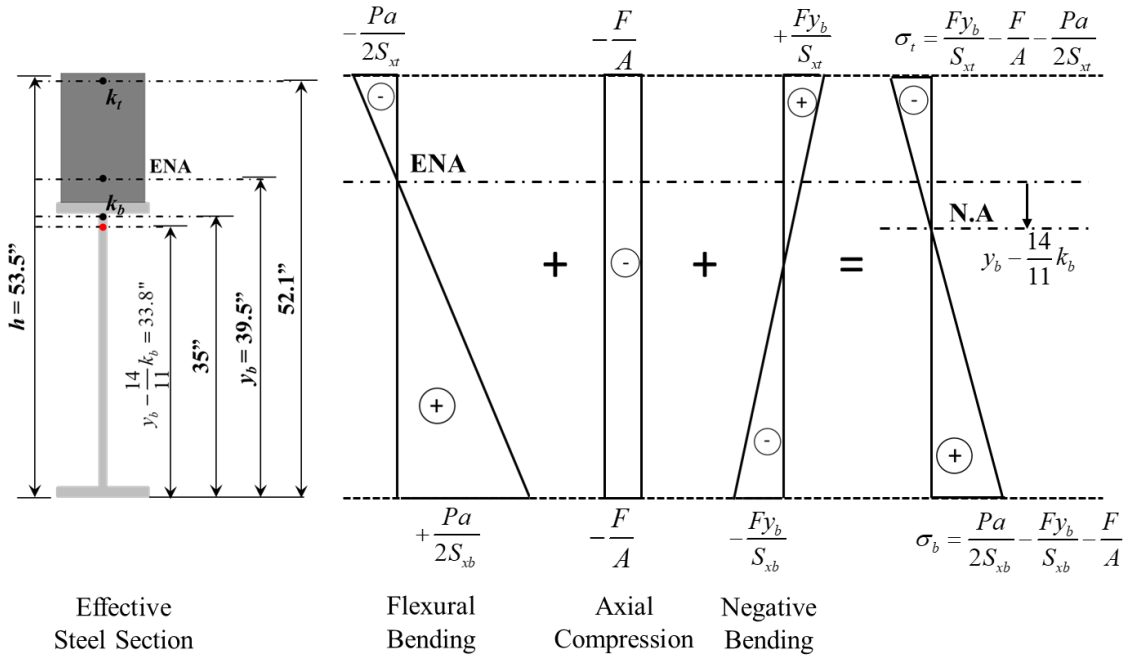

(b) Stress Profile for Point Loads Case

Figure B.3. Effect of Semi-Rigid Bearing Seats on a Simply Supported Concrete Slab on Steel Girder Span (Point Loads Without Concrete Creep Case).

B.3.2. Distributed Load

The truck load is treated as a uniformly distributed load, w along the length of the beam. As shown in Figure B.4a, when the support is rigid, the fixed end moment can be calculated as:

$$M^F = \frac{wL^2}{12} \tag{B.21}$$

The longitudinal force F can be determined by:

$$F = \frac{wL^2}{12y_b} \tag{B.22}$$

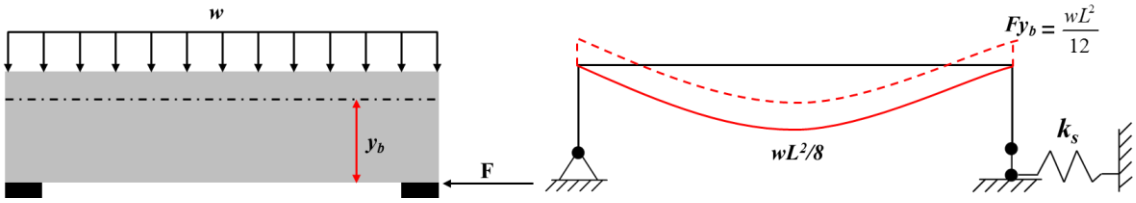

(a) Distributed Load Case Illustration

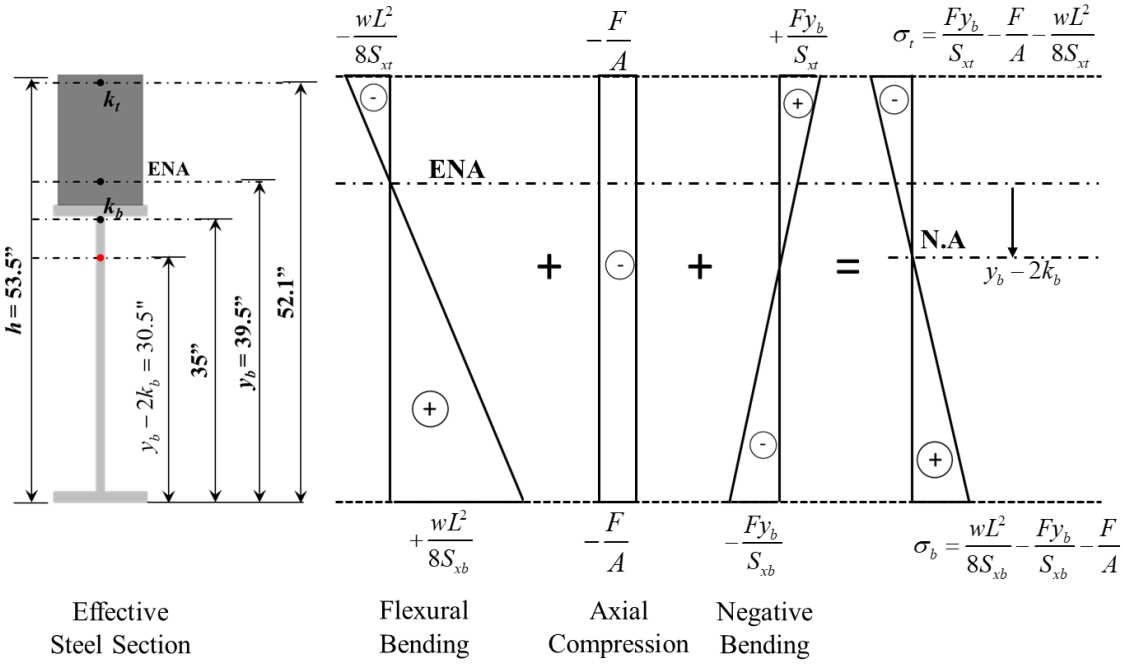

(b) Stress Profile for Distributed Load Case

Figure B.4. Effect of Semi-Rigid Bearing Seats on a Simply Supported Concrete Slab on Steel Girder Span (Distributed Load Without Concrete Creep Case).

From Figure B.4b, the sum of the two stresses is:

$$\sigma_b + |\sigma_t| = \frac{wL^2}{24}\left(\frac{1}{S_{xt}} + \frac{1}{S_{xb}}\right) \tag{B.23}$$

The bottom stress and the sum of the stresses can be simplified as:

$$\sigma_b = \frac{wL^2}{24}\frac{y_b - 2k_b}{k_b y_b A} \tag{B.24}$$

$$\sigma_b + |\sigma_t| = \frac{wL^2}{24}\left(\frac{h - y_b}{k_b y_b A} + \frac{y_b}{k_b y_b A}\right) = \frac{wL^2}{24}\frac{h}{k_b y_b A} \tag{B.25}$$

The apparent neutral axis location can be calculated as:

$$N.A = h\frac{\sigma_b}{\sigma_b + |\sigma_t|} = h\frac{\frac{wL^2}{24}\frac{y_b - 2k_b}{k_b y_b A}}{\frac{wL^2}{24}\frac{h}{k_b y_b A}} = y_b - 2k_b \tag{B.26}$$

B.4. Summary

This section presents the theoretical analyses of the effects of the concrete modulus and longitudinal induced force on apparent neutral axis location. Two concrete modulus (with and without concrete creep) and three load cases were considered. The apparent neutral axis locations are calculated for the combinations and the results are summarized in Table B.3.

Table B.3. Apparent Neutral Axis Calculation Summary.

Apparent Neutral Axis Location (inch) versus Load Cases and Concrete Modulus				
Concrete Modulus	**Theoretical ENA**	**Load Cases**		
		Centric Load	Point Loads	Distributed Load
Without Concrete Creep	39.5	35	33.8	30.5
With Concrete Creep	34.8	27.3	25.3	19.8

The initial neutral axis with fully flexible bearing seats were calculated as 39.5 inch (without concrete creep) and 34.8 inch (with concrete creep), respectively. From the ambient data in Section 7, the average neutral axis movement (downward) under service load was approximately 6 inches. Therefore, the point loads without concrete creep combination had the closest result.